The Impact of Sea-Level Rise and Climate Change on Department of Defense Installations on Atolls in the Pacific Ocean (RC-2334)

Report to the U.S. Department of Defense Strategic Environmental Research and Development Program

USGS science for a changing world

NOAA National Oceanic and Atmospheric Administration U.S. Department of Commerce

Deltares Enabling Delta Life

University of Hawai'i

Cover image: Wave-driven runup and flooding of Roi-Namur Island, Kwajalein Atoll, Republic of the Marshall Islands, on 3 March 2014.

REPORT DOCUMENTATION PAGE

Form Approved
OMB No. 0704-0188

1. REPORT DATE *(DD-MM-YYYY)*	2. REPORT TYPE	3. DATES COVERED *(From - To)*
08/31/2017	Final Report	

4. TITLE AND SUBTITLE
The Impact of Sea-Level Rise and Climate Change on Department of Defense Installations on Atolls in the Pacific Ocean

5a. CONTRACT NUMBER

5b. GRANT NUMBER

5c. PROGRAM ELEMENT NUMBER

6. AUTHOR(S)
Curt D. Storlazzi, Stephen Gingerich, Peter Swarzenski, Olivia Cheriton, Clifford Voss, Ferdinand Oberle, Joshua Logan, Kurt Rosenberger, Theresa Fregoso, Sara Rosa, Adam Johnson, and Li Erikson (U.S. Geological Survey); Don Field, Greg Piniak, Amit Malhotra, and Mark Finkbeiner (National Oceanic and Atmospheric Administration); Ap van Dongeran, Ellen Quataert, Arnold van Rooijen, Edwin Elias, and Mattijs Gawehn (Deltares)

5d. PROJECT NUMBER
RC-2334

5e. TASK NUMBER

5f. WORK UNIT NUMBER

7. PERFORMING ORGANIZATION NAME(S) AND ADDRESS(ES)
U.S. Geological Survey
400 Natural Bridges Drive
Santa Cruz, CA 95060

8. PERFORMING ORGANIZATION REPORT NUMBER
RC-2334

9. SPONSORING/MONITORING AGENCY NAME(S) AND ADDRESS(ES)
Strategic Environmental Research and Development Program
4800 Mark Center Drive, Suite 17D03
Alexandria, VA 22350-3605

10. SPONSOR/MONITOR'S ACRONYM(S)
SERDP

11. SPONSOR/MONITOR'S REPORT NUMBER(S)
RC-2334

12. DISTRIBUTION/AVAILABILITY STATEMENT
Distribution A: unlimited public release

13. SUPPLEMENTARY NOTES

14. ABSTRACT
The U.S. Geological Survey (USGS), National Oceanographic and Atmospheric Administration (NOAA), Deltares, and University of Hawaii (UH) conducted a study to provide basic understanding and specific information on the impact of climate change and sea-level rise on Roi-Namur Island on Kwajalein Atoll in the Republic of the Marshall Islands, which is part of the Ronald Reagan Ballistic Missile Test Site. The primary goal of this joint investigation was to determine the influence of climate change and sea-level rise on wave-driven flooding and the resulting impacts to infrastructure and freshwater resources on atoll islands.

15. SUBJECT TERMS
Sea-Level Rise, Climate Change, Atolls, Global Climate Model, Global Navigation Satellite System, Global Positioning System, Infragravity, Infrared, Precise Point Positioning, Submarine Groundwater Discharge, Sea Surface Temperature, Tropical Cyclone, Terrestrial Lidar Scanning, Universal Transverse Mercator

16. SECURITY CLASSIFICATION OF:			17. LIMITATION OF ABSTRACT	18. NUMBER OF PAGES	19a. NAME OF RESPONSIBLE PERSON
a. REPORT	b. ABSTRACT	c. THIS PAGE			Curt Storlazzi
					19b. TELEPHONE NUMBER *(Include area code)*
UNCLASS	UNCLASS	UNCLASS	UNCLASS	139	831-460-7521

The Impact of Sea-Level Rise and Climate Change on Department of Defense Installations on Atolls in the Pacific Ocean (RC-2334)

By

Curt D. Storlazzi, Stephen Gingerich, Peter Swarzenski, Olivia Cheriton, Clifford Voss, Ferdinand Oberle, Joshua Logan, Kurt Rosenberger, Theresa Fregoso, Sara Rosa, Adam Johnson, and Li Erikson (U.S. Geological Survey)

Don Field, Greg Piniak, Amit Malhotra, and Mark Finkbeiner (National Oceanic and Atmospheric Administration)

Ap van Dongeran, Ellen Quataert, Arnold van Rooijen, Edwin Elias, and Mattijs Gawehn (Deltares)

Annamalai Hariharasubramanian, Matthew Widlansky, Jan Hafner, and Chunxi Zhang (University of Hawaii)

Report to the U.S. Department of Defense Strategic Environmental Research and Development Program

Suggested citation:
Storlazzi, C.D., et al., 2017, The Impact of Sea-Level Rise and Climate Change on Department of Defense Installations on Atolls in the Pacific Ocean (RC-2334): U.S. Geological Survey Administrative Report for the U.S. Department of Defense Strategic Environmental Research and Development Program, 121 p.

Contents

Tables

Figures

Abbreviations

1 sigma	One standard deviation
1D	One-dimensional
2D	Two-dimensional
3D	Three-dimensional
AGI	Advanced Geosciences Inc.
AWAC	Acoustic Wave and Current Meter
BCC-CSM1.1	Beijing Climate Center Climate System Model
CMIP5	Coupled Model Inter-Comparison Project, phase 5
d	day
DEM	Digital Elevation Model
DOD	Department of Defense
ENSO	El Niño Southern Oscillation
ERT	Electrical Resistivity
ET	Evapotranspiration
FWL	Freshwater-lens System
GCM	Global Climate Model
GFDL-ESM2M	Geophysical Fluid Dynamics Laboratory – Earth System Model
GNSS	Global Navigation Satellite System
GPS	Global Positioning System
IC	Incident
IG	Infragravity
INM-CM4	Institute for Numerical Mathematics, Russia, Climate Model
IPCC	Intergovernmental Panel on Climate Change
IR	Infrared
ISODATA	Iterative Self-Organizing Data Analysis Technique
kg	Kilogram
LE95	Linear Error with 95% confidence interval
LN	Natural Logarithm
m	Meter
MHHW	Mean Higher High Water
MHW	Mean High Water
MIROC5	Model for Interdisciplinary Research on Climate
Misc.	Miscellaneous
MLLW	Mean Lower Low Water
MLW	Mean Low Water
MME	Multi-Mean Ensemble
MMU	Minimum Mapping Unit
Mo	Molybdenum
MSL	Mean Sea Level
NE	Northeast
NOAA	National Oceanographic and Atmospheric Administration
NTDE	National Tidal Datum Epoch
NW	Northwest
Pa	Pascal
PIPS	Passivated Implanted Planar Silicon
PPP	Precise Point Positioning
PSU	Practical Salinity Unit
PVC	Poly-Vinyl-Chloride
RCP	Representative Concentration Pathway
RMSE	Root Mean Square Error
RTS-USAKA	Ronald Regan Test Site/United States Army Kwajalein Atoll
s	second
SCI	Scatter Index

SDB	Satellite Derived Bathymetry
SGD	Submarine Groundwater Discharge
SST	Sea Surface Temperature
TC	Tropical Cyclone
TIN	Triangulated Irregular Network
TLS	Terrestrial Lidar Scanning
UH	University of Hawaii
USGS	U.S. Geological Survey
UTC	Coordinated Universal Time
UTM	Universal Transverse Mercator
VLF	Very-Low Frequency
WGS84	World Geodetic System 1984 terrestrial reference system
WGS84[G1674]	World Geodetic System 1984 terrestrial reference system – most current realization

Variables

c_f	Friction coefficient for currents and infragravity wave friction
dx	Numerical grid size
f_w	Friction coefficient for incident waves
H_{m0}	Offshore incident significant wave height
$H_{rms,IC}$	Incident root-mean-squared wave heights
$H_{rms,IG}$	Infragravity root-mean-squared wave heights
$H_{s,IC}$	Incident significant wave heights
$H_{s,IC}$	Infragravity significant wave heights
$H_{s,mean}$	Mean significant wave height
$H_{s,storm}$	Mean significant storm wave height
$H_{s,VLF}$	Very-low frequency significant wave heights
K_H	Horizontal permeability
K_V	Vertical permeability
R_v	Return value
T_p	Peak period for offshore incident waves
$T_{p,mean}$	Mean peak wave period
$T_{p,storm}$	Mean peak storm wave period
θ_w	Wave direction
$\theta_{w,mean}$	Mean wave direction
$\theta_{w,storm}$	Mean storm wave direction
K_r	Reflection coefficient

Chemistry

Ba	Barium
Cl^-	Chloride
NH_4^+	Ammonium
PO_4^{3-}	Phosphate
Po	Polonium
^{214}Po	Polonium isotope 214
^{218}Po	Polonium isotope 218
Rn	Radon
^{222}Rn	Radon isotope 222
Si	Silica
U	Uranium

The Impact of Sea-Level Rise and Climate Change on Department of Defense Installations on Atolls in the Pacific Ocean (RC2334)

By

[1] Curt D. Storlazzi, Stephen Gingerich, Peter Swarzenski, Olivia Cheriton, Clifford Voss, Ferdinand Oberle, Joshua Logan, Kurt Rosenberger, Theresa Fregoso, Sara Rosa, Adam Johnson, Susan Cochran, and Li Erikson

[2] Don Field, Greg Piniak, Amit Malhotra, and Mark Finkbeiner

[3] Ap van Dongeran, Ellen Quataert, Arnold van Rooijen, Edwin Elias, and Mattijs Gawehn

[4] Annamalai Hariharasubramanian, Matthew Widlansky, Jan Hafner, and Chunxi Zhang

1 Abstract

1.1 Project Objectives

The U.S. Geological Survey (USGS), National Oceanographic and Atmospheric Administration (NOAA), Deltares, and University of Hawaii (UH) conducted a study to provide basic understanding and specific information on the impact of climate change and sea-level rise on Roi-Namur Island on Kwajalein Atoll in the Republic of the Marshall Islands, which is part of the Ronald Reagan Ballistic Missile Test Site. The primary goal of this joint investigation was to determine the influence of climate change and sea-level rise on wave-driven flooding and the resulting impacts to infrastructure and freshwater resources on atoll islands.

1.2 Technical Approach

This investigation focused on Roi-Namur Island, which is on the northernmost tip of Kwajalein Atoll in the Republic of the Marshall Islands. Physics-based numerical oceanographic and hydrogeologic models were used to forecast how future sea-level rise and climate change will affect wave-driven flooding of the island and evaluate its resulting impacts to infrastructure and freshwater resources. In order to make accurate projections, such modeling requires physical process formulation and field-data collection for validation and calibration. First, the morphology

[1] U.S. Geological Survey
[2] National Oceanic and Atmospheric Administration
[3] Deltares
[4] University of Hawaii

and benthic habitats of the atoll were mapped to determine the influence of spatially varying bathymetric structure and hydrodynamic roughness on wave propagation over the coral reefs that make up the atoll. Second, historic meteorologic and oceanographic data were analyzed to provide historical context for the limited in situ data and comparison to previous seawater overwash and flooding events. These data were then used to calibrate and validate physics-based, dynamically-downscaled numerical models to forecast future atmospheric and oceanic forcing for a range of climate change scenarios. Third, in situ observations were made to better understand how changes in meteorologic and oceanographic forcing controlled wave-driven water levels, seawater flooding of the island, and the resulting hydrogeologic response. These data were then used to calibrate and validate physics-based, numerical hydrodynamic and hydrogeologic models of the island. The hydrodynamic model was used to forecast future wave-driven island overwash and seawater flooding for a range of climate change and sea-level rise scenarios. The output of those hydrodynamic simulations were then used as input to the hydrogeologic model to evaluate the impact of projected annual wave-driven flooding on the atoll island's freshwater aquifer and at what rate the aquifer can recover. Lastly, the "tipping points" – when the recurrence interval of island overwash and seawater intrusion events is shorter than the recovery times for the impact – were forecast.

1.3 Results

The future climate simulation developed here project that deep-water wave heights and wind speeds around Kwajalein Atoll will decrease slightly, resulting in a small decrease in the magnitude and frequency of the threat to marine operations. The decrease in the frequency of tropical storms and typhoons will also reduce the frequency of weather-based disruptions to marine and terrestrial operations, although the slight increase in intensity of typhoons may result in greater impact of a given storm despite their much less frequent occurrence. The projected slight decrease in rainfall will cause a small reduction in freshwater availability. The potential effects of these changes, however, will likely be insignificant in comparison to the impact of projected increases in sea level in the region. These increases in sea level will result in greater wave-driven runup and island flooding.

The impact of sea-level rise inundation combined with annual wave-driven flooding will begin to significantly negatively impact Roi-Namur when mean sea level is 0.4 meters higher than at present. At this point, without active management measures, the annual amount of seawater flooded onto the island during storms will be of sufficient volume to make the groundwater non-potable year-round. At this level of sea-level rise, much of the isthmus that connects Roi and Namur will be flooded annually, negatively impacting the facilities in those locations. Thus the "tipping point" – the time at which potable groundwater on Roi-Namur will be unavailable – is projected to be reached before 2035 for the RCP8.5+icesheet collapse climate scenario, the 2030-2040 time frame for the RCP8.5 climate scenario, and 2055-2065 for the RCP4.5 scenario. Although active management practices such as post-flood short-term intensive withdrawal and artificial recharge will allow for 3-4 months of potable groundwater on Roi-Namur during the rainy season at higher sea levels, it is not clear as to the sustainability of such operations over the long term with increasing frequency and intensity of wave-driven flooding and island overwash.

Even if the groundwater supply was supplemented or replaced with another source (e.g., desalinization or delivery of freshwater from elsewhere), the annual wave-driven flooding will disrupt operations on Roi-Namur. When mean sea level is 1.0 m higher than at present due to sea-

level rise, at least half of the island is projected to be flooded annually; the areas that will not experience annual flooding include just the runway, the southern portion of the isthmus and associated infrastructure, and the northern portion of Roi where the housing is located. This "tipping point" – at which the majority of Roi's land would be flooded annually – is projected to be reached in the 2055-2065 time frame for the RCP8.5+icesheet collapse climate scenario, the 2060-2070 time frame for the RCP8.5 climate scenario, and sometime after 2105 for the RCP4.5 scenario. Many of the adjacent islands on Kwajalein Atoll that are inhabited and/or have US Department of Defense facilities (Ebeye, Ennylabegan, Ebadon, Ennubirr, Gagan, Gellinam, Gugeegue, Illeginni, Legan, Meck, Omelek) will face a similar fate. Together, these results provide an improved understanding of the planning and management strategies necessary to protect infrastructure and natural resources on low-lying atoll islands globally in the face of future climate change.

Although the focus of the effort presented here was on low-lying atoll islands, there is high relevance of the findings presented here to other tropical, reef-lined islands. Because the majority of housing and critical infrastructure (ports, roads, airports, hospitals, power plants, water treatment plants, etc.) on most tropical high islands such as the Hawaiian Islands, Guam and the Commonwealth of the Northern Mariana Islands, American Samoa, Puerto Rico, and the US Virgin Islands are located within a few meters of current sea level, they, too will confront threats similar to those faced by atolls resulting from increased wave-driven flooding of coastal zones due to sea-level rise. The results presented here, therefore, provide coastal managers an estimate of the effect of different oceanographic, geomorphic, geologic, and hydrologic characteristics on potential coastal hazards caused by wave-driven flooding of coral reef-lined coasts globally and how these may change in the future.

1.4 Benefits

This study provided new understanding of how atoll islands may be affected by projected rises in global sea level and climate change; such information has broad application to atolls and coral reef-lined coastlines worldwide. These results provide an improved and updated timeline of the threats these low-lying atoll islands face to their infrastructure and natural resources due to future climate change. A next step is to comprehensively identify atoll islands managed by the US Department of Defense, both active (e.g., Kwajalein, Wake, Diego Garcia) and decommissioned (e.g., Midway and Johnston), that are most vulnerable to sea-level rise and associated impacts over the next 20 to 50 years using these results and those from theoretical simulations covering the range of reef island morphologies and climate forcing conditions so that managers can prioritize funding for further place-based studies and/or restoration and adaptation efforts. Further, this information, when applied broadly to all islands, will be critical to political leaders globally because it will enable them to identify which island nations and human populations will be displaced and when this displacement is likely to occur. If these impacts are not addressed or adequately planned for, as it becomes necessary to abandon or relocate island nations, significant geopolitical issues could arise.

2 Introduction

The goal of this joint U.S. Geological Survey (USGS), National Oceanographic and Atmospheric Administration (NOAA), Deltares, and University of Hawaii (UH) study was to (1) provide basic understanding and specific information on storm ocean surface wave-driven flooding of atoll islands that house Department of Defense (DOD) installations and (2) assess the resulting impact of sea-level rise inundation and storm wave-driven flooding on infrastructure and freshwater availability under a variety of sea-level rise and climatic scenarios, based on historic information, sea-level rise predictions, and global climate model (GCM) wind, wave, and precipitation output. Products include information on the timing, frequency, and spatial impact of such events at present and in the future, and also defined "tipping points", or those times at which the impact of infrequent events becomes cumulative and therefore more damaging. This information is needed in order to develop climate-change adaptation plans for DOD infrastructure and associated water resources, as well as to develop adequate response strategies by providing the range of parameters under which infrastructure and freshwater supplies may realistically be threatened from sea-level rise inundation and storm wave-induced island overwash.

This investigation focused on Kwajalein Atoll in the Republic of the Marshall Islands. Kwajalein is a large (maximum width ~100 kilometers) atoll system with a large, deep lagoon and large islands that support freshwater lenses. The investigation focuses on the coupling between inundation due to sea-level rise, wave-driven flooding, and the atoll islands' freshwater lenses; the study included in situ field data collection for validation and calibration of physics-based, numerical oceanographic and hydrogeologic models of wave-driven flooding and groundwater dynamics, respectively. Once the models were shown to accurately portray past and present conditions at Kwajalein Atoll, predictive modeling of sea-level rise and climatic impacts to infrastructure and freshwater availability based on sea-level rise projections and GCM wind, wave, and precipitation output was conducted.

This study was designed to provide new understanding of how atoll islands may be affected by projected rises in global sea level and climate change; such information has broad application to atolls worldwide. One direct application is critical information about DOD-managed atolls, both active (e.g., Kwajalein, Wake, Diego Garcia) and decommissioned (e.g., Midway, Johnston) that are most vulnerable to sea-level rise and climate-change impacts over the next 100 years. This provides the understanding needed to prioritize funding for remediation efforts and/or further research (e.g., impacts to threatened and endangered species). Additionally, this study provides new understanding of the impact of climate change on atoll systems and its potential for geopolitical consequences caused by relocation of atoll island-states throughout the world's oceans.

2.1 Project Objectives

The primary goal of this joint investigation was to determine the influence of climate change and sea-level rise on wave-driven flooding and the resulting impacts to infrastructure and freshwater resources on atoll islands. Meteorologic and oceanographic model hindcast data were analyzed first to provide historical context for the limited in situ data and comparison to previous inundation events. Second, the morphology and benthic habitats of the atoll were mapped using high-resolution, remotely sensed, multispectral imagery to determine the influence of spatially varying bathymetric structure and hydrodynamic roughness on wave propagation over the coral

reefs that make up the atolls. Third, in situ observations of waves and water levels under different sets of meteorologic and oceanographic forcing provided a better understanding of how changes in water level over coral atolls affect the propagation of waves of different heights and wavelengths across the reefs and their resulting impact on wave-driven flooding of the atoll islands. Fourth, in situ observations of how the atoll islands' freshwater lenses respond to variations in meteorologic and oceanographic forcing were used to evaluate the impact of wave-driven runup and flooding on an atoll island's freshwater aquifer, determining the rates at which saltwater intrudes into the freshwater lens, and at what rate the aquifer can recover. Lastly, the frequency at which point flooding of facilities and saltwater intrusion events will occur under different projected sea level and climate change scenarios were projected, and these "tipping points", or when the recurrence interval exceeds the impact's recovery times were forecast.

2.2 Background

Observations (e.g., Vermeer and Rahmstorf, 2009; Merrifield et al., 2009) show that global sea level is rising at a rate almost double the Intergovernmental Panel on Climate Change's (IPCC) 2007 report. The high rates of sea-level rise in the western tropical Pacific Ocean where many of the world's (and DOD-managed) atolls are located have recently been tied to an intensification of the easterly trade winds that appear to be driven by variations in the latent heat content of the earth's warming atmosphere, suggesting the possibility that these recent trends may continue under projected emission scenarios (e.g., Merrifield, 2011). Recent estimates (Kopp et al., 2014; Hall et al., 2016) that include rise due to thermal expansion and ice melting show possible sea levels in the tropics exceeding 2 m above 2000 levels by the end of the 21st century. Although a number of other processes drive variations in sea level (e.g., tides, mesoscale eddies, atmospheric circulation), there is no consensus at this point as to how these processes may be affected by global climate change (IPCC, 2007; Collins et al., 2010; Knutson et al., 2010). Thus while the rates of sea-level rise and the ultimate elevations of global sea-level by 2100 are debated, the existing data and predictive models all suggest that eustatic sea-level will be higher by the end of the century and that it will have a profound impact on low-lying coastal areas (Nicholls and Cazenave, 2010).

Sea-level rise is particularly critical for unconsolidated low-lying coral atoll islands, many of which have maximum elevations of less than 4 m above present sea level (Woodroffe, 2008; Dickinson, 2009). Subaerial atoll islands are Holocene features that support 2000 year-old cultures, yet the amount of land and water available for human habitation, water and food sources, and ecosystems is limited and extremely vulnerable to inundation from sea-level rise. Recent observations (Webb and Kench, 2010; Ford and Kench, 2015) have shown that atoll islands' planform areas have migrated under varying wave conditions but relatively maintained themselves over a period of limited (<0.3 m) sea-level rise during the 20th century, suggesting that island planform area (and thus significant erosion or accretion) is unlikely over the next decades. Because published optimal vertical coral reef flat accretion rates for coral reefs exposed to open-ocean storm waves (1-4 mm/yr per Buddemeier and Smith, 1988; Montaggioni, 2005) are up to an order of magnitude smaller than the rates of sea-level rise projected for the years 2000-2100 (8-20 mm/yr per Kopp et al., 2014; Hall et al., 2016), projected sea-level rise will outstrip potential new reef flat accretion, resulting in a net increase in water depth over exposed coral reef flats during the 21st century.

Storm wave-driven overwash and island flooding impacts terrestrial infrastructure and may contaminate the thin freshwater lens underlying islands with saltwater (Wright, 2006), making the islands unsuitable for agriculture and/or habitation. Rising sea levels may exacerbate the impacts of storms and wave action on adjacent coral reefs by reducing wave-energy dissipation due to interactions with the seabed (Gourlay, 1996; McDonald et al., 2006), primarily by reducing wave breaking at the reef crest and increasing the water depth relative to the hydrodynamic roughness over the reef flat (Gourlay, 1996; Pequignet et al., 2009, 2011).

By reducing wave energy dissipation at the reef crest and over the reef flat, sea-level rise will cause larger waves to directly impact the coastline (Storlazzi et al., 2015a) and potentially drive erosion. These larger waves at the shoreline will also increase the resulting wave-driven set-up and run-up (Pequignet et al., 2009; Vetter et al., 2010). Because the corals reefs that form atolls are spatially heterogeneous and storm directions and the resulting wave heights and wavelengths vary in space and time, the wave-driven set-up, run-up, and resulting wave-driven flooding that will result from sea-level rise will also vary both spatially and temporally, especially for locations such as atolls in the Pacific Ocean that are exposed to more than 5 meter-high waves numerous times each year. It is important to note that these resulting temporal and spatial variations in wave-driven run-up and inundation driven by sea-level rise have not yet been addressed; studies to-date use simple geographic information system (GIS)-based passive "bath tub" models of sea-level rise that simply "flood" the land surface up to the projected future sea level (e.g., Titus and Richman, 2001; Mickler, 2009). By not incorporating wave effects, "bath tub" models underestimate the amount and duration of overwash and marine flooding.

2.3 Study Area

This investigation focused on the island of Roi-Namur on Kwajalein Atoll in the Republic of the Marshall Islands (FIGURE 1). Kwajalein is a large (maximum width ~100 kilometers) atoll system with a large, deep lagoon and large islets that support freshwater lenses (Gingerich, 1996; Hunt, 1996) and houses the Ronald Reagan Test Site/United States Army Kwajalein Atoll (RTS-USAKA). Observations (e.g., Vermeer and Rahmstorf, 2009; Merrifield et al., 2009) show that global sea level was rising by 2010 at a rate almost double the Intergovernmental Panel on Climate Change's (IPCC) 2007 report in this area, resulting in a greater frequency of high water levels (TABLE 1). The high rates of sea-level rise in the western tropical Pacific Ocean where

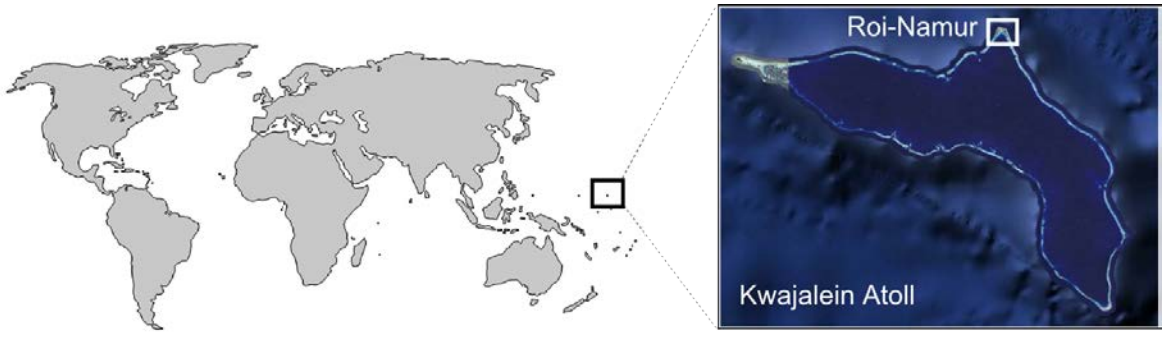

Figure 1. Map showing the location of the study area on Roi-Namur Island, Kwajalein Atoll, Republic of the Marshall Islands.

Kwajalein is located have recently been tied to an intensification of the easterly trade winds that appear to be driven by variations in the latent heat content of the earth's warming atmosphere, suggesting the possibility that these recent trends may continue under projected emission scenarios (e.g., Merrifield, 2011). Recent estimates (Jevrejeva et al., 2009; Milne et al., 2009) and syntheses (Grinsted et al., 2009; Nicholls and Cazenave, 2010) that include rise due to thermal expansion and ice melting show a highly probable sea level increase by the end of the 21st century of up to 2.0 meters above 2000 levels. Although a number of other processes drive variations in sea level (e.g., tides, mesoscale eddies, atmospheric circulation), there is no consensus at this point as to how these processes may be affected by global climate change (IPCC, 2007; Collins et al., 2010; Knutson et al., 2010). Thus while the rates of sea-level rise and the ultimate elevations of global sea-level by 2100 are debated, the existing data and predictive models all suggest that eustatic sea-level will be higher by the end of the century and that it will have a profound impact on low-lying coastal areas (Nicholls and Cazenave, 2010).

Table 1. Variations in decadal sea level statistics at Kwajalein (NOAA, 2013).

Decade	Observations (#)	Mean Sea Level (cm)	Maximum Sea Level (cm)	Observations >95th percentile (#)
1950s	87,648	140.6	253.0	889
1960s	87,672	142.5	256.0	1140
1970s	87,648	145.8	256.0	1479
1980s	87,672	143.9	259.1	1416
1990s	87,648	144.9	262.0	1498
2000s	87,672	153.0	269.5	2931

Sea-level rise is particularly critical for unconsolidated low-lying coral atoll islands like Roi-Namur, many of which have maximum elevations of less than 4 meter above present sea level (Woodroffe, 2008; Dickinson, 2009). Subaerial atoll islands are Holocene features that support 2000 year-old cultures, yet the amount of land and water available for human habitation, water and food sources, and ecosystems is limited and extremely vulnerable to inundation from sea-level rise (FIGURE 2). Because published optimal vertical coral reef flat accretion rates for coral reefs exposed to open-ocean storm waves (1-4 millimeters/year per Buddemeier and Smith, 1988; Montaggioni, 2005) are up to an order of magnitude smaller than the rates of sea-level rise projected for the years 2000-2100 (8-16 millimeters/year per Grinsted et al., 2009; Nicholls and Cazenave, 2010), projected sea-level rise will outstrip potential new reef flat accretion, resulting in a net increase in water depth over exposed coral reef flats. Storm wave-induced flooding and overwash threatens terrestrial infrastructure and can contaminate the thin freshwater lens underlying islets with saltwater (e.g., Wright, 2006), making the islands unsuitable for agriculture and/or habitation. Infrastructure and freshwater supplies on Kwajalein Atoll were impacted by anomalously high sea level and wave-driven flooding in 2008 (Fletcher and Richmond, 2010; FIGURE 3).

Our study site was Roi-Namur Island, located at the northern point of Kwajalein Atoll, (FIGURE 4). Although some sheltering effects are possible from surrounding atolls and islands, in general, owing to their relative orientations, Roi-Namur is subject to swell events out of the north

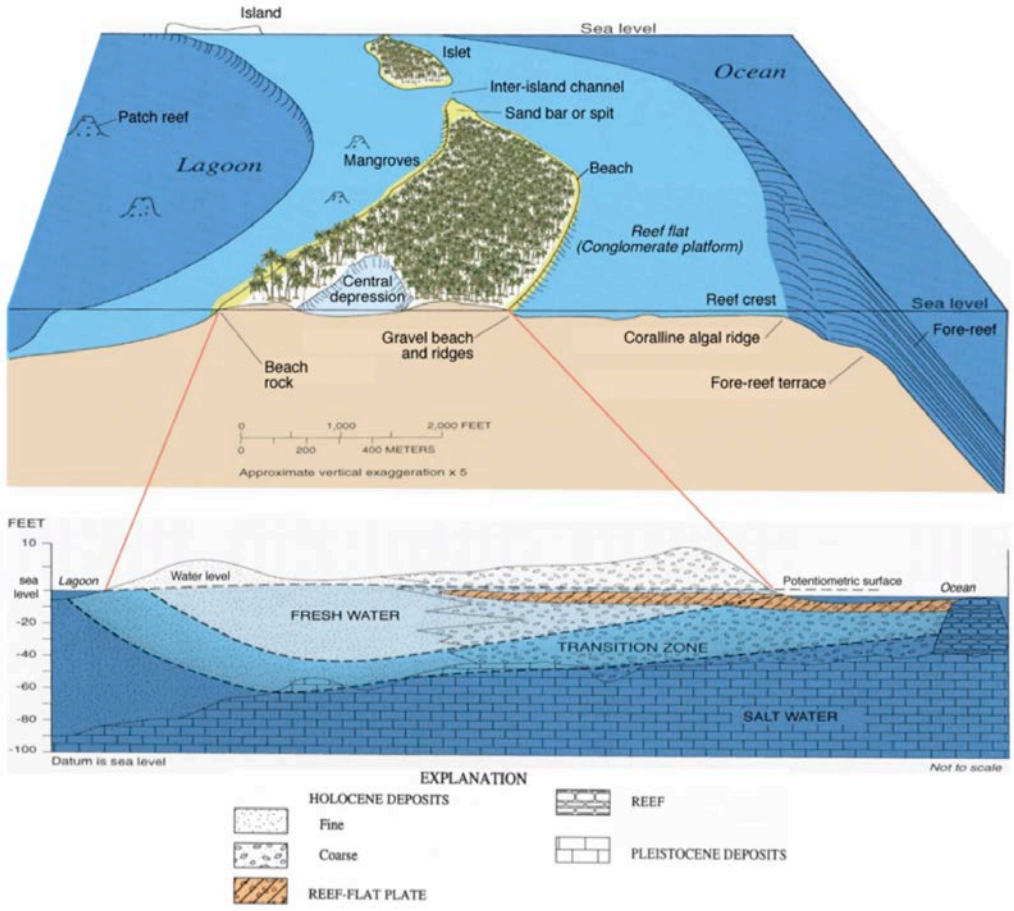

Figure 2. Schematic drawing showing the features of a typical atoll (Fletcher and Richmond, 2010). The exposed ocean side beaches on the atoll islet are commonly steep and gravel rich, whereas the lagoon side beaches are more protected and tend to be gently-sloping and sand rich. Shown are saltwater, transition zone, and freshwater zones.

Figure 3. Photographs of high surf caused saltwater overwash onto freshwater well fields and facilities at Roi Namur Island, Kwajalein Atoll, December 2008 (DOD, Kwajalein Atoll).

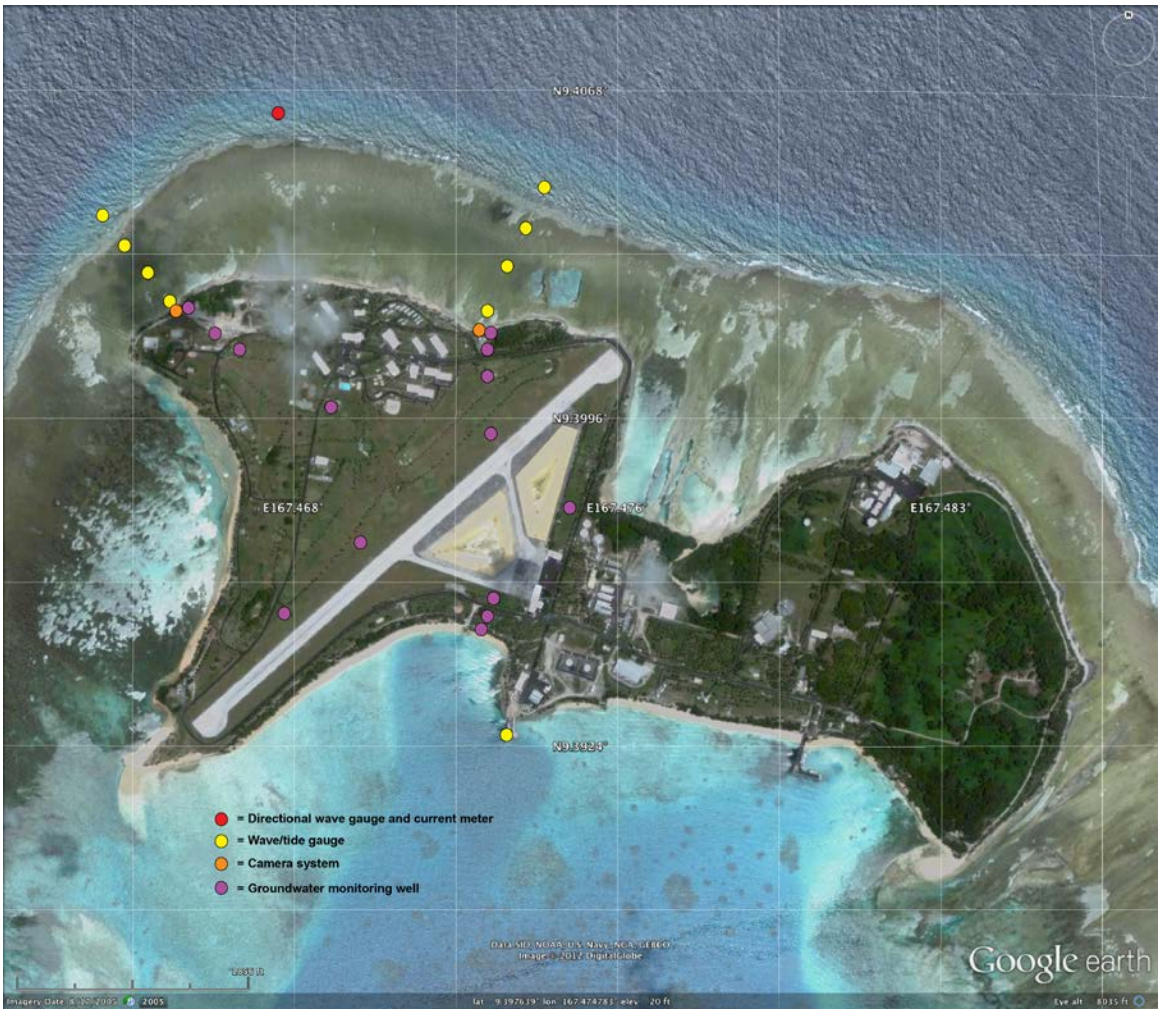

Figure 4. Photograph of Roi-Namur showing location of instrumentation deployed on Roi for this study. The colored circles represent the following: red = directional wave/tide gauge; yellow = non-directional wave/tide gauges; orange = time-lapse camera systems; purple = groundwater wells.

and trade wind waves. Trade winds out of the east-northeast are strongest during winter months (December-February) and weakest in the summer and late fall (July-October); precipitation is greater in the summer and fall than in the winter and spring. The fringing reef is characterized by a gently sloping platform (slope ~ 1:110) that reaches from a narrow sandy beach to a slightly elevated reef crest. The width of the reef flat is 250-350 meter on Roi-Namur. The reef flat sites are fully exposed (dry) at lower low tide (FIGURE 5). Offshore of the reef crest, the fore reef has a steeper slope (~1:6) and greater coral coverage.

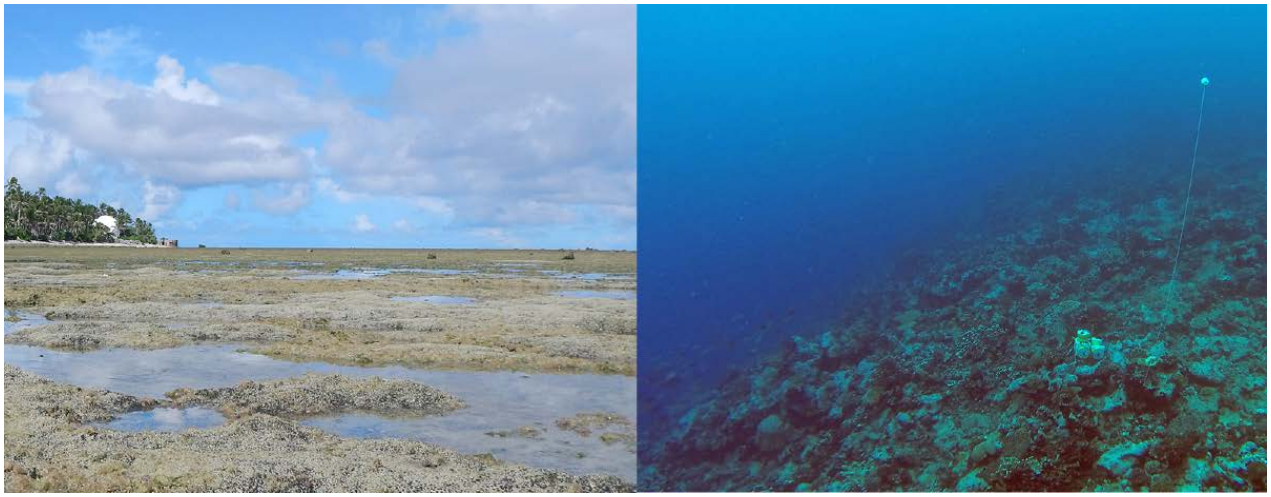

Figure 5. Photographs showing the morphology of Roi's reef flat (left) and fore reef (right).

3 Methods and Results

This investigation focused on the interactions between inundation due to sea-level rise and wave-driven flooding and the resulting impacts to infrastructure and freshwater resources using a series of hydrodynamic models; this required in situ field data collection on Roi-Namur for validating and calibrating the hydrodynamic models. This hydrodynamic model's output was then used as input to a hydrogeologic model to understand the coupling between wave-driven flooding and fresh groundwater resources. Once these coupled models were shown to accurately predict past and present conditions, predictive modeling of sea-level rise and climate change impacts on infrastructure and freshwater resources were then conducted.

3.1 Topographic and Bathymetric Data

The hydrodynamic and hydrogeologic models need to be run on a high-resolution, seamless bathymetric and topographic ("topobathy") digital elevation model (DEM) of Roi (the western portion of the Roi-Namur Island complex). To create the DEM, topographic data from Global Positioning System (GPS) and terrestrial lidar scanning (TLS) collected on the island were combined with bathymetry derived from satellite imagery. Although Roi was the main focus of the study, an approximate shoreline for the adjacent connected island of Namur was also derived for inclusion with the DEM to allow hydrographically valid flow models to be run using the data. The interior portions of Namur were not mapped in detail.

3.1.1 Topographic Data Acquisition

The topographic surveys of Roi were conducted during two field campaigns. In November 2013, geodetic control was established, and portions of the island and reef flat were mapped using static GPS and GPS rovers. In April 2014, TLS was conducted to map the majority of Roi and the surrounding shallow reef flat. The survey equipment used in the topographic surveys is shown in FIGURE 6.

3.1.1.1 Geodetic control

Although pre-existing survey benchmarks are located on the island, published survey control coordinates were not available for those markers at the time of the study. To establish vertical and horizontal survey control for the project, static GPS occupations were conducted on an existing benchmark. A centrally located Defense Mapping Agency benchmark (stamped "GOLF") was chosen as the primary benchmark. A total of five valid static GPS occupations spanning four days were conducted, totaling more than 46 hours of static GPS data. These occupations were post-processed and averaged to determine a survey grade position for the benchmark. Due to the lack of nearby publically available continuously operating GPS reference stations, Precise Point Positioning (PPP) was used for static GPS post-processing within the Novatel Waypoint Grafnav software. PPP uses the precise position and clock data from Global Navigation Satellite System (GNSS) satellites to determine the position of an autonomously operating GPS receiver with a sub-decimeter level of precision (Novatel, 2014). The horizontal and vertical standard deviations of the five averaged position solutions for "GOLF" were 0.019 meter and 0.044 meter, respectively. Although there are no established USGS guidelines for GPS

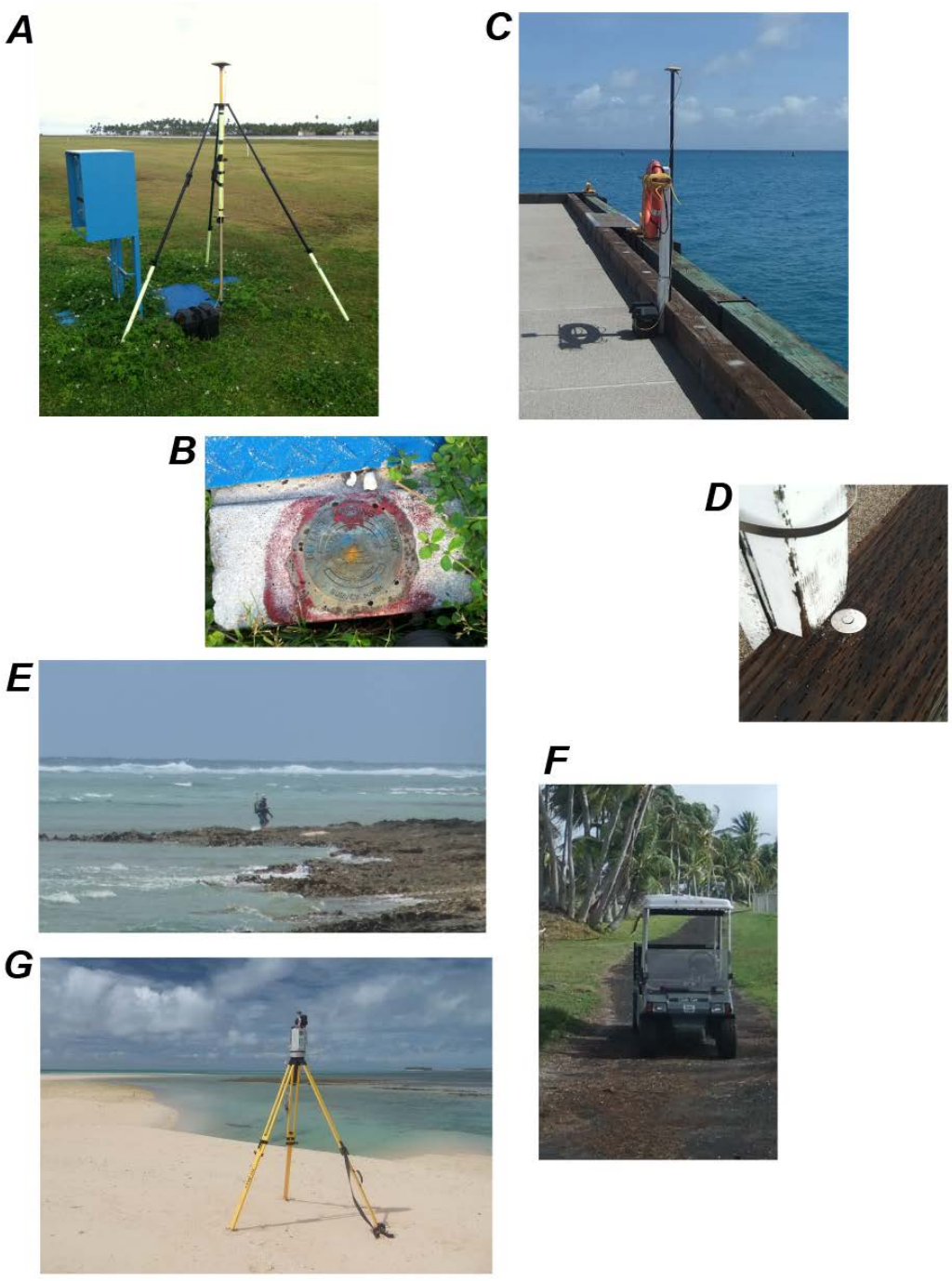

Figure 6. Photographs of some of the instruments and benchmarks used to develop the topobathy DEM of Roi-Namur. A. Static GPS base station used to establish horizontal and vertical survey control on "GOLF" benchmark. B. Defense Mapping Agency "GOLF" benchmark. C. Static GPS occupation on USGS "TIDE" benchmark above temporary tide station. D. "TIDE" benchmark consisting of a nail with a washer stamped "USGS". E. Surveyor using a GPS backpack to collect GPS data on the reef flat during low tide. F. Golf cart with survey-grade GPS unit used to collect topographic GPS data. G. Tripod-based terrestrial lidar scanner (TLS) used to collect topographic point cloud data on the island.

measurements using PPP processing, the number and duration of occupations, the vertical peak-to-peak values, and the standard deviation of elevations for the occupations correspond to a USGS Level III quality established for differential GPS (Rydlund, 2012). The horizontal datum for these coordinates is World Geodetic System 1984 (WGS84); the vertical datum is the WGS84 ellipsoid. In order to allow the survey data from this project to be more easily transformable into the North American Datum 1983 (NAD83) PA11 datum, the final reference coordinates for "GOLF" were transformed into a common epoch of 2010.000 using the National Geodetic Survey HTDP software.

All elevation data for this project were referenced to the WGS84 ellipsoid. To derive a vertical transformation between the WGS84 ellipsoid and the water-level datums developed for the project, a temporary tidal benchmark ("TIDE") consisting of nail with a washer stamped "USGS" was established above the pressure sensor located on the fuel pier. A total of five valid static GPS occupations were conducted on this benchmark. These occupations were post-processed differentially using the GPS base station located at GOLF as the reference station. These solutions were averaged to calculate a precise WGS84 ellipsoid height at the tidal benchmark. The horizontal and vertical standard deviation of the position solutions for "TIDE" was 0.001 meter and 0.008 meter, respectively. The coordinates for the GOLF and TIDE benchmarks are listed in TABLE 2.

Table 2. Vertical transformations from the WGS84 ellipsoid to project water level datums.

Vertical Datum	Transformation from WGS84 Ellipsoid (m)
WGS84 Ellipsoid	0.000
Mean higher high water (MHHW)	32.073
Mean high water (MHW)	31.865
Local mean sea level (MSL)	31.356
Mean low water (MLW)	30.831
Mean lower low water (MLLW)	30.748

3.1.1.2 Water level datums

In order to establish water-level datums for the project, a temporary tide station consisting of an RBR Solo D.Tide pressure sensor was deployed at the Roi fuel pier. The instrument was fastened to the pier using a securely mounted bracket which allowed the instrument to be removed for servicing and replaced at the exact same elevation the pier. The vertical offset between this position and the tidal benchmark established above it was measured at 5.709 meters.

Following the techniques described in *NOAA Special Publication NOS CO-OPS 2*, the tidal record collected at this station was used to derive local water-level datums equivalent to the current (1983-2001) National Tidal Datum Epoch (NTDE). Using the Standard Method (also known as the Range Ratio Method) the observed water levels for the 10-month period from May 2014 to February 2015 were tabulated and compared with published monthly water level data from the NOAA Kwajalein tide station (NOAA Station ID #1820000), located approximately 80 kilometers south of Roi-Namur. The Kwajalein station is situated in the same atoll lagoon as the

Roi-Namur station, making it an appropriate primary station for deriving the Roi-Namur datums. Using the published monthly water level from the Kwajalein station, the observed water level datums at the Roi-Namur station were corrected to their estimated NTDE equivalents. By fitting a regression to the stated accuracies for different durations of water level records listed in *NOAA Special Publication NOS CO-OPS 2*, we determined that with 10 months of data, the estimated accuracy of the NTDE equivalent water level datums is 0.019 meter (NOAA, 2003). Using the GPS-determined WGS84 ellipsoid height for the Roi-Namur station, transformations between the ellipsoid and the various water levels were calculated. These datums and their relations to the WGS84 ellipsoid are shown in FIGURE 7. Direct vertical transformations from the WGS84 ellipsoid to the project water level datums are listed in TABLE 3.

3.1.1.3 Topographic GPS surveys

Topographic GPS surveys were conducted during two field operations in November 2013 and April 2014. For areas on the island that were accessible by vehicle, these surveys were conducted by mounting a Topcon GRS1 dual-frequency GPS receiver to the upper roof support of an electric golf cart. Accurate vertical offset measurements were made between the antenna and the ground, and were applied during post-processing to derive ground-level measurements. All accessible roads, runways and flat areas of the island were surveyed with this method.

For beaches and other areas that were not accessible with the vehicle, surveys were conducted on foot, using a GPS backpack. A Topcon GRS1 GPS receiver was mounted to the backpack while the surveyor walked to collect continuous data. Accurate vertical offset measurements between the antenna and the ground were applied during post-processing to provide ground-elevation measurements. The shallow intertidal reef flat was also surveyed on foot with a GPS backpack. Surveys were timed to coincide with low tide so that as much of the reef flat as possible could be surveyed.

Because the study area is located on an active military base with stringent limitations on radio frequency transmissions, all GNSS surveys for this project were conducted without real-time data links for kinematic processing. For topographic GPS surveys, raw data from GPS rovers was collected in autonomous mode, and kinematic post-processing (PPK) was conducted after the survey using Novatel Waypoint GrafNav software. Baselines were processed to the locally established temporary GPS base station located on the GOLF benchmark. All data was collected using survey-grade dual-frequency receivers collecting continuous data at a rate of 1 Hz. A total of 99,561 GPS measurements were collected. Some radio frequency interference, possibly related to nearby military equipment, was noted during the post-processing of these data. Poor data quality was also noted in some areas with an overhead vegetation canopy. Data with poor quality indicators calculated by the post-processing software were filtered out before inclusion into the final data for DEM creation. All of the GPS data was projected in the Universal Transverse Mercator (UTM) coordinate reference system (zone 58 North, meters), referenced to the WGS84 datum. Elevation values were referenced to the WGS84 ellipsoid.

3.1.1.4 Terrestrial lidar scanning (TLS)

TLS surveys were conducted on the island of Roi during the April 2014 field operation. A Riegl VZ-1000 tripod-based lidar scanner was placed at 31 locations on the island during 6 days of field operations. These scan positions were chosen to provide maximum line-of-sight coverage of the island and the exposed portions of the reef flat during low tides. Scans were typically

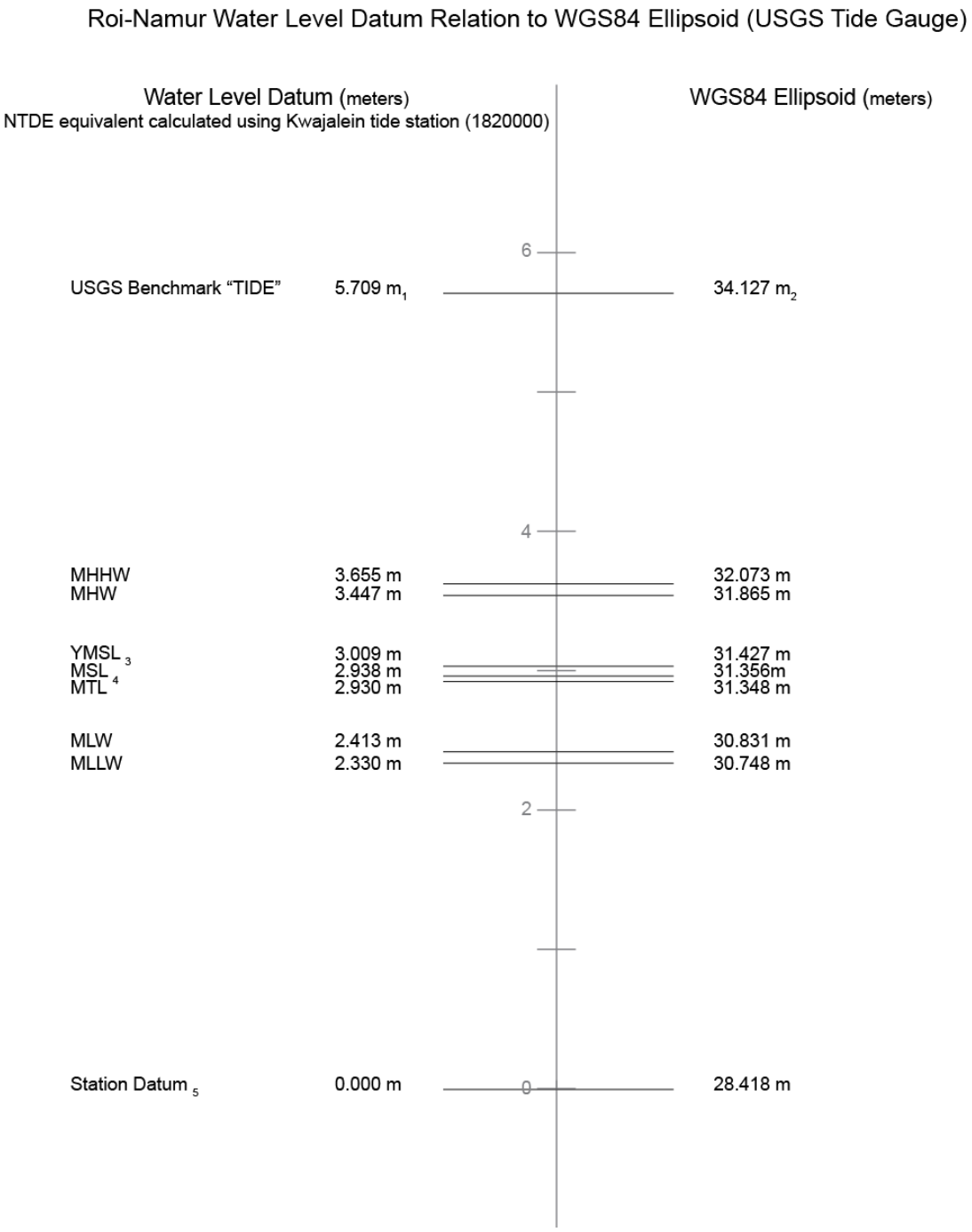

Figure 7. Chart showing project water level datums developed for temporary Roi-Namur tide station, and their relations to the WGS84 ellipsoid. Water level datums are adjusted to the current National Tidal Datum Epoch (NTDE) using the Kwajalein tide station (NOAA ID 1820000). Notes: 1) Established on Roi-Namur fuel pier directly above pressure sensor; 2) Ellipsoid height determined through static GPS observations at benchmark; 3) Yearly Mean Sea Level computed using available data between 24 April 2014 and 15 March 2015.

conducted in panoramic mode, creating a detailed point cloud of all unobstructed surfaces in a 360 degree view of the scanner within a maximum range of 1.4 kilometers. In total, approximately 620 million precise point measurements were collected during these surveys.

Table 3. GPS-derived coordinates for survey benchmarks used for the project.

	Geographic Coordinates (WGS84[G1674])		UTM Coordinates, Zone 58 North (WGS84[G1674])		Ellipsoid Height (WGS84, m)
BM ID	Latitude	Longitude	Northing (m)	Easting (m)	
GOLF	N 9º 23' 50.25291"	E 167º 28' 13.21624"	1039731.614	771302.064	32.852
TIDE	N 9º 23' 33.80879"	E 167º 28' 23.59100"	1039228.382	771622.314	34.127

Spatial registration of the scanner locations was accomplished using cylindrical reflective targets placed in the scanner's field of view. The precise position of each target was measured using 1-minute long PPK GPS occupations using a Trimble R10 GPS receiver. These occupations were post-processed using the Trimble Business Center software package, using the temporary GPS base station located on the GOLF benchmark to maintain consistency with other survey datasets in the project. Point cloud registration and initial editing was performed using the Riegl Riscan Pro software package. In several of the scan positions, mismatches with adjacent point clouds were noted. These errors likely resulted from poor GPS precision while measuring the positions of one or more of the reflectors. For these scans, improved registration was attempted by disabling the reflectors with the poorest residuals. If this did not improve registration, a point cloud matching routine within Riscan Pro called Multi-Station Adjustment (MSA) was utilized to improve the point cloud position in relation to adjacent point clouds. In all cases, scan position solutions adequate for DEM construction were achieved.

Point cloud cleaning and filtering were performed on the registered point clouds to produce a subset of ground measurements suitable for constructing a bare-earth DEM. Using Riscan Pro, several filtering techniques were used on each point cloud: 1) Octree filtering was performed using a 10-centimeter window to reduce data density; 2) all data points further than 400 meters from the scanner were filtered to remove points with potentially higher spatial uncertainty; 3) erroneous data points (noise) were manually removed. These cleaned point clouds were then exported as LAS files, and imported into Maptek I-Site Studio software for further manual editing and triangulated irregular network (TIN) creation. For the purpose of creating a bare earth TIN, buildings and large areas of vegetation were manually removed. For scan positions near the water, a reflectance or intensity based filter was used to remove erroneous data points that likely resulted from reflections off the water surface. A cell-based minimum elevation filter was then applied to select the lowest point in a 0.5-meter cell. This served to remove most high vegetation such as palm trees and bushes that were present in the data. The remaining points were visually inspected and any remaining vegetation points were manually removed. The final points were exported as a single point cloud for DEM creation in ArcGIS. All of the TLS point data were projected in the Universal Transverse Mercator (UTM) coordinate reference system (zone 58 North, meters), referenced to the WGS84 datum. Elevation values were referenced to the WGS84 ellipsoid.

3.1.2 Bathymetric Data Acquisition

There are currently no high-resolution bathymetric data for the study area. This situation is typical in many remote areas around the globe, where the cost of higher resolution bathymetry generated by technologies like multibeam sonar or airborne lidar is prohibitive. Even in developed countries like the United States, cost restrictions usually limit updating bathymetry to areas directly related to shipping. For areas not related to shipping, it is common to see bathymetric charts and data that have not been updated since the late 1800s.

It has long been recognized that certain bathymetric features are obvious in many types of remotely sensed imagery. Since Lyzenga (1978, 1981) first introduced the theory behind determination of bathymetry using passive remote sensing, there has been considerable research in this area. Lyzenga (1978) developed his initial theories and then applied them to Landsat Multispectral Scanner and airborne Multispectral Scanner simulator (Lyzenga 1981). Philpot (1989) and Maritorena et al. (1994) followed with further development, documenting the validity and limitations of using passive remote systems for bathymetric mapping. More recently, heightened interest in coral reefs due to global bleaching events has caused increased interest in deriving bathymetry from new entries into the multi- and hyperspectral sensor market. For example, Stumpf et al. (2003) used IKONOS to map bathymetry over two coral reef atolls in the Hawaiian Islands, and Mishra et al. (2004) used IKONOS and QuickBird (Mishra et al. 2006) to map the bathymetry of Roatan Island, Honduras. The use of hyperspectral imagery to map bathymetry has been investigated by Lee et al. (1999, 2001, 2002) and Wozencraft et al. (2003). Depth of light penetration obviously limits passive remote systems, with accurate depths reported up to 25 meters by Green et al. (2000) and nearly 30 meters by Stumpf et al. (2003). These accuracies were obtained in clear water; turbidity can drastically reduce these maxima.

3.1.2.1 Satellite data

The WorldView-2 (launched 8 October 2009) and WorldView-3 (launched 13 August 2014) commercial imaging satellites were used in this study. Both satellites acquire 16-bit data in eight multispectral bands including coastal (0.400 – 0.450 micro-meter), blue (0.450 – 0.510 micro-meter), green (0.510 – 0.580 micro-meter), yellow (0.585 – 0.625 micro-meter), red (0.630 – 0.690 micro-meter), red edge (0.705 – 0.745 micro-meter), near infrared 1 (0.770 – 0.895 micro-meter) and near infrared 2 (0.860 – 1.040 micro-meter) and one panchromatic band (0.770 – 0.895 micro-meter). There is a slight difference in spatial resolution for the two satellites, WorldView-2 at nadir is 1.84 meters, WorldView-3 at nadir is 1.24 meters. Prior to initiation of field activities for this project, a WorldView-2 satellite image (collection date 12 September 2009) of the Roi-Namur study area (FIGURE 8) was acquired from the US Department of Agriculture. This image served as the source of the initial, draft satellite-derived bathymetry (SDB) product as well as a guide for field operations during the April 2014 field mission.

Although the water clarity of the 2009 image allowed for visualization of benthic habitats as deep as 30 meters in the lagoon, wind at the time of image acquisition caused considerable wave action with obvious white caps and ocean swell—which made derivation of SDB difficult. To improve on the draft SDB product, NOAA leveraged an existing contract with the satellite vendor, DigitalGlobe to task additional satellite imagery acquisitions. However, issues with wind, and cloud cover continued to hamper image acquisition. From April 2014 to January 2015 an additional nine satellite images of the study site were collected—six WorldView images (2-meter pixel size, 8 spectral bands) and three IKONOS images (4-meters pixel size, 4 spectral bands). All

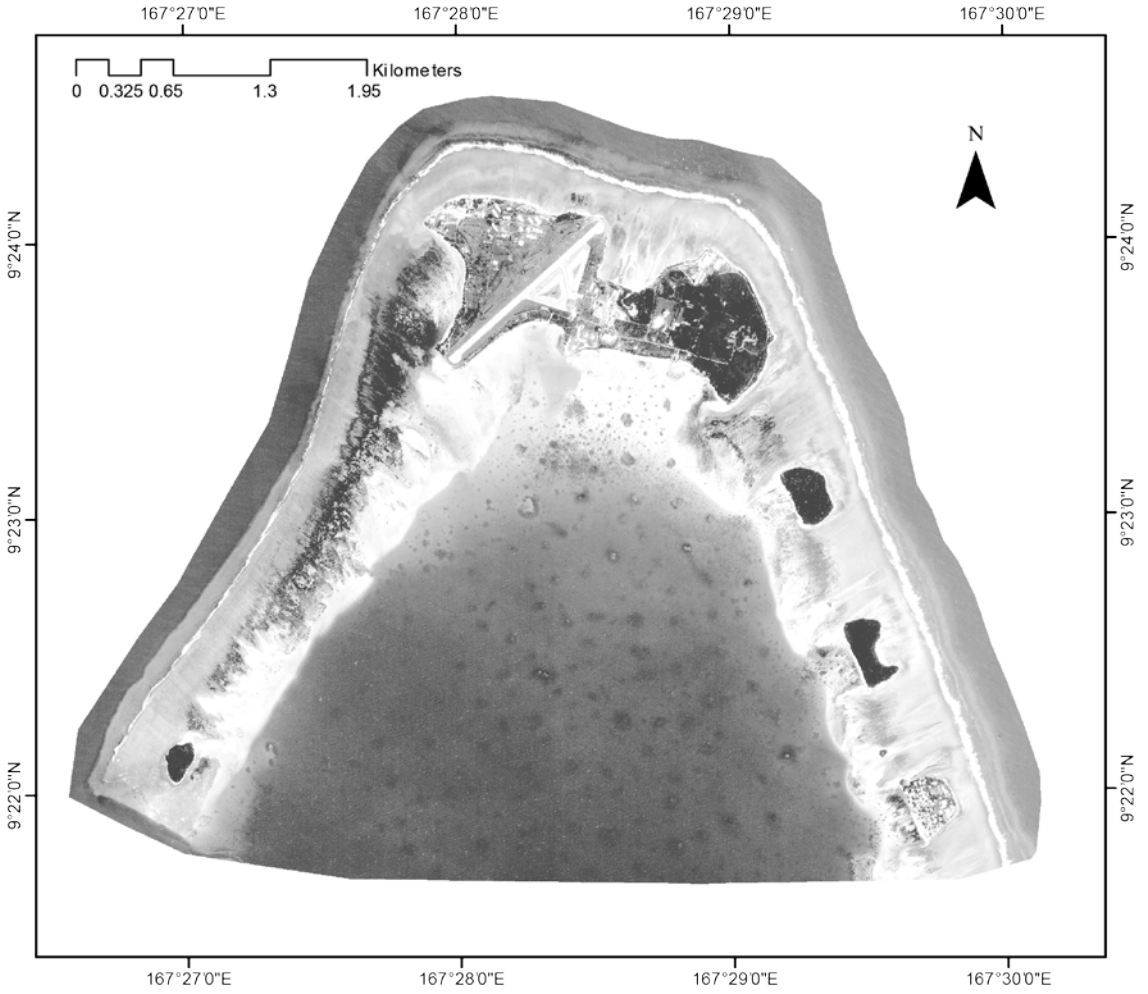

Figure 8. WorldView-2 satellite image of the Roi-Namur study area collected on 12 September 2009 showing band 2 with a histogram equalize stretch.

images had their limitations. As a result, the final SDB and mapping products were a composite of several images. The 24 September 2014 WorldView-3 image (FIGURE 9) had the lowest ocean swell and wind conditions (approximately 7 kilometers/hour), and served as the primary image. However, that image also suffered from cloud cover, so areas under the clouds and cloud shadows were assessed using the original 9 December 2009 WorldView-2 image obtained from USDA. The primary image happened to be collected at low tide, with little to no water present on the reef flat. To provide depth estimates for the reef flat, two WorldView-2 images acquired at higher tides (29 December 2014 and 23 January 2015) were used to fill that gap.

3.1.2.2 Bathymetric field data acquisition

Water depth reference data was collected during a field mission in the Roi-Namur study area during 25-29 April 2014. Water depth was recorded using a Garmin Fathometer (Model 898) in conjunction with a Trimble GeoExplorer GPS (6000 series Geo XH with Trimble Tornado antenna). There were no water level recorders or tide gauges functional during the April 2014 field mission. In lieu of tide gauge data, survey grade GPS (Trimble R7 with a Trimble "Zephyr

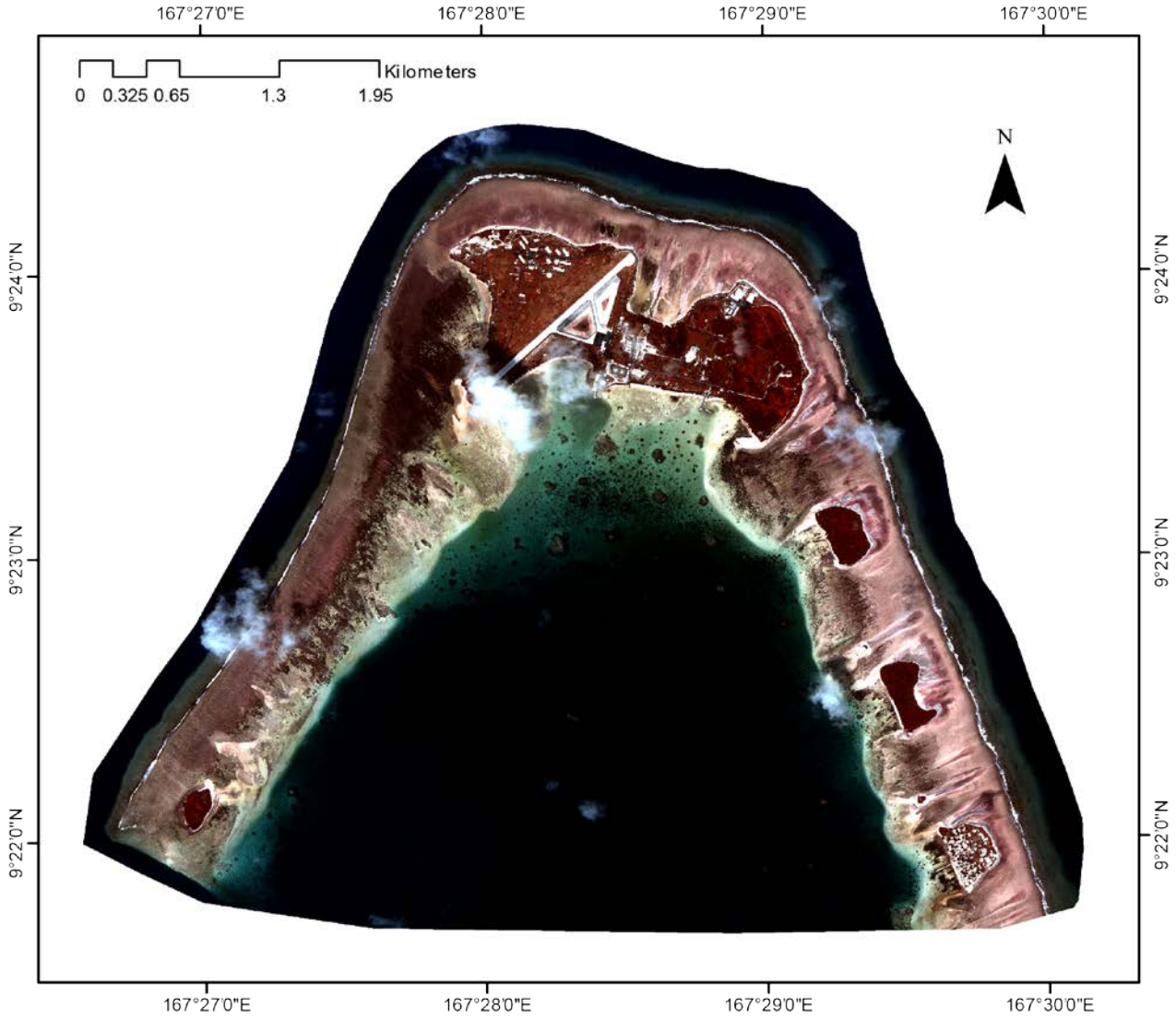

Figure 9. WorldView-3 satellite image of the Roi-Namur study area collected on 24 September 2014.

Model 2" antenna) was used to approximate tidal fluctuations and correct the data from the fathometer. The survey grade GPS/Antenna combination (rover) logged data continuously onboard the vessel during all field operations The GPS data were post-processed using the locally established temporary GPS base station located on the GOLF benchmark. These data were then used to tidally correct the fathometer data.

For the wave-driven flood modeling, water depths on the ocean side of the study site were needed that were deeper than estimates that could be reliably provided by the SDB. To provide bathymetry estimates deeper than 20 meters on the ocean side of Roi-Namur, the fathometer was used to record shore normal transects, approximately every 200 to 250 meters. The transect began in water as shallow as the vessel could access then would move offshore till the fathometer lost bottom signal on the rapidly descending sides of the atoll. Due to winds during the field mission that seldom decreased below 9 meters/second, wave conditions on the ocean side of Roi-Namur seldom allowed the vessel to risk accessing waters less than 3.0 meters. For waters too shallow for

the vessel to access in the lagoon (approximately 2.5 meters), depth was measured manually by personnel that waded out to approximately 1.5 meters depth. Location was recorded with a WAAS-enabled, water-resistant GPS (Garmin GPS Map 76). After removal of obvious errors, 33,224 points collected with the fathometer during the field mission were corrected for tide and used as training or accuracy assessment of the final bathymetry product (FIGURE 10).

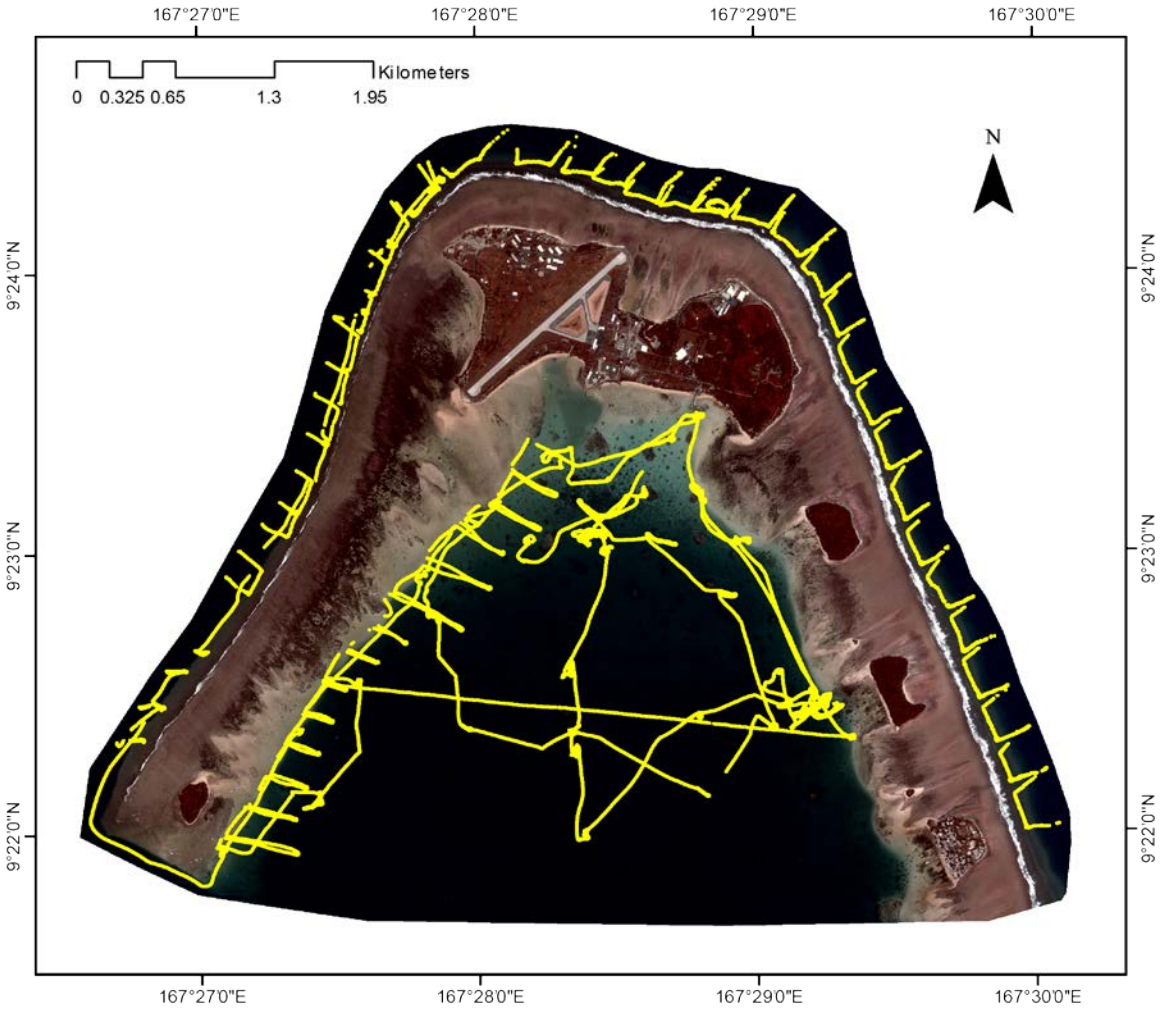

Figure 10. The 33,224 depth soundings (in yellow) collected during the April 2014 field mission overlaid on the 9 December 2009 WorldView-2 image.

3.1.2.3 Image preprocessing

Primary radiometric corrections were performed for the WorldView-2 and -3 images by the vendor. These corrections remove spatial variations or artifacts that may occur in the digital data. Unlike satellites such as Landsat-7, the WorldView satellites do not have onboard calibration, but post-launch calibrations were established and are available from the vendor. The data provided by the vendor in raw digital numbers were converted to reflectance using sensor calibration files and corrected for atmospheric effects as described in Stumpf et al. (2003).

3.1.2.4 Depth determination

To meet the needs of the models to be used in this project, the authors used methods developed by Stumpf et al. (2003), and modified by Field (2007) to derive bathymetry from WorldView-2 and WorldView-3 multispectral satellite imagery. Although there are several techniques available to generate bathymetry from multispectral data, the procedure outlined in Stumpf et al. (2003) was chosen for this study because it only required two tunable parameters and because of its applicability to low albedo features, like some of the coral habitats present in this study area.

Stumpf et al. (2003) used a ratio of two spectral bands, one with higher absorption than the other and hence lower reflectance. The use of two bands was based on earlier proposals by Lyzenga (1978, 1985) that suggested a two-band ratio could help alleviate confusion caused by reflection off of various benthic habitats. Namely, benthic habitats like seagrass and algae can have very dark signatures, in some cases darker than adjacent optically deep water. When using two bands, benthic habitats affect both bands similarly (Philpot 1989), but changes in depth affect the higher absorption band more. Therefore, the authors derived a ratio that should approximate depth independently of bottom albedo and need only be scaled to the actual depth:

$$Z = m_1 * \ln(nR_w(\lambda_i))/\ln(nR_w(\lambda_j)) - m_0$$

Where Z is depth, $R_w(\lambda_i)$ is the water leaving reflectance in band i, m_1 is a tunable constant to scale the ratio to depth, n is a fixed constant for all areas, and m_0 is the offset for a depth of 0 meters (Z = 0). The fixed value of n is chosen to assure both that the logarithm will be positive under any condition and that the ratio will produce a linear response with depth.

In the above equation, m_1 and m_0 are tunable parameters. Previous work (Field 2007) showed m_1 and m_0 were best chosen with “clean” sand references in mind, as microalgal mats or drift algae cause absorption of light that could alter reflectance values. In the present study, when clean sand points with known depths (from the sounder) were used, the regression of natural log (LN) LN blue/LN green vs. depth resulted in a straight line down to approximately 15 meters. Past that, the predictive value of the regression rapidly decreased. Therefore, the process was modified and much larger subsamples of points from the depth sounder (FIGURE 11), covering all bottom types were used in nonlinear regressions, resulting in lines with better fits.

Stumpf and Holderied (personal communication) indicated that a depth estimate based on the ratio of LN blue/LN red might be more sensitive for areas down to 3 or 4 meters deep. Based on that recommendation, the ratio of LN blue/LN green was used to estimate depths greater than 2.3 meters and the ratio of LN blue/LN red was used to estimate depths between 0 and 2.3 meters. Initial model runs indicated that one equation was inadequate for the entire study area. Therefore, the study area was segmented into three regions: lagoon, ocean and reef flat. The ocean was further segmented into two areas, one for the west and north sides of the study area and one for the east side. For each of these areas, separate equations to predict depth were generated. The graph for the lagoon of LN blue/LN green vs. depth from the sounder and the associated regression equation is shown in FIGURE 12.

It was initially thought that the shorter wavelength “coastal” band (band 1) of the WorldView satellites would have better water penetration than the earlier satellites with blue as their shortest wavelength. That was not the case in this study and was observed by Kanno et al. (2014). Visual inspection of the coastal band showed hazier, less defined benthic features than the

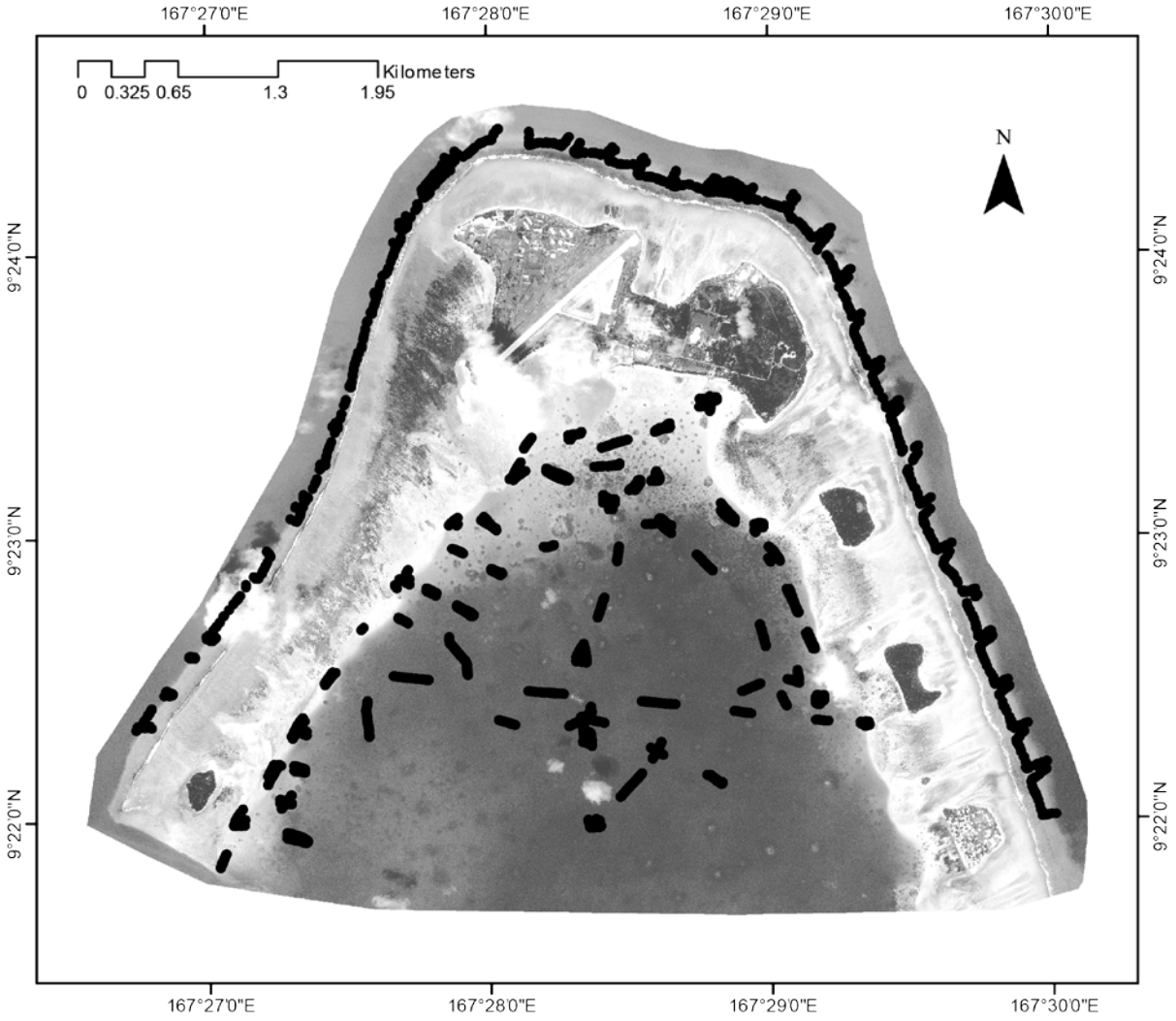

Figure 11. Depth sounder points used in the depth determination model for the ocean and lagoon regions shown on band 2 of the 24 September 2014 WorldView-3 image.

blue band (FIGURE 13). This could be caused by atmospheric Rayleigh scattering of the shorter wavelength coastal band (Kanno et al., 2014) or absorption in the water due to water column constituents.

Bathymetric maps for the ocean, reef flat and lagoon were generated and merged into one product (FIGURE 14). As previously mentioned, depths on the ocean side (down to 22.5 meters) were a combination of depths generated from the above model; greater than 22.5 meters, depths were taken from an interpolated surface from the depth-sounder ocean points. In some areas, this merging created artificial shelves or ridges. These features were manually edited. A 3x3 low-pass convolution filter was used on the final product to eliminate single pixel anomalies.

3.1.3 Bathymetric Data Accuracy Assessment

A separate exercise was conducted to understand the minimum field data requirement to generate useable SDB products. The total depth-sounder points collected over 5 days during the

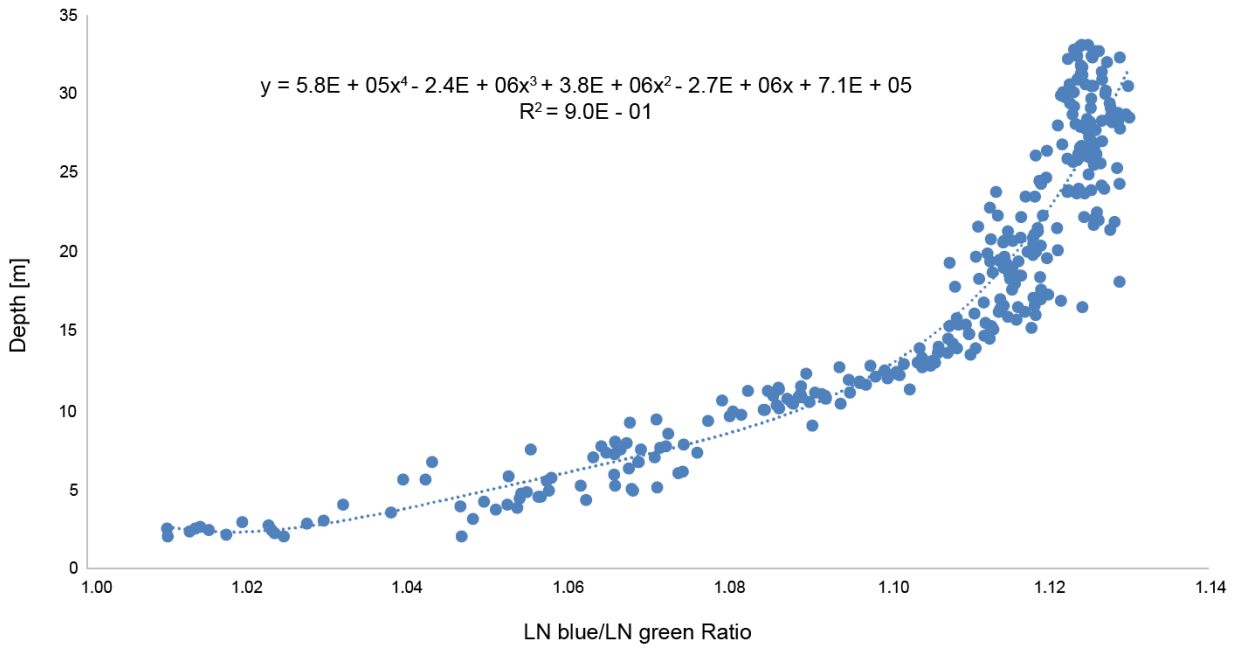

Figure 12. Plot of LN blue to LN green band ratio versus depth from depth sounder and associated regression equation for the lagoon.

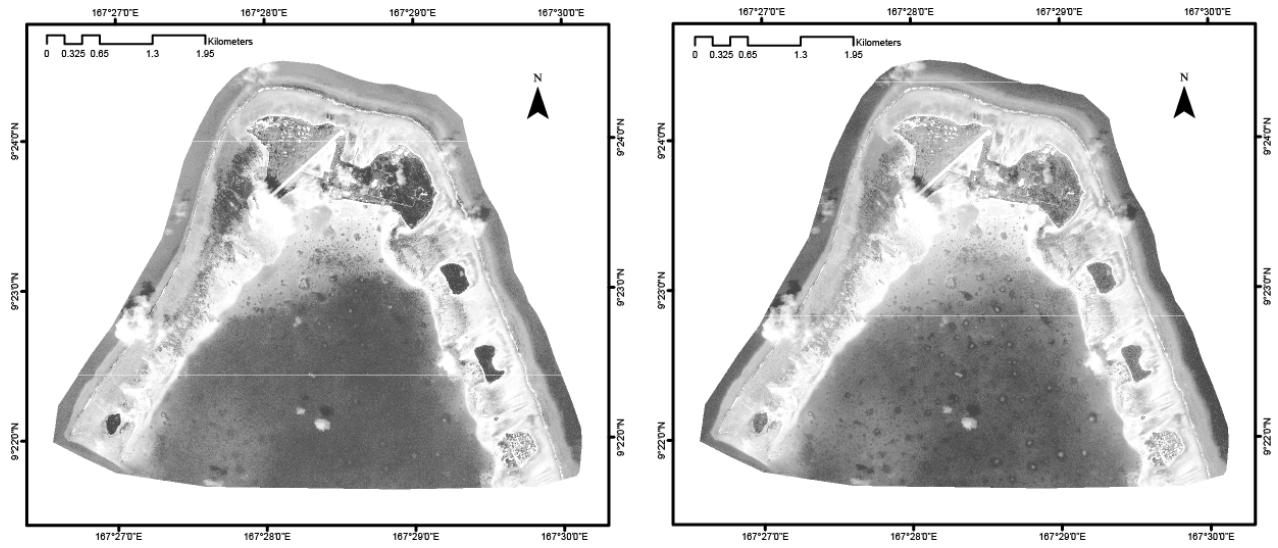

Figure 13. WorldView-3 satellite image from 24 September 2014. On the left is band 1, the coastal band, and on the right is Band 2, the blue band. Band 2 shows better definition of patch reefs in the lagoon indicating better water penetration.

2014 field mission were incrementally reduced to estimate the amount field time to produce a useable bathymetric product. Only the ocean and lagoon regions were considered, the reef flat was excluded due to limited field elevation data over the entire study area. For this exercise, all of the corrected depth-sounder points were used. A random sample of 70 percent of these points were

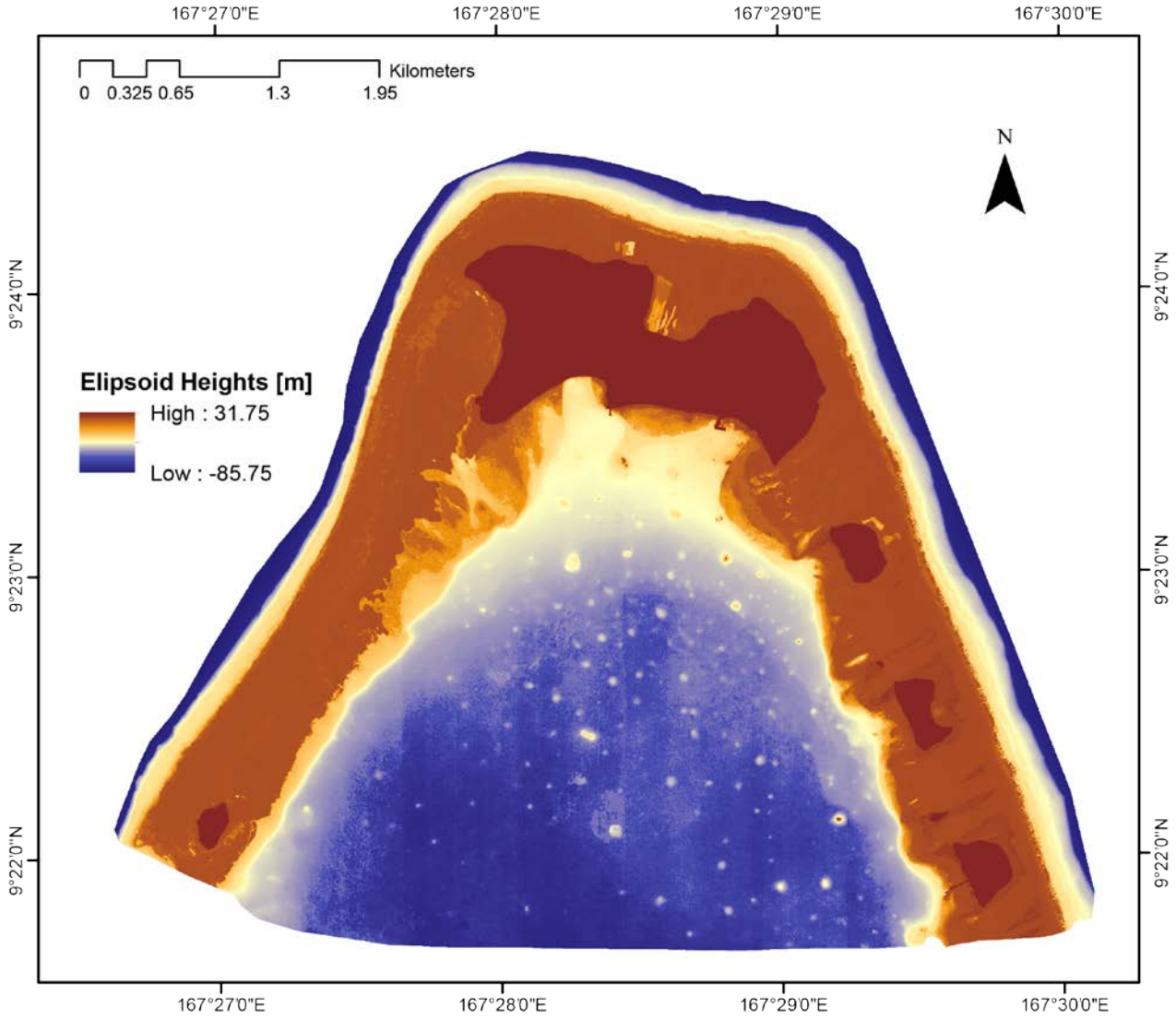

Figure 14. Map showing the final merged satellite-derived bathymetry (SDB) for the Roi-Namur study area. The satellite images used to create this product included a WorldView-3 image acquired 24 September 2014 and WorldView-2 images from 19 December 2009, 29 December 2014, and 23 January 2015.

used for model generation (resulting in 19,101 points for the lagoon and 4,184 points for the ocean), the remaining 30 percent (9,919 total points, 8,166 points in the lagoon, 1,753 points in the ocean) were reserved for accuracy assessment. The points used for model generation were then incrementally reduced by random sampling, as shown in TABLE 4. Therefore, 9 models were run producing 9 bathymetry maps for the lagoon and ocean. The same 9,919 accuracy assessment points described above were used to assess the accuracy of each of the 9 bathymetric maps. Since elevation data for the intertidal reel flat were collected for only a small portion of the study area, the reef flat was not included in this assessment. Values from the bathymetry maps were extracted at the 9,919 randomly selected depth sounder points and root-mean-square-error (RMSE) for the estimated depth vs. depth from the sounder was calculated for the lagoon in FIGURE 15, and the ocean in FIGURE 16.

Table 4. Estimates of minimum field data and the resulting accuracy (shown by Root Mean Squared Error, RMSE) required to produce a satellite-derived bathymetry (SDB) product.

Percentage of points	Lagoon (# of points)	Lagoon RMSE (m)	Ocean (# of points)	Ocean RMSE (m)
70 percent	19101	1.416	4184	1.374
60 percent	16372	1.415	-	-
50 percent	13643	1.389	3472	1.348
40 percent	10914	1.454	-	-
30 percent	8185	1.463	2083	1.353
20 percent	5457	1.427	-	-
10 percent	2727	1.416	694	1.373
5 percent	1168	1.471	347	1.387
1 percent	175	1.526	70	1.584

The relative accuracies presented here for the WorldView satellites were similar to those of Stumpf et al. (2003), Mishra et al. (2004) and Field (2007) down to 15 meters. At water depths greater than 15 meters, the nonlinear techniques used here produced better results. For the lagoon, relative accuracies varied from an RMSE of approximately 0.6 at 3 meters depth to approximately 2.0 at 40 meters depth. The depths for the lagoon bottom (not including the pinnacle patch reefs) were fairly uniform. It deepened rapidly off of the reef flat in most areas, with gradual fluctuations between 30 and 40 meters that were well represented in the SDB. On the ocean side of the study

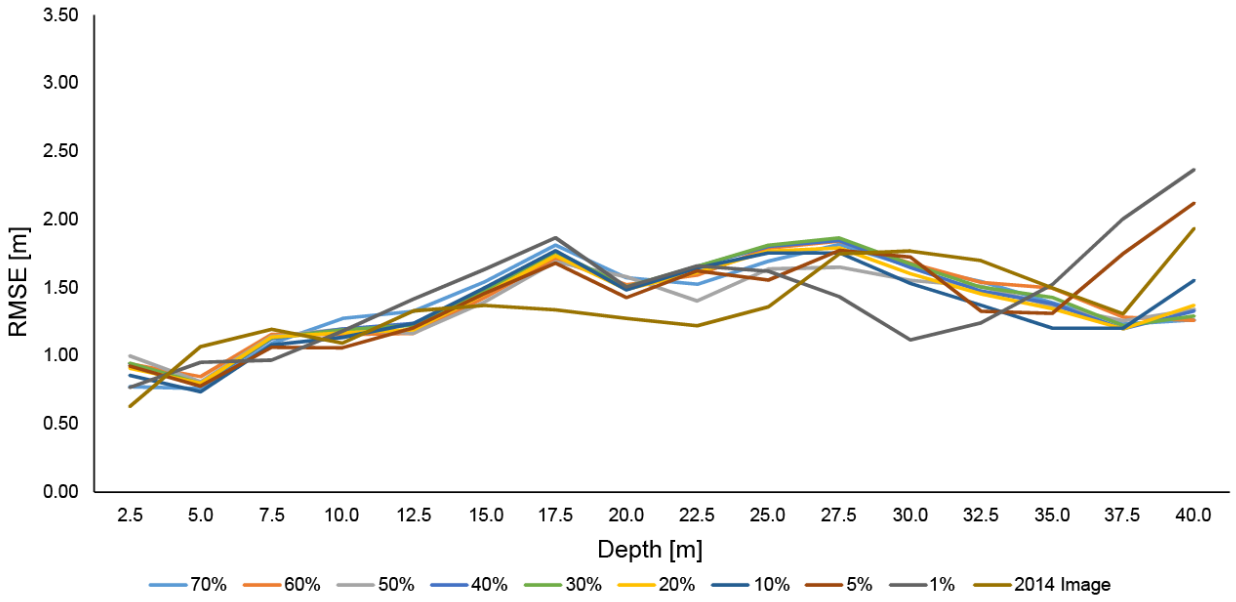

Figure 15. Plot showing the Root Mean Square Error (RMSE) in 2.5-m bins for the 8,166 lagoon depth-sounder points, for the incremental reduction of model points.

area, the SDB was only used down to 22.5 meters. Past that depth, the sides of the atoll dropped off very rapidly and were not well represented in the SDB.

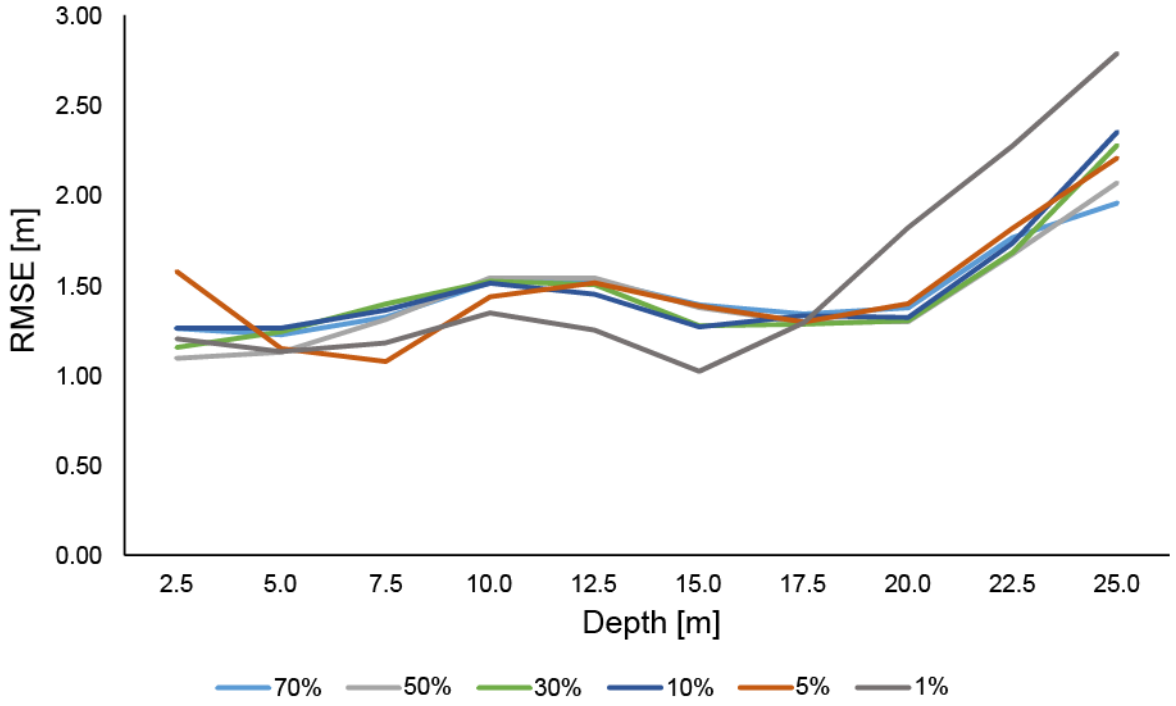

Figure 16. Plot showing the Root Mean Square Error (RMSE) in 2.5-m bins for the 1,753 ocean depth-sounder points, for the incremental reduction of model points.

The pinnacle patch reefs in the lagoon posed unique challenges. With some pinnacles marked as navigation hazards, extreme caution during the 2014 field mission led to few pinnacles being directly sampled with the depth sounder. In addition, due to the remote nature of this study area, there were some issues related to the spatial accuracy of the imagery. Comparison of survey grade GPS data collected on Roi-Namur to photo-identifiable features on the imagery showed offsets of approximately a pixel (4 square meters). However, visual comparison of coral pinnacles and other submerged features in the lagoon in different dates of imagery showed offsets of up to several pixels. Further visual comparisons of the few depth-sounder transects that went directly over coral pinnacles showed considerable disagreement between SDB depth estimates and the depth-sounder data on the steep slopes of the sides of the pinnacles. This was probably due inherent problems with spatial accuracy of the imagery in the lagoon. It appears that these inaccuracies in the lagoon caused the increase in RMSE between approximately 25- and 35-meter water depths, as shown in FIGURE 17. Image segmentation was used to overcome this issue. The image segmentation process required additional time to derive the equations, and to manually smooth seams between segments.

The incremental point reduction exercise indicated that in this study area, a reduction to 5 percent of the points (1,168 points in the lagoon, and 347 points in the ocean, 1,515 total points) generated a product similar to the final subtidal bathymetry product (not including the reef crest).

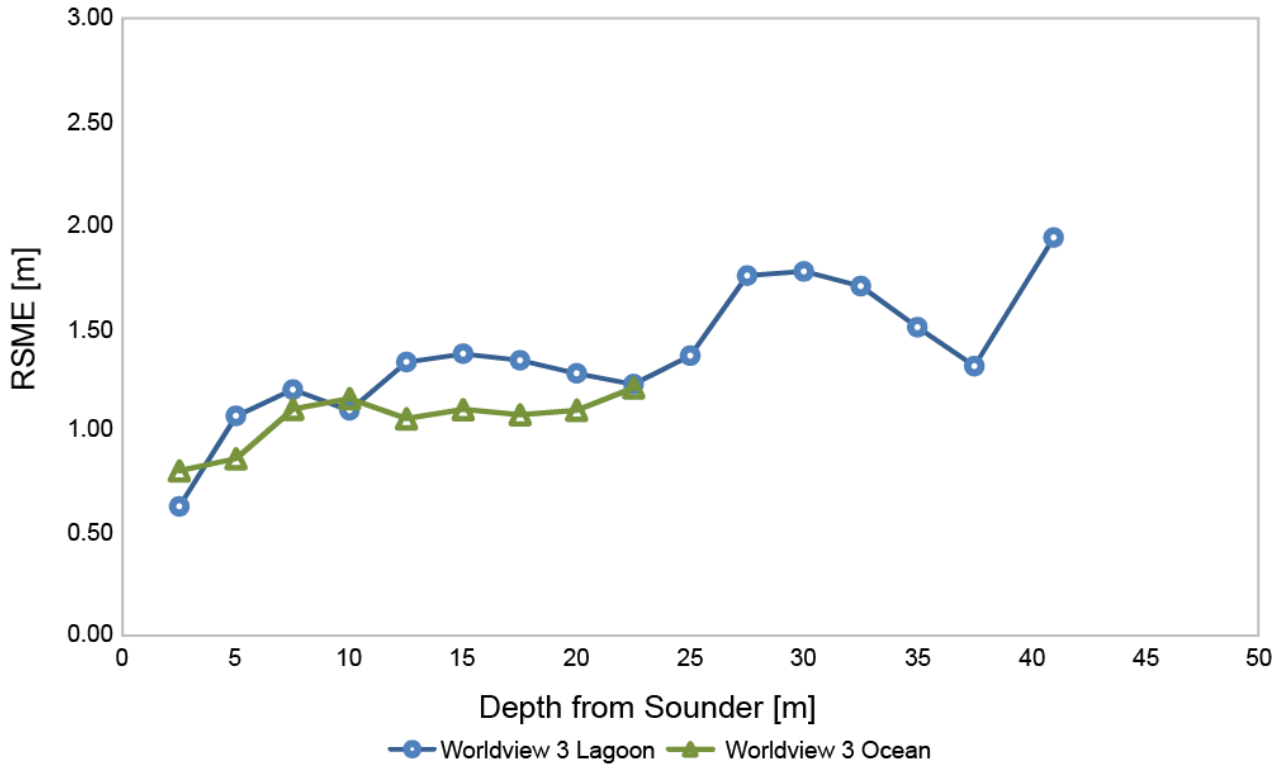

Figure 17. Plot showing the Root Mean Square Error (RMSE) in 2.5-m bins for the 8,166 lagoon and the 1,753 ocean depth-sounder points.

During the 2014 field mission, 5 days on the boat collecting data for depth estimation and habitat mapping produced a data set of 33,224 depth sounder points. From these data, it appears that for similar areas, one day of boat time with efforts to cover the full range of depths in the study area, may produce adequate points to generate a reasonable bathymetry layer. This approximation may not hold up for study areas of varying size, complexity or water quality. For intertidal areas like the reef crest in this study area, the field effort would have to be considered separately. Due to tide and wave conditions, landing field crews on other remote reef crest areas may be difficult or impossible.

3.1.4 Topographic and Bathymetric ("topobathy") Digital Elevation Model (DEM) Creation

To create the seamless topobathy DEM of Roi-Namur, TLS, GPS and SDB were combined into a 0.5-meter grid. For the island and intertidal reef flat areas with ellipsoid heights above 31.250 meters (-0.106 mean sea level [MSL]), TLS and GPS data were combined into a triangulated irregular network (TIN) model. Due to the higher data density, TLS data were used preferentially wherever it was available. GPS data were used in addition to TLS data in areas where the TLS data density was low (less than 1 point per square meter). Breaklines were manually added to improve TIN interpolation in areas of high relief and low data density, such as the vegetated sections of the small beach berm on the north- and west-facing shores of the island. After the TIN was created in ArcGIS, it was rasterized to produce a 0.5-meter grid of the onshore data.

For the reef flat and offshore areas, TLS and SDB data were combined. In order to produce a more consistent DEM without large vertical discontinuities, a comparison between the two data sets was done in areas with overlapping data. The comparison showed an average vertical offset of 0.062 meter between the two data sets, with the TLS being higher than SDB. Because SDB has a higher uncertainty than TLS, the bathymetry data was vertically adjusted upward by 0.062 meter to more closely match TLS data. The reef flat TLS data was then gridded with a 0.5-meter cell size. Gaps in TLS data smaller than 2.5 meters were filled using a focal mean operator in ArcGIS. The resulting grid of TLS data was then mosaicked with SDB data for the reef flat and fore reef. In areas where the TLS data overlapped the bathymetry data on the reef flat, the TLS data was preferentially used due to its higher vertical precision.

To produce the final seamless 0.5-meter resolution topobathy DEM, the onshore and offshore grids were combined (FIGURE 18). For all areas with ellipsoid heights higher than 31.250 meters, the more precise TIN-derived TLS-GPS onshore DEM was used. For offshore

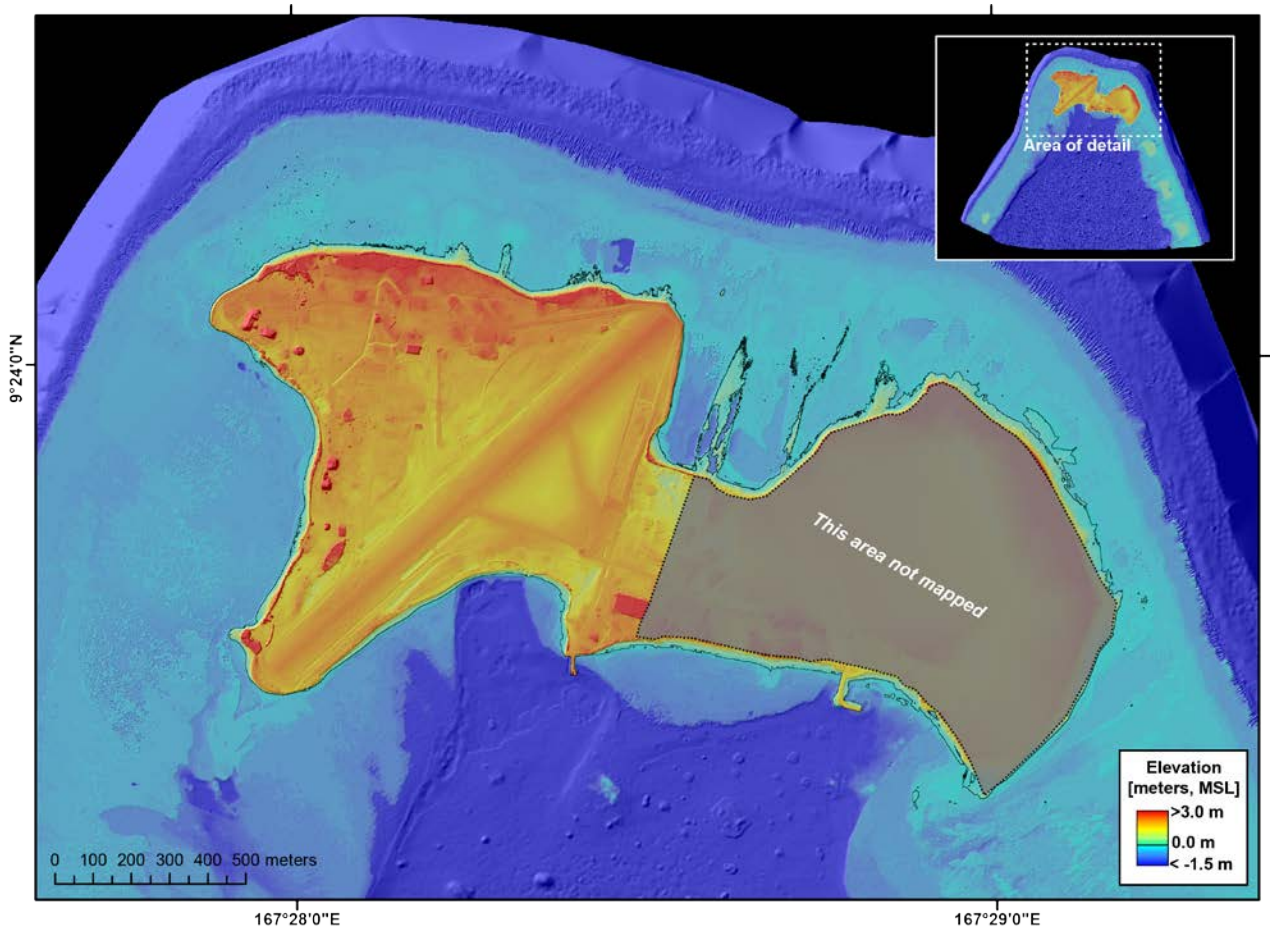

Figure 18. Map showing the seamless topobathy DEM for Roi-Namur. Black contour line represents project local mean sea level (MSL) derived from temporary tide gauge deployed on pier. Grey area represents interior portions of Namur Island that were not mapped.

areas lower than 31.250 meters, the grid-derived TLS-SDB DEM was used. The grid elevation values are referenced to the WGS84 ellipsoid, but can be easily transformed into a water level datum using the transformations listed in TABLE 3.

An additional DEM with building footprints was also produced for hydrodynamic simulations. Building footprints were digitized from WorldView imagery, and base elevations were derived from the topobathy DEM. To produce contiguous shapes that would impede shallow-water flow in a hydrodynamic simulation, a height of 5 meters above the ground was assigned to each building by adding 5 meters to the base height of each footprint. The resulting building footprints were rasterized and inserted into the topobathy DEM.

3.1.4.1 Topographic and bathymetric ("topobathy") digital elevation model (DEM) uncertainty analysis

For the purposes of this project, uncertainty analysis of the final topobathy DEM was restricted to vertical elevation values only. Horizontal uncertainty is estimated to be small relative to vertical uncertainty, and is unlikely to have a significant impact on the modeling efforts in this project. The final topobathy DEM is a composite product derived from three data sources: GPS, TLS and SDB. Each data source has unique uncertainties associated with the technique used to derive it. To estimate uncertainty, the DEM was spatially segmented into three regions based on the contributing data source. These regions are: 1) island and reef flat areas mapped with TLS only, 2) island and reef flat mapped with TLS and GPS, and 3) reef flat and offshore areas mapped with SDB as shown in FIGURE 19.

To assess the uncertainty of the portions of the DEM derived from the TLS only (for example, the island and reef flat), DEM elevation values were compared with GPS check data collected in areas of dense TLS data coverage. The GPS validation data set consisted of 5,596 high precision GPS measurements. The data set was limited to points with high vertical precision, collected in areas of low relief. Only measurements that were not used in the final DEM product were used as the validation data set. To account for errors caused by rasterizing the fine-scale TLS point data in 0.5-meter cells, the GPS validation data were rasterized into cells coincident with the DEM cells using the mean elevation operator. The DEM was subtracted from the resulting GPS raster to produce an estimate of DEM error relative to the GPS data. The resulting elevation differences are normally distributed with a mean of -0.007 meter (GPS on average higher than TLS) and an RMSE of 0.047 meter.

For the portions of the DEM where TLS data density was low and GPS measurements were used in conjunction with TLS data, it was expected that the uncertainties are similar or slightly greater than those estimated for portions of the DEM derived from only the TLS data. The uncertainty for topographic GPS point measurement was estimated by the Waypoint Grafnav post-processing software as a standard deviation of positions relative to the base station. For the 7,265 GPS measurements that contributed to the DEM, the mean of these horizontal and vertical standard deviations was 0.017 meter and 0.032 meter, respectively. However, these points were combined with TLS data for TIN interpolation, so both data sets and their associated uncertainties contribute to the final elevation in these areas. Because the TLS data have the higher uncertainty estimate between the two data sets, we use this value (0.047 meter) as the estimate for these areas. It should be noted that GPS data was used only in areas of low TLS point density. Low TLS point density often resulted from the presence of thick vegetation, which precluded mapping with TLS. These data gaps (some as large as 30 meters) were mapped by interpolating across them. This increases the level of uncertainty in these areas in an unquantifiable way. We estimate that due to

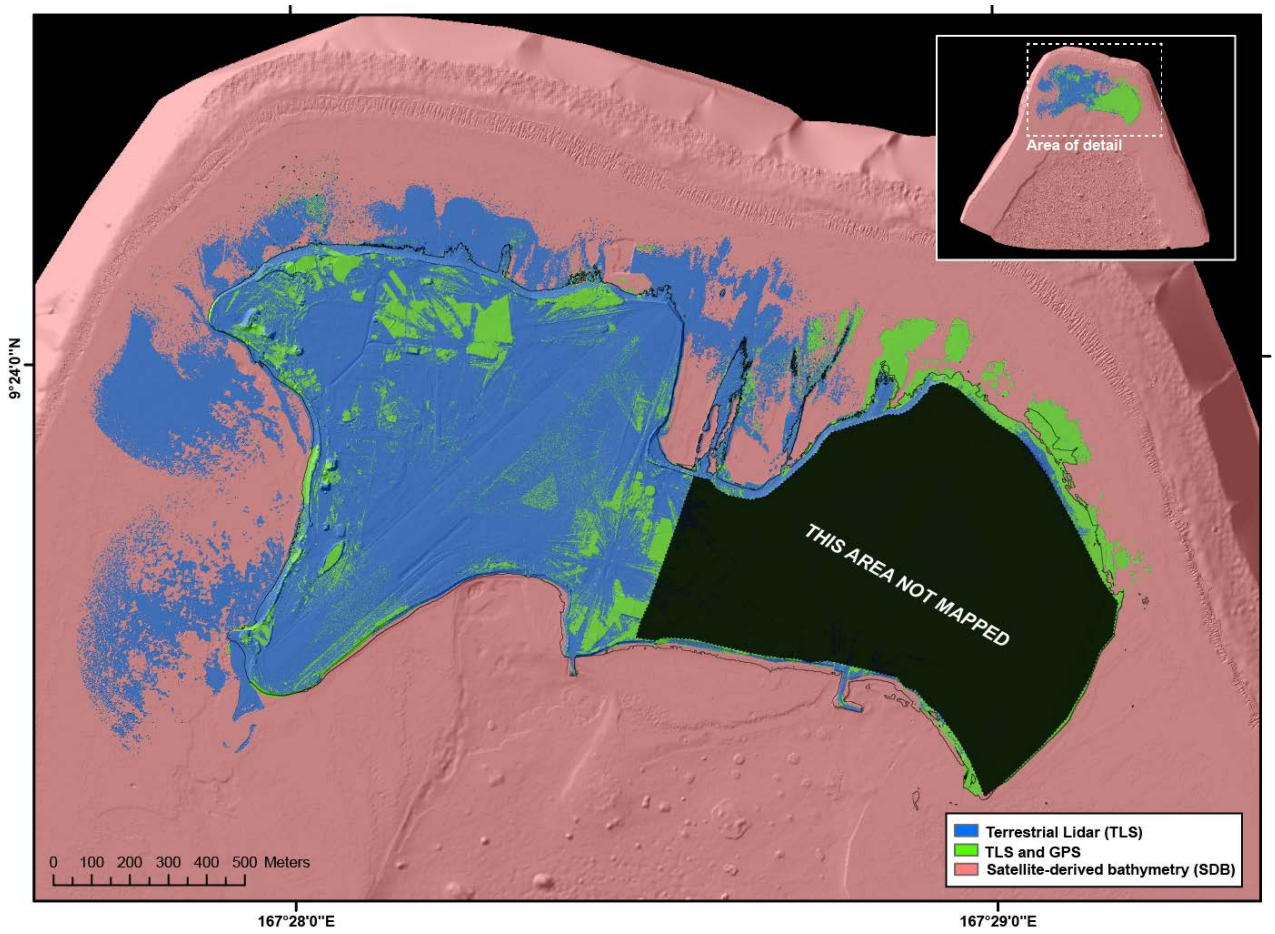

Figure 19. Map showing data sources used to develop Roi-Namur topobathy DEM. Blue areas were mapped exclusively with terrestrial lidar scanner (TLS); green areas were mapped using TLS and survey-grade GPS; pink areas were mapped using satellite-derived bathymetry (SDB).

the relatively low topographic relief on the island, these few data gaps do not greatly contribute to the overall uncertainty in the DEM.

The uncertainty of the reef flat and offshore areas mapped using SDB was assessed by comparing the mapped data to the echo-sounder data collected during the survey as discussed previously. To derive general estimates of SDB uncertainty from the depth-varying uncertainty, the RMSE values were grouped and averaged into four depth ranges. Additional sources of error were identified that also contribute to overall uncertainty in the final DEM. Due to the lack of publically available survey control for the island, control for the project had to be established through post-processed static occupations on the GOLF benchmark. Precise Point Positioning (PPP) processing was used due to the lack of nearby GPS reference stations for differential methods. The standard deviation of elevation values derived for the benchmark through PPP processing was 0.044 meter. Because these reference coordinates determine the absolute positioning of all GPS measurements for the project, this uncertainty must be included in the overall error estimates for the project.

Additionally, there are errors associated with the derivation of the water-level datums for the project which must be accounted for in the total error budget. The RBR water-level sensor

used to collect the short-term tide record has a stated accuracy of ±0.01 meter. The short-term tide record used to derive the NTDE equivalent water level datums had a duration of 10 months. The derivation of water-level datums from this length of a record has an estimated vertical uncertainty of 0.019 meter (based on regression fit to discreet uncertainty values presented in *NOAA Special Publication NOS CO-OPS 2*, 2003). Measuring the elevation of the water-level sensor using static differential GPS occupations introduced additional uncertainty. The 5 static occupations used to derive the elevation for TIDE had a standard deviation of 0.008 meter. Finally, the vertical offset between the TIDE benchmark on the pier and the pressure sensor on the piling below it was measured using a nylon tape measure. Although this measurement was made carefully, it is estimated that an additional 0.030 meter of uncertainty could have been introduced by this measurement. These uncertainties related to water-level datum only apply to the DEM once it has been transformed into a water-level datum and do not apply to the DEM referenced to the ellipsoid.

The various uncertainties discussed above are shown in TABLE 5. Because these uncertainties stem from independent sources, they are summed in quadrature. The linear error at 95 percent confidence (LE95) was derived directly from RMSE (RMSE × 1.96, which assumes a normal distribution of error; FGDC, 1998) and is also listed in TABLE 5.

Table 5. Vertical uncertainties (root-mean squared error and standard deviation [1 σ]) in source data and the combined topobathy DEM.

DEM Zone	Elevation RMSE (m)	**Geodetic control σ** (m)	Water level sensor accuracy (m)	Tidal benchmark **elevation σ** (m)	Tidal benchmark vertical offset (m)	DEM referenced to ellipsoid, combined uncertainty (m)		DEM referenced to water level datums, combined uncertainty (m)	
						1 σ	LE95	**1 σ**	LE95
TLS derived	0.047	0.044	0.01	0.008	0.03	0.064	0.126	0.07	0.14
TLS and GPS derived	0.047	0.044	0.01	0.008	0.03	0.064	0.126	0.07	0.14
SDB depths 2.5 m – 10 m	0.989	0.044	0.01	0.008	0.03	0.990	1.940	0.99	1.94
SDB depths 10 m – 20 m	1.097	0.044	0.01	0.008	0.03	1.098	2.152	1.10	2.15
SDB depths 20 m – 30 m	1.495	0.044	0.01	0.008	0.03	1.496	2.931	1.50	2.93
SDB depths 30 m – 41 m	1.610	0.044	0.01	0.008	0.03	1.611	3.157	1.61	3.16

3.2 Benthic Habitat Mapping

Coral reefs are topographically complex structures, at a variety of spatial scales. Incident waves begin to interact with benthic features on the fore reef, break as they approach the wave crest, and can continue to interact with the bottom as they approach the shoreline. Hydrodynamic modeling uses a variety of equations with different coefficients to describe these dynamics. The most common approaches utilize friction coefficients, drag coefficients, or a variety of roughness parameters (roughness height, roughness length, Nikuradse height, Manning roughness, etc.).

Directly quantifying these parameters with field data is technically demanding (and only marginally easier in the lab). As a result, modeling efforts frequently solve for these parameters empirically or make assumptions based upon literature.

Roi-Namur Island in the Kwajalein chain is a typical atoll (FIGURES 4-5), in that the bottom rises steeply over a narrow fore reef to a spur-and-groove system in front of the reef crest. The reef flat is mostly lithified rock that is fairly shallow but tidally variable. Behind the emergent land, the bottom falls away to a fairly deep and sandy lagoon. To reflect this complex mixture of habitat and depths, the hydrodynamic modeling component of this project required a spatially variable map as input data. These data were derived by generating a habitat map via semi-automated and manual image-processing techniques (utilizing the same WorldView-2 and -3 satellite images used in SDB), and assigning the habitat types friction coefficients based upon a literature review.

In general, the benthic habitat mapping methods used here followed those of another National Centers for Coastal Ocean Science mapping effort on nearby Majuro Atoll (Kendall et al., 2012). Benthic habitats were mapped using spectral classification with the Iterative Self-Organizing Data Analysis Technique (ISODATA) unsupervised clustering algorithm (Jensen, 2005) in combination with on-screen, heads-up digitizing. The ISODATA algorithm was used on the reef flat and shallow (<10 meters) sides of the lagoon where spectral signatures were strongest. On screen, heads-up digitizing was used in the deeper parts of the lagoon and ocean where signatures were weaker due to wave action and water column attenuation. The on-screen digitizing was performed at scale of 1:2,000. The minimum mapping unit (MMU) in the areas where ISODATA was used was at the pixel level (4 square meters). The MMU in the areas where on-screen digitizing was used was 30 square meters. The benthic habitat map was produced using a non-hierarchical classification system similar to the scheme used on the Majuro Atoll (Kendall et al., 2012).

To aid in the habitat classification, 154 sites were visited during the April 2014 field mission. Seventy-seven sites were visited on the reef flat and in the very shallow waters of the lagoon. In addition, 77 sites were examined via drop camera images collected during the bathymetric surveys. A Sartek color (model SDC-CSS) video camera was mounted in a stainless steel frame that was lowered to depth by hand. A Trimble GeoExplorer GPS (6000 series Geo XH with Trimble Tornado antenna) was used to obtain locational data for all video collected. To geo-locate every frame of video, GPS coordinates were stamped, along with Coordinated Universal Time (UTC) time into every video frame using a Horita video-labeling device.

The resulting habitat map was converted to a spatially varying friction coefficient map, using values for similar coral reef habitats from the literature (TABLE 6; details in next section). The friction map served as input data for the USGS wave modeling efforts. The various roughness parameters (roughness length, friction coefficient, etc) are inter-related. However given the variety of assumptions across the models in the coral reef hydrodynamic literature, it was decided to work solely with reported friction coefficient values, rather than making additional assumptions about conversion factors to re-calculate all metrics into a common format.

3.2.1 Benthic Habitat Classification and Hydrodynamic Friction

Twenty different benthic habitat classes were delineated in the study area (FIGURE 20). The primary need of the habitat map is to provide the basis for the habitat friction coefficients needed for the hydrodynamic models for this project. Therefore, a detailed presentation of the distribution and abundance of these habitats will not be presented. However, the hydrodynamic

Table 6. Literature review of coral reef habitat various friction parameter values.

Habitat (Location)	Reported parameter	value	Paper
Fore reef (Kwajalein)	Incident wave friction coefficient f_w	0.3	Quataert et al., 2015
Coral substrate (Ningaloo)	Friction factor f_w	0.6	Pomeroy et al., 2013
Ningaloo reef (model)	Wave friction f_w	0.6	Van Dongeren et al., 2013
Ningaloo reef (model)	Friction coefficient cf	0.1	Van Dongeren et al., 2013
Fore reef (Kwajalein)	Infragravity wave friction coefficient c_f	0.1	Quataert et al., 2015
Fore reef (Palmyra)	Wave friction factor f_w	1.80 ± 0.07	Monismith et al., 2015
Fore reef (Paopao Bay)	Wave friction factor f_w	0.29 ± 0.01	Monismith et al., 2013
Fore reef (Paopao Bay)	Wave friction factor f_w	0.21 ± 0.01	Monismith et al., 2013
Fore reef (Guam)	Friction coefficient c_f	0.2 ± 0.05	Pequignet et al., 2011
Fore reef spur and groove (Palmyra)	Drag coefficient C_d	0.1	Rogers et al., 2015
Fore reef (Molokai)	Drag coefficient C_d	0.06	Rogers et al., 2013
Coral reef (Ala Moana)	Friction coefficient f_w	0.1-0.5	Gerritsen., 1980
Reef flat/fore reef	Drag coefficient C_d	0.01	Falter et al., 2013
Reef flat (simulated)	Friction coefficient c_f	0.04-0.05	Baird & Atkinson, 1997
Reef flat Kwajalein	Infragravity wave friction coefficient cf	0.01	Quataert et al., 2015
Reef flat, Kanehoe	Wave friction factor f_w	0.28 ± 0.04	Lowe et al., 2005
Reef flat, Kanehoe	Quadratic drag coefficient C_d	0.02	Lowe et al., 2009a
Reef flat, Kanehoe	Quadratic drag coefficient C_d	0.01-0.02	Lowe et al., 2009b
Reef flat (Guam)	Friction coefficient c_f	0.06 ± 0.02	Pequignet et al., 2011
Reef flat (Ningaloo/Kanehoe)	Frictional drag C_d	0.1	Hearn, 1999
Reef flat (Bora Ba, Ryukyus)	Drag coefficient C_d	0.1	Kraines et al., 1998
Reef flat *Porites rus* bommies (Moorea)	Bulk drag coefficient C_d	0.3	Hench and Rosman, 2013
Fringing reef (Ishigaki)	Bottom friction coefficient c_f	0.035	Tamura et al., 2007
Fringing reef (Eilat)	Drag coefficient C_d	0.009-0.015	Reidenbach et al., 2006
Reef flats (Ningaloo)	Drag coefficient C_d	0.017	Zhang et al., 2011
Coral substrate (Ningalo)	Friction coefficient c_f	0.05	Pomeroy et al., 2013
Back reef (Moorea)	Drag coefficient C_d	0.066-0.1	Hench and Rosman, 2011
Back reef (Paopao Bay)	Drag coefficient C_d	0.1	Monismith et al., 2013
Sand (Ningaloo)	Friction coefficient c_f	0.003	Pomeroy et al., 2013
Sand	Coefficient of friction C_d	0.0025	Hearn et al., 2001
Sandy lagoon bottom (Nigaloo/Kanehoe)	Frictional drag C_d	0.0025	Hearn, 1999
Sand (Eilat)	Drag coefficient C_d	0.002-0.004	Reidenbach et al., 2006
Fringing reef lagoon (Puerto Morales)	Friction coefficient c_f	0.015	Coronado et al., 2007
Fringing reef (Mamala Bay)	Drag coefficient C_d	0.030 ± 0.005	Jones et al., 2008
Lagoon	Drag coefficient C_d	0.03	Falter et al., 2013
High relief rubble (flume)	Friction coefficient c_f	0.101-0.111	Thomas and Atkinson, 1997
Low relief rubble (flume)	Friction coefficient c_f	0.045-0.053	Thomas and Atkinson, 1997
Porites compressa (flume)	Friction coefficient c_f	0.109-0.264	Thomas and Atkinson, 1997
Porites damicornis (flume)	Friction coefficient c_f	0.063-0.126	Thomas and Atkinson, 1997
(Tague Bay)	Friction coefficient c_f	1	Lugo-Fernandez et al., 1998
(Northern Great Barrier Reef shelf)	Drag coefficient C_d	~0.02	Wolanski, 1983
(Bligh Entrance)	Drag coefficient C_d	~0.05	Woalnski and Thomson, 1983
Britomart Reef	Drag coefficient C_d	~0.02	Wolanski and Pickard, 1983
(Central Great Barrier Reef shelf)	Drag coefficient C_d	~0.001	Wolanski and Bennett, 1983
Reef (Berau)	Drag coefficient C_d	0.021	Tarya et al., 2010
Shelf (Berau)	Drag coefficient C_d	0.00039	Tarya et al., 2010

models used in this project indicate that potential coastal hazards caused by wave-driven flooding are most affected by the structure of the fore reef and reef flat (Quataert et al., 2015). Therefore, a brief description of the benthic habitats in those areas is given here.

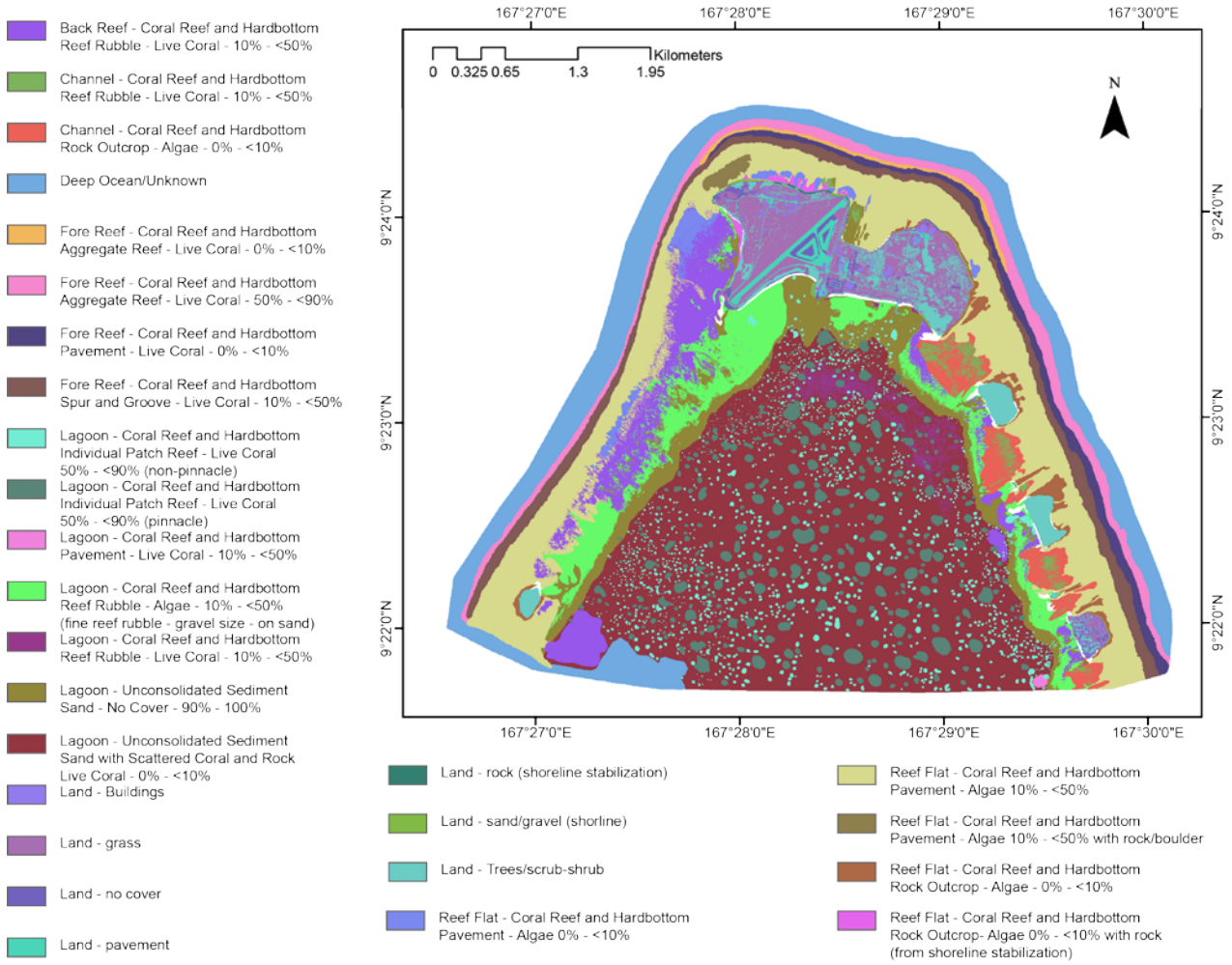

Figure 20. Map showing the benthic habitat classification for the Roi-Namur study area developed using spectral classification in combination with on-screen, heads-up digitizing.

The fore reef, from depths of 10-15 meters down to the depths of the bank/shelf escarpment, was dominated by aggregate reef with high densities (50-90 percent) of live corals, often with small pockets of the calcareous algae *Halimeda* sp. (FIGURE 21). In the slightly shallower waters of the fore reef, particularly on the north side of Roi-Namur, are moderately rugose areas with lower (10-50 percent) live coral coverage (FIGURE 22). For most of the north and east ocean side of the study area, slightly deeper than the spur and groove reef habitat, lies a band of pavement, low rugosity habitat with low (0-10 percent) live coral cover (FIGURE 24). Spur and groove reef habitat that radiates out from the reef flat all the way around the study area down to a depth of 5 meters is shown in FIGURE 24. Typical reef flat is shown in FIGURE 25; this is a low-relief habitat with a cover of microalgae and turf algae. In some areas of the reef flat around the islands and channels are much higher rugosity rock outcrops (FIGURE 26).

Figure 21. Underwater photograph showing an example of the diverse coral communities at depths greater than 15 meters on fore reef. The green at the bottom edge of the photo are calcareous algae.

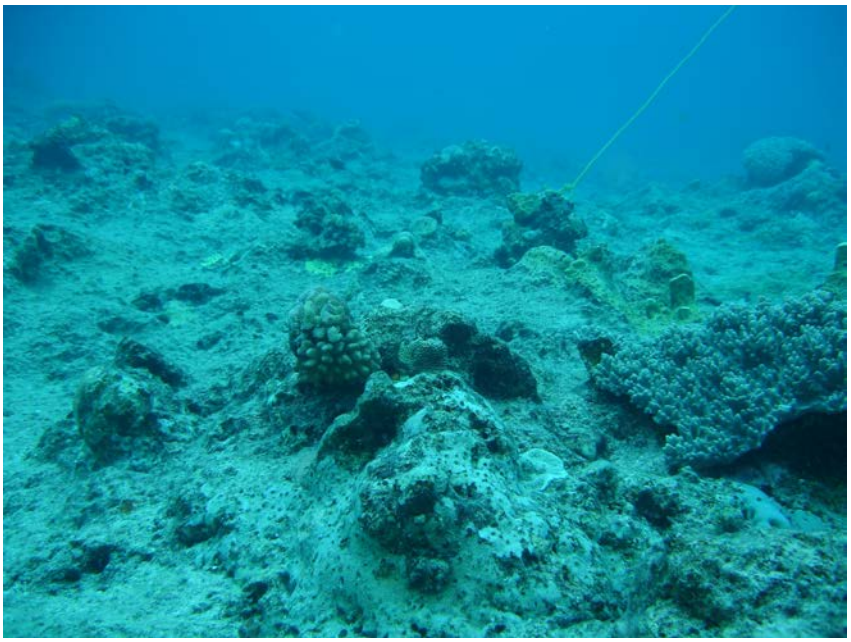

Figure 22. Underwater photograph showing an example of lower coral cover, moderate rugosity habitat at depths of 10-15 meters on the fore reef.

Figure 23. Underwater photograph showing an example of lower rugosity, lower coral cover pavement, at depths of 5-10 meters just seaward of the spur and groove reef habitat.

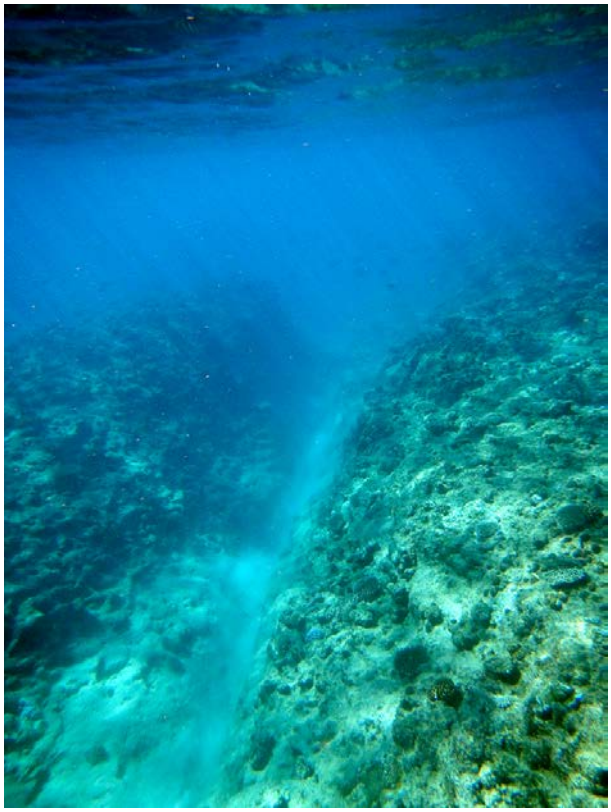

Figure 24. Underwater photograph showing an example of spur and groove reef habitat at a depth of 1-5 meters that abuts the ocean side of the reef crest.

Figure 25. Photograph of the gently sloping reef flat, which extends from the shoreline 20-350 meters to the reef crest (where waves are breaking) at low tide.

Figure 26. Photograph of the higher rugosity intertidal areas dominated by beachrock, mostly in the channels and some other areas of the reef flat off Namur.

Based upon the literature review (TABLE 6), friction coefficient values of 0.003 for sandy bottom, 0.01 for the back reef, 0.03 for the reef flat, 0.05 for low-coral cover fore reef, 0.1 for fore reef spur-and-groove, and 0.125 for high-coral cover fore reef were selected, with 0.3 for the offshore wave friction coefficient (FIGURE 27).

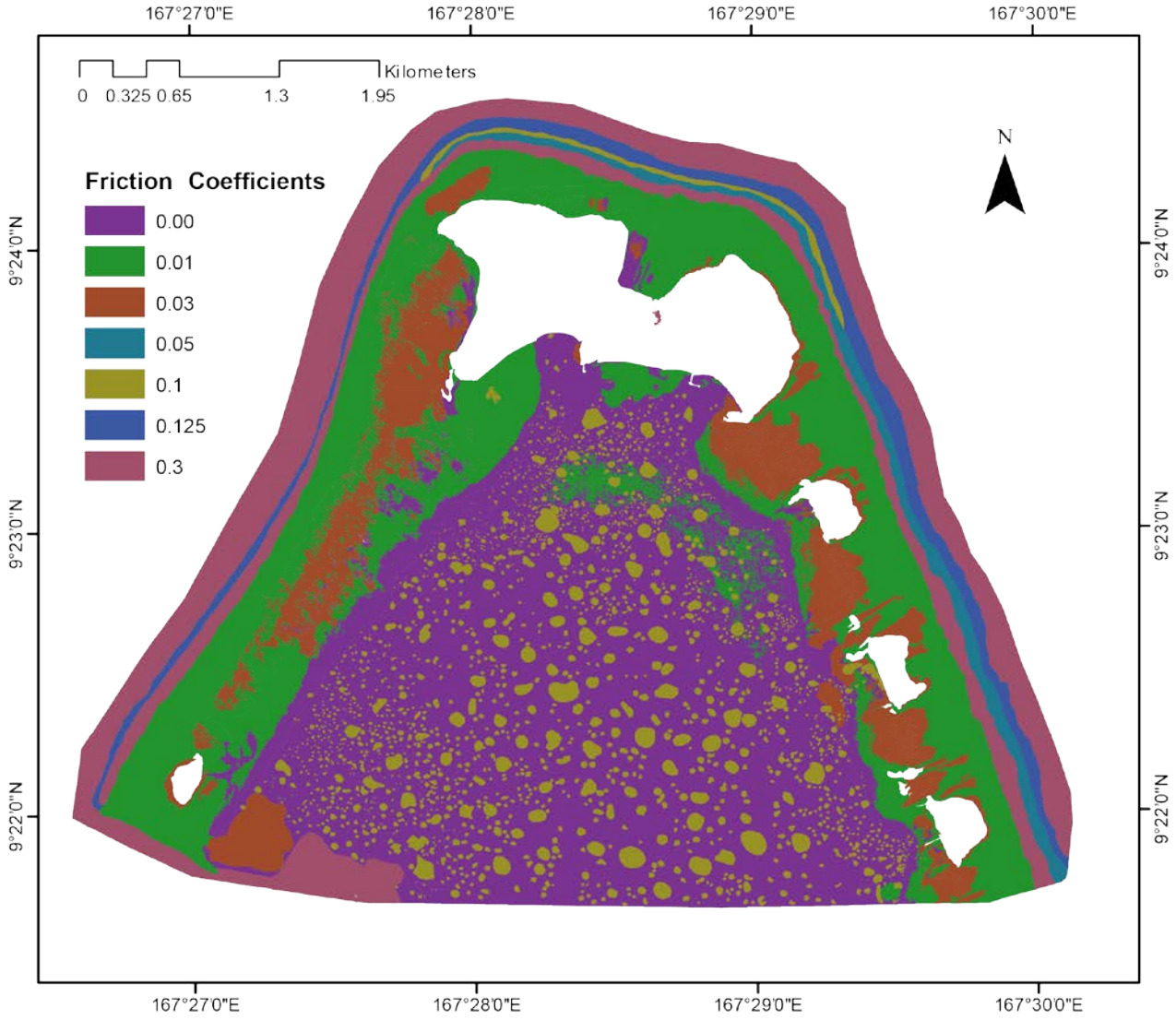

Figure 27. Map showing friction coefficients for benthic habitats in the Roi-Namur study area based on literature values listed in TABLE 6.

3.3 Terrestrial Habitat Mapping

Although it was communicated that high-resolution land cover data already existed for Roi-Namur, we came to learn that was not the case and thus had to embark on collecting data on the island's land cover to determine how much of any given land cover class would be inundated for a given future wave and sea-level scenario. Half-meter true-color and three-band color infrared satellite imagery was used as base layers to develop the terrestrial land cover map. ArcGIS 10.2.2 Interactive Supervised Classification tool, which accelerates the maximum likelihood classification process, was used on training samples for 15 distinct land cover classes by creating histograms and scatterplots to confirm the distinctness of each class. A majority filter was applied using eight closest cells. The result of the majority filter was a raster that was converted to polygons that were grouped by land cover classification. The Error Inspector was used to create a

seamless land cover map that has no overlapping features or gaps. For some of the larger tree and grass-covered areas, polygons generated from the supervised classification were selected, cleaned up, and placed into the correct land cover layer.

The finished land cover map product had 852 polygons in 15 different categories over the 1,150,310 square meters of Roi-Namur (FIGURE 28, TABLE 7). Trees and vegetation areas were the most problematic. Many of the trees were nearly invisible, and what was seen on the image was in fact the shadow. Attempts were made to locate the actual tree, not just the shadow. Another issue involved the tree crown overlapping other features. Efforts were made to minimize the tree crown when next to buildings and other features such as roads. It was also often difficult to distinguish in some areas between trees and brush and other vegetation.

Figure 28. Map showing land cover classes on Roi derived from satellite imagery.

3.4 Future Oceanographic Modeling

The potential future changes in ocean surface gravity (storm) waves were quantitatively forecast using models driven by historical hindcast data and projected conditions based on Global Climate Model (GCM) output. Three-hourly GCM wind speed and wind direction output were assimilated for the area encompassing Kwajalein Atoll from the Coupled Model Inter-Comparison

Table 7. Land cover classes and their respective coverage on Roi.

Type	Count	Area (m^2)	Percent of total
Athletic Area	4	2,854	0.25
Beach	9	70,594	6.14
Building	100	36,561	3.18
Catchment Basin	3	45,878	3.99
Grass	72	517,786	45.01
Misc Feature	60	11,115	0.97
Misc Paved	8	5,766	0.50
Non-grass	1	953	0.08
Parking Area	7	4,909	0.43
Paved Road	3	84,856	7.38
Runway	1	76,766	6.67
Standing Water	1	958	0.08
Tree	556	197,278	17.15
Unpaved	22	80,624	7.01
Vegetation	5	13,411	1.17
Total	852	1,150,310	100.00

Project, phase 5 (CMIP5, World Climate Research Programme, 2011). To reduce uncertainty in model variability, wind speed and wind direction from four different GCMs (TABLE 8) were used as boundary conditions to the physics-based WAVEWATCH3 (Tolman 1997, 1999, 2009) numerical wave model. Criteria for selection of the four GCMs was based on availability of projected near surface (10-meter height) winds out to the year 2100, output frequency (3-hourly non-averaged synoptic winds), and completed GCM simulations at the time of project's initiation

Table 8. List of Global Climate Models (GCMs) used in the wave modeling, wave model used, and the model resolutions.

Model	Resolution: latitude x longitude (°)
BCC-CSM1.1	2.8 x 2.8
INM-CM4	2.0 x 1.5
MIROC5	1.4 x 1.4
GFDL-ESM2M	2.5 x 1.5
WAVEWATCH-III	1.25 x 1.00

in 2013. Two climate change scenarios were modeled: the representative concentration pathway (RCP)4.5 and RCP8.5, representing a medium mitigation and a high emissions scenario, respectively (Thomson et al., 2010; Riahi et al., 2010). Modeled time-periods were limited to a historic period (1976-2005) for model validation and future projections for the years 2026-2045 and 2085-2100, as prescribed by the CMIP5 modeling framework. CMIP5 wind speed and wind direction data were extracted and used as input for the WAVEWATCH3 model. The resulting modeled hourly deep-water wave heights, wave periods, wave directions, wind speeds, and wind directions were analyzed using the methods as described by Storlazzi et al. (2015b) and Shope et al. (2016) for the historic hindcast data to compute projections for the range of increases in end-member (top 5 percent) wave heights. Although there were no wave buoys in the study area during the 1976-2005 time frame that provided data to compare to the historical model output for the area to assess the model's skill, the model mean absolute error for locations where historic buoy data exists was 0.38 meter in significant wave height and 1.6 seconds in peak wave period. (Storlazzi et al., 2015b; Shope et al., 2016).

Under the RCP4.5 scenario during mid-century (2026-2045), the mean wave heights are projected to decrease 0.1 meter during the fall and winter months, with little change the rest of the year (FIGURE 29, TABLE 9); the top 5 percent wave heights are projected to follow similar decreasing trends (FIGURE 30, TABLE 9). The return interval wave height projections follow similar trends (TABLE 10). The mean and top 5 percent wave periods are projected to remain relatively the same. In terms of wave direction, the top 5 percent waves are projected to rotate 5 to 10 degrees counterclockwise during the fall at Kwajalein but become less variable during the spring. Under RCP8.5 during mid-century (2026-2045), the mean and top 5 percent wave heights wave heights are projected to decrease during the fall and winter months, similar to those under RCP4.5, but larger decreasing trends (0.2 meter). The mean and top 5 percent wave periods are projected to remain relatively the same. The top 5 percent waves are projected to rotate 10 to 20 degrees counterclockwise and become more variable during the fall at Kwajalein.

Under the RCP4.5 scenario during end-century (2081-2100), the mean wave heights are projected to decrease up to 0.2 meter during the fall and winter months, with little change the rest of the year (FIGURE 29, TABLE 9); the top 5 percent wave heights are projected to follow similar decreasing trends (FIGURE 30, TABLE 9). The return interval wave height projections follow similar trends (TABLE 10). The mean and top 5 percent wave periods are projected to remain relatively the same. The top 5 percent waves are projected to rotate 10 to 20 degrees counterclockwise during the fall and more variable during the summer at Kwajalein. Under RCP8.5 during end-century (2026-2100), the mean and top 5 percent wave heights wave heights are projected to decrease during the fall and winter months, similar to those under RCP4.5, but larger decreasing trends (0.2 meter). The mean and top 5 percent wave periods are projected to remain relatively the same. The mean waves are projected to rotate 5 to 10 degrees clockwise during the fall at Kwajalein, whereas the top 5 percent waves' directions are projected to become less variable during the spring and more variable during the summer and fall. See Storlazzi et al. (2015b) and Shope at al. (2016) for additional information on future trends in waves and winds through the 21st century.

3.5 Oceanographic Data Acquisition

In order to calibrate and validate the physics-based, numerical hydrodynamic model, an 18-month field experiment was conducted on Roi Namur Island in Kwajalein Atoll at the same

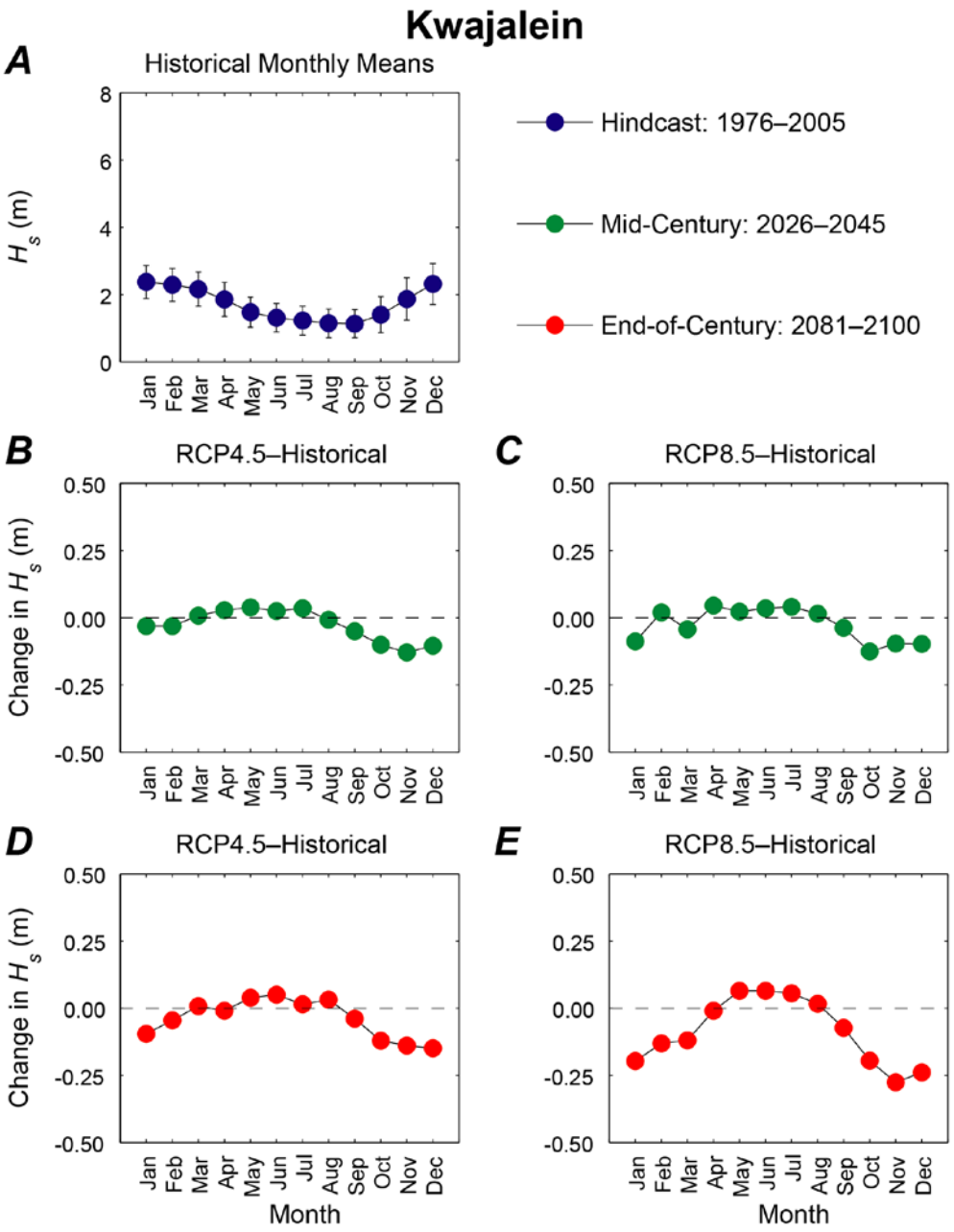

Figure 29. Time series plots showing time series of monthly mean significant wave height (Hs) at Kwajalein Atoll. A. Hindcast (1976–2005) mean significant wave heights by month with associated error bars. B. Plot of the change in mean 2026–2045 significant wave heights for the RCP4.5 scenario from hindcast monthly significant wave height means. C. Plot of the change in mean 2026–2045 significant wave heights for the RCP8.5 scenario from hindcast monthly significant wave height means. D. Plot of the change in mean 2081–2100 significant wave heights for the RCP4.5 scenario from hindcasted monthly significant wave height means. E. Plot of the change in mean 2081–2100 significant wave heights for the RCP8.5 scenario from hindcast monthly significant wave height means.

Table 9. Kwajalein monthly means and mean of the top 5 percent for significant wave height, peak wave period, and peak wave direction.

[Years: Hindcast = 1976–2005; RCP mid = 2026–2045; RCP end = 2081–2100. Wave directions are "coming from"]

Month	Jan	Feb	Mar	Apr	May	Jun	July	Aug	Sep	Oct	Nov	Dec
Mean Wave Height (meter)												
Hindcast	2.4±0.5	2.3±0.5	2.2±0.5	1.9±0.5	1.5±0.4	1.3±0.4	1.2±0.4	1.1±0.4	1.1±0.4	1.4±0.5	1.9±0.6	2.3±0.6
RCP4.5 - mid	2.3±0.5	2.3±0.5	2.2±0.5	1.9±0.5	1.5±0.4	1.3±0.4	1.3±0.4	1.1±0.5	1.1±0.4	1.3±0.5	1.7±0.5	2.2±0.6
RCP8.5 - mid	2.3±0.5	2.3±0.5	2.1±0.5	1.9±0.5	1.5±0.5	1.3±0.4	1.3±0.5	1.2±0.5	1.1±0.4	1.3±0.4	1.8±0.6	2.2±0.6
RCP4.5 - end	2.3±0.5	2.2±0.5	2.2±0.5	1.8±0.5	1.5±0.4	1.4±0.5	1.2±0.4	1.2±0.5	1.1±0.4	1.3±0.5	1.7±0.6	2.2±0.6
RCP8.5 - end	2.2±0.5	2.2±0.5	2.0±0.5	1.8±0.4	1.5±0.4	1.4±0.	1.3±0.4	1.2±0.5	1.1±0.4	1.2±0.4	1.6±0.5	2.1±0.5
Top 5 percent Wave Height (meter)												
Hindcast	3.6±0.4	3.5±0.3	3.4±0.5	3.1±0.4	2.5±0.3	2.3±0.3	2.4±0.4	2.3±0.7	2.3±0.6	2.9±0.7	3.5±0.5	3.8±0.6
RCP4.5 - mid	3.5±0.3	3.5±0.4	3.3±0.3	3.0±0.2	2.5±0.3	2.4±0.3	2.4±0.4	2.5±0.7	2.2±0.5	2.6±0.6	3.2±0.4	3.6±0.4
RCP8.5 - mid	3.5±0.3	3.7±0.4	3.3±0.3	3.2±0.7	2.6±0.5	2.4±0.3	2.5±0.5	2.5±0.7	2.3±0.5	2.5±0.5	3.5±0.6	3.5±0.4
RCP4.5 - end	3.4±0.3	3.4±0.3	3.4±0.3	2.9±0.2	2.5±0.2	2.4±0.4	2.4±0.7	2.6±0.8	2.5±0.6	2.6±0.5	3.2±0.6	3.5±0.4
RCP8.5 - end	3.2±0.3	3.3±0.3	3.1±0.2	2.8±0.3	2.4±0.2	2.4±0.3	2.4±0.5	2.6±0.9	2.1±0.7	2.5±0.6	3.1±0.4	3.2±0.3
Mean Wave Period (seconds)												
Hindcast	11±2	10±2	10±2	9±2	9±1	9±2	9±2	9±2	9±2	10±2	10±2	11±2
RCP4.5 - mid	11±2	10±2	10±2	9±1	9±1	9±2	9±2	9±2	9±2	10±2	10±2	10±2
RCP8.5 - mid	11±2	10±2	10±2	9±2	9±1	9±2	9±1	9±2	9±2	10±2	10±2	11±2
RCP4.5 - end	11±2	11±2	10±2	9.5±2	8.9±1	8.7±1	8.9±1	9.1±2	9.2±2	9.8±2	10±2	11±2
RCP8.5 - end	11±2	10±2	10±2	9±2	9±1	9±1	9±1	9±2	9±2	10±2	10±2	10±2
Top 5 percent Wave Period (seconds)												
Hindcast	11±2	11±2	10±2	10±1	9±1	8±1	9±1	9±2	9±2	10±2	10±1	11±1
RCP4.5 - mid	11±3	11±2	10±2	10±1	9±1	8±1	8±1	9±2	9±2	10±2	10±2	10±2
RCP8.5 - mid	11±2	11±2	10±1	10±1	9±1	8±1	8±1	8±2	9±2	10±2	10±2	11±1
RCP4.5 - end	11±2	11±2	10±1	10±1	9±1	8±1	9±2	9±2	9±2	10±2	10±2	10±2
RCP8.5 - end	11±3	10±2	10±2	9±1	9±1	8±1	8±1	9±2	9±2	9±2	10±2	11±2
Mean Wave Direction (°)												
Hindcast	50±17	49±18	55±16	61±15	69±18	80±25	89±32	100±43	85±49	56±37	49±22	49±17
RCP4.5 - mid	49±17	50±18	55±15	62±14	69±15	80±21	90±33	104±39	95±41	60±39	48±22	51±18
RCP8.5 - mid	49±17	51±17	54±16	62±16	69±16	79±20	92±33	108±46	95±51	60±38	48±22	50±17
RCP4.5 - end	48±19	48±19	55±15	61±15	68±14	79±19	90±33	104±47	98±49	56±44	47±24	51±18
RCP8.5 - end	48±19	50±19	56±15	62±11	71±14	81±20	88±33	105±38	98±43	63±38	51±20	51±16
Top 5 percent Wave Direction (°)												
Hindcast	55±14	52±17	54±19	59±28	69±31	73±32	90±67	191±10	267±11	67±68	59±32	54±18
RCP4.5 - mid	49±18	57±17	56±12	62±18	69±18	74±40	93±56	172±89	194±12	47±105	49±28	55±17
RCP8.5 - mid	54±16	57±13	57±11	62±34	73±26	77±33	111±65	192±83	239±94	34±90	52±45	54±13
RCP4.5 - end	51±20	53±16	57±12	62±17	66±9	79±37	113±75	209±74	214±78	355±10	49±45	57±18
RCP8.5 - end	49±17	55±12	60±15	62±12	70±15	80±44	86±75	194±78	170±13	67±75	55±27	54±13

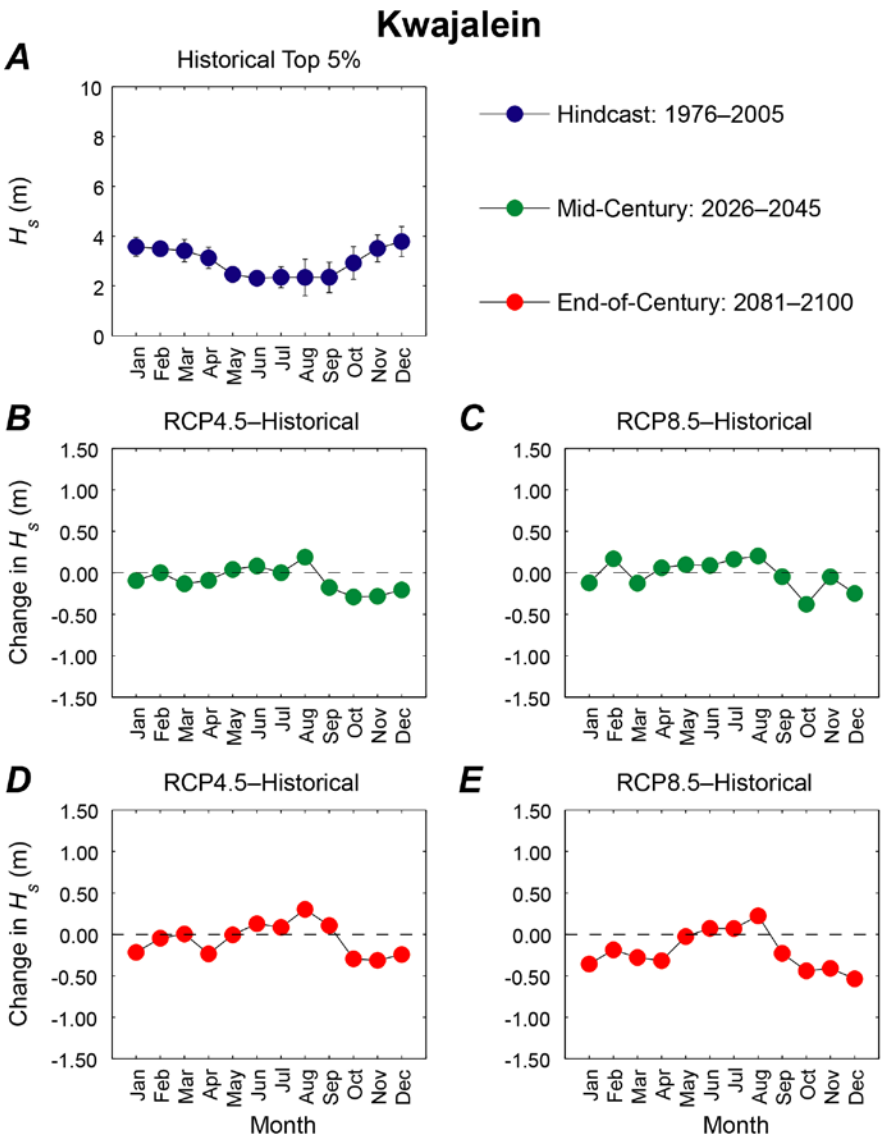

Figure 30. Time series plots showing time series of monthly mean of the top 5 percent of significant wave heights (Hs) at Kwajalein Atoll. A. Hindcast (1976–2005) mean of the top 5 percent of significant wave heights by month with associated error bars. B. Plot of the change in mean of the top 5 percent of 2026–2045 significant wave heights for the RCP4.5 scenario from hindcast top 5 percent of monthly significant wave height means. C. Plot of the change in mean of the top 5 percent of 2026–2045 significant wave heights for the RCP8.5 scenario from hindcast top 5 percent of monthly significant wave height means. D. Plot of the change in mean of the top 5 percent of 2081–2100 significant wave heights for the RCP4.5 scenario from hindcast top 5 percent of monthly significant wave height means. E. Plot of the change in mean of the top 5 percent of 2081–2100 significant wave heights for the RCP8.5 scenario from hindcast top 5 percent of monthly significant wave height means.

Table 10. Return values of ensemble-average significant wave heights of hindcast and forecast scenarios, including lower and higher 95 percent confidence intervals, at the Kwajalein location.

[Years: Hindcast = 1976–2005; RCP mid = 2026–2045; RCP end = 2081–2100. Wave height values are in meters]

Scenario	Hindcast			RCP4.5 - mid			RCP8.5 - mid			RCP4.5 - end			RCP8.5 - end		
	Low	R_v	High	Low	R_v	High	Low	R_v	High	Low	R_v	High	Low	R_v	High
2-year	4.73	5.35	6.42	4.28	4.80	5.92	4.50	5.16	6.51	4.45	5.07	6.22	4.21	4.77	5.80
5-year	5.15	6.30	8.55	4.45	5.35	7.64	4.76	5.91	8.70	4.74	5.81	8.11	4.48	5.46	7.58
10-year	5.48	7.18	10.87	4.57	5.82	9.51	4.94	6.56	11.10	4.95	6.45	10.09	4.69	6.08	9.48
20-year	5.83	8.23	14.07	4.68	6.34	12.07	5.11	7.31	14.39	5.15	7.17	12.71	4.89	6.79	12.03
50-year	6.31	9.94	20.21	4.81	7.13	16.96	5.32	8.47	20.72	5.40	8.27	17.50	5.14	7.90	16.83
100-year	6.69	11.54	26.92	4.90	7.82	22.27	5.47	9.49	27.63	5.59	9.23	22.51	5.33	8.89	21.95

time far-field, deep-water wave, and wind-forcing data were acquired to determine the influence of water depth (as related to tidal and atmospheric forcing) on wave propagation across the atoll rim and over the reef flats over a range of oceanographic and meteorologic conditions.

Three 6-month deployments were carried out on Roi-Namur Island (TABLE 11). The deployments involved installing two cross-shore arrays of bottom-mounted RBR wave gauges (i.e., pressure sensors) over the reef flat and fore reef (FIGURES 31-32). Each array consisted of three gauges on the reef flat and one gauge on the fore reef. Between the two adjacent transects, an upwards-looking 600-kHz Nortek Acoustic Wave and Current Meter (AWAC) was placed deeper on the fore reef (~21 meter depth; FIGURE 4-5). Every hour the wave gauges collected pressure measurements at 2 Hz in 34-minute bursts (4096 samples) and the AWAC recorded pressure at 1 Hz in 34-minute bursts (2048 samples). The AWAC also collected hourly profiles of 10-minute averaged current velocity in 1-meter vertical bins throughout the water column. In addition, to capture wave and tidal conditions in the lagoons, an RBR wave gauge and an RBR tide gauge were placed on the fuel dock pier in the lagoon. Several of the RBR wave gauges utilized during Deployment 1 experienced failure due to flooding through the pressure port. This flooding occurred due to a manufacturing defect in the instruments. As a result, for Deployment 3, an entirely new suite of RBR wave and tide gauges was deployed; this deployment was marred by poor battery performance and most of the instruments stop recording 2 months earlier than planned (TABLE 11).

Table 11. List of oceanographic deployment time frames.

Deployment	Start date	End date
D-1	03 November 2013	23 April 2014
D-2	26 April 2014	21 October 2014
D-3	25 October 2014	18 February 2015

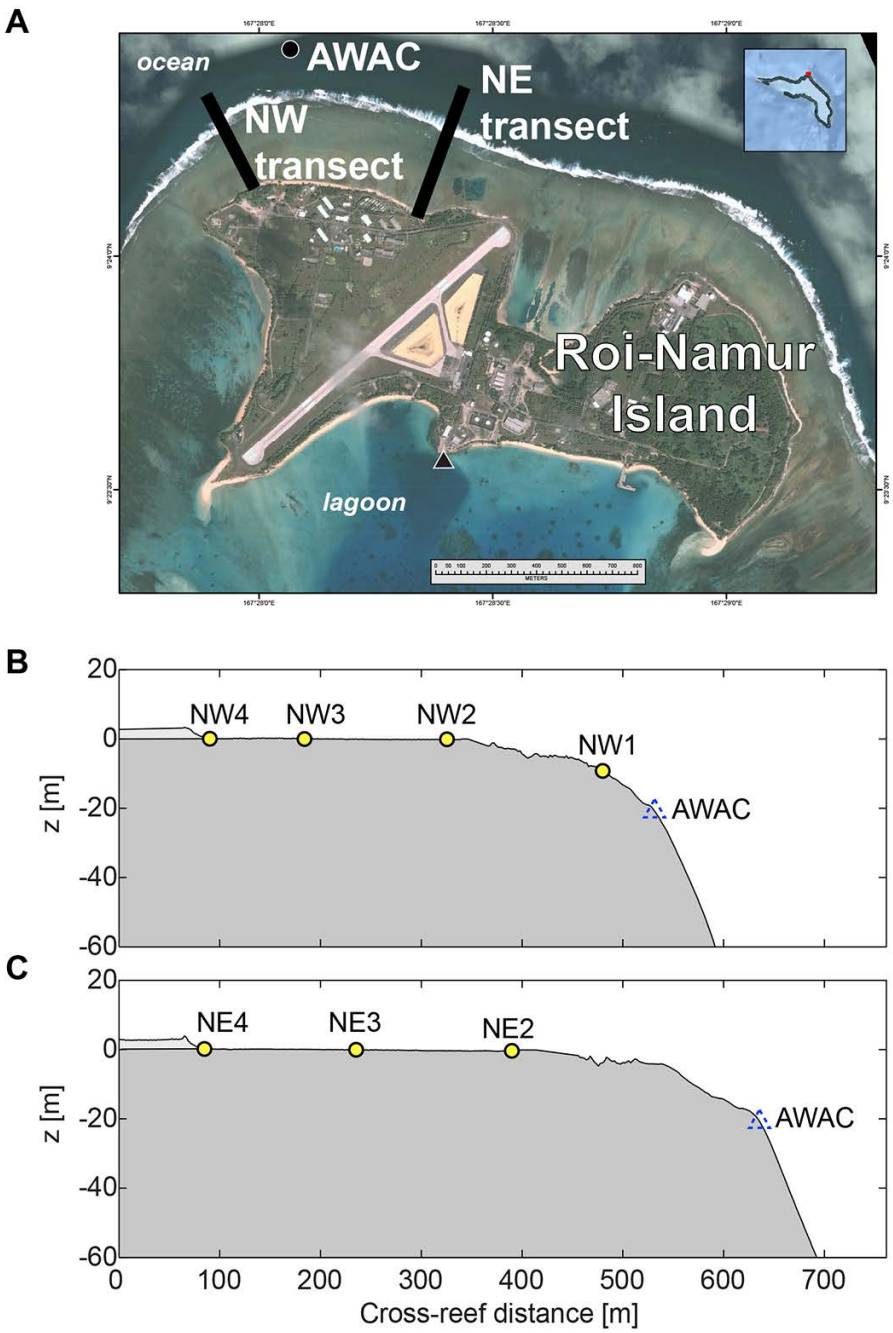

Figure 31. Locations of the oceanographic study sites on Roi-Namur. A. Map showing locations of cross-reef transects (solid black lines), the offshore AWAC (black circle), and the lagoon sensors (black triangles). B. Bathymetric profile of the northwest (NW) cross-reef transect. C. Bathymetric profile of the northeast (NE) cross-reef transect. Relative locations and depths are shown for the pressure (wave) gauges (yellow circles) and the offshore AWAC (dashed triangles), as well as their cross-shore distances. Please note that the AWAC location shown in B and C is only meant to show relative depth to the other sensors; because the AWAC was not directly in-line with either transect, the cross-reef distances may not be not accurate.

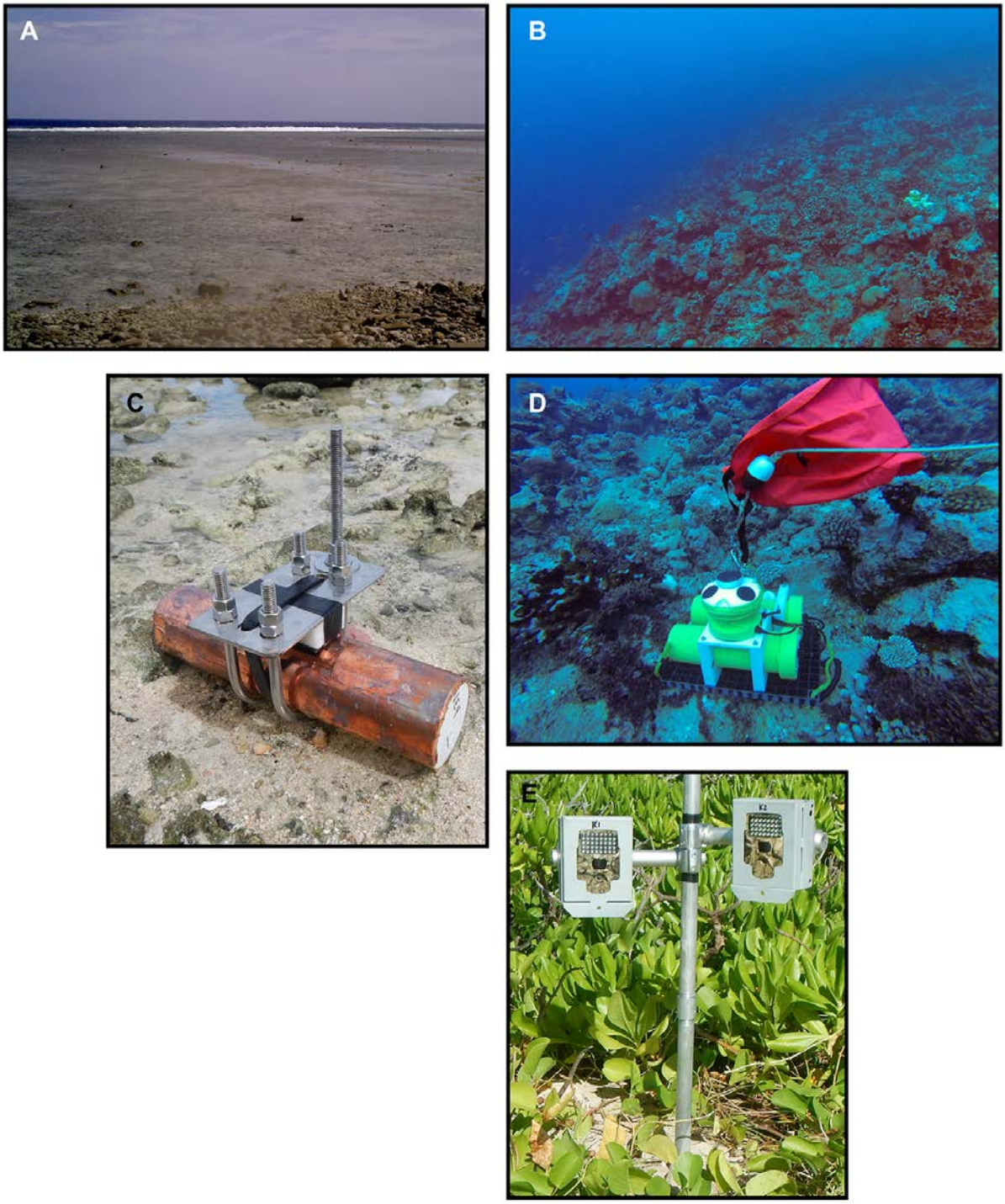

Figure 32. Photographs of study area and instrument installations. A. The relatively smooth reef flat during low tide. B. The steep fore reef with high coral coverage. C. An RBR wave gauge on the reef flat during low tide. D. Deployment of the AWAC on the fore reef (line and float were for deployment operations). E. Time-lapse cameras installed on the beach.

In addition to the oceanographic instrument suite, Covert infrared (IR) time-lapse cameras were used to capture photos of beach runup and morphologic change (FIGURE 4). On the backbeach at each array site, two IR cameras were installed on metal poles and were oriented so that one faced across-shore (i.e., offshore) and the other along-shore (i.e., down the beach). These cameras took an IR photo every 15 minutes. At the conclusion of each 6-month deployment, all 9 oceanographic instruments and 4 cameras from each island were recovered, the data downloaded, the instruments cleaned, refurbished, reprogrammed, and redeployed as quickly as possible. The IR cameras frequently failed recording after a few months due to water penetrating the housing and ruining the batteries.

The full record of meteorological and offshore oceanographic conditions during the entire study is shown in FIGURE 33; similar data for Deployment 1 are shown in FIGURE 34. Wind conditions recorded at the Kwajalein Airport were dominated by northeasterly trade winds. Tides at both sites were predominantly semi-diurnal, ranging from approximately -0.5 meter below to +0.5 meter above MSL. Wave parameters were examined across different frequency ranges: incident or short-period (IC) waves with periods (T) within the range 5 seconds < $T \leq$ 25 seconds; infragravity (IG) waves of 25 seconds < $T \leq$ 250 seconds; and very-low frequency (VLF) waves with a range of 250 seconds < $T \leq$ 1000 seconds. Although IC waves dominate over the fore reef and at the reef crest, lower frequency waves in the IG and VLF bands become increasingly important over the reef flat (FIGURE 35). At both sites, IC significant wave heights, $H_{s,IC}$, decrease moving inshore across the reef flat, whereas IG significant wave heights, $H_{s,IG}$, and VLF significant wave heights, $H_{s,VLF}$, increase towards shore. These wave heights are also strongly controlled by water levels (i.e., tide stage), as greater water levels over the reef flat allow the propagation of larger waves (Cheriton et al., 2016).

The two largest wave events, with maximum recorded wave heights exceeding 6 meters, occurred during the first deployment: (1) 19 December 2013 and (2) 2-3 March 2014 (FIGURE 34; Cheriton et al., 2016). The March 2014 large wave event produced substantial overwash on the northern portion of Roi-Namur (FIGURE 36). This event coincided with a spring tide, fore reef $H_{s,IC}$ that exceeded 4 meters, and maximum recorded offshore wave heights of approximately 7 meters (FIGURE 37). During this event, $H_{s,IC}$ at the outer reef flat reached over 1.0 meter, while over the reef flat, $H_{s,IG}$ reached nearly 1.0 meter and $H_{s,VLF}$ 0.8 meter. The comparable magnitudes of these long-period wave heights indicates that VLF waves may be an important factor in run-up and overwash events at Roi-Namur (Cheriton et al., 2016; Gawhen et al., 2016). During the low tide phases, total water-level setup over the reef flat was greater than 1 meter. Taking the peak water levels measured over the reef flat, which represent the combined combination of short- and long-period waves, the maximum water levels exceeded the burst averages by over 1.5 meters. This, in summation with tidal stage and setup, puts total water levels at 2.5-3.3 meters over the reef flat, sufficient for overwash of beach barrier structures (FIGURE 36).

3.6 Wave-driven Flood Modeling

In general, coastal flooding is caused by a combination of waves, tides and wind-induced surges. In the case of reef-lined coasts, such as Kwajalein Atoll, coastal flooding can occur during storm events but also in “blue sky conditions” when remotely-generated incident swell (IC) waves impact the coast. In this case the local surge is small, and tides and waves, especially locally-generated IG motions, are dominant. When modeling such events, it is important to apply a model that incorporates all these processes to accurately predict the frequency and magnitude of flood

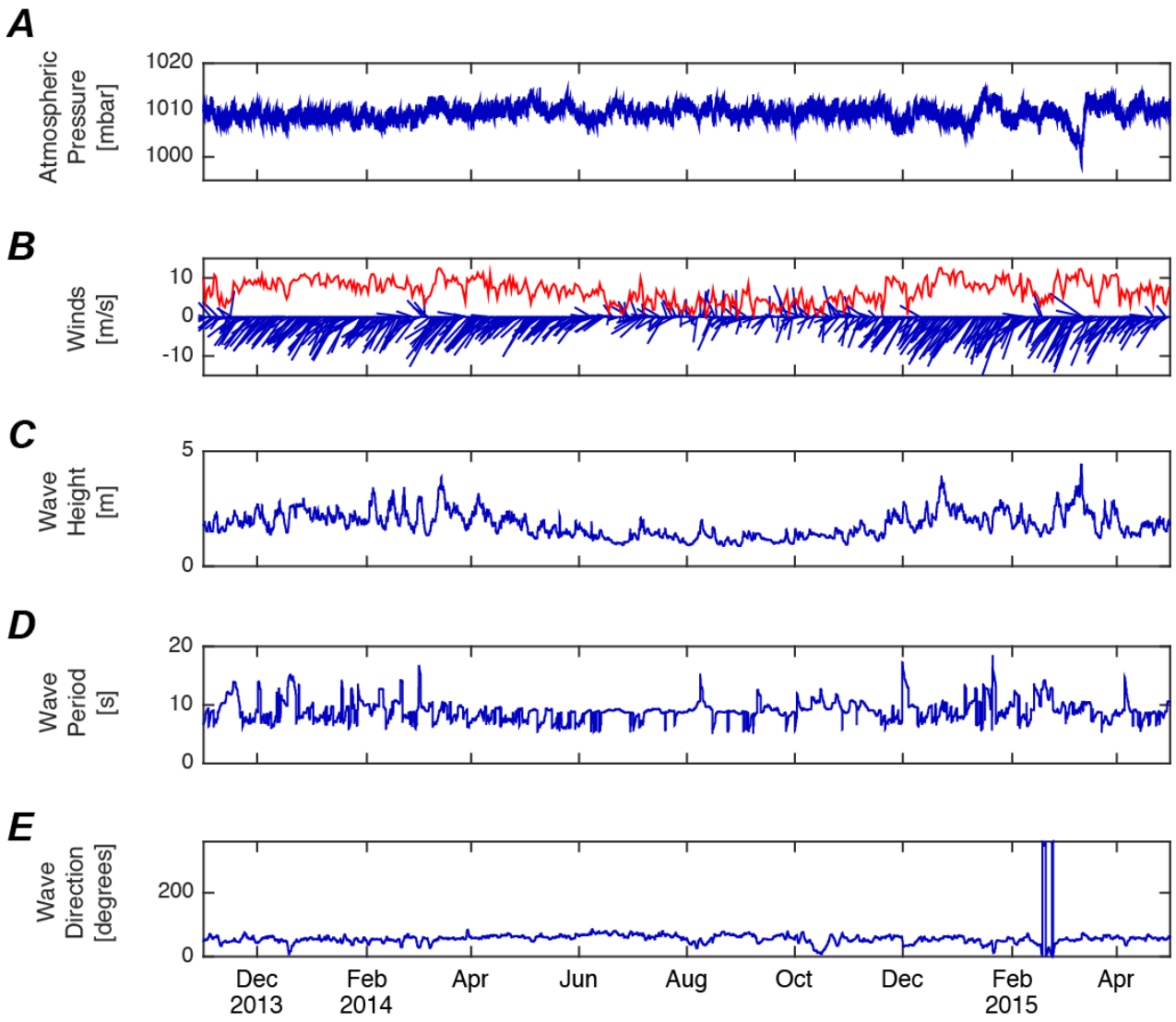

Figure 33. Time series plots showing time series of meteorological forcing from Kwajalein Airport and oceanographic conditions off Roi-Namur during Deployments 1-3 from November 2013-February 2015. A. Atmospheric pressure. B. Wind speed and velocity. C. Deep-water significant wave height (incident band). D. Deep-water peak wave period (incident band). E. Deep-water mean wave direction.

events. In this study, we use a number of high-resolution implementations of the XBeach model, a high-fidelity, physics-based two-dimensional area model for the nearshore and coast (Roelvink et al., 2009; van Dongeren et al., 2013; Quataert et al., 2015) to simulate wave transformation and coastal flooding on Kwajalein Atoll.

3.6.1 XBeach model description and options

The model can be run in two modes: in surf-beat mode and in non-hydrostatic mode. The surf-beat mode takes into account the temporal variation of wave height on the wave-group scale, which drives IG waves. For non-hydrostatic XBeach calculations, depth-averaged flow due to

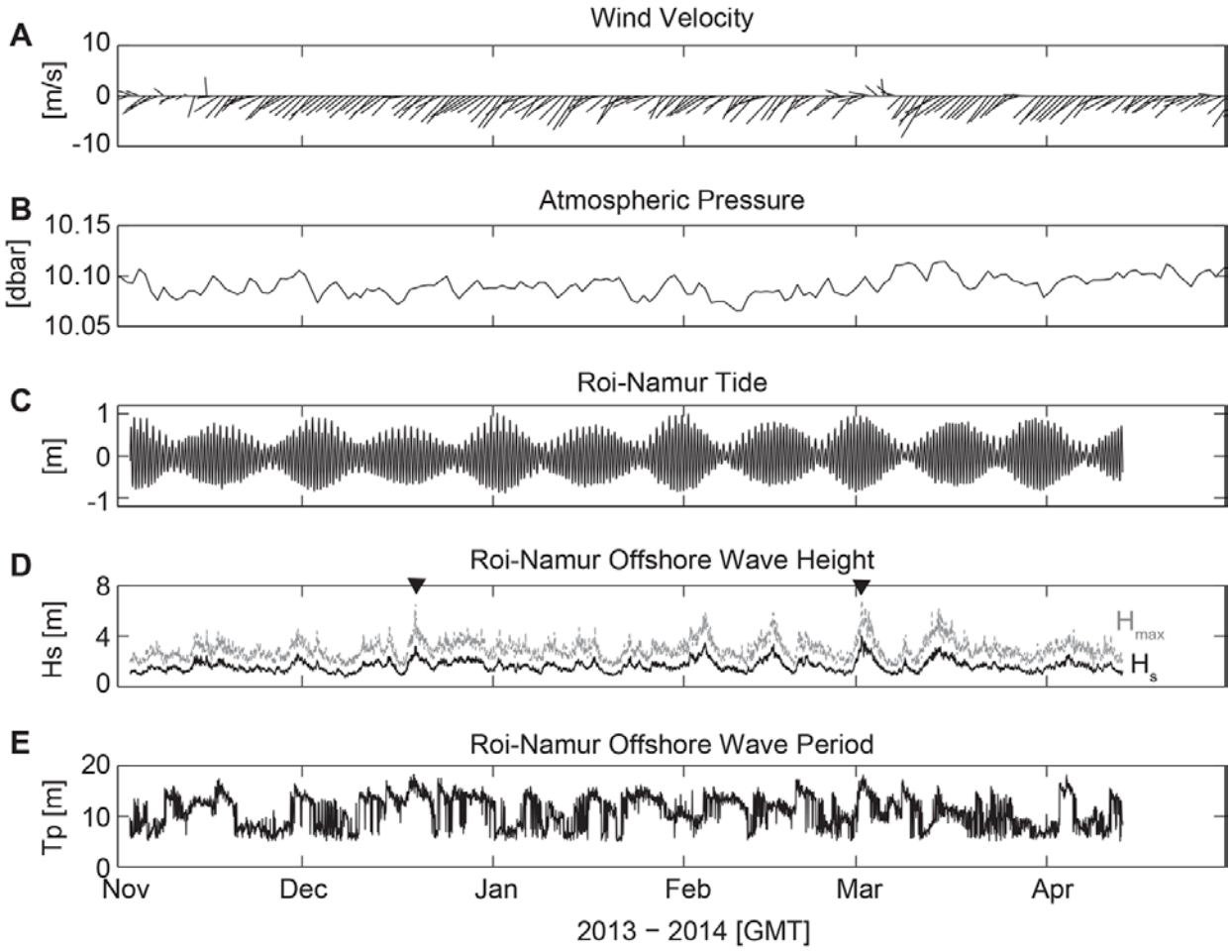

Figure 34. Time series plots showing time series of meteorological forcing from Kwajalein Airport and oceanographic conditions at Roi-Namur during Deployment 1 from 3 November 2013 to 30 April 2014. A. Daily-averaged wind velocity. B. Atmospheric pressure. C. Tide. D. Significant wave height (incident band). E. Peak wave period. Triangles denote the two large wave events.

waves and currents are computed using the non-linear shallow water equations, including a non-hydrostatic pressure. The main advantage of the non-hydrostatic mode is that the IC motions, including runup and overwash, are resolved in the model. This is especially important on steep slopes where incident-band motions may be large, but has the disadvantage of being computationally more expensive than the surf-beat mode.

XBeach in surf-beat mode has been applied in coral reef environments (Pomeroy et al., 2012; Van Dongeren et al., 2013) and proved to accurately predict the key reef hydrodynamics. To include the effect of higher bottom roughness on incident wave decay, the IC wave friction coefficient (f_w) was added to the formulations in surf-beat mode by Van Dongeren et al. (2013). The friction coefficient (c_f) is associated with both the mean currents and IG waves in both surf-beat and non-hydrostatic mode.

Two models were set up: a one-dimensional (1D) surf-beat model along a transect and a two-dimensional (2D) non-hydrostatic model. The 1D surf-beat model was used to examine the effects of different coral reef characteristics, such as reef dimensions and hydrodynamic

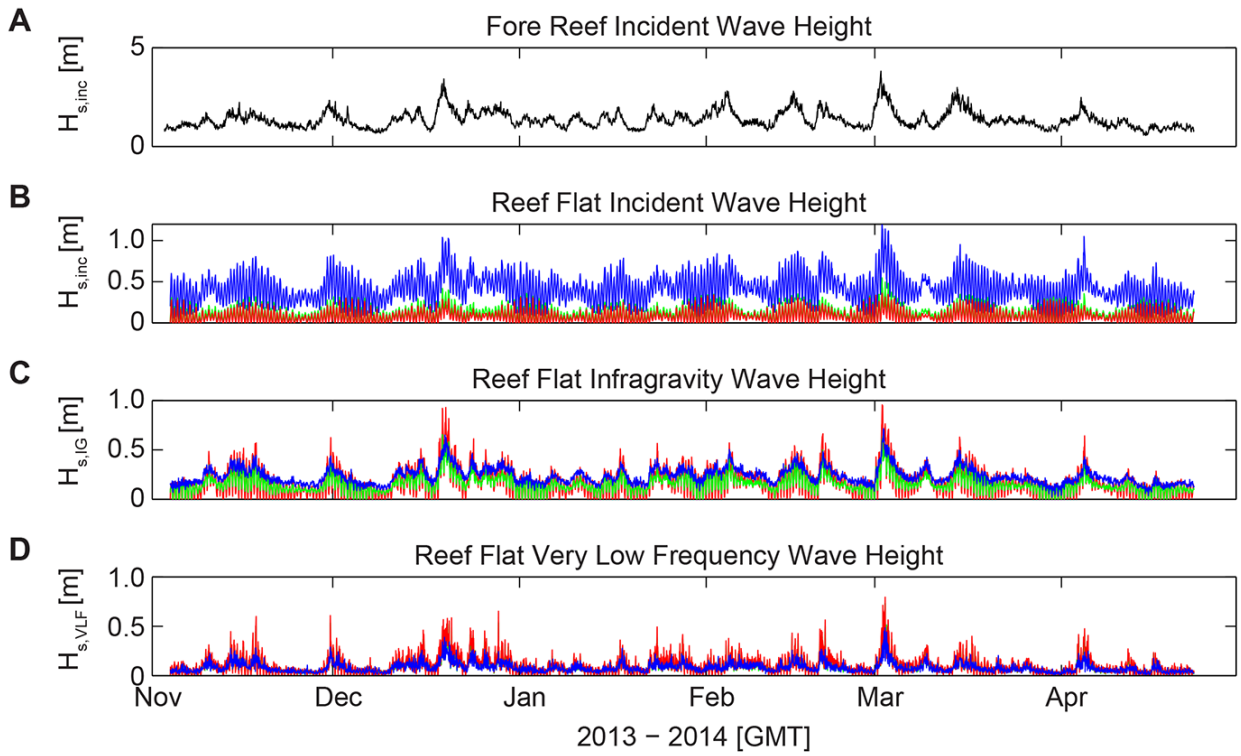

Figure 35. Time series plots showing time series from Deployment 1 of wave heights across the fore reef and reef flat off Roi-Namur. A. Incident band (5 seconds < period ≤ 25 seconds) waves on the fore reef. B. Incident band (5 seconds < period ≤ 25 seconds) waves on the reef flat. C. Infragravity band (25 seconds < period ≤ 250 seconds) waves on the reef flat. D. Very low frequency (250 seconds < period ≤ 1000 seconds) waves on the reef flat. For all panels the line colors indicate the following: gray = offshore (AWAC); black = fore reef; blue = outer reef flat; green = mid reef flat; red = inner reef flat.

roughness, on potential coastal hazards caused by wave-driven flooding and how these effects may be altered by projected climate change. The goal of the 2D non-hydrostatic model was to provide estimates of flooding extents and depths on Roi-Namur Island under a number of sea-level rise and climatic scenarios. Although XBeach can compute storm-driven erosion and deposition, based on the (a) heavy armoring of the seaward shoreline of Roi, and (b) observations by Webb and Kench (2010) and Ford and Kench (2015) that showed that atoll islands' planform areas have relatively maintained themselves over a period of limited sea-level rise during the 20th century, projections of island morphologic change were not included in the XBeach simulations and thus the topobathy DEM developed for this project was used for all future simulations.

3.6.2 XBeach One-Dimensional (1D) Hydrodynamic Modeling

For the 1D model, the measured cross-shore profile of the Roi-Namur northwestern transect ('NW' in FIGURE 31) was used as bathymetric profile. The same numerical grid was used for all simulations and varied in size from dx = 20 meters offshore to dx = 1 meter in nearshore. At the offshore boundary a weakly reflective boundary condition was applied, such that outgoing waves and currents could pass through with minimal reflection. A no flux/wall boundary

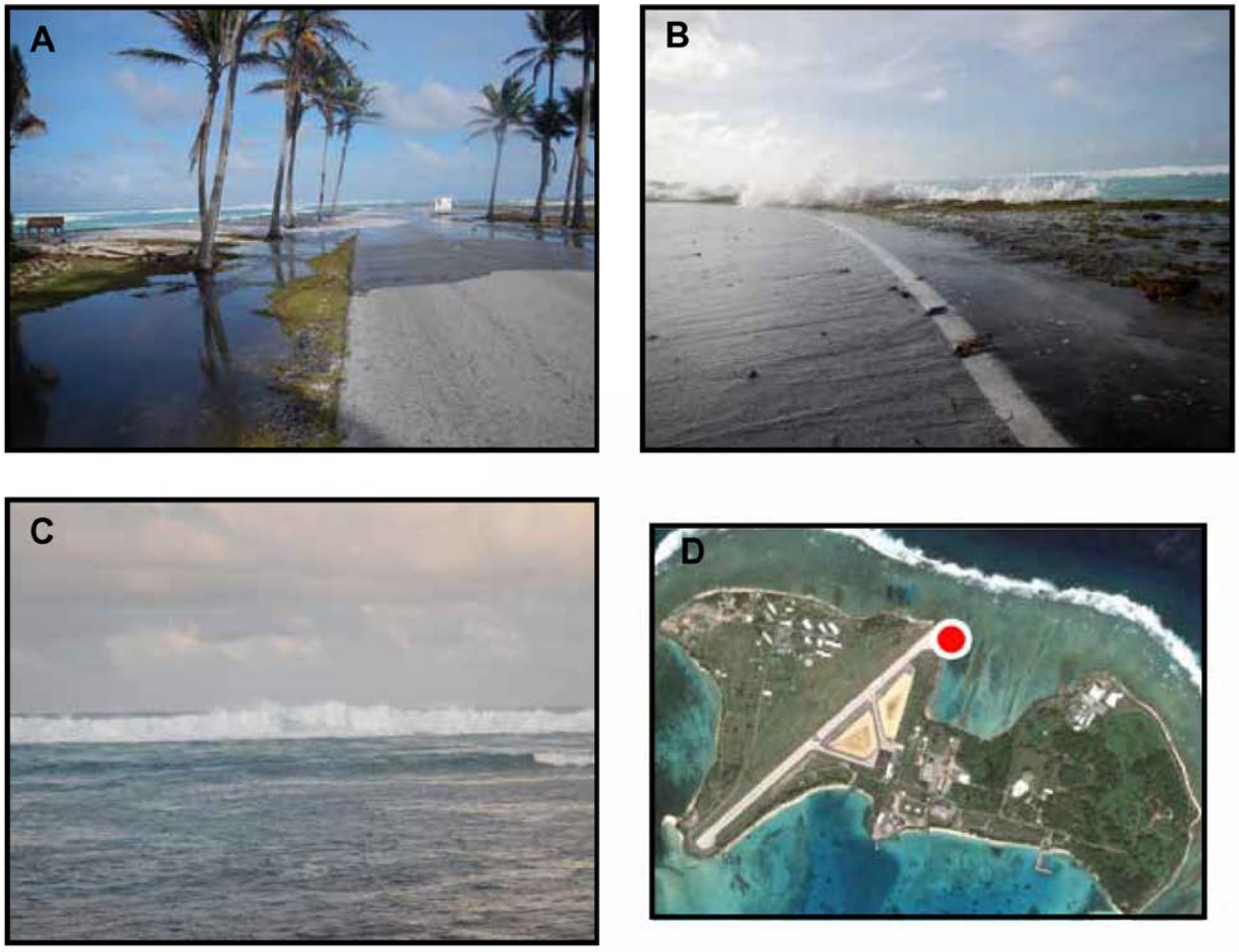

Figure 36. Photographs taken at the northeastern end of the runway during the 2-3 March 2014 overwash event on Roi-Namur. A. Seawater flooding on the road. B. Waves overtopping the dike and flooding the road. C. Large waves breaking on the reef crest. D. Map showing approximate location of where photos were taken on the island.

was applied at the shoreward model boundary. At the lateral boundaries a Neumann boundary condition was used, in which there were no gradients in surface elevation and velocities in the alongshore direction. The offshore tidal elevation and wave conditions from the collected water level and wave data were applied to the offshore boundary of the model domain. From the wave conditions (wave height, wave period, mean direction, and directional spreading), a sequence of hourly varying JONSWAP spectra were created. From these spectra, XBeach generated time series data for the IC and bound IG waves with an approach described by van Dongeren et al. (2003). The measured offshore water level was averaged per hourly burst of data and subsequently used as initial surface elevations at the offshore model boundary.

3.6.2.1 XBeach 1D model calibration and validation

The 1D model was calibrated and validated for model parameters f_w and c_f, with all other model parameters kept at default values. Model results were compared with the wave and water

level data measured at the NW transect. The validated 1D model results were then used as a base case in the variation simulations. In these simulations reef dimensions, bathymetry, hydrodynamic roughness, and wave and tidal conditions were changed to assess their impact on the nearshore hydrodynamics. The observations of water levels and waves on the Roi-Namur NW transect (FIGURE 37) were used to calibrate and validate the 1D surf-beat model. The model parameters f_w and c_f were calibrated for a 48-hour simulation period using the March 2014 large wave event, with all other parameters of the model at default values. Subsequently, the model was validated for the December 2013 large wave event.

The model skill was assessed by comparing measured and modeled values of mean water levels, and root-mean-squared IC and IG wave heights ($H_{rms,IC}$ and $H_{rms,IG}$, respectively) along the cross-shore profile (FIGURE 38). Quantitatively, the performance of the model was determined by calculating the bias and scatter index (SCI) as proposed by van der Westhuysen (2010) for wave models. Best results were achieved with a $f_w = 0.3$ and a spatially varying current friction coefficient, where $c_{f,fore\ reef} = 0.1$ and $c_{f,reef\ flat} = 0.01$ on the sloping fore reef and reef flat, respectively. The spatial variation of these current friction coefficients is consistent with the Roi-Namur reef topography. The validation confirms the calibrated model settings, shown by the red dots in FIGURE 38. The bias and SCI for water levels, $H_{rms,inc}$, and $H_{rms,IG}$ across the reef show very good correspondence between the modeled and measured data for most parameters and locations, with a few exceptions. The $H_{rms,inc}$ on the outer reef flat is under-predicted by the model (bias of -0.069 and -0.087, SCI of 0.141 and 0.182), as waves are predicted to dissipate more rapidly along the fore reef in the model by choosing the default settings for the breaker model. The optimum friction coefficients found for the Roi-Namur study site were lower than those applied in the Ningaloo reef XBeach model: $f_w = 0.6$ and $c_f = 0.1$ (van Dongeren et al., 2013). This is consistent with Roi-Namur's much smoother topography (FIGURES 5, 32) as compared to the subaqueous Ningaloo reef flat.

The parameter values found for the Roi-Namur reef fall within the range for other reef sites where previous hydrodynamic studies have been carried out. The 1D model was used to assess the impact of changing reef dimensions, bathymetry, hydrodynamic roughness, and wave and tidal conditions on the nearshore hydrodynamics. The calibrated 1D model settings were used as a base case in the variation simulations. For each simulation one parameter of the base case (Roi-Namur reef) was varied: fore reef slope, reef flat width, bed friction (hydrodynamic roughness), offshore wave height and reef flat water depth. Each of the fifty simulations was run for one cosine-shaped tidal cycle of 12 hours with an amplitude of 1 meter with respect to MSL. A constant JONSWAP spectrum was generated from the highest measured waves at Roi-Namur during the March 2014 event and was applied to the offshore model boundary ($H_{m0} = 3.9$ meters and $T_p = 14$ seconds).

Model results were post-processed to derive hourly-averaged water levels, wave-induced setup (local mean water level minus offshore tidal elevation), $H_{rms,IC}$, and $H_{rms,IG}$ at the toe of the beach. Since the model was not validated for wave runup, XBeach model results of wave runup were not used. The $z_{2percent}$ wave runup (wave runup level exceeded by 2 percent of incident waves) was calculated from the modeled hydrodynamics (water level, $H_{rms,IC}$ and $H_{rms,IG}$) at the toe of the beach to obtain a composite quantity that is an indicator of coastal flooding. For this calculation, the wave runup prediction method by van Gent (2001) was used, which was originally designed for breakwaters, can be used for conditions with shallow foreshores, and takes the combined effects of IC and IG waves $\left(\sqrt{{H_{rms,IC}}^2 + {H_{rms,IG}}^2}\right)$ into account.

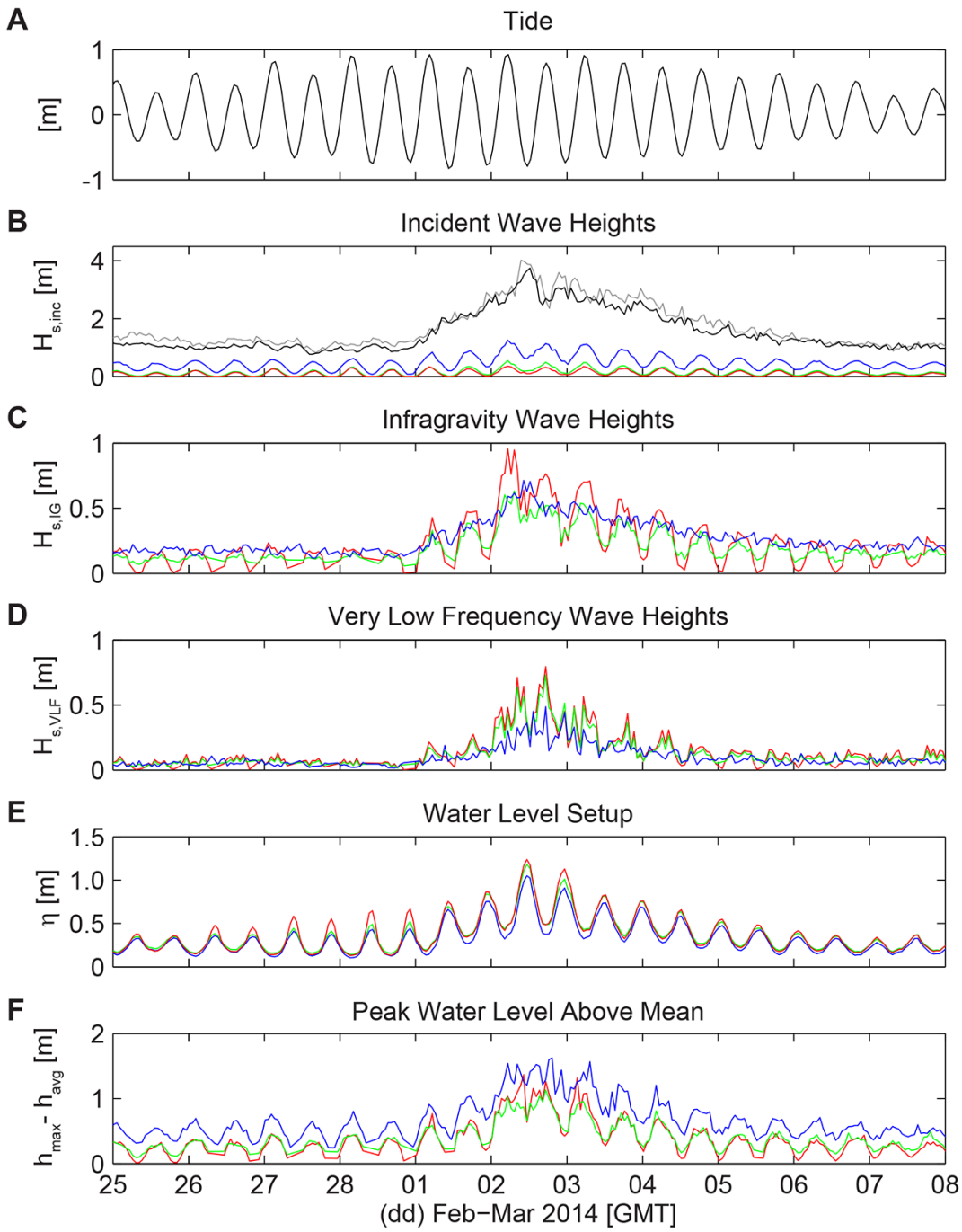

Figure 37. Time series plots showing time series from the Roi-Namur NW transect during the 2-3 March 2014 overwash event. An 11-day period of 25 February through 8 March 2014 is shown. A. Tide levels. B) Incident wave heights on fore reef and reef flat. C. Infragravity wave heights over the reef flat. D. Very low frequency wave heights over the reef flat. E. Water level setup on the inner reef flat. F. Peak (maximum) measured water levels above the mean on the inner reef flat. For all panels the line colors indicate the following: gray = offshore (AWAC); black = fore reef; blue = outer reef flat; green = mid reef flat; red = inner reef flat.

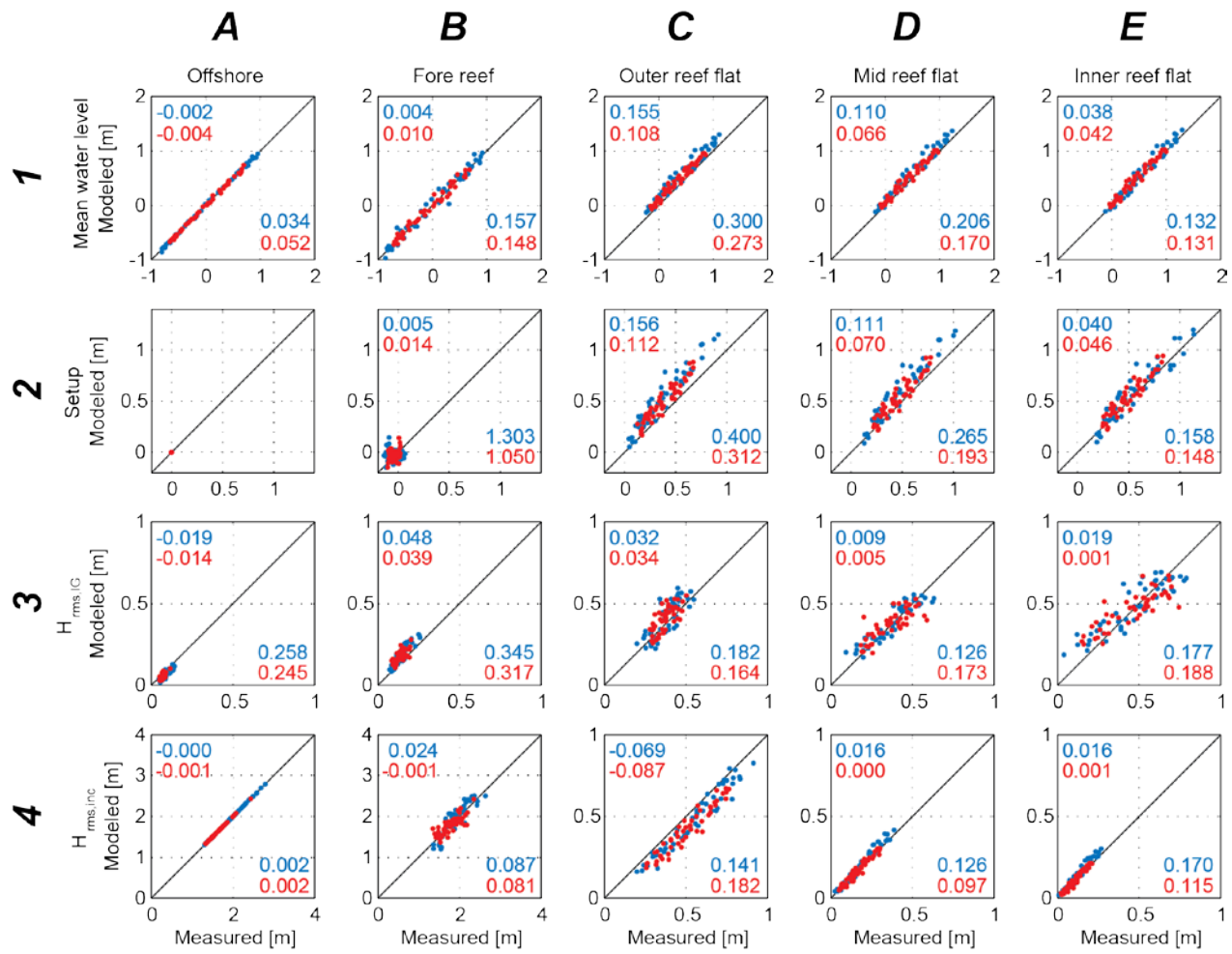

Figure 38. Comparison of measured and modeled burst-averaged data used to calibrate and validate the 1D XBeach model. 1. Mean water level. 2. Wave-induced setup. 3. Infragravity wave height ($H_{rms,IG}$). 4. Incident wave height ($H_{rms,inc}$) for the different instrument locations. A. Offshore. B. Fore reef. C. Outer reef flat. D. Middle reef flat. E. Inner reef flat. Best model results for calibration (blue) and validation (red) for: f_w = 0.3, $c_{f,fore\ reef}$ = 0.1 and $c_{f,reef\ flat}$ = 0.01. Predictive model skill calculated with bias (top left corner) and scatter index (SCI, bottom right corner).

3.6.2.2 XBeach 1D model insights into important hydrodynamic and geomorphic properties

The results of the simulations (FIGURE 39) show that the wave runup increases with smaller reef flat width, steeper fore reef slopes, decreased friction on the reef flat, and increased friction on the fore reef slope. The wave runup also increases with increased offshore sea level and wave heights. Variations in the reef flat width did not affect the mean water levels, as the wave-induced setup is generated on the fore reef and is constant across the reef flat itself. Note that the setup is inversely related to the offshore water level. For narrower reef flats the $H_{rms,IG}$ and $H_{rms,inc}$ at the toe of the beach increase, which suggests reef flat width affects frictional dissipation rates in wave height transformation across the reef (Lowe et al., 2005; Pomeroy et al., 2012).

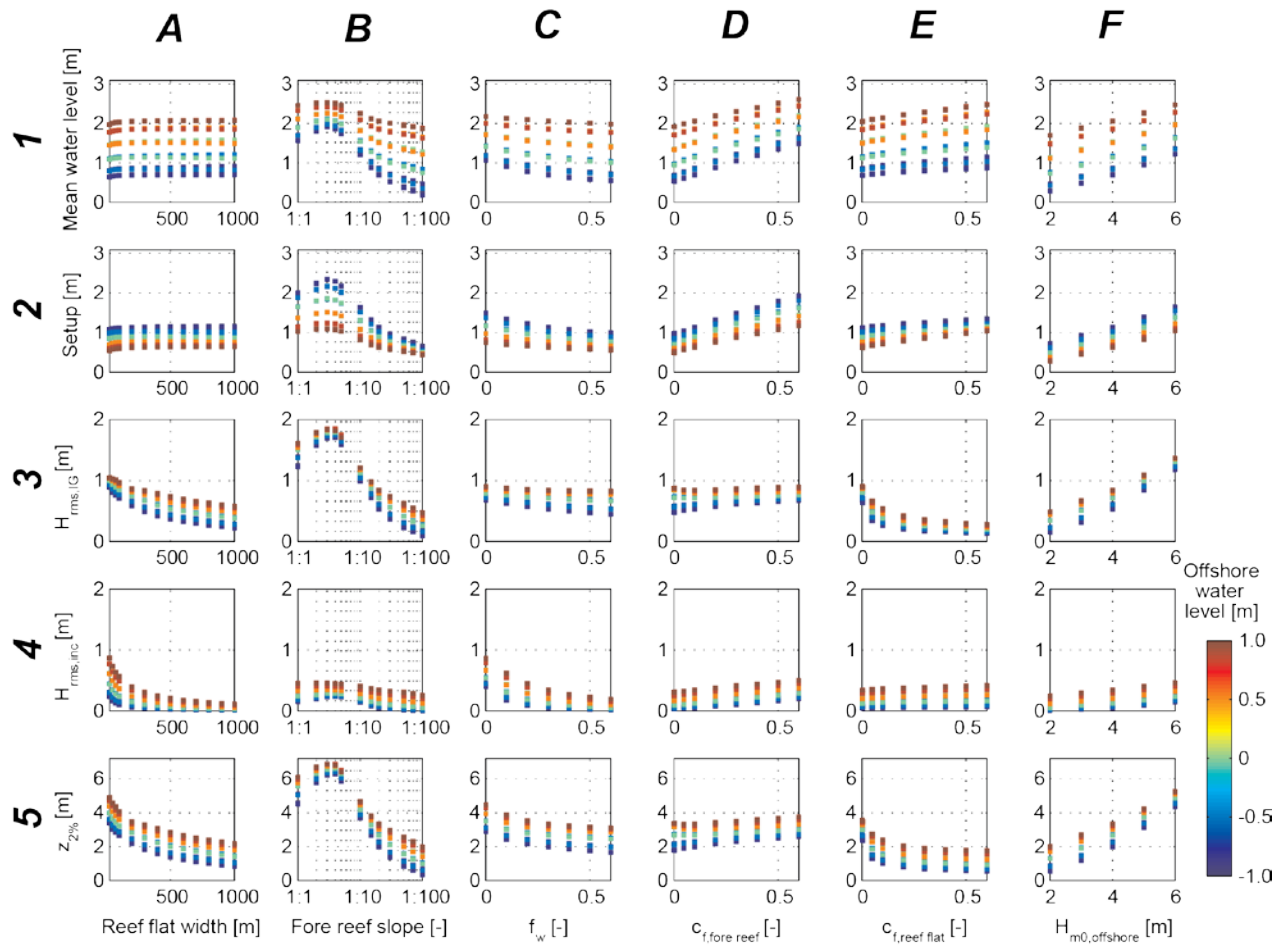

Figure 39. Response of nearshore hydrodynamics at the beach toe on the innermost reef flat to variations in reef characteristics for hourly varying offshore water levels. 1. Mean water level. 2. Wave-induced setup. 3. Infragravity wave height ($H_{rms,IG}$). 4. Incident wave height ($H_{rms,inc}$) 5. Top 2 percent run-up ($z_{2\%}$). A. Reef flat width. B. Fore reef slope. C. Wave friction factor (f_w). D. Current friction factor on the fore reef ($c_{f,fore\ reef}$). E. Current friction factor on the reef flat ($c_{f,reef\ flat}$). F. Offshore significant wave height ($H_{m0,offshore}$). Offshore water levels are represented by color.

As the fore reef slope increases the mean water level increases due to increasing setup (FIGURE 39). Steeper fore reefs induce a higher pressure response in the cross-shore momentum balance as waves break more suddenly in shallower water and therefore result in a greater setup. When the fore reef slope becomes steeper than 1:3, the amount of setup decreases, likely because waves are increasingly reflected on the steep fore reef slope and, therefore, resulting in less wave-induced setup being generated. A simple estimate of the reflection coefficient, K_r (Battjes, 1974, 1975), indicates that for the offshore wave conditions during the March 2014 event (H_{m0} = 3.9 meters and T_p = 14 seconds) the ratio of reflected to IC wave energy becomes greater than 1 for slopes steeper than approximately 1:3. In addition, the effect of the tidal elevation on the setup variability increases as the fore reef slope increases. The $H_{rms,IG}$ on the inner reef flat is strongly dependent upon the fore reef steepness as it controls the IG wave generation through the breakpoint mechanism (Symonds et al., 1982; Pomeroy et al., 2012). The $H_{rms,inc}$ is not dependent

on the fore reef slope as these waves are saturated. The strong response of setup and $H_{rms,IG}$ to a steeper fore reef results in an equal increase in wave runup.

A smaller incident wave friction coefficient (f_w) not only results in larger $H_{rms,inc}$, but also increases setup on the reef flat (FIGURE 39). The f_w directly affects the frictional dissipation term in the wave action balance in XBeach and therefore, for a higher f_w, the frictional dissipation increases. As frictional dissipation increases, less wave energy is dissipated by wave breaking and thus less setup is generated. The $H_{rms,IG}$ are hardly affected by the increased short wave frictional dissipation. The combined effect of increased mean water level and $H_{rms,IC}$ for smaller f_w values results in higher wave runup.

The infragravity and current friction coefficient, c_f, controls $H_{rms,IG}$ and mean water levels by influencing the bed shear stress. A higher c_f along the fore reef slope increases the setup gradients needed to balance the bed shear stress (Svendsen, 2003), resulting in a higher wave setup and water depth at the toe of the beach. The c_f variability on the fore reef ($c_{f,fore\_reef}$) does not appear to have a significant effect on $H_{rms,IG}$ near the shore, but a smaller roughness increases the sensitivity to lower offshore water levels due to the limited water depth. The $H_{rms,IC}$ increases slightly for higher $c_{f,fore\_reef}$ values, which is caused by the fact that the incident waves are saturated and dependent on the increasing reef flat water depth. The friction on the fore reef affects the wave runup only for lower offshore water levels, due to the increase in $H_{rms,IG}$ with increasing friction.

An increase in the frictional value on the reef flat, $c_{f,reef\ flat}$, causes a larger pressure gradient to balance the bed friction, and this, in turn, drives larger setup and deeper water depths (FIGURE 39). The spatial variability of $c_{f,reef\ flat}$ mainly affects $H_{rms,IG}$ at the inner reef, as decreasing $c_{f,reef\ flat}$ results in less frictional dissipation for the infragravity waves towards shore. $H_{rms,IC}$ increases slightly due to the increased water depths.

Together, the results of varying the three bottom friction coefficients (f_w, $c_{f,reef\ flat}$ and $c_{f,fore\_reef}$) demonstrate that bottom roughness affects wave-induced setup, $H_{rms,IC}$, and $H_{rms,IG}$. A smoother reef flat bathymetry (lower $c_{f,reef\_flat}$ and f_w) would result in larger $H_{rms,IC}$ and $H_{rms,IG}$ near the shoreline and, therefore, would also increase wave runup significantly. Forcing the model with higher H_{m0} results in more wave-induced setup due to increasing radiation stress gradients. Consequently the mean water levels, wave heights, and wave runup increase almost linearly with increasing H_{m0}. For more information on the 1D modeling, see Quataert et al. (2015).

3.6.3 XBeach Two-Dimensional (2D) Hydrodynamic and Wave-driven Flood Modeling

The 2D model of the Roi-Namur Island was set up using the topobathy DEM. The model was set up as a rectilinear model with varying mesh grid sizes (FIGURE 40). Grid sizes were smaller (2 x 5 meters) on the reef at the northern side of the island, since waves propagate to shore from the northern offshore boundary. In order to avoid adverse computational effects, the model boundaries were in deep water so that wave and water level boundaries could be specified all around the model area. Since waves propagate in from the northern offshore boundary, this did not affect the wave transformation around the area of interest. At the northern boundary, a weakly reflective boundary condition was applied where outgoing waves and currents could pass through to deep sea with minimal reflection. A weakly reflective boundary condition was also applied at the lagoon (southern) model boundary so outgoing waves and currents could pass through to the lagoon with minimal reflection. The 2D model was forced with hourly-varying JONSWAP spectra and initial surface elevations at the offshore model boundary using the time-varying wave and water-level data measured in situ.

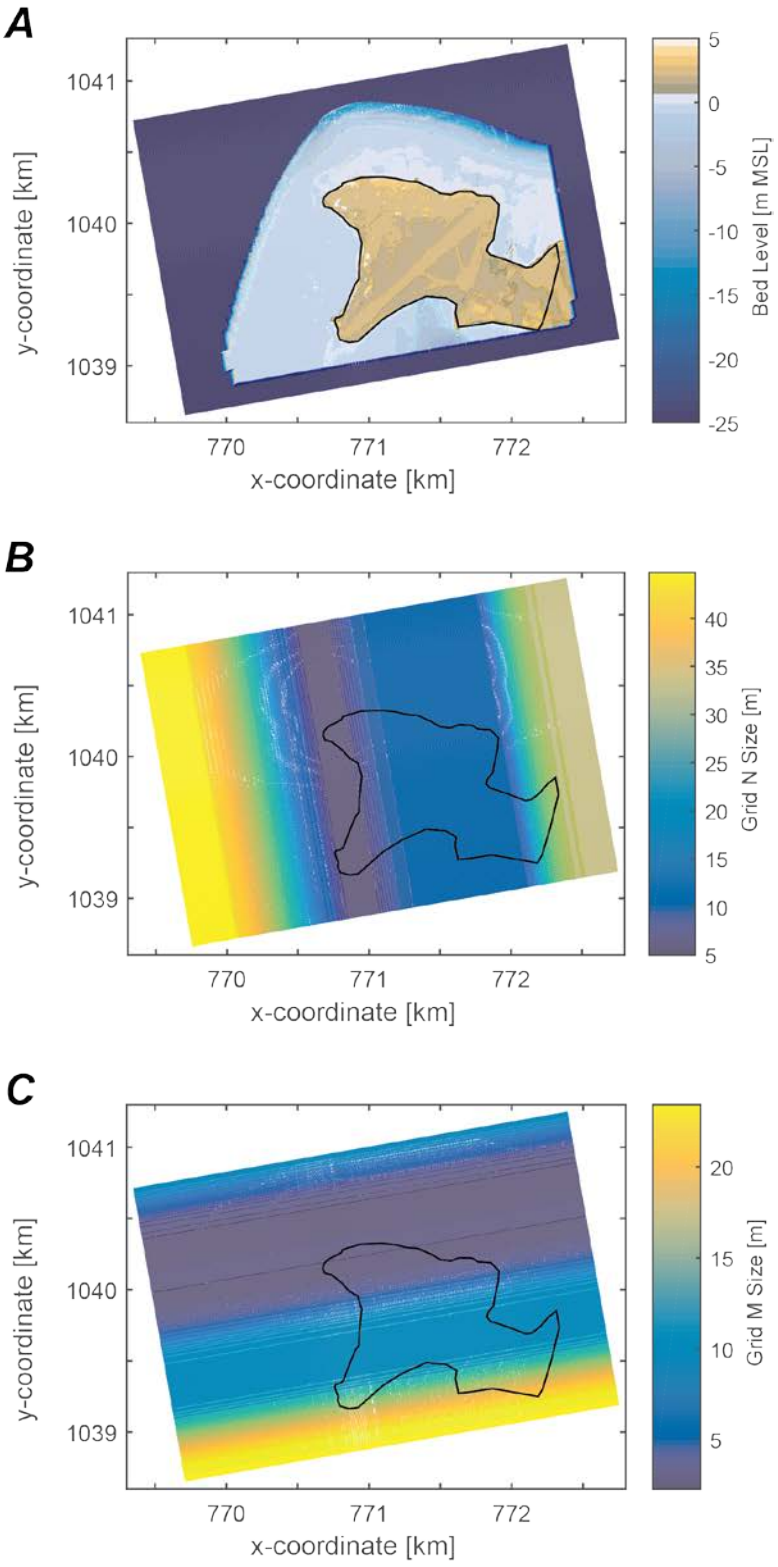

Figure 40. Map plots showing the 2D XBeach model grid properties. A. Bed elevation. B. Size of grid cells in N-direction (east-west). C. Size of grid cells in M-direction (north-south).

3.6.3.1 XBeach 2D model calibration and validation

The 2D model was calibrated for the current friction coefficient c_f by comparing modeled and measured wave and water level data for both NW and northeast (NE) transects (FIGURE 31). The calibrated 2D model was then used to assess the impact of three climate change scenarios (RCP4.5, RCP8.5 and RCP8.5+icesheet collapse) on the inundation extents and depths on the island. The climate change scenarios were included in the model by increasing the initial water level and changing wave height (H_s), wave period (T_p), and wave direction (θ_w) based on the future oceanographic modeling in the JONSWAP spectra. The modeled time periods were the years 2035 to 2105 at 10-year intervals.

The XBeach model produces runup elevations and the thickness of water over topography; in conjunction with information on the duration of large wave events driving flooding from the historical data, overtopping volumes that would fill topographic depressions or infiltrate through permeable surfaces directly into the subsurface can be estimated. Thus XBeach provided water volumes and durations of inundation events, necessary boundary information for the hydrogeologic modeling. Because the long-term (1950s-2000s) rates of sea-level rise at Kwajalein (+1.43 millimeters/year; National Ocean Service, 2011) before the acceleration in the late 1990s are approximately equal to the rates of global sea-level rise (e.g., Nicholls and Cazenave 2010), it can assumed that there is no significant net vertical land motion (e.g., uplift or subsidence) of the atoll. The bathymetry and topography that exist today therefore should be accurate over the predicted timeframe (100+ years) that the model results are valid.

For the calibration of the 2D non-hydrostatic model, a 24-hour simulation period during the March 2014 overwash event was used (FIGURE 36-37). The model was calibrated for the only free bed-friction coefficient in non-hydrostatic mode; c_f. Spatially-varying roughness was applied to include the high density live coral patches on the reef flat (FIGURE 27) based on the benthic habitat mapping. The grid cells within these patches were set with a $c_f = 0.04$, based on the c_f value used in the 2D model in van Dongeren et al. (2013). The model was calibrated by finding the optimum value for c_f in the areas with low bed roughness.

Modeling results were compared with the measured mean water levels, root-mean-squared IC, IG, and VLF (Gawhen et al., 2016) wave heights at Roi-Namur, along both NW and NE transects (FIGURE 41-42). The predictive skill of the model was again determined by calculating the bias and SCI. The best results both in terms of bias and SCI were achieved for $c_f = 0.002$. However, the inner reef mean water levels were underestimated by the model for both transects, even though the water level was predicted correctly at the other reef flat wave gauges. This was caused by a systematic offset in the mean burst pressure measured by the inner reef wave gauges due to biofouling of the sensors.

The optimum friction coefficient found for the 2D non-hydrostatic model ($c_f = 0.002$ and $c_f = 0.04$) was lower than applied in the 1D surf-beat model ($c_f = 0.01$ and $c_f = 0.1$). In the 1D surf-beat model, only shore-normal currents are generated by the IC energy, whereas in the 2D model lateral currents are also forced. Therefore, the generation of IG wave energy was overestimated in 1D mode relative to 2D mode and needed to be balanced by higher bottom frictional dissipation. The 1D model thus required a higher value of c_f than the 2D model to match the field observations.

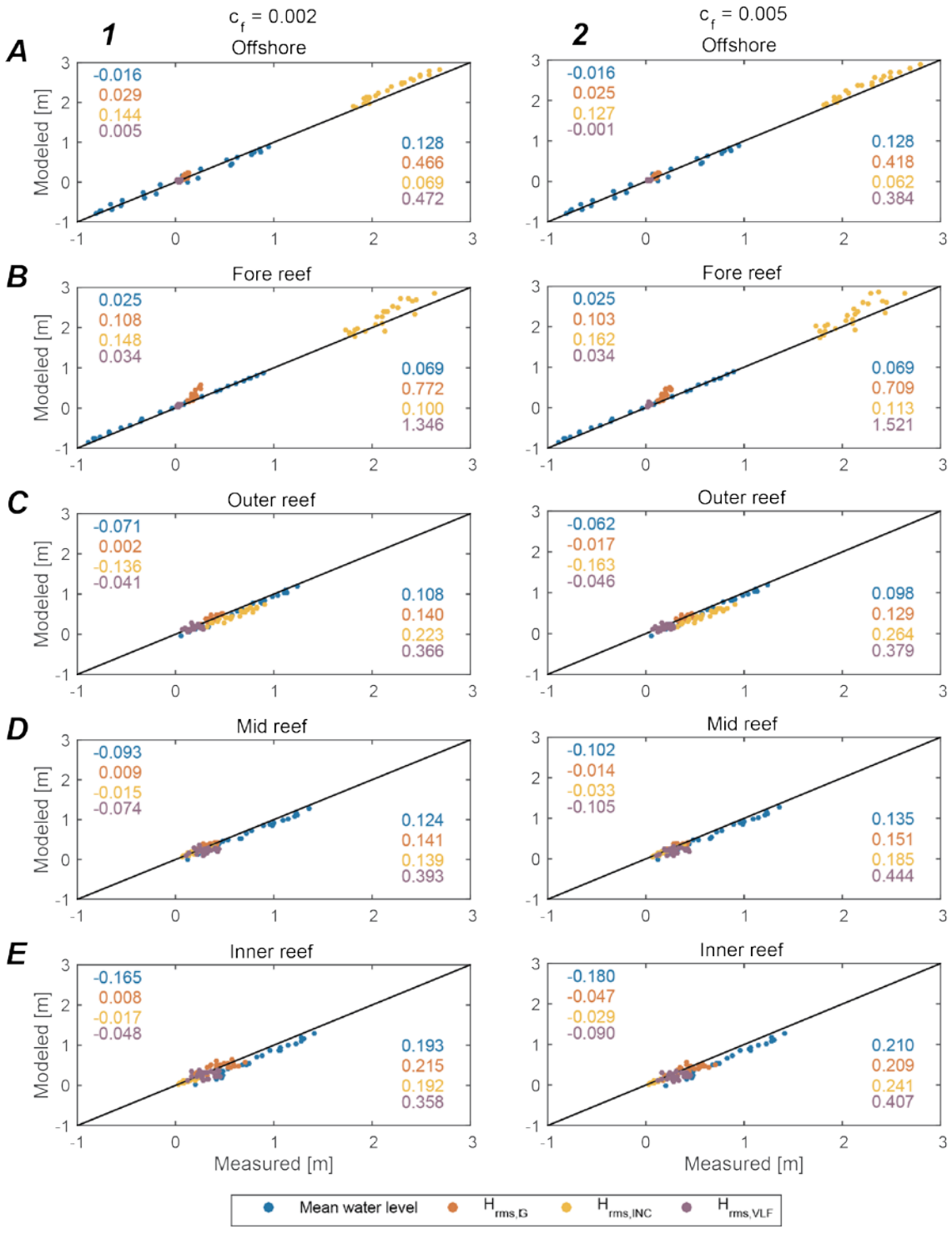

Figure 41. Scatter plots comparing the measured field data and 2D XBeach modeled hydrodynamics for the NW transect. 1. With c_f = 0.002. 2. With c_f = 0.005. A. Offshore. B. Fore reef. C. Outer reef flat. D. Middle reef flat. E. Inner reef flat. For all key hydrodynamics; mean water levels (blue), incident wave height (IC, yellow), infragravity wave height (IG, red), and very-low frequency wave height (VLF, purple). Top left corner indicates the bias and bottom right corner the scatter index (SCI).

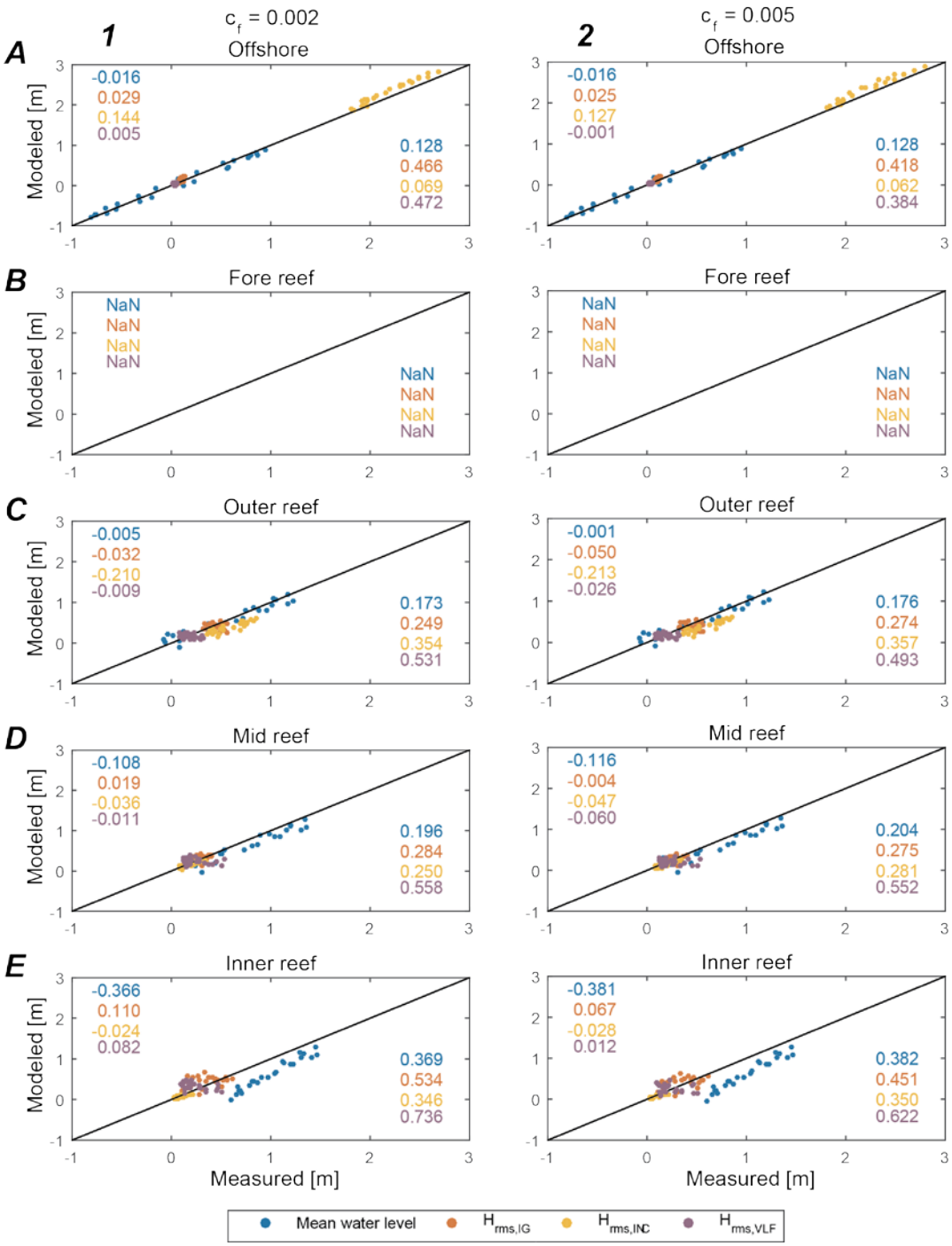

Figure 42. Scatter plots comparing the measured field data and 2D XBeach modeled hydrodynamics for the NE transect. 1. With c_f = 0.002. 2. With c_f = 0.005. A. Offshore. B. Fore reef. C. Outer reef flat. D. Middle reef flat. E. Inner reef flat. For all key hydrodynamics; mean water levels (blue), incident wave height (IC, yellow), infragravity wave height (IG, red), and very-low frequency wave height (VLF, purple). Top left corner indicates the bias and bottom right corner the scatter index (SCI).

3.6.3.2 XBeach 2D modeling results

The modeled wave-driven overwash extents for the modeled March 2014 flooding event (FIGURE 36) were compared qualitatively with the observations during the March 2014 overwash event (FIGURE 43). The reported overwash on the northeast corner near the runway was not simulated by the model. However, small areas at the western side of the island are flooded

Figure 43. Map of modeled wave-driven flooding depth for the calibrated 2D XBeach model during the March 2014 overwash event on Roi-Namur. The color bar denotes the maximum water depth on the island during the March 2014 overwash event.

in the model. The calibrated 2D model was then forced with a range of climate-change scenarios (RCP4.5, RCP8.5 and RCP8.5+icesheet collapse), which includes sea-level rise values based on Hall et al. (2016) ranging from +0.2 to +2.9 meters and offshore wave heights of 2.2 to 5.1 meters (TABLE 12) based on the aforementioned wave projections from future oceanographic modeling. These inputs were used to perform 24 simulations, each consisting of six cosine-shaped 12-hour tidal cycles that had an amplitude of 0.717 meter with respect to mean higher high water (MHHW), as shown in FIGURE 44. For each scenario simulation, the tidal signal was uniformly increased with the sea-level rise value from TABLE 12. A JONSWAP spectrum was generated from the wave parameters in TABLE 12 and was applied to the offshore model boundary. In the 3-day storm, over the first 30 hours the waves ramp up from a mean wave height (H_{mean}) to a 12 hour storm maximum wave height ($H_{s,storm}$) and then over the last 30 hours decreased back to H_{mean}. A peak in the tidal cycle occurs in the middle of the 12-hour storm maximum, to include a worst-case scenario.

Table 12. Overview of sea-level rise and wave parameters per climate change scenario for each year used in the 2D hydrodynamic and wave-driven flood modeling.

Conditions	Year							
	2035	2045	2055	2065	2075	2085	2095	2105
Sea-level Rise Scenario								
RCP4.5 (m)	0.2	0.3	0.3	0.5	0.5	0.6	0.7	0.7
RCP8.5 (m)	0.4	0.5	0.8	1.0	1.2	1.5	1.8	2.0
RCP8.5+icesheet collapse (m)	0.5	0.6	0.9	1.3	1.6	2.0	2.4	2.9
Wave Parameters								
$H_{s,mean}$ (m)	2.3	2.3	2.3	2.3	2.2	2.2	2.2	2.2
$T_{p,mean}$ (s)	11	11	11	11	11	11	11	11
$\theta_{w,mean}$ (°)	346	347	346	347	347	346	346	346
$H_{s,storm}$ (m)	5.3	5.2	5.2	5.1	5.1	5.0	4.9	4.9
$T_{p,storm}$ (s)	15	15	15	15	15	15	15	15
$\theta_{w,storm}$ (°)	351	353	352	352	352	351	351	351

Model results were post-processed into water depths on the island at the end of the simulation for each scenario (FIGURE 45). The resulting flooding maps show that overwash and flooding extents and depths during storm conditions increase into the future due to sea-level rise and with increasing RCP scenario. For the RCP8.5 scenarios later in the 21st century, the island is completely overwashed annually by wave-driven flooding.

3.7 Future Meteorologic Modeling

Detailed climate projections for Kwajalein Atoll were derived using GCM results available from the CMIP5 (2011) project. Observations over the past 5-6 decades provide evidence for systematic warming of the ocean surface and intensification of monsoon circulation over the western North Pacific (Annamalai et al., 2011), a decrease in the sea surface salinity (Delcroix et al., 2007), and changes in typhoon characteristics (Knutson et al. 2010). Observations suggest that the climate of Kwajalein Atoll is influenced by variations in sea-surface temperature over the entire tropical Indo-Pacific region (Annamalai et al., 2007; Sooraj et al., 2012). The availability of multi-member ensembles of present day and warming scenario simulations from over 20 GCMs (CMIP5, 2011) provides a unique opportunity to examine the ability of global models to represent the climate including the observed long-term trends in the tropical Pacific and Indian Ocean regions over recent decades (e.g., Deser et al., 2010).

3.7.1 Global Climate Model Selection

A set of objective metrics was devised that show how each model simulates the mean state and inter-annual variability of the present-day climate in the Indo-Pacific region (FIGURE 46) and used them as the basis for selecting a subset of “best” global models. The metrics included pattern correlation and RMSE similarity between observed (for example, from the Global Precipitation Climatology Project) and CMIP5 model-simulated rainfall climatology during May-

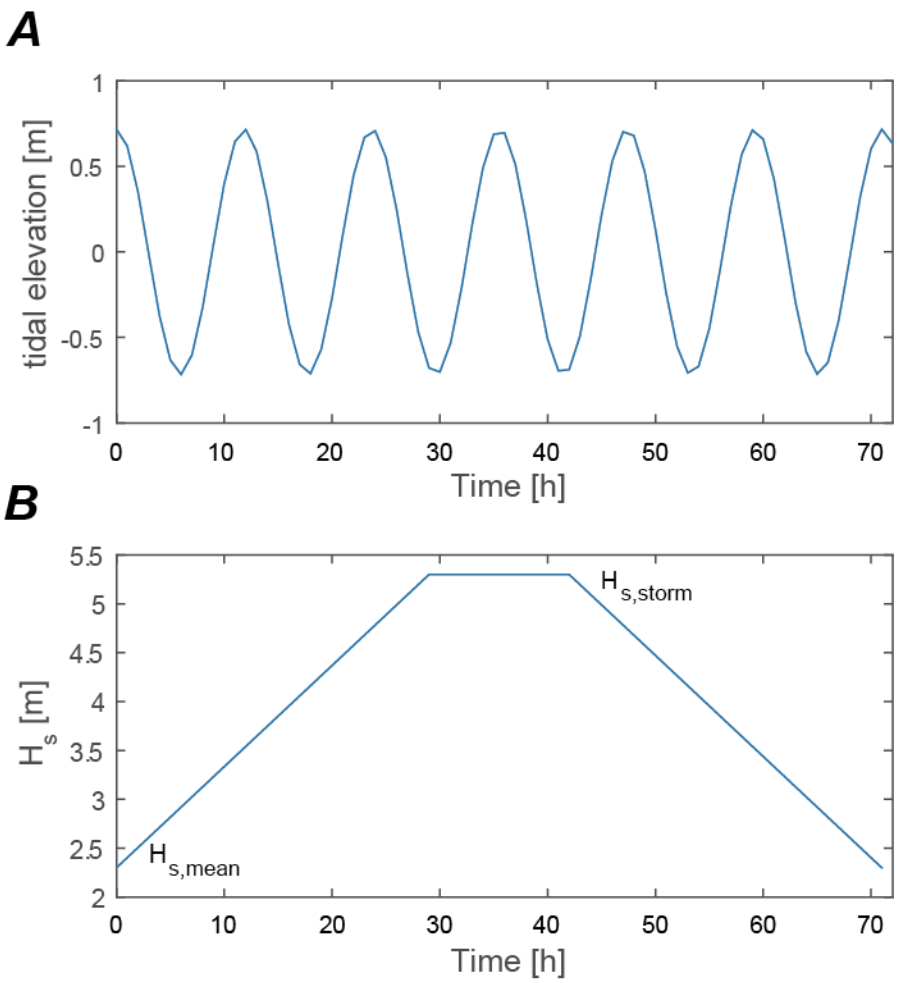

Figure 44. Time series plots showing tidal and wave forcing for the climate change scenario simulations with the 2D XBeach model. A. Tidal elevation is with respect to mean higher-high water (MHHW) and no sea-level rise. B. Wave heights build up from $H_{s,mean}$ to $H_{s,storm}$ and then decrease back down to $H_{s,mean}$ after the storm.

November (rainy season). To get finer details, a simulated annual cycle of rainfall over Kwajalein (observed peak in October and dry in February) was also examined. At interannual timescales, seasonal rainfall over Kwajalein is influenced by El Niño–Southern Oscillation (ENSO). Therefore, the top five performing models' fidelity in capturing interannual variations of rainfall was also used as an objective metric.

Although CMIP5 global models do not adequately simulate the intensity of fully developed tropical cyclones (TCs), we evaluated the genesis and early life of TCs in these models over the west Pacific, and examined the storms' statistical properties around Kwajalein. The TRACK program, a mathematically and physically developed objective procedure, was applied on the daily or 6-hourly model output to diagnose tropical storms over the west Pacific region. TRACK objectively identifies TCs through analysis of the time series of meteorological fields.

All the required meteorological and oceanic variables from all the participating CMIP5 models (40+ models) were collected and made them available for diagnostics. As introduced above, a set of metrics was developed and used to evaluate models' performance in representing

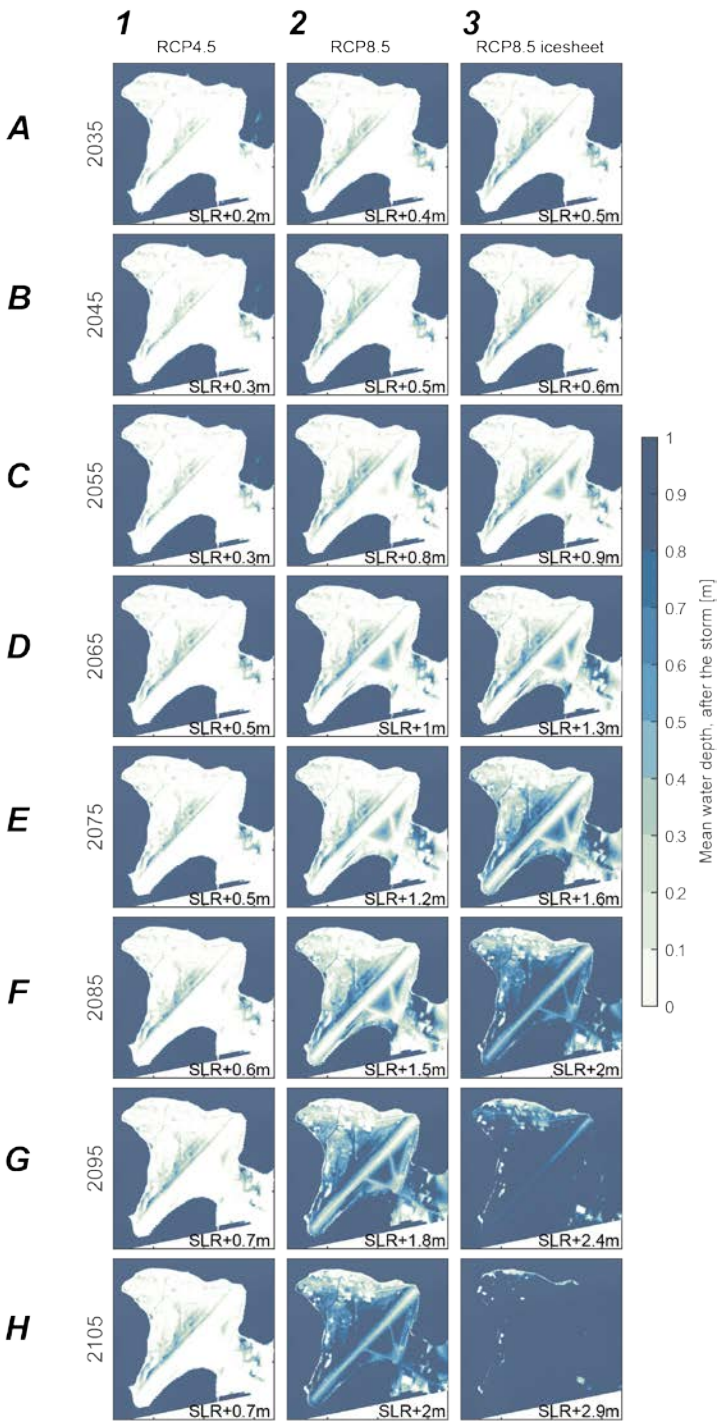

Figure 45. Maps showing projected annual wave-driven flooding water depth on top of Roi using the 2D XBEACH model. 1. IPCC-AR5 RCP4.5 climate scenario. 2. IPCC-AR5 RCP8.5 climate scenario. 3. IPCC-AR5 RCP8.5 climate scenario plus ice sheet collapse. The years shown in A-H are approximate, and due to El Nino-induced annual sea-level variability, these should be considered ±5 years. The sea-level rise (SLR) values for the different climate scenarios and time frames are listed in the bottom right corner of each subplot.

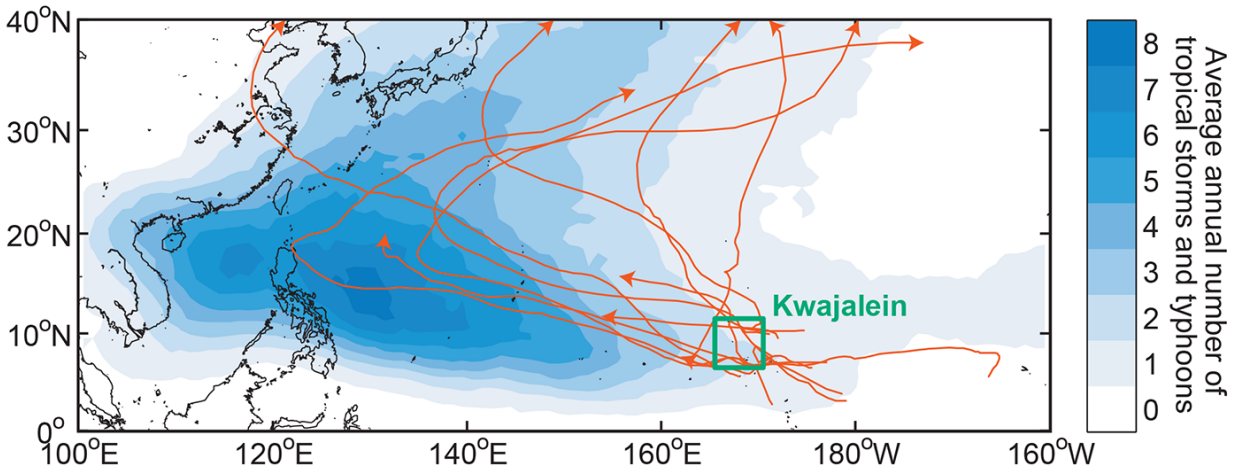

Figure 46. Map showing climatology (1979–2012) of observed tropical storm and typhoon frequency (blue shading). Storm tracks passing near Kwajalein during 1997—one of the most active typhoon seasons in the northwestern Pacific—are indicated in orange.

current climatic conditions, to include SST, total spatial precipitation patterns, and spatial precipitation variability. For model validation, observations (e.g., satellite-based estimates) and objectively analyzed fields were employed. The task included:

- Examined historical simulations (1971-2005) to assess the models' ability to realistically simulate the annual-mean precipitation, winds, and sea surface temperature (SST). Specifically, the models' skill in simulating the current climate over the tropical Pacific was assessed by comparing their simulations to observations and reanalysis fields. Primary tools applied were: (i) Spatial pattern correlation, (ii) Centered Pattern Root Mean Square Difference and (iii) Taylor Skill Score, which ranks models according to pattern correlation and similarity between model variance and observed variance.
- Examined the models' skill in capturing the annual mean pattern of the warm pool and rain bands.
- Evaluated the annual cycle of precipitation to assess the models' skill in simulating the rainy season (and the dry season) at island spatial scales.
- Finally, models are ranked according to their average score of each (normalized) skill metric.
- Based on a suite of metrics, the top 5 performing models that demonstrated high skill in representing current climatological conditions (hereafter referred to as "top 5") were selected for detailed analyses. Their skill in capturing interannual variations in seasonal rainfall during rainy season was examined.
- Finally, for all the 40+ models, and for the top 5 models, mean annual changes in rainfall, SST and winds were assessed for future projections.

The mean annual SST and rainfall climatology from observations and multi-mean ensemble (MME) average of the top 5 CMIP5 models is shown in FIGURE 47. Although the

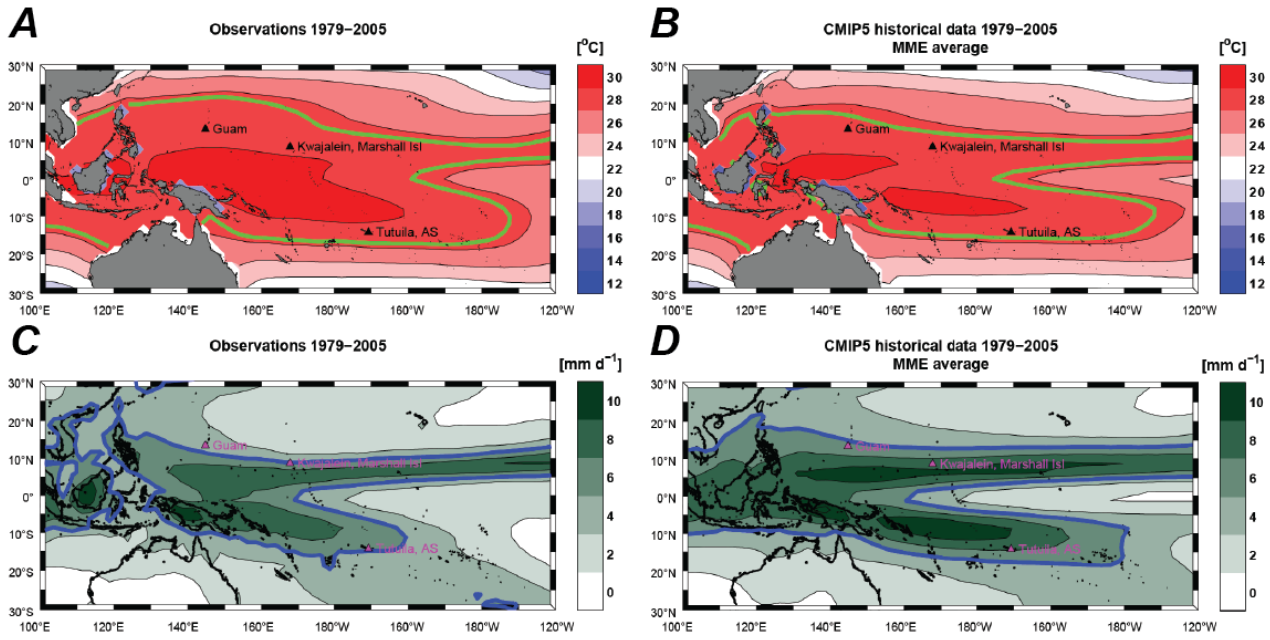

Figure 47. Maps showing the comparison between the observations and modeled historical period. A. Observed mean annual sea-surface temperature (SST). B. Top 5 model multi-mean ensemble (MME) average annual sea-surface temperature (SST). C. Observed mean annual rainfall. D. MME average annual rainfall. In the SST plots, the 27.5°C contour (green) illustrates warm pool regions in the tropical Pacific, and major rainfall bands (values > 5 millimeters/day) in rainfall plots are highlighted.

MME average captures major observed features in SST and rainfall climatology, there are clear shortcomings as well. For example, compared to observations, major rainfall band in the tropical South Pacific extends further eastwards, and the eastern equatorial Pacific cold tongue extends into the equatorial central Pacific. Some of these shortcomings are improved in the top 5 models selected (not shown).

For these top 5 models, the interannual variations (e.g., ENSO-rainfall association) were examined and compared with observations. Although CMIP5 global models do not adequately simulate the intensity of fully developed TCs, the genesis and early life of TCs in the top 5 models over the west Pacific was evaluated by applying the TRACK program (Hodges; 1995; 1998; 2008) on the 6-hourly model output to diagnose tropical storms over the west Pacific region. TRACK objectively identifies TCs through analysis of the time series of meteorological fields.

Given the low terrain of the Kwajalein Atoll, very high spatial resolution dynamical downscaling may not add much information to the projections of rainfall, wind, and temperature from the global models. However, the GCM results were supplemented by applying the University of Hawaii's International Pacific Research Center (UH-IPRC) regional atmospheric model (iRAM) to investigate the important issue of long-term changes in TC behavior connected with global warming. iRAM is a hydrostatic regional model that has been successfully applied in simulating the atmospheric circulation, clouds and precipitation over tropical and subtropical ocean regions (e.g., Lauer et al., 2009, 2010; Wang et al., 2011). iRAM has also been applied to investigation of climate change influences on TCs in the western Pacific (Stowasser et al., 2007) and the Indian Ocean region (Stowasser et al., 2009). These earlier TC climatology studies were extended with a focus on the low-latitude western Pacific region that includes Kwajalein Atoll

using the top 5 CMIP5 GCM results for lateral and surface boundary conditions. Several multi-decadal "time-slice" iRAM simulations with horizontal resolution of order 20 kilometers and 6 hour time steps were conducted. Results for rainfall, temperature, surface solar flux, near-surface wind and model-computed evapotranspiration (ET) were generated. The expected changes in mean climatic elements were assessed, as well as in the variability on sub-monthly to inter-annual timescales.

Future projections of rainfall over the tropical Pacific for northern hemisphere summer (June-August) and winter (December-February) seasons for RCP4.5 scenario are shown in FIGURE 48. In the vicinity of Kwajalein, the top 5 models project a seasonal-mean dryness (in both summer and winter seasons) and a reduction in rainfall at the end of this century. Note that the projected decrease in rainfall is consistent with reduction in the number (frequency) of storms over Kwajalein.

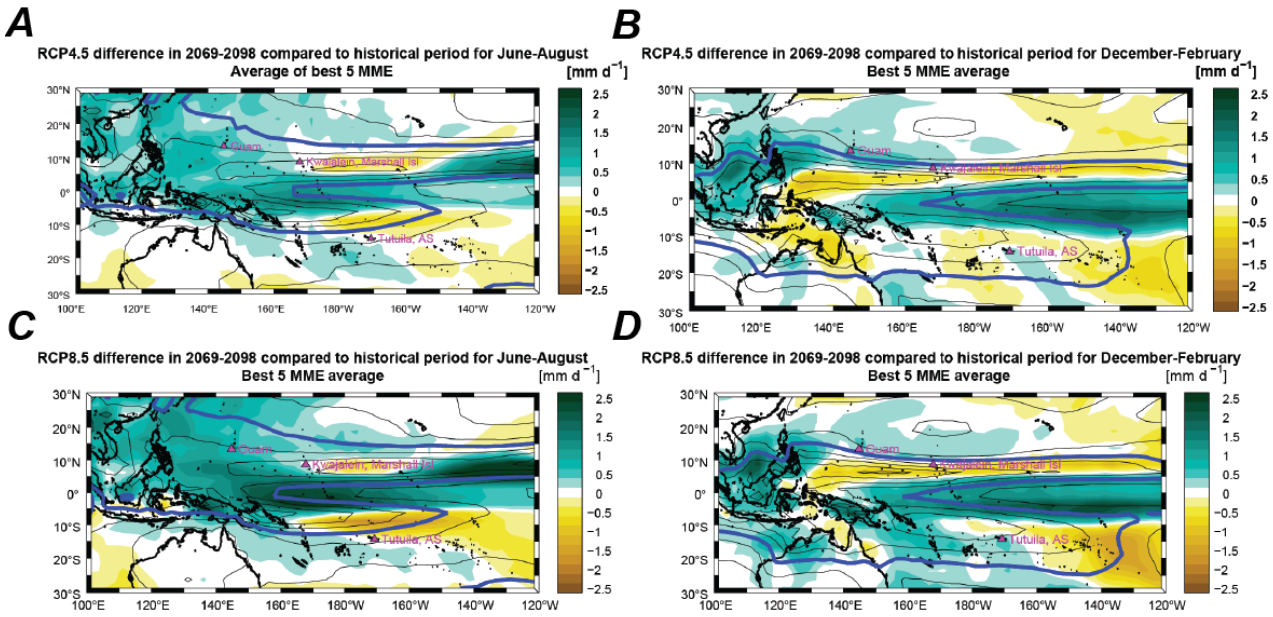

Figure 48. Maps showing the comparison of seasonally-average daily precipitation rates between the top 5 model multi-mean ensemble (MME) average for the historical period and future climate scenarios. A. Difference in the boreal summer during 2069-2089 under scenario RCP4.5 compared to 1979-2005. B. Difference in the boreal winter during 2069-2089 under scenario RCP4.5 compared to 1979-2005. C. Difference in the boreal summer during 2069-2089 under scenario RCP8.5 compared to 1979-2005. D. Difference in the boreal winter during 2069-2089 under scenario RCP8.5 compared to 1979-2005. The blue lines denote the major rainfall bands (values > 5 millimeters/day).

The top 5 models' SST biases (model values minus observations) during winter season and future projections in SST over the tropical Pacific are shown in FIGURE 49. It is important to examine SST projections to assess its impact on rainfall and storms' characteristics. In terms of model biases, although the patterns look similar, the top 5 models' amplitudes perform better than the MME (not shown). This is one demonstration that the objective metrics employed here to assess the models' skill works reasonably well. In terms of future projections, the 5 selected models that that have realistic warm pool region simulations, suggest a basin-wide warming (or increase in SST) but the warming does not extend well into the equatorial central-western Pacific

as projected by the MME. In summary, from the pool of 40+ climate models that participated in CMIP5 exercise, the objective procedure of model selection used here identified 5 models that have lesser bias.

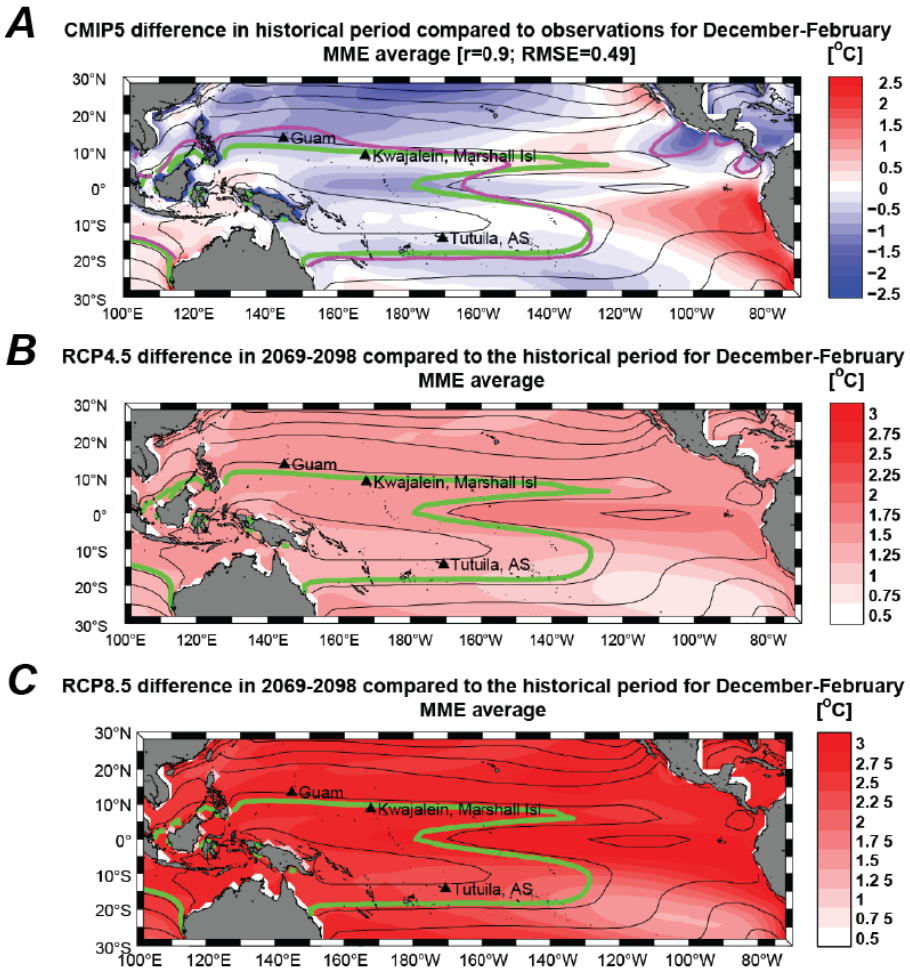

Figure 49. Maps showing the top 5 models' bias in sea-surface temperatures (SST) during the boreal winter for the historical period and future climate scenarios. A. Difference between observed and top 5 model multi-mean ensemble (MME) average for 1979-2005. B. Difference between MME average for 2069-2089 under scenario RCP4.5 compared to 1979-2005. C. Difference between MME average for 2069-2089 under scenario RCP8.5 compared to 1979-2005. In the plots, the 27.5°C contour (green) illustrates the observed warm pool regions in the tropical Pacific Ocean; the purple line in A denotes the MME 27.5°C contour.

3.7.2 Storm Characteristics

CMIP5 GCMs were used to assess the potential changing climate threats in the tropical North Pacific, focusing on the frequency and intensity of tropical cyclone occurrence near Kwajalein Atoll. Kwajalein Atoll experiences typhoons, although with less frequency and typically weaker intensity than in the western tropical Pacific Ocean. For example, Super Typhoon Paka in 1997 followed a classical tropical cyclone track, strengthening as it passed over

the warm waters around the Marshall Islands; the islands experienced moderate damage from coastal wave-driven flooding. Later, Super Typhoon Paka reached peak intensity near Guam, where Anderson Air Force Base recorded arguably the world's highest winds speeds and caused widespread damage.

Using an objective TC tracking algorithm as previously mentioned, GCMs were found to capture the observed climatology and interannual variability associated with ENSO—the leading mode of natural variability other than the annual cycle—but with notable biases in genesis location and storm tracks. Forcing these models with increasing greenhouse-gas concentrations and correcting for known biases shows that only small changes in interannual storm frequency are likely by the end of the 21st century. The majority of the top 5 climate models, however, project that the overall TC occurrence will decrease with greenhouse warming (FIGURE 50) as less moisture rises to the layer of the atmosphere where convection is strongest. For different reasons,

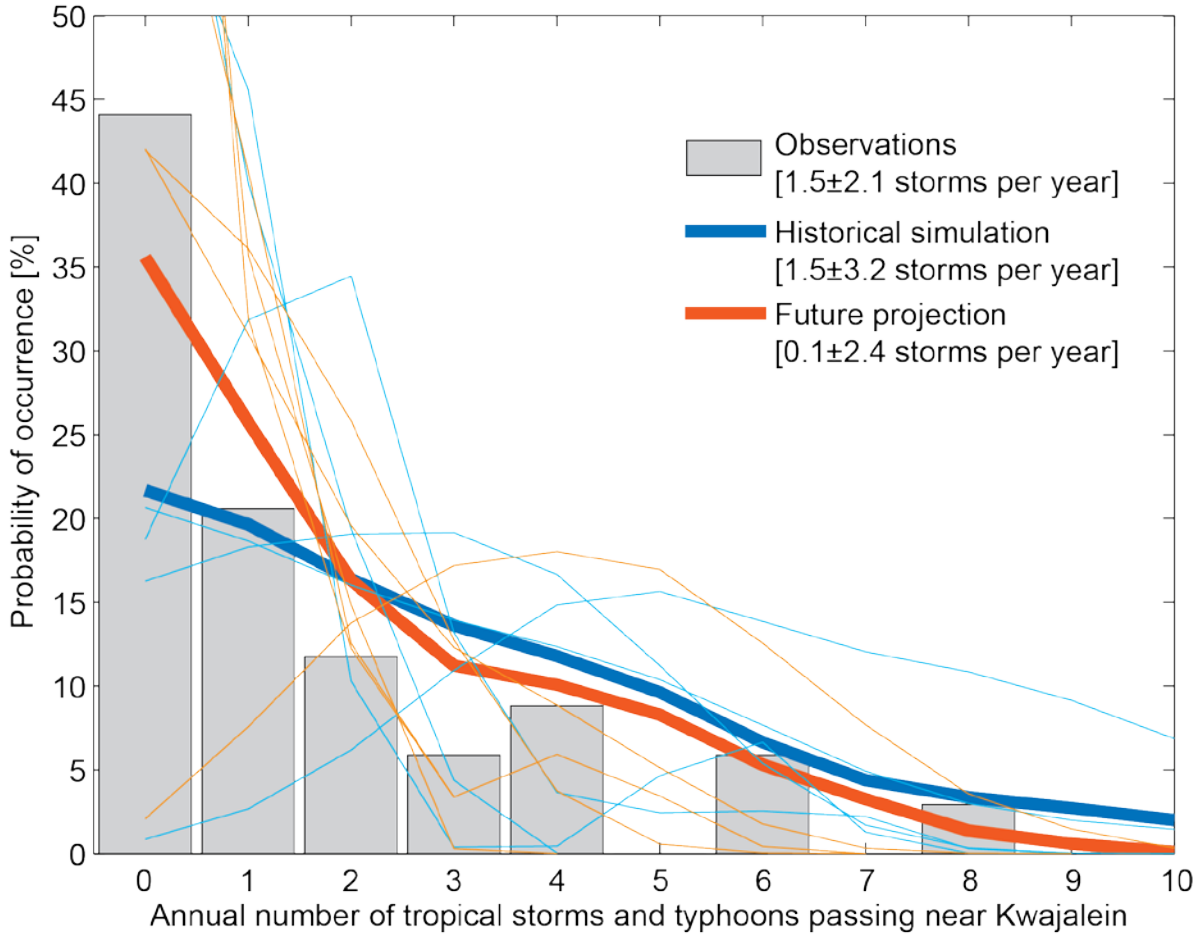

Figure 50. Histogram plot showing the probability of occurrence of tropical storms and typhoons passing near Kwajalein from observations (gray bars, years 1979-2012) and for simulations of the historical period (blue line, years 1976-2005) and the RCP8.5 climate scenario (red line, years 2071-2100). The thick lines are the top 5 best multi-mean ensemble (MME) averages and the thin lines are the individual top 5 models. Mean storm counts (and likely range) are listed. The simulations are scaled to remove model bias in storm genesis and tracks.

including higher sea-surface temperatures and a more unstable atmosphere in the future, the same models suggest that the strongest typhoons that do occur are likely to be more intense (e.g., a 2 meters/second increase in maximum wind speed is perceivable; FIGURE 51).

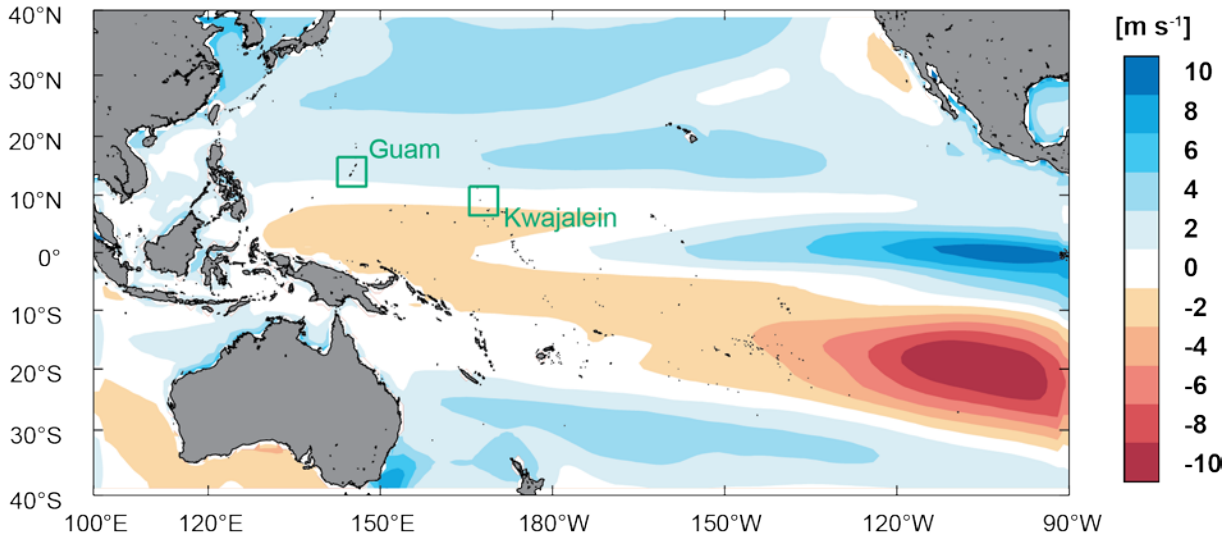

Figure 51. Map showing the top 5 models multi-mean ensemble (MME) average projected change in maximum typhoon near-surface wind speeds (intensity) across the tropical Pacific Ocean during 2071-2100 for the RCP8.5 climate scenario compared to the historical period (years 1976-2005).

3.8 Groundwater Data Acquisition

An assessment of the Roi-Namur shallow groundwater lens was carried out from November 2013 to April 2015. This assessment included surveys of groundwater levels, temperature and specific conductivity (salinity) in a suite of wells and temporary piezometers strategically placed around the island, multi-channel electrical resistivity surveys, radon time series deployments, and a geochemical survey of the groundwater quality.

3.8.1 Groundwater Physical and Chemical Properties

The wells are constructed of 4-centimeter diameter poly-vinyl-chloride (PVC) pipe with a 60-centimeter screened section at 15 centimeters above the bottom to allow groundwater to flow into the well. Time-series groundwater levels and specific conductivity measurements were performed every 15 minutes using calibrated Solinst LTC Leveloggers, while time-series groundwater temperature measurements were obtained every 20 minutes using calibrated Onset Hobo temperature loggers. Additionally, depth-specific groundwater samples were collected with an AMS “Piezometer Groundwater Sampling Kit alongside a calibrated YSI 556 multi-probe meter between wells C1 and C2 using protocols of the USGS National Field Manual (U.S. Geological Survey, 1998). The samples were analyzed for ammonium (NH_4^+), dissolved silica (DSi), total dissolved phosphorus (PO_4^{3-}), molybdenum (Mo), barium (Ba), uranium (U), and pH. As per methods summarized in Swarzenski et al., (2007) nutrients were determined on a Lachat Instruments QuickChem 8000 at Woods Hole Oceanographic Institute (WHOI), while the suite of

trace elements was analyzed on a HR-ICPMS at the University of Southern Mississippi. From these measurements, tidal lag and efficiency could also be determined, useful for estimating aquifer information such as permeability and storage properties (Hunt, 1996).

3.8.2 Electrical Resistivity

The use of electrical resistivity to examine the fresh water/salt water interface in coastal groundwater is well established (Manheim et al., 2004; Swarzenski et al., 2006, 2007a,b). The multichannel electrical resistivity (ERT) surveys were conducted along two transects during high and low tides in March 2013. Because the survey cable remained fixed in position during the high tide/low tide and no parameters were altered, the observed changes in resistivity should only be a function of the tidally modulated pore-fluid exchange. Transects were aligned perpendicularly to the shoreline and located at 0.75 meter above mean sea level (MSL). An Advanced Geosciences Inc. (AGI) R8 SuperSting system was used to measure the electrical resistivity of the subsurface along a 56-electrode cable (consistently spaced 1 to 2 meters apart). Each electrode was pinned to the underlying sediment by a 35-centimeter stainless steel spike. The electrical resistivity measurements were acquired using a Schlumberger array. The relative elevation of each electrode was measured using a laser level and incorporated into inverse modeling routines (AGI EarthImager).

3.8.3 Submarine Groundwater Discharge

Submarine groundwater discharge (SGD) is part of a highly dynamic and complex hydrological and hydrogeological problem that involves two interrelated processes: submarine discharge into seas and oceans, and seawater intrusion into the shore (Zektser and Dzyuba, 2014). Quantification of SGD, particularly in atoll settings, is essential to address groundwater transport and exchange mechanisms and fluxes. The utility of the radon isotope ^{222}Rn as a water-mass tracer is convenient due to its very short half-life (3.8 days) and its enrichment in groundwater relative to surface water (Swarzenski, 2007). A Duridge RAD7 system was employed that monitors Rn-in-air with the help of a water/air exchanger. This setup allows for a near real-time calculation of the aqueous radon concentration by measuring the air ^{222}Rn concentration and knowing the temperature-dependent ^{222}Rn partitioning coefficient (Burnett et al., 2006, 2003; Burnett and Dulaiova, 2003; Dulaiova et al., 2006; Schubert et al., 2012; Swarzenski et al., 2006). A peristaltic pump was used to produce a continuous stream of surface water into the water/air exchanger, while air from the exchanger is continuously pumped into the radon monitor. The monitor contains a solid-state, planar, Si alpha Passivated Implanted Planar Silicon (PIPS) detector and converts alpha radiation into usable electronic signals that can discriminate various short-lived daughter products (e.g., polonium isotopes ^{218}Po, ^{214}Po) from ^{222}Rn (Swarzenski et al., 2013). Time-series measurements of surface water ^{222}Rn were obtained using a single RAD7 radon monitor setup for 30-minute counting intervals. For the ^{222}Rn time-series, the surface- and bottom-waters were instrumented with Solinst LTC Leveloggers that continuously measured pressure, conductivity, and temperature of ambient seawater. A simple non-steady-state Radon mass-balance box model was then employed for calculations of SGD following methods developed by Burnett and Dulaiova (2003) and Burnett et al. (2006). Site locations for these surface water time-series deployments were strategically placed based on perceived gradients in geologic-, oceanographic-, and hydrologic-controls, as well as the level of anthropogenic perturbations.

3.8.4 Groundwater Tidal Lag and Efficiency

On atoll islands such as Roi-Namur, ocean tides cause a hydraulic pressure signal that propagates from the island perimeter inward through the geologic framework of the island. The measurement of the attenuation of the tidal signal is captured as tidal efficiency and tidal lag. Tidal efficiency is the amplitude ratio between the magnitudes of the response seen in a well and the corresponding tides. Tidal lag is the time difference or phase lag between the tidal peak and the aquifer response peak. In general this pressure signal is dampened by frictional losses related to the conductivity and the poroelastic storage capacity of the aquifer. Tidal efficiencies from this study range from 7-63 percent and tidal lags range from 40-170 minutes for wells measured at 3 meters groundwater depth relative to mean sea level. The measurements of tidal lag and efficiency attained from multiple coastal wells fit well (R^2 = 0.9) with the previously published data by Gingerich (1992) and Peterson (1997) and clearly suggest that tidal attenuation is strongly dependent on the distance to shoreline (FIGURE 52).

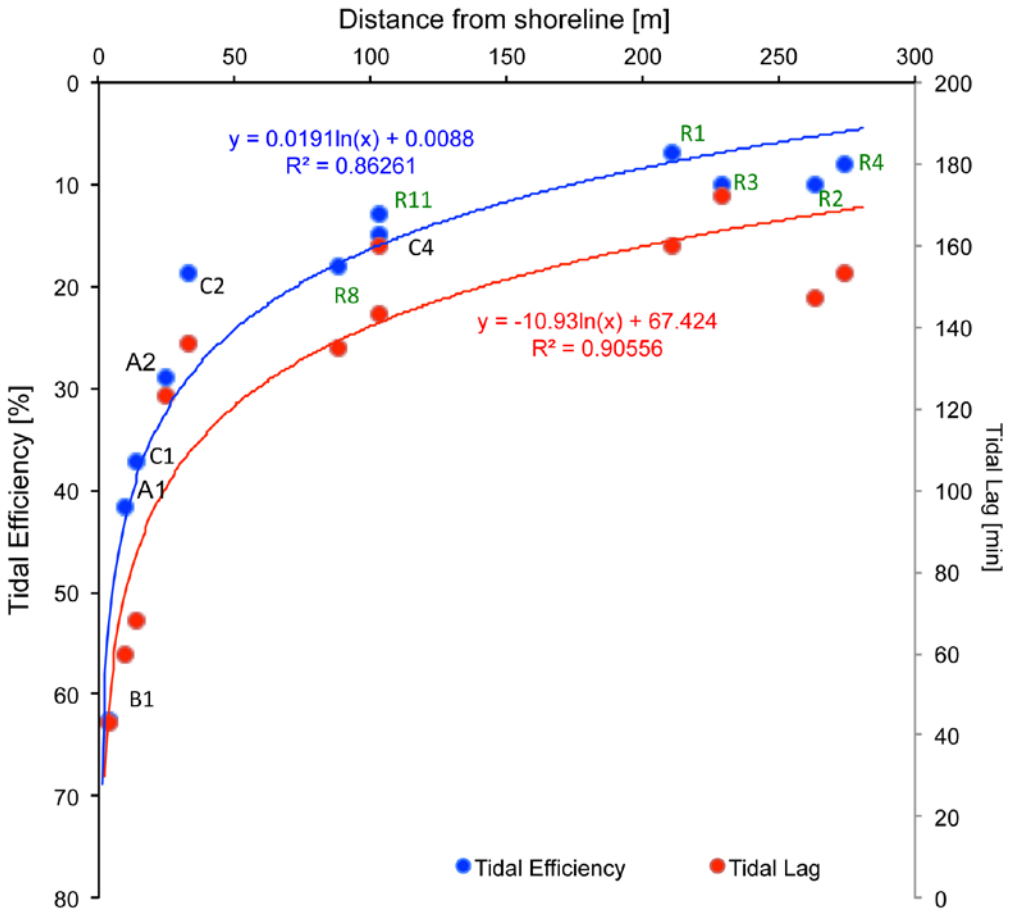

Figure 52. Scatter plot showing tidal efficiency and calculated tidal lags for the groundwater wells.

3.8.5 Tidal Oscillation Effect on Groundwater

The dominant driver for repetitive hourly changes in salinity and groundwater level is tidal oscillation on Roi-Namur (FIGURE 53). Our measurements show that conductivity can vary with a range of up to 10000 micro-Siemens/centimeter within a single tidal cycle. These changes in salinities are also synchronized with changes in groundwater levels both temporally and in magnitude. Consequently, spring tides cause the greatest rise of groundwater levels (maximum = 75 centimeters) and salinity (maximum = 10000 micro-Siemens/centimeter), while neap tides are expressed as having a significantly lower groundwater levels (maximum = 20 centimeters) and salinities (maximum = 2000 micro-Siemens/centimeter).

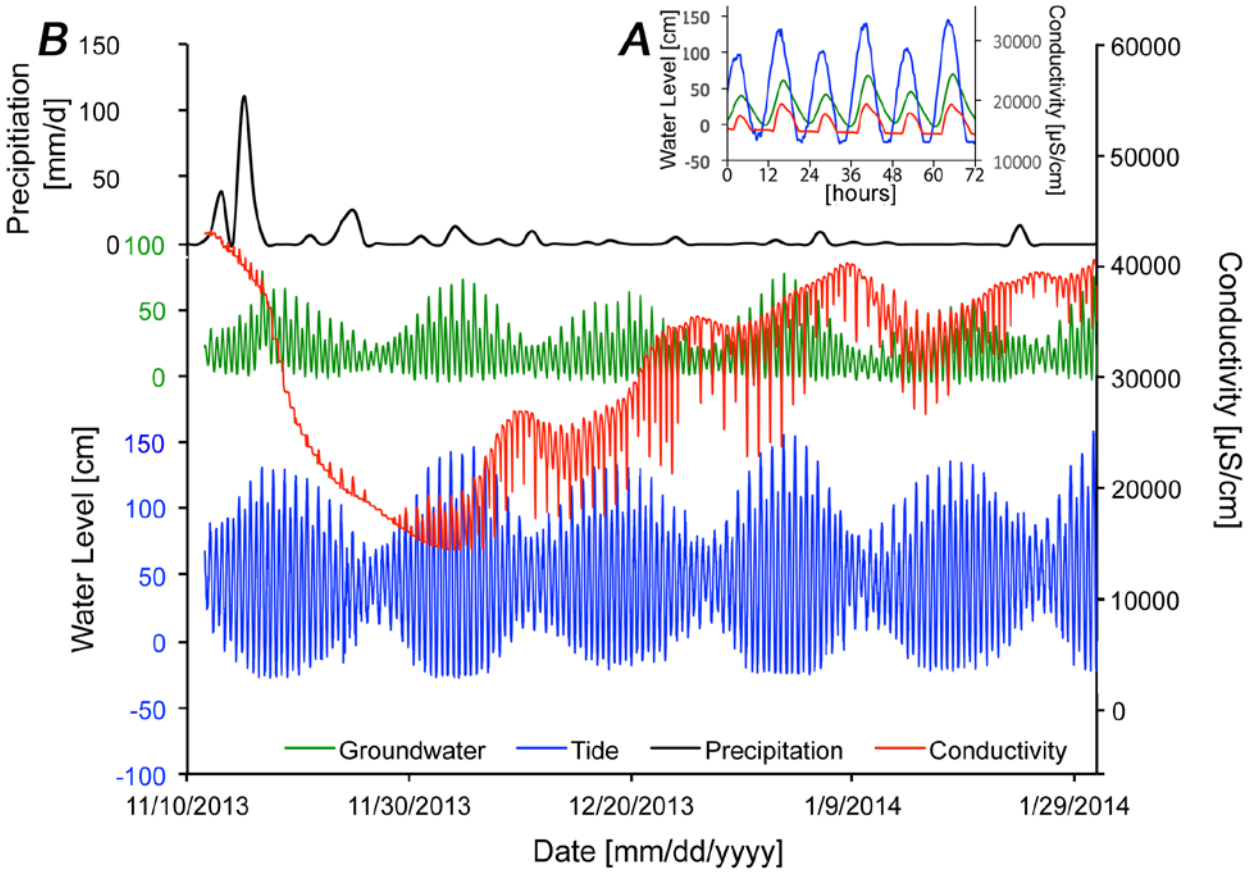

Figure 53. Time series plots showing tidal forcing of groundwater levels and salinity, as well as the observed response to a large rain event. A. From 11 November 2013 through 29 January 2014. B. From 1 December through 4 December 2013.

Although the ERT profiles generally maintain a discernable separation between saline, brackish, and freshwater resources (FIGURE 54), they also record the same oscillating salinity levels seen in the conductivity measurements of groundwater wells. The ERT profiles also visualized the vertical shift of the freshwater lens with tidal movement. Integrating groundwater well locations into ERT profiles also clarified that the base of the groundwater wells were in freshwater during low tides and in seawater during high tides. Furthermore, the horizontal

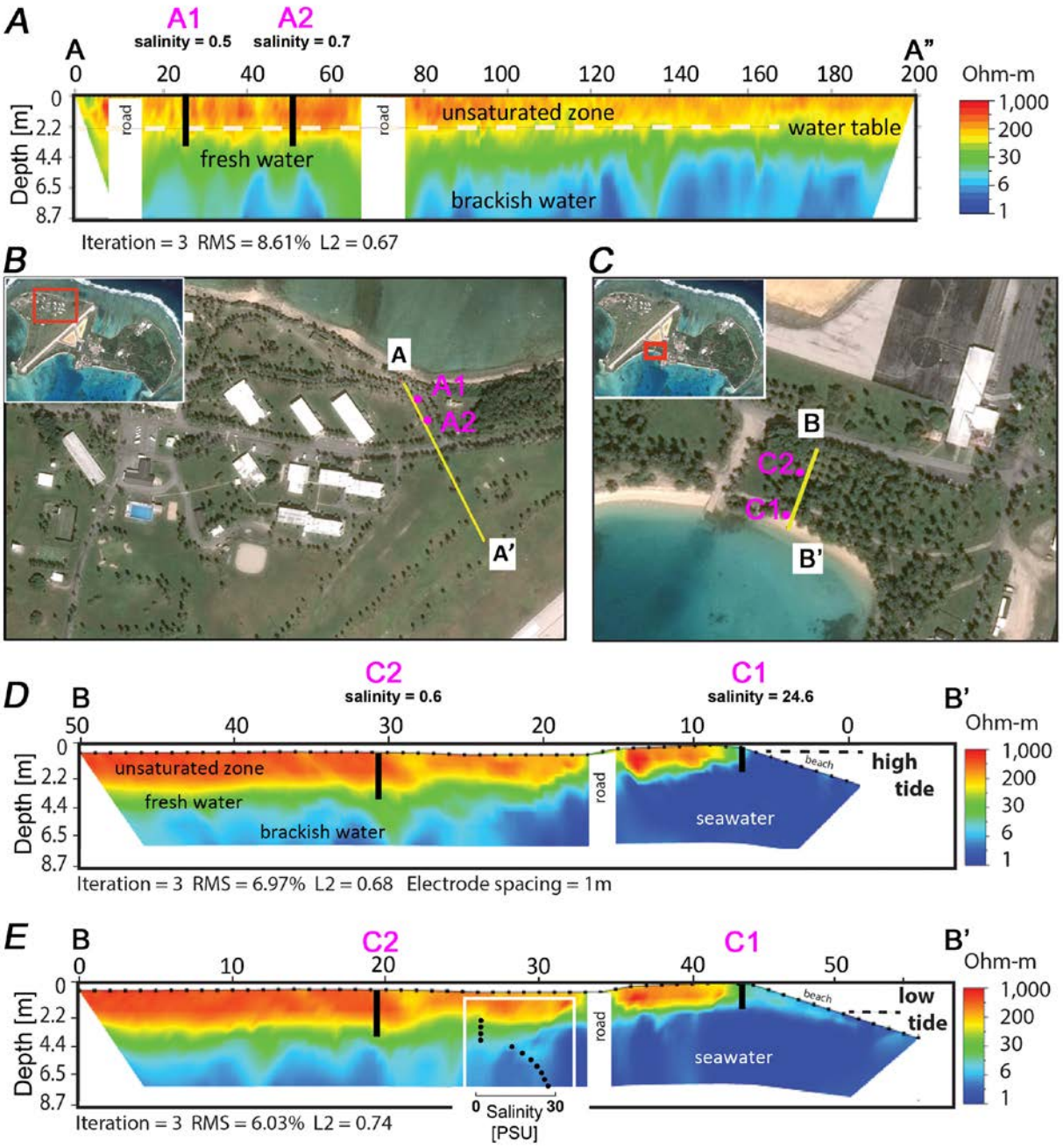

Figure 54. Locations and examples of Electrical Resistivity Tomography (ERT) profiles. A. ERT profile A-A´ on the ocean side of Roi. B. Map showing location of ERT profile A-A´. C. Map showing location of ERT profile B-B´. D. ERT profile B-B´ on the lagoon side of Roi at high tide. E. ERT profile B-B´ on the lagoon side of Roi at low tide. The locations of wells A1, A2, C1, and C2 are denoted in magenta.

variability in the ERT profiles showed that freshwater fingers in the brackish or saline layers occurred at different locations, possibly suggesting tidally induced convective forcing.

3.8.6 Submarine Groundwater Discharge and Groundwater Geochemistry

On the same tidally controlled temporal scale, SGD also fluctuated between high and low tide (FIGURE 55). While SGD was generally low (average 1 centimeter/day) SGD rates varied between 0-3 centimeter/day. Increased SGD rates were observed shortly after low tide, while high tides caused a landward seawater hydraulic head that prevented SGD. The ERT profiles support this aquifer dynamic (FIGURE 54), displaying no obvious SGD during high tide but increased freshwater and brackish discharge during low tide.

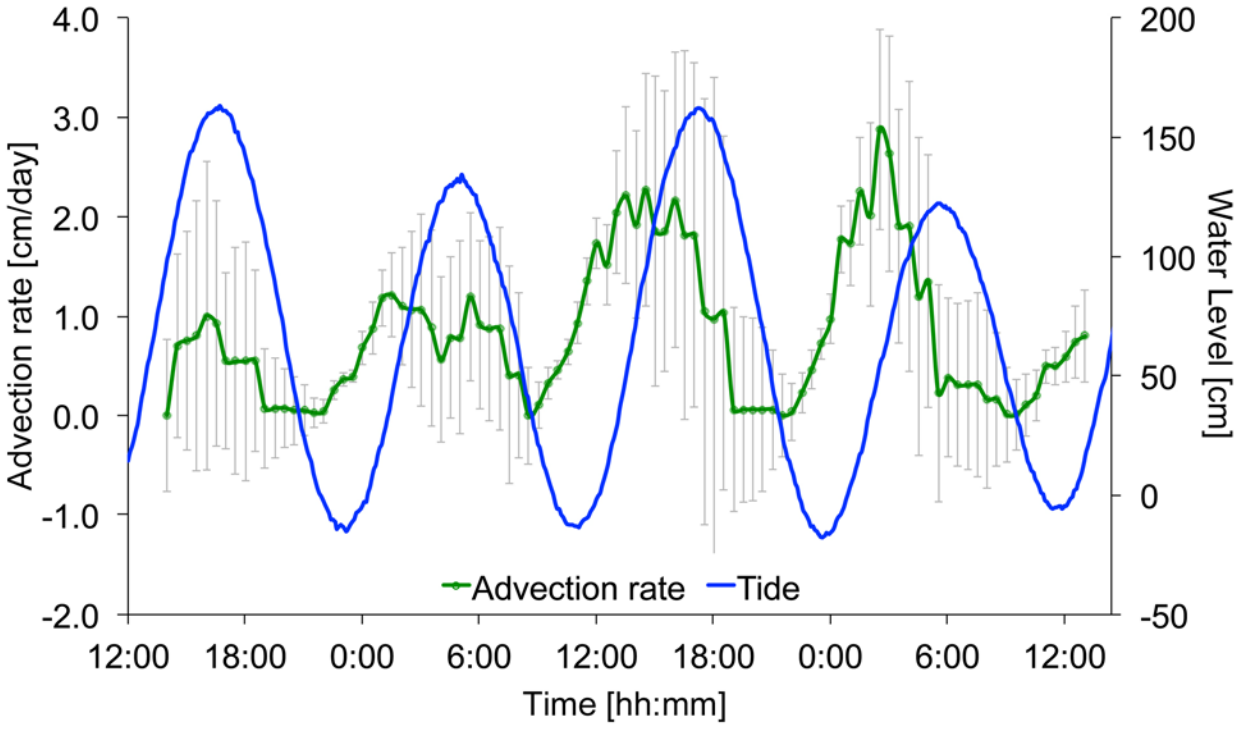

Figure 55. Time series plot showing ocean water levels (tides, in blue) and the computed submarine groundwater discharge (SGD, in green) advection rates. The error bars denote ± 1 standard deviation

The ERT profiles clearly identified a distinct freshwater lens floating atop seawater, which could be confirmed in geochemical groundwater sampling (FIGURE 56) along the same lagoon transect (FIGURE 54). Most geochemical analyses record a sharp transition zone below 4 meters depth, indicating a differentiation of water masses. Salinities sharply increase below 4 meters from a freshwater environment (1 practical salinity unit, 'PSU') to a saline environment (28 PSU). Roughly 4-fold similar increases between the water masses can be seen in the measurements of NH_4^+, PO_4^{3-}, Mo, U, and pH. On the other hand, Ba and Si are highest near the surface and decrease with depth at more gradual rates.

3.8.7 Large Rain Event Impact on Groundwater

The speed at which the freshwater lens freshens depends on the effective flushing rate from rainfall (and possible artificial recharge). Consequently, the more severe a rainfall event is, the greater its immediate impact on salinity. The instruments captured a large scale rain event

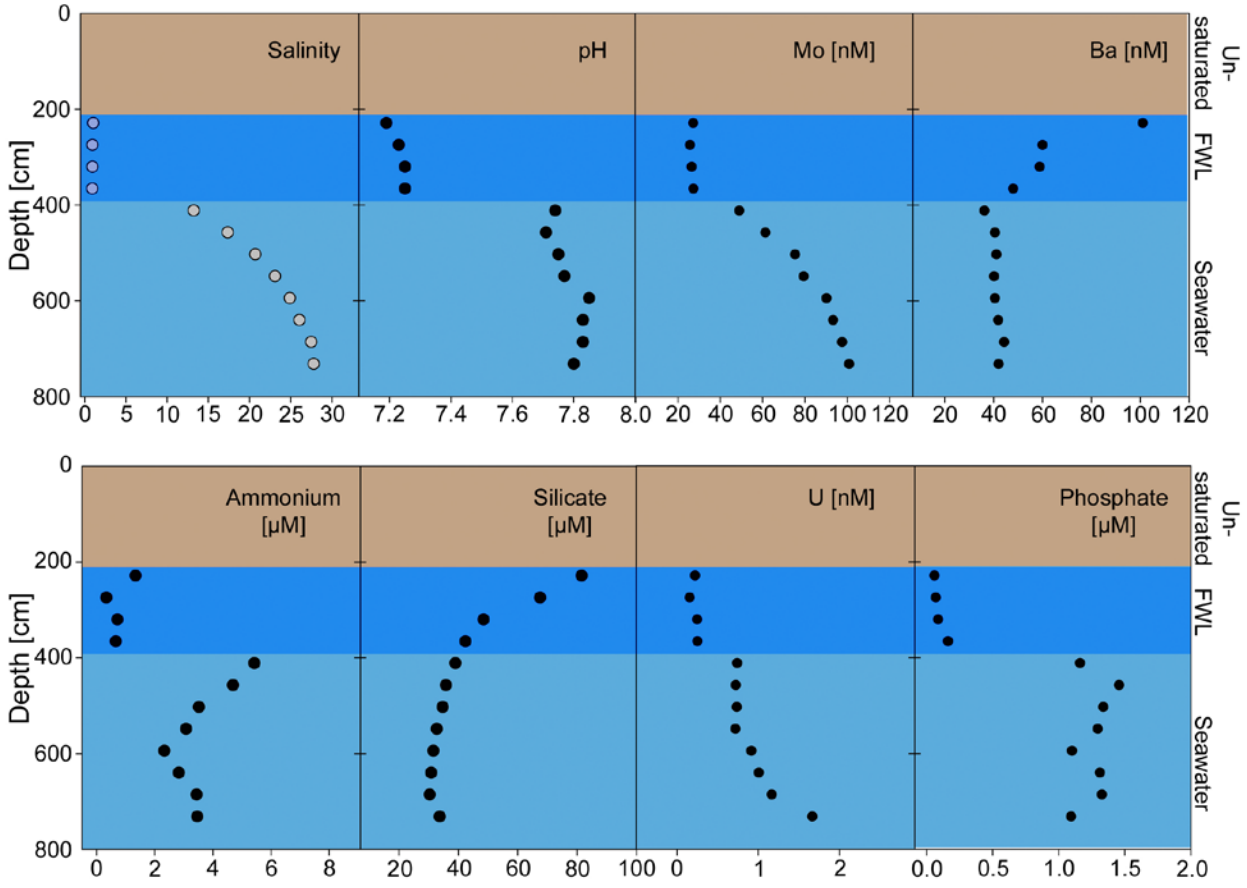

Figure 56. Plots of geochemical porewater profiles indicating a sharp transition between the freshwater lens and the underlying seawater. Vertical variations in salinity, pH, molybdenum, barium, ammonium, silica, uranium, and phosphate are shown. Location of profile indicated on FIGURE 54 between wells C1 and C2.

(FIGURE 53) lasting 5 days, during which approximately 10 percent of the annual rainfall (~160-190 centimeters/year) occurred (Gingerich, 1992; Gingerich et al., 2017). Such rainfall events are coupled by major storm systems and are not uncommon on Roi-Namur. The rain event was recorded in wells by a relatively fast freshening of the aquifer followed by a gradual increase in salinity. The initial decrease in salinity (by 25000 micro-Siemens/centimeter) caused by this rain event occurred over a three-week period while the return to salinity levels prior to the rain event took approximately 3 months during which little rain fell (8 centimeters). The groundwater level observed in wells was only slightly elevated (25 centimeters) for a short period (24 hours) directly after the large rainfall. This indicates that increased rates in SGD due to precipitation are likely to occur only for a short time period following the rain event, but are not correlative with the associated decreases or increases in salinity.

3.8.8 March 2014 Overwash Event's Impact on Groundwater

On 2-3 March 2014, Roi-Namur experienced an overwash event that caused seawater to flood inland. The oceanographic forcing that lead to this event is documented in FIGURES 36-37.

The event was evidenced in all groundwater wells where it caused maximum salinity levels to be recorded (FIGURE 57). The overwash event was also accompanied by a sudden and significant rise in groundwater level (20 percent over the tidally attributed effect). The overwash's effect on recorded salinities in wells was likely dampened by two large rain events that occurred 10 days prior and 1 day (FIGURE 58) after the overwash event, causing a much more gradual signal of increasing salinity than is typical of saline intrusion. The salinity levels at the near-shore well location closest to the inundated areas returned to pre-overwash levels within 1 month. Groundwater wells on the lagoon side of the island returned to pre-overwash salinity levels within 3 days after the overwash event.

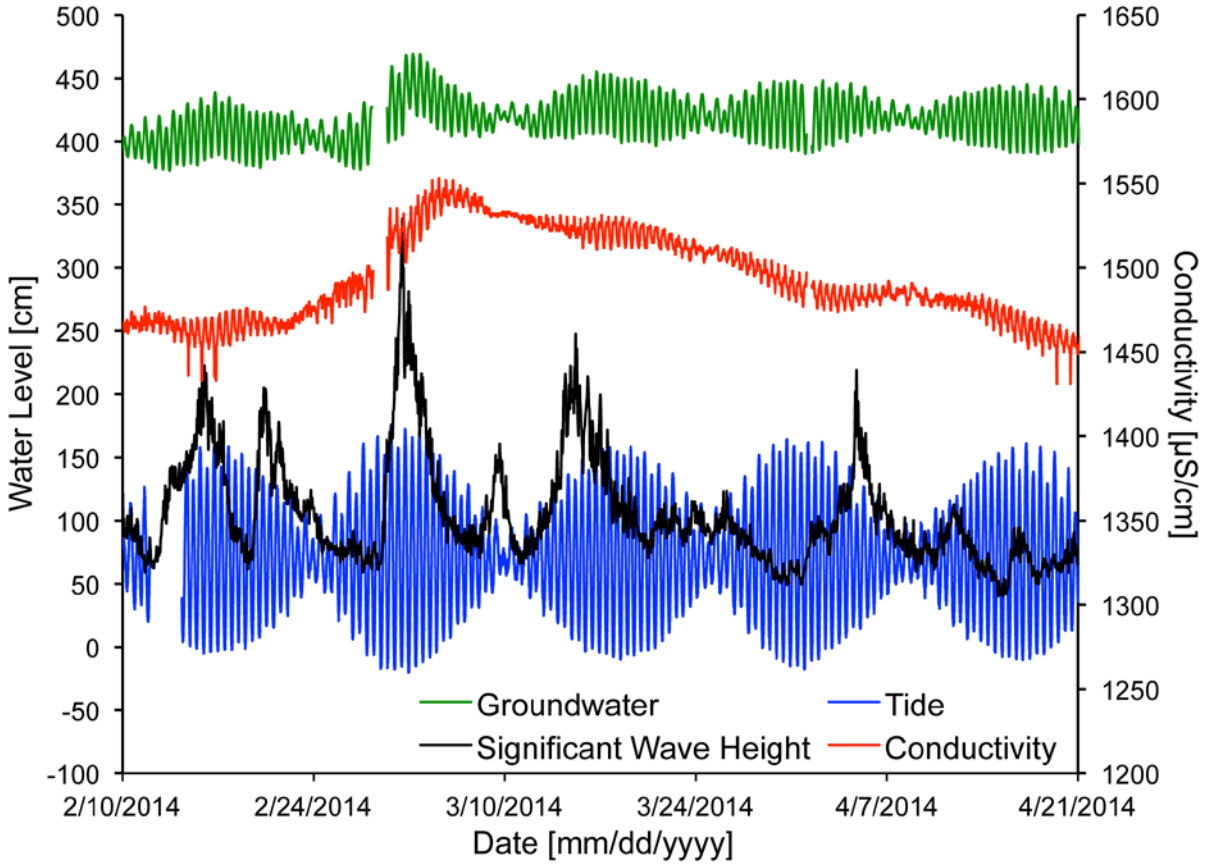

Figure 57. Time series plot showing variations in tide (blue), significant wave height (black), groundwater level (green), and conductivity of water (red) in well A1 observed during the 2-3 March 2014 overwash event.

3.8.9 Long-term Precipitation Impact on Groundwater

With the exception of the two large rain events during November 2013 and March 2014, the collected data supports the known precipitation patterns: a relatively dry season from December to April followed by a wetter season with maximum precipitation occurring between August and October (FIGURE 58). Between November 2013 and February 2015, precipitation on Roi-Namur amounted to a total of 274 centimeters, or 198 centimeter/year. Both large rain events

occurred in the form of two significant storm events followed by periods of significantly reduced rainfall. The annual fluctuation of salinity in groundwater wells was directly related to the annual precipitation patterns, as well as the large storm-induced precipitation events in November 2013 and March 2014 that caused a rapid reduction in conductivity by 1000 micro-Siemens/centimeter in inland wells. Although these storm events also caused a sudden increase in groundwater levels, these increases were short-lived (maximum of 2 days) and long-term precipitation trends could not be linked to groundwater levels, which steadily decreased over the duration of this study.

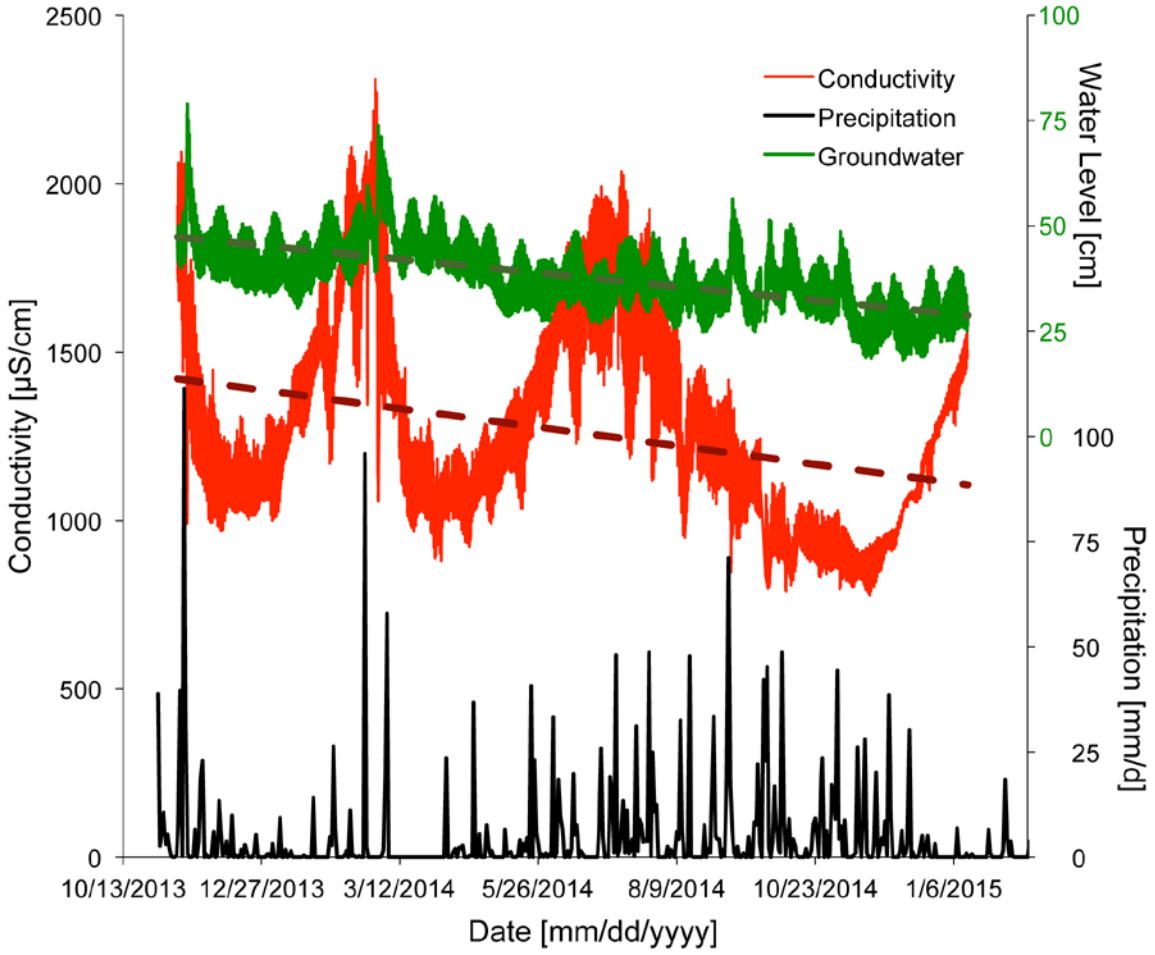

Figure 58. Time series plot showing variations in precipitation (black), groundwater level (green), and conductivity of water (red) in well C3 observed between November 2013 and February 2015. Linear fits to the data are denoted by thick lines.

3.8.10 Sea-level Change Impact on Groundwater

Over the monitored time period (16 months), both salinity and groundwater levels in all wells fell roughly by 29 percent and 68 percent, respectively (FIGURE 58). The observed negative trend in groundwater height is closely related to the varying levels of decline in mean sea level (average 59 percent) during this time period (FIGURE 59). Although mean sea level (MSL) measured by tide gauges since 1948 has, on average, been rising in Roi-Namur by 2.2

millimeter/year, the monitoring period of this study fell into a timeframe during which ENSO climate cycles caused a rapid reduction in local MSL (Chowdhury et al., 2007; Becker et al., 2012) of 13.56 centimeter total, or 11.56 centimeter/year. Discrepancies between groundwater levels and the fall of MSL are most pronounced during January-February 2014. A large drop in salinity during the time period of this study suggests that artificial recharge of the freshwater lens system as described by Gingerich et al. (2017) may have contributed to this discrepancy, yielding higher groundwater levels than from natural sea-level forcing alone.

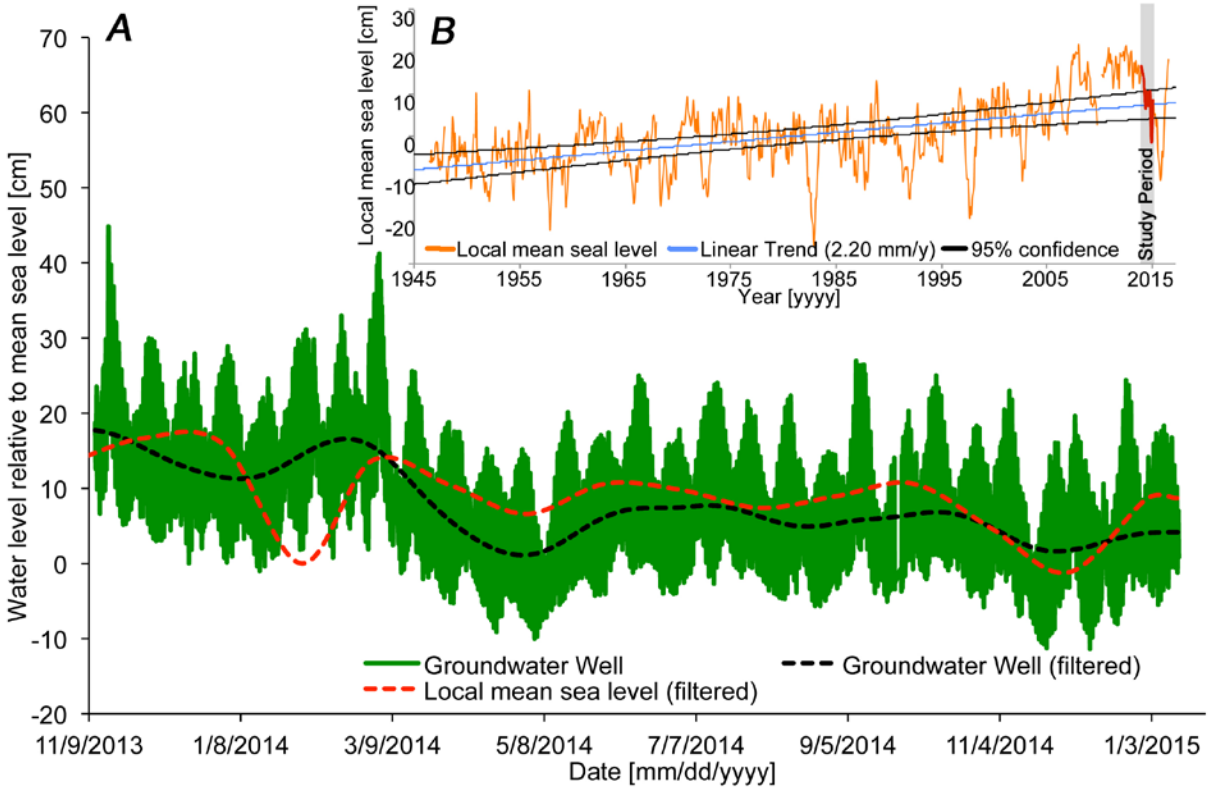

Figure 59. Time series plot showing variations in sea level (red), and hourly (blue) and 40-hour filtered groundwater level (green) in inland well R11.

3.9 Groundwater Modeling

Using observations of the December 2008 seawater overwash event that occurred on Roi-Namur, a basic framework of the salinization and recovery processes that impact water supply on low-elevation islands was developed. This framework was then used to evaluate both management of the freshwater supply and mitigation options following overwash events, as well as future trends in groundwater supply on low-lying islands.

3.9.1 Hydrogeologic Setting and SUTRA Groundwater Model

3.9.1.1 Roi-Namur Island

About 20 percent of Roi is paved, including a 1,370-meter long asphalt airport runway and two adjacent concrete-lined rainwater-catchment basins (FIGURE 60). The rainfall-catchment system from the runway provides enough water for the island's needs during the wet season

Figure 60. Map showing location of select hydrologic features on Roi-Namur. Monitoring-well clusters are shown as orange circles.

(May–November) but groundwater withdrawal is needed for water supply during the dry season (December–April) as described by Gingerich (1996). About 70 percent of the average annual rainfall occurs during the wet season. Most of the groundwater that is used in the water-supply system comes from a 1,000-meter long horizontal skimming well that was constructed adjacent

and parallel to the Roi runway, at a depth of about 2 meters below the ground surface, which corresponds to a few tens of centimeters below sea level.

The shallow aquifer at Roi-Namur Island is composed mostly of unconsolidated, reef-derived, calcium-carbonate sand and gravel (FIGURE 61), but also of a few layers of consolidated rock such as coral, sandstone, and conglomerate (Gingerich, 1996). The uppermost geologic unit was heavily altered by intensive bombing of Roi and Namur Islands during World War II and was re-leveled thereafter to create smoother surfaces for the airport and other island infrastructure.

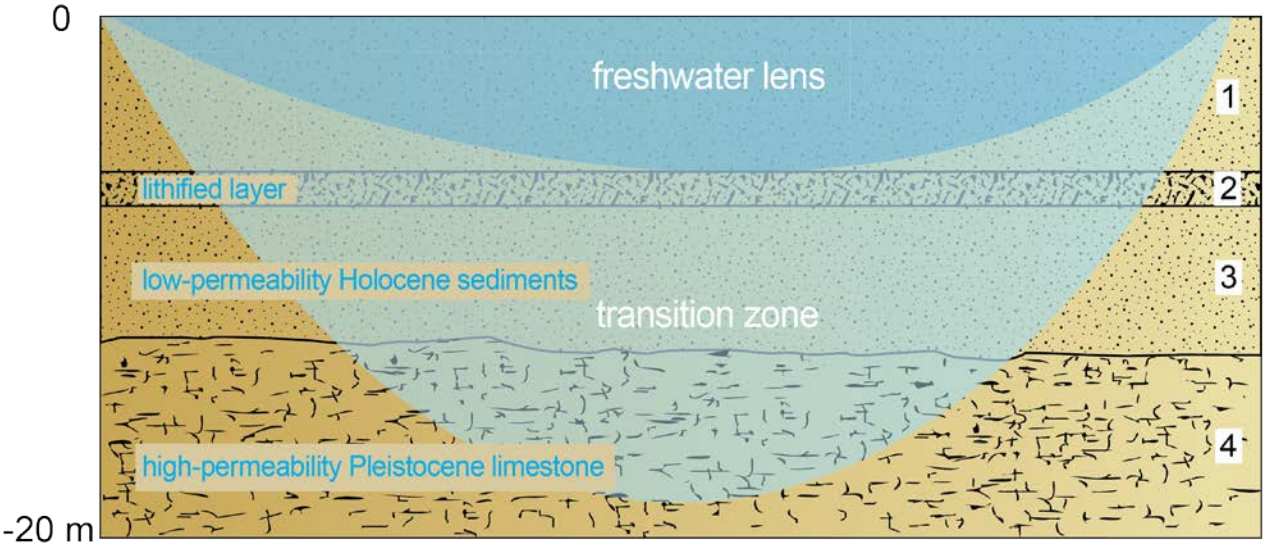

Figure 61. Simplified cross-sectional view of island lithology, modified from Peterson and Gingerich (1995).

During 2000-2008, rainfall averaged about 163 centimeters/year (Stan Jazwinski, Chugach Management Services, Inc., written comm.). Spatially distributed recharge to the freshwater lens was estimated for 2000-2012 using a detailed water-budget model with a daily computation interval (Johnson et al., 2014). Information available for Roi-Namur was used to create select data inputs used in the water-budget computations: land cover, forest-canopy cover, and records of daily rainfall and surplus catchment water discharged to the ground. Owing to insufficient information available for Roi-Namur, the remaining data inputs (soil properties, land-cover properties, and ET) were estimated. The water-budget computations included the assumptions of spatially-uniform rainfall and reference ET, and no fog interception, irrigation, or runoff. A dataset of monthly recharge distributions during 2000-2012 is available at https://dx.doi.org/10.5066/F7GM85H0; the metadata of this dataset includes descriptions of the assumptions and how the data inputs, recharge and other water-budget components were estimated. Natural recharge from rain for 2000-2012 is estimated to average about 945 x 10^6 liters/year (equivalent to about 65 centimeters/year over the unpaved areas of the island). ET is estimated to be about 64 percent (104 centimeters/year) of the annual rainfall.

Beginning in July 2009, water managers began the practice of discharging water (surplus water after filling three large storage tanks in the rainfall-catchment system) to a swale directly above the skimming well. This applied water infiltrates rapidly with no runoff and little chance for evaporation allowing for efficient artificial recharge. The quantity of artificial recharge from the surplus catchment water averaged 33 x 10^6 liters/year (about 238 centimeters/year in the

application area) during the wet seasons of 2009–2012. The estimated island-wide recharge for the year with the highest recharge (74 centimeters) after artificial-recharge application began (2010), and annual totals for 2000-2012 are shown in FIGURE 62. The application of artificial recharge continues to the present day, and is applied during periods whenever the on-island water storage tanks are full, typically peaking during September-October of each year.

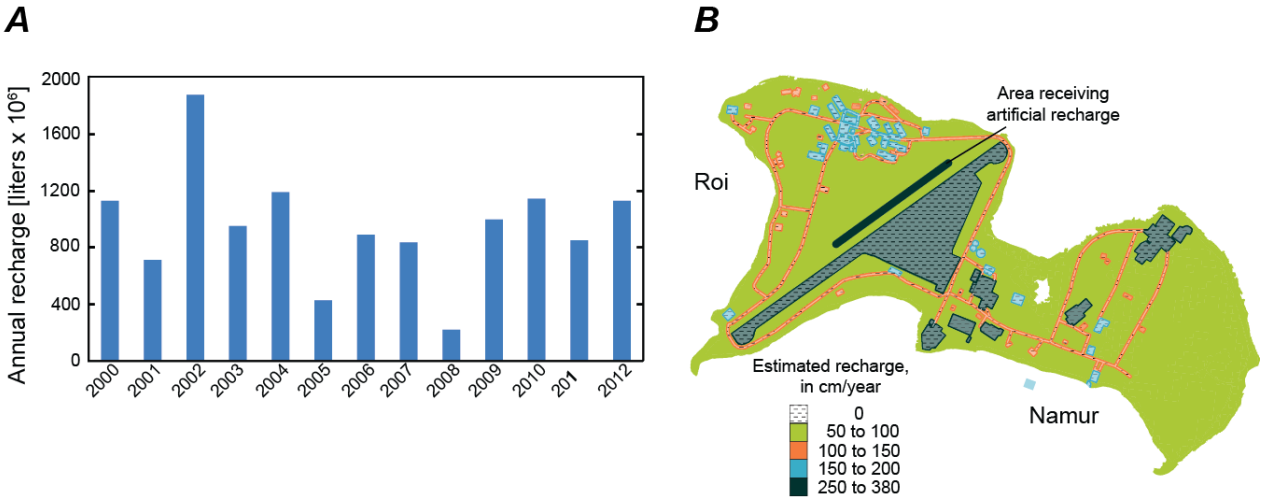

Figure 62. Temporal and spatial recharge on Roi-Namur. A. Plot showing estimated annual recharge for 2000–2012. B. Map showing areal recharge distribution for 2010. Recharge is enhanced along the edges of impervious (hatched) areas upon which runoff accumulates and within the strip parallel to the runway of in which artificial recharge is applied.

3.9.1.2 The 2008 seawater flooding event and its impact on the freshwater supply

On 7-9 December 2008, wave-driven seawater overwash and flooding occurred on many low-elevation central-Pacific islands including Kwajalein Atoll. The flooding was caused by the arrival of extra-tropical storm swell during a time of anomalously high regional sea levels linked with ENSO and regional sea-level rise (Hoeke et al., 2013). Roi-Namur experienced several episodes of seawater flooding during subsequent high tides along the northern coast, resulting in damage to buildings, as well as widespread ponding of seawater in the maintenance area on the isthmus connecting Roi and Namur and on the golf course overlying the freshwater lens on Roi. According to personal accounts and photos taken, the ponded seawater infiltrated into the subsurface within a few days after initial flooding occurred, including directly into the horizontal skimming well adjacent to the runway on Roi.

Prior to the flooding event, local utility staff had a standard procedure to regularly analyze chloride (Cl^-) concentration in water collected from the horizontal skimming well at risers along 6 interconnected galleries. Immediately after the seawater flooding, the sampling frequency was increased to daily measurements and then later reduced to weekly measurements. For the three months prior to the flooding event, skimming-well Cl^- concentrations had ranged from 53-195 milligrams/liter in individual galleries (all monitoring data provided by Stan Jazwinski, Chugach Management Services, Inc., written comm.). The range in concentration of the pre-flood samples collected from the individual galleries reflects the differences in salinity due to the distance from the coast of each gallery and the practice of withdrawing water from different galleries at different

rates and times. Two days after the flooding event, reported Cl^- concentrations increased to 10,080-20,880 milligrams/liter (compared to seawater concentration of 19,600 milligrams/liter Cl^-) as shown in FIGURE 63. By 10 days after the flooding, the concentrations had rapidly dropped to 1,800-3,960 milligrams/liter Cl^-. However, it wasn't until 22 months after the flooding event that Cl^- concentrations from all of the galleries reached potable values, on par with those measured prior to the flooding event. The impact of the flooding event on the freshwater lens was likely exacerbated by the lack of rainfall during the previous year, which had been only about 58 percent of the average rainfall that had occurred during 2000-2012, likely leading to a freshwater lens that was thinner than usual.

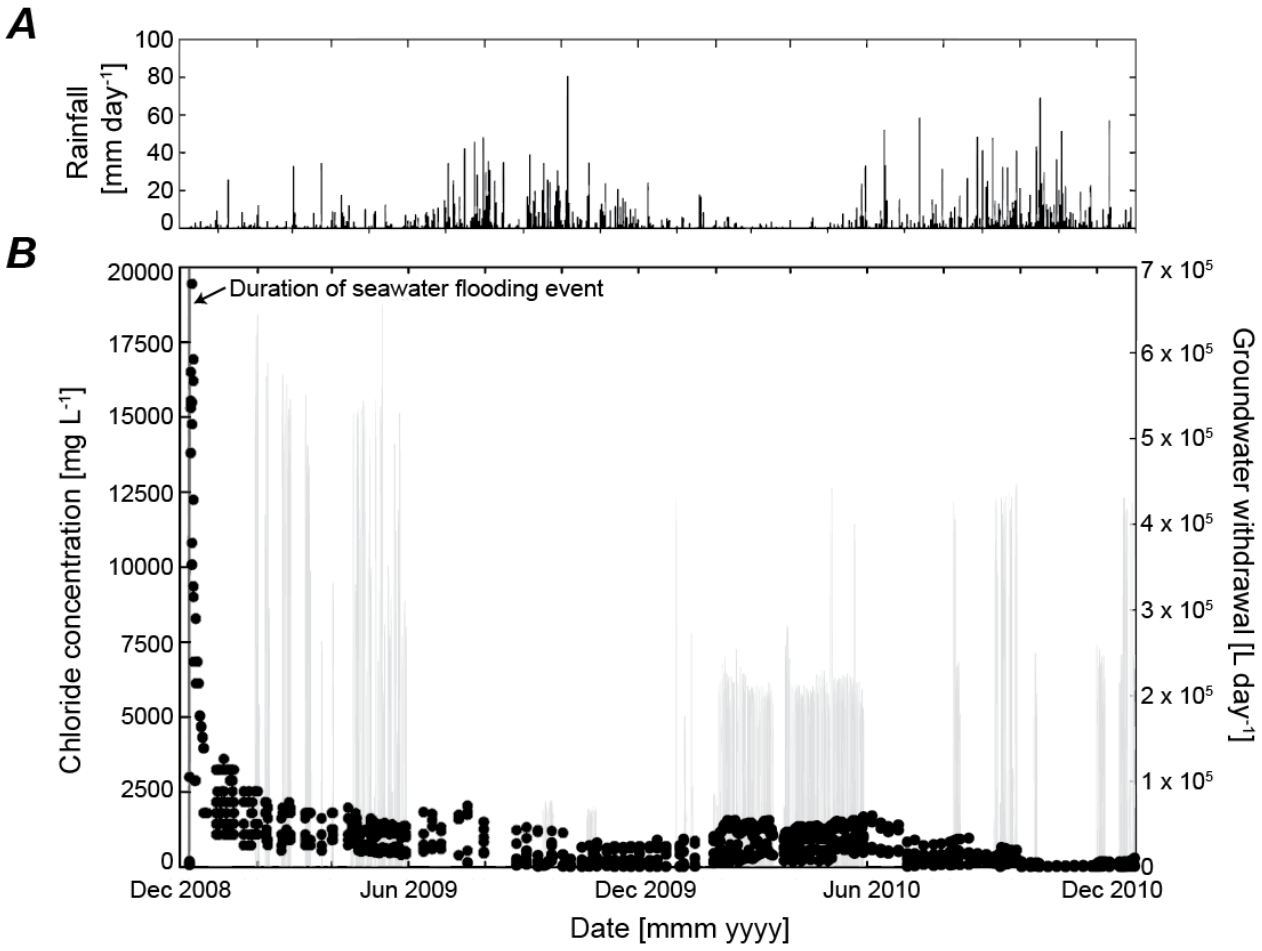

Figure 63. Time series plots of the response of groundwater to rainfall and withdrawals. A. Rainfall. B. Skimming-well chloride concentration and groundwater withdrawals after the December 2008 seawater flooding event. Chloride samples (dark gray circles) collected at 1-6 standpipes along the length of the skimming well during withdrawal. Observed chloride concentrations greater than 20,000 milligrams/liter are not shown.

During the first month after the flooding event, rainwater that was stored in tanks during the previous wet season was used for supply, but the stored water was not sufficient for the island's needs during the subsequent 5-month dry season, so in January 2009, potable water was barged in from Kwajalein Island, 145 kilometers to the south. Groundwater withdrawal for

consumption (sometimes consumed after treatment with a temporary reverse osmosis system) during February-May and October 2009 was intermittent, while a golf course well (shown as "8151" on FIGURE 60) was pumped at a much higher rate than normal, due to the water emergency, resulting in roughly equal withdrawal amounts from that and the skimming well. During 2010, only the skimming well was pumped. During January-May, September, and December 2010, withdrawal was sustained for weeks rather than intermittently as in 2009 (FIGURE 63).

The natural seasonal recharge during the period from the overwash and flooding event until the end of May was lower than normal. Rainfall was only 31 centimeters, which is 63 percent of the average for this same period during the years 2000-2012. In July 2009, when higher seasonal rainfall returned, the utility managers began, for the first time on Roi-Namur, to artificially recharge the freshwater lens by discharging the surplus rainfall captured (after filling the tanks) onto the ground surface above the skimming well. The impact of the rainfall history and artificial recharge on post-flood recovery are also evaluated in this study.

3.9.1.3 SUTRA model of Roi groundwater

As a basis for evaluating the physics of flood salinization processes and controlling factors, a three-dimensional (3D) finite-element model of variable-density groundwater flow and salt transport in the island aquifer was created using the USGS SUTRA code (Version 2.2, Voss and Provost, 2002). The model domain includes Roi and some distance offshore to a depth of about 105 meter below sea level (FIGURE 64). The topobathy DEM developed here was used as the model's land surface. The geologic structure shown in FIGURE 61 is represented as a set of horizontal hydrogeologic units in the model. Based on what is understood about Roi hydrogeology, each unit is assigned uniform properties throughout the model. The skimming well is modeled as a horizontal line at 0.15 meter below sea level, represented by a line of nodes in the finite-element mesh.

Two versions of the 3D model were used for the analysis. In the first version, used for representing hydraulic response to tides, a simplified unsaturated zone is represented above the water table. This allows estimation of permeabilities and aquifer-specific yield. To approximate water-table movement and its response to tides, a linear saturation-pressure relation was used, which entails zero entry pressure, a minimum water saturation of 0.01 occurring at pressure of -19,545 kilograms/(meter-second^2), and a constant permeability that is not dependent on saturation (relative permeability is set to 1). The second 3D model version, used for all subsequent seawater-flooding analyses, does not require representation of the unsaturated zone, avoiding long computational times for the 2-year simulations. For this model, the SUTRA code was modified to account for water-table storage by including the aquifer-specific yield in the governing equations, as was done by Souza and Voss (1987) and Gingerich and Voss (2005). Other data describing the model are given in TABLE 13. The digital files for the model and all of the results discussed in the here are available at:
https://water.usgs.gov/GIS/metadata/usgswrd/XML/sutra_freshwater_flow.xml.

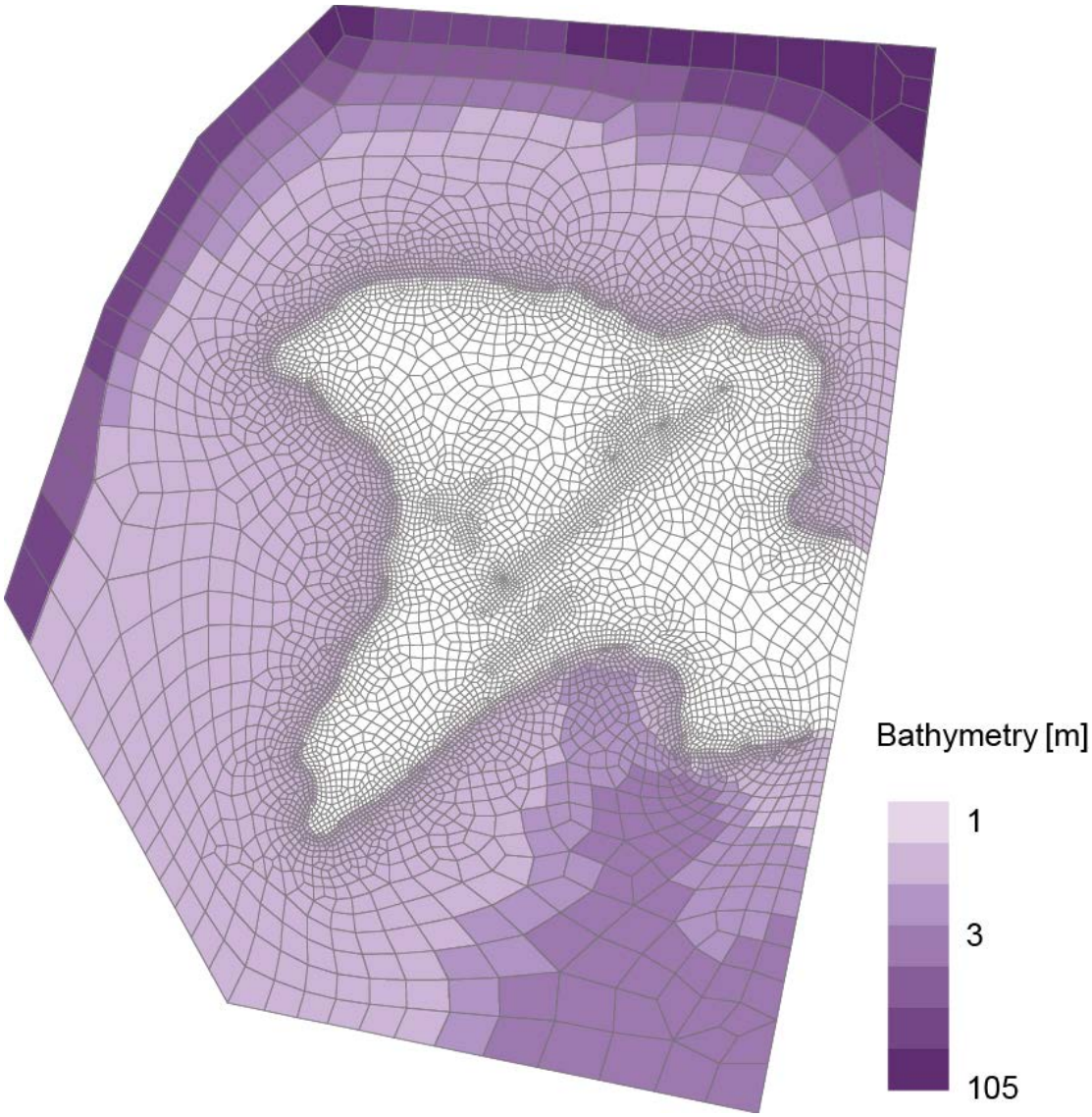

Figure 64. Map showing the SUTRA model mesh and bathymetry.

3.9.2 SUTRA Simulation of the 2008 Seawater Overwash and Flooding Event

3.9.2.1 Initial salinization

The area of flooding and subsequent seawater ponding on Roi Island for the December 2008 overwash is shown in FIGURE 65 (patterned areas); this area was based on pictures taken during the event and anecdotal descriptions from island residents. The ponding area is the source of the post-flood aquifer salinization. To represent the seawater infiltration that occurred for 2 days, nodes at the top of the model within this area were assigned a specified fluid flux equivalent to a volume of seawater (1.22×10^8 liters) ponded to a depth of 0.53 meter, infiltrating over 2 days.

Hydrologic stresses (recharge and withdrawal) are simulated in two alternative ways: 1) using a yearly average, and, 2) using monthly averages, with both methods based on reported rainfall and well-production data (Stan Jazwinski, Chugach Management Services, Inc., written

comm.). A profile of the simulated salinization pattern 2 days after flooding is shown in FIGURE 66. This is the initial condition for all post-flooding simulations.

Table 13. Parameters for SUTRA groundwater model.

[Note: model values are derived from earlier 2-D studies (Peterson and Gingerich, 1995) with the exception of horizontal hydraulic conductivity]

Parameter	Units	Value	Value	Value	Value
Freshwater density	(kg/m^3)	1000.00			
Seawater density	(kg/m^3)	1024.99			
Water compressibility	(Pa^{-1})	$4.47x10^{-10}$			
Fluid viscosity	(kg/m/s)	8.3^{-4}			
Molecular diffusivity	(m^2/s)	$1.0x10^{-9}$			
Specific yield	(1)	0.04			
Aquifer matrix compressibility	(Pa^{-1})	$1.0x10^{-9}$			
		Layer 1	Layer 2	Layer 3	Layer 4
Horizontal hydraulic conductivity	(m/d)	70	9	50	1000
Anisotropy ratio, (K_H/K_V)	(1)	1	18	25	2
Effective porosity	(1)	0.3	0.3	0.3	0.3
Horizontal longitudinal dispersivity, α_{LH}	(m)	2	2	2	2
Vertical longitudinal dispersivity, α_{LV}	(m)	0.1	0.1	0.1	0.1
Horizontal transverse dispersivity, α_{TH}	(m)	0.1	0.1	0.1	0.1
Vertical transverse dispersivity, α_{TV}	(m)	0.1	0.1	0.1	0.1

3.9.2.2 Post-flooding managed recovery

Selected simulated combinations of recharge and withdrawal, following the seawater-flooding event, are summarized in TABLE 14. A scenario that employs average annual recharge and withdrawal represents the most typical approach that might be used when modeling saltwater inundation above a freshwater lens. Using this approach, the simulation reproduces the rapid decrease in the salinity of water at the skimming well during the first 2 months of recovery (FIGURE 67). Due to the evolution of the density-driven circulation in the model, the simulated concentration drops to less than the lowest measured levels, becoming nearly potable (assumed here to be less than 250 milligrams/liter Cl^- [seawater fraction of 1.28 percent] after 2 months. However, with constant recharge and withdrawal, the simulated salinity becomes much too low or high compared to observations at the skimming well throughout most of subsequent time in the 2-year simulation. This means that when average recharge and withdrawal conditions do not adequately represent field conditions, simulated recovery behavior will not be satisfactory, and long-term salinization – the greatest concern regarding water supply – may not be correctly predicted.

The match of the model results to the measured evolution of salinity is improved when employing monthly estimates of recharge (including artificial recharge) and withdrawal, based on daily rainfall and withdrawal data (FIGURE 67). The model approximately simulates the rapid

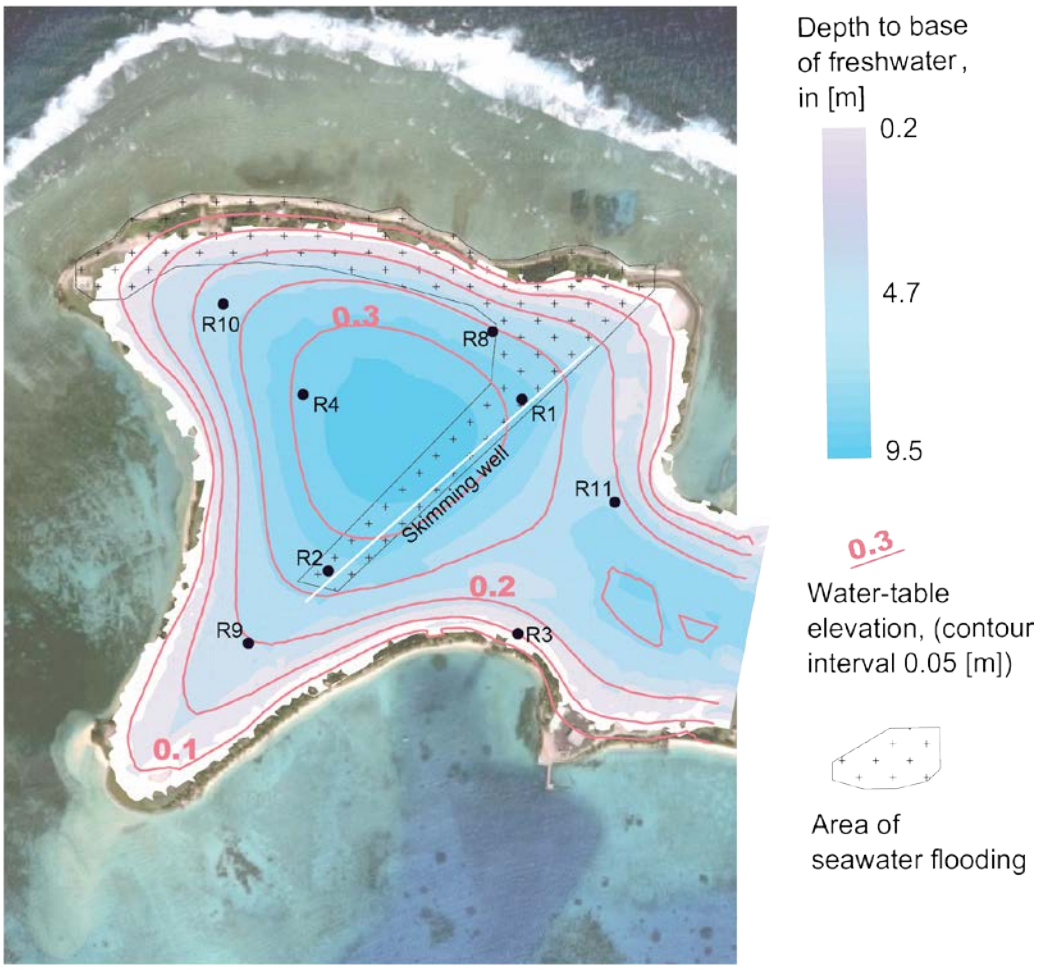

Figure 65. Map showing simulated water-table elevation and bottom elevation (shading) of the freshwater lens (less than 2.5-percent seawater fraction). Patterned area shows extent of seawater flooding and is the seawater source area used in the SUTRA simulations.

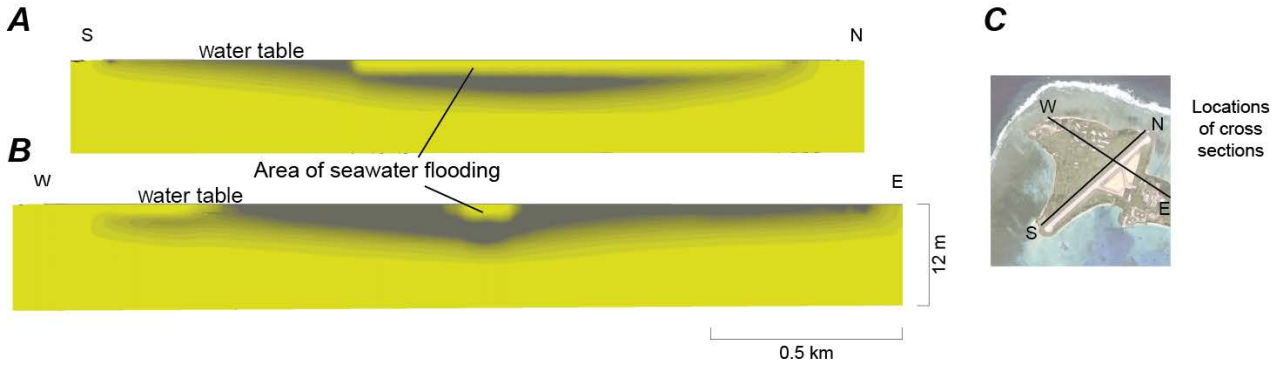

Figure 66. Initial SUTRA model configuration of the Roi freshwater lens after seawater flooding. A. Cross-section running south-north. B. Cross-section running west-east. C. Map showing location of cross-sections. Color represents seawater fraction ranging from 100 percent (yellow) to 2.5 percent (dark gray).

Table 14. Summary of recharge and withdrawal scenarios for December 2008–December 2010 recovery period.

Simulation	Recharge and withdrawal conditions	Artificial Recharge
Average annual recharge and withdrawal	0–21 days: 2008 average recharge and withdrawal 22–365 days: 2009 average recharge and withdrawal 366–730 days: 2010 average recharge and withdrawal	None Includes Jul–Dec artificial recharge Includes Jun–Dec artificial recharge
Monthly recharge and withdrawal	0–21 days: Dec 2008 recharge and withdrawal 22–365 days: Jan–Dec 2009 recharge and withdrawal 366–730 days: Jan–Dec 2010 recharge and withdrawal	None Includes Jul–Dec artificial recharge Includes Jun–Dec artificial recharge
No withdrawal; no artificial recharge	0–21 days: Dec 2008 recharge 22–365 days: Jan–Dec 2009 recharge 366–730 days: Jan–Dec 2010 recharge	None None None
No artificial recharge	0–21 days: Dec 2008 recharge and withdrawal 22–365 days: Jan–Dec 2009 recharge and withdrawal 366–730 days: Jan–Dec 2010 recharge and withdrawal	None None None
No withdrawal	0–21 days: Dec 2008 recharge 22–365 days: Jan–Dec 2009 recharge 366–730 days: Jan–Dec 2010 recharge	None Includes Jul–Dec artificial recharge Includes Jun–Dec artificial recharge
Wet-season withdrawal and artificial recharge	0–12 days: Dec 2008 recharge and withdrawal 13–217 days: Jul–Dec 2009 recharge and withdrawal	None Includes Jul–Dec artificial recharge

decrease in concentration at the beginning of recovery, then reproduces the elevated salinities through the dry months of 2009 (January-June) and the increase in salinity during the first few months of 2010 when rainfall was low and withdrawal was relatively steady and prolonged. The model also reproduces the measured decrease in salinity during the wet months of September–December 2009 and late 2010, when artificial recharge was added to the freshwater lens immediately above the skimming well.

For the case of uniform recharge and withdrawal, the evolution of post-flood aquifer salinity over the 2 years of simulated recovery is shown in a cross section (viewed from south) view in FIGURE 68. Natural convection in the model is initiated as fingers along the outside edges of the flooded area. Thereafter fluid-density-driven convection occurs chaotically, in multiple fingers and circulation cells within the flooded area, causing rapid decreases in salinity near the water table, while mixing and distributing the intruded seawater across the entire freshwater lens. When natural and artificial recharge begins after 6 months, freshwater again accumulates at the water table and slowly pushes the saltier intruded flood water deeper in the freshwater lens and toward the coast.

3.9.3 SUTRA Simulations of Hydrologic Stresses Controlling Freshwater Lens Recovery

The measured salinity values and their time-evolution allow quantitative model evaluation of factors that may control water quality following an overwash event. The sensitivity of simulated salinity to potential hydrologic stress factors is evaluated here. The factors considered are the individual and combined impacts of natural recharge, artificial recharge, groundwater withdrawal, and, whether the overwash event occurs in the wet or dry season.

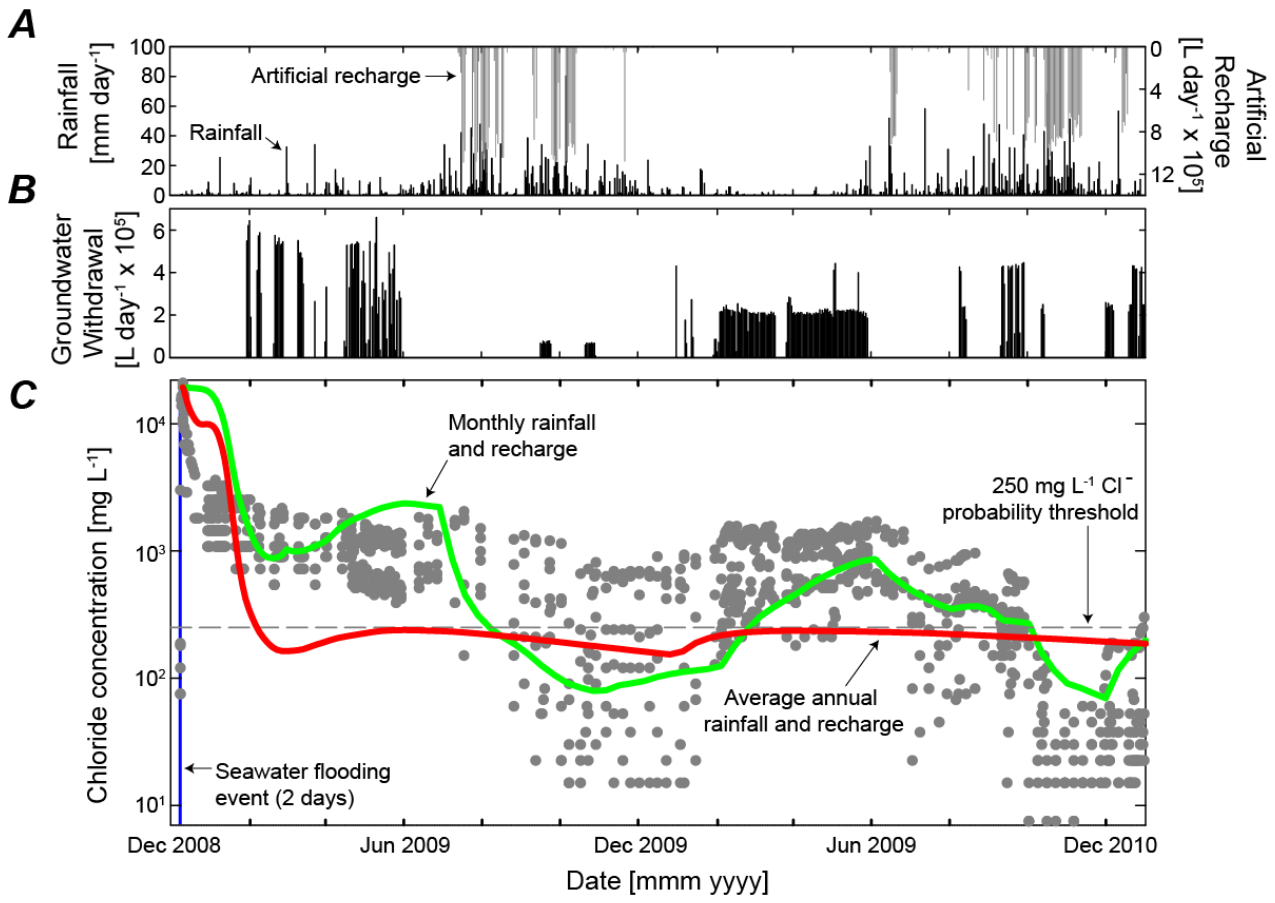

Figure 67. Time series plots of the observed and simulated skimming-well salinity after the December 2008 seawater flooding event A. Rainfall (black) and artificial recharge (gray). B. Groundwater withdrawals. C. Chloride concentrations measured (gray circles) at the skimming well and simulations for the same location using average annual recharge and withdrawal (red line) and monthly recharge and withdrawal (green line) relative to the 250 milligrams/liter potability threshold.

3.9.3.1 Undisturbed recovery (no withdrawal, no artificial recharge)

Long-term undisturbed recovery of the freshwater lens after a seawater-flooding event would take place in the absence of any groundwater withdrawal or artificial recharge. This is the most representative scenario of seawater flooding on a typical atoll island on which little or no infrastructure is available for sustained groundwater withdrawal or artificial recharge. This case illustrates recovery in a completely unmanaged system with no groundwater usage (the actual system on Roi experienced a managed recovery and groundwater was pumped).

Simulated undisturbed recovery of the freshwater lens without pumping or artificial recharge occurs more quickly than did the recovery observed on Roi (FIGURE 69). This is due to the absence of groundwater withdrawal in the modeled natural system. During February-September 2009, the salinity of the pumped water in the natural system is initially lower than that on Roi because the simulated freshwater lens is not being depleted by groundwater withdrawal. For undisturbed recovery (February-July 2009), the Cl^- concentrations at locations where the well would be average about 440 milligrams/liter, compared with about 1,160 milligrams/liter during

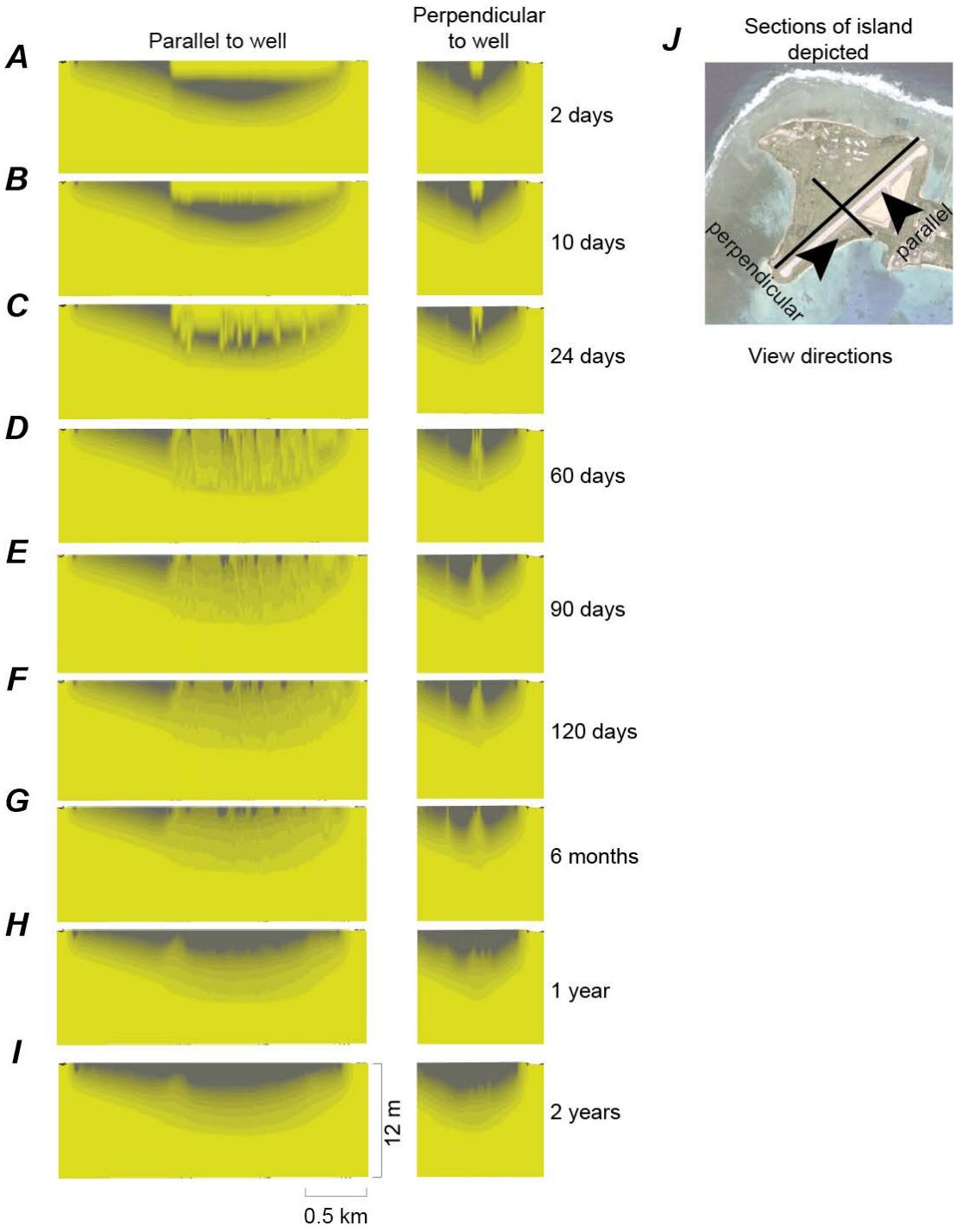

Figure 68. Simulated recovery of Roi freshwater lens after seawater flooding. A. After 2 days. B. After 10 days. C. After 24 days. D. After 60 days. E. After 90 days. F. After 120 days. G. After 6 months. H. After 12 months. I. After 24 months. J. Map showing locations of cross-sections. Color represents seawater salinity ranging from 100 percent (yellow) to 2.5 percent (dark gray). Vertical exaggeration is 400 times.

the observed recovery; these undisturbed recovery values are lower, but still significantly above the potable level of 250 milligrams/liter Cl^-. For September 2009-February 2010, the Cl^- concentration at the skimming well location is about the same for both cases, averaging about 110 milligrams/liter. During March-October 2010, the undisturbed recovery Cl^- concentrations remain below that for the managed recovery, at about 120 milligrams/liter, before decreasing to as low as 60 milligrams/liter after the 2010 wet season. In contrast, the managed recovery Cl^- concentrations remained above 250 milligrams/liter during March-October 2010, when withdrawal from the skimming well was highest.

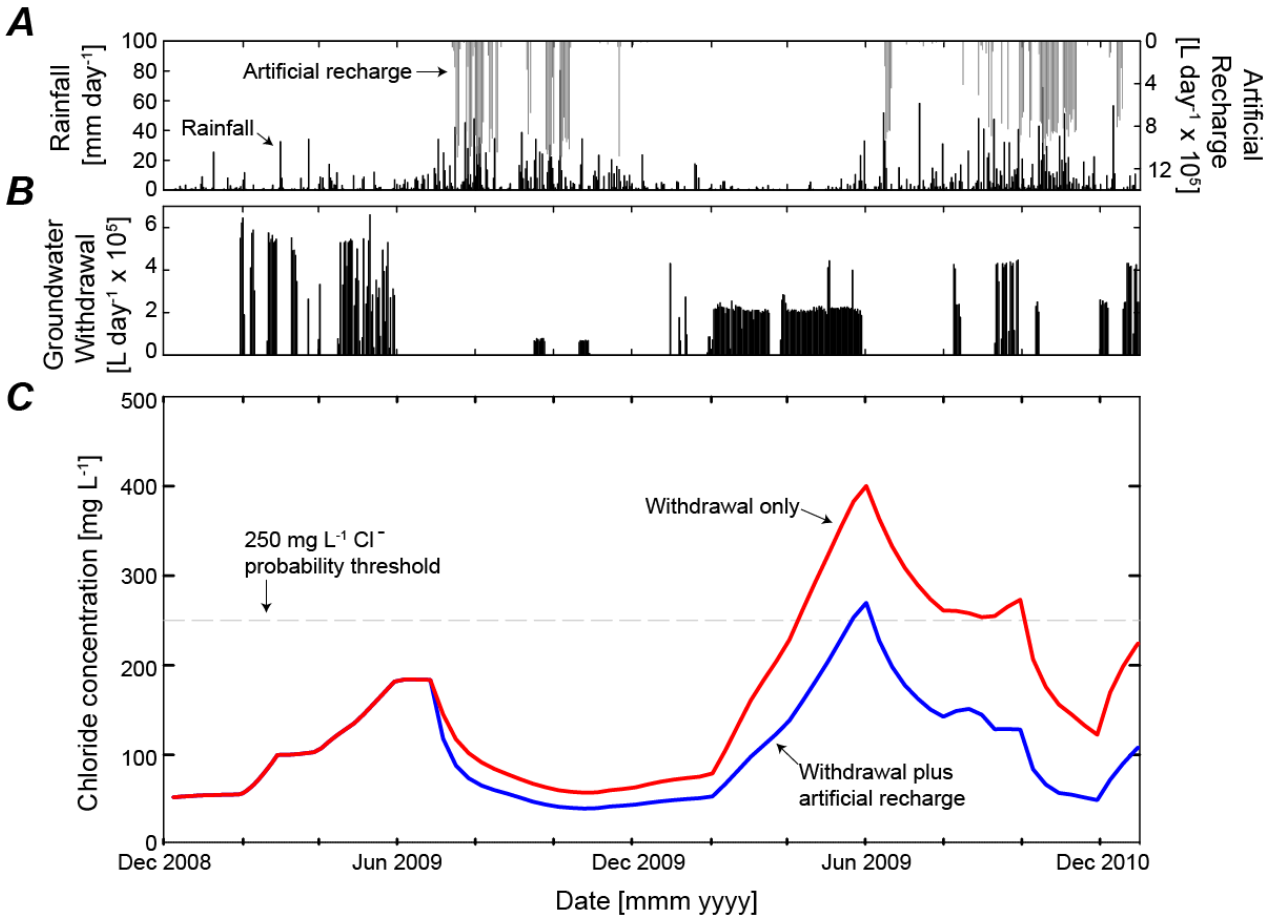

Figure 69. Time series showing impacts of the December 2008 seawater flooding event on groundwater and responses to various management options. A. Rainfall (black) and artificial recharge (gray). B. Groundwater withdrawals. C. Simulated chloride concentrations due to withdrawal only (red) and withdrawal plus artificial recharge (blue) relative to the 250 milligrams/liter potability threshold.

3.9.3.2 Impact of artificial recharge on recovery

Artificial freshwater recharge to the freshwater lens is an obvious choice for mitigating the effects of seawater flooding after the seawater has infiltrated into the freshwater lens. On Roi, water managers began discharging surplus water from the rain catchment system to the ground

surface above the skimming well in July 2009, about 7 months after the overwash and flooding event. In 2010, artificial recharge was carried out from June through December, and the practice has continued during subsequent rainy periods through 2016.

Comparison of results without artificial recharge (FIGURE 69) with the results of the managed recharge scenario (with full monthly recharge estimates that include artificial recharge) confirms that the salinity of water withdrawn by the skimming well is higher without artificial recharge, in which case the simulated Cl^- concentration in skimming-well water averages about 500 milligrams/liter higher from July 2009 through the end of 2010. Even during January-May 2010, when recharge is the same in both simulations, the skimming-well water has Cl^- concentrations about 520 milligrams/liter higher in the simulation without artificial recharge, indicating that the benefits of wet-season artificial recharge persist during the dry season. Without artificial recharge, the average Cl^- concentration of skimming-well water remains above the 250 milligrams/liter potability threshold for the entire 2-year simulation; in contrast, with artificial recharge, the simulated concentration is below this threshold for about 9 months.

3.9.3.3 Impact of long-term groundwater withdrawals on recovery

Groundwater withdrawal during the post-flooding recovery period might be expected to increase the salinity of water withdrawn from the skimming well because the withdrawal increases the mixing in the freshwater lens and captures more of the saline water from deeper in the transition zone. The effects of withdrawal become clear when comparing a zero-withdrawal simulation (FIGURE 69) with the managed-recovery simulation that uses monthly withdrawal. During February-June 2009, a period with intermittent withdrawal for the managed-recovery simulation, the simulated zero-withdrawal Cl^- concentration at the skimming-well location averages about 920 milligrams/liter lower, but both situations result in simulated concentrations significantly above potable levels. After the onset of wet-season rainfall and artificial recharge, the Cl^- concentrations in the zero-withdrawal scenario average about 90 milligrams/liter lower, even when no groundwater is withdrawn. However, Cl^- concentrations of skimming-well water for both cases remain below 250 milligrams/liter during this wet season. After the onset of sustained withdrawal in February 2010, Cl^- concentrations in the simulation with withdrawal increases to more than 770 milligrams/liter higher than in the zero-withdrawal simulation by the end of June 2010. These increases appear to be mainly due to saltwater entrainment from the transition zone, brought on by the period of sustained withdrawal during the dry season; these are apparently not a result of the saltwater flooding in the previous year. Thus, avoidance of post-flooding groundwater withdrawal generally improves the speed of recovery of water quality in the lens, irrespective of other hydrologic factors.

3.9.3.4 Impact of overwash timing (wet season versus dry season) on recovery

The December 2008 overwash and flooding event was followed by a dry season with more than five months (January–May 2009) of very low rainfall (average 1.8 millimeters/day) and no artificial recharge (FIGURE 63). Had the flooding event instead occurred at the beginning of a wet season, the following five months (July-November 2009) would have had both abundant rainfall (average 8.3 millimeters/day) and artificial recharge (average 265,000 liters/day) enhancing the recovery of the freshwater lens. The simulated salinity evolution in the case where the wet-season recharge (including artificial recharge) begins immediately after the flooding event is shown in FIGURE 70. After the July 2009 recharge is applied in the model, the simulated Cl^-

concentration of skimming-well water undergoes a rapid decrease over 2.5 months to below 250 milligrams/liter. In contrast, the simulated Cl^- concentration of skimming-well water drops below 250 milligrams/liter only after 8 months (about 5.5 months slower), during the observed recovery that occurred during the dry season. This indicates that a wet-season flooding event results in lower salinities and potable pumped water for the latter 5 months of the season. However, during the following season, the outcomes are reversed as pumping causes the salinities to rise during the dry season. This indicates that during a rainy season, freshwater lens salinities tend to be lower irrespective of when a flood has occurred.

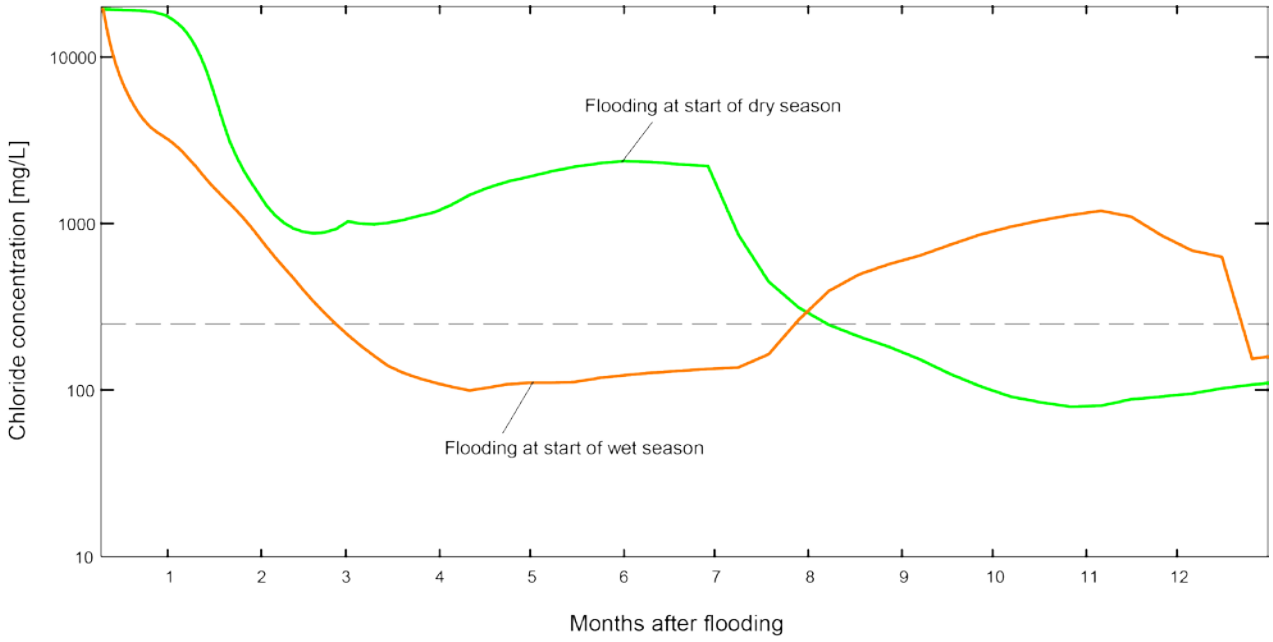

Figure 70. Time series plot showing comparison of simulations with seawater overwash and flooding at start of dry season (green line) and at start of wet season (orange line) relative to the 250 milligrams/liter potability threshold.

3.9.4 SUTRA Simulations of the Overall Impact of Artificial Recharge on Water Quality

The application of artificial recharge of rainfall water collected from impervious surfaces allows the freshwater lens to maintain lower salinity values. Simulations of freshwater lens conditions using 2009-2010 recharge and withdrawal conditions (with no seawater flooding), but with and without artificial recharge, demonstrate the impact of artificial recharge on the freshwater lens (FIGURE 69). After artificial recharge begins in July 2009 and through the end of 2010, the simulated Cl^- concentrations of the water withdrawn from the skimming well average about 70 milligrams/liter lower than without artificial recharge. Without artificial recharge, the simulated average Cl^- concentration is above 250 milligrams/liter for almost 6 months during 2010 due to sustained groundwater withdrawal. With artificial recharge, the salinity is above this potability threshold for only a few days during the period of greatest withdrawal in May and June. The effect of the artificial recharge is persistent, as the withdrawn-water Cl^- concentration is about 90 milligrams/liter lower, even during the 7 months in which artificial recharge is not applied.

Thus, artificial recharge using captured rainwater has a clear benefit: lowering the salinity of pumped groundwater no matter when or under which conditions it is applied.

3.9.5 Findings from the 2008 Seawater Overwash and Flooding Event

- The time variability of rainfall recharge is an important factor controlling post-flood recovery of salinities, especially with regards to the long-term evolution, because the duration of salinization is the greatest concern regarding water supply.
- Avoidance of long-term groundwater withdrawal generally improves the speed of recovery of the freshwater lens' water quality, irrespective of other hydrologic factors.
- The seasonal timing of a seawater flooding event does impact the length of the recovery process; during rainy seasons, lens salinities tend to be lower regardless of whether a flood has occurred.
- The salinity of water withdrawn by the skimming well is higher without artificial recharge, irrespective of other hydrologic conditions. Artificial recharge of captured rainwater provides a clear benefit, lowering the salinity of pumped groundwater no matter when or under which conditions it is applied.
- Even for an island water supply that is not impacted by a seawater-flooding event, artificial recharge, to enhance the freshwater lens water quality, provides a significant benefit in decreasing pumped groundwater salinity. The benefit of the wet-season artificial recharge persists through the following dry season, when no artificial recharge is applied.

3.9.6 SUTRA Simulations of the Fate of Island Groundwater Supply with Sea-level Rise

Considering the possibility of future sea-level rise of up to +2.9 meters, it might reasonably be expected that low-level islands will either disappear entirely (most of Roi-Namur is at or below 2 meters elevation) or, at least, will reduce in area. Fresh groundwater supply will diminish in quantity due to reduced area of natural rainfall infiltration and lateral encroachment of seawater in the subsurface, which will reduce the volume of the freshwater lens and will make pumping of low salinity water even more difficult than under present sea-level conditions. Furthermore, for a given magnitude of overwash event, the impact will increase because higher sea levels will allow more wave energy to impact the shoreline, thus increasing the potential for flooding to reach the island interior.

The future impacts of seawater overwash and subsequent flooding on the freshwater lens were investigated using the SUTRA groundwater model. Instead of employing the approximate location of the ponded seawater following the 2008 flood as the source of saline infiltration, this evaluation uses a situation with estimated future recharge, various stages of higher sea level, and estimated saltwater ponding distributed over most of the surface of Roi. The potability evolution was simulated following annual overwash events, with the same groundwater pumping distribution as occurred in the years following the 2008 flooding event (FIGURE 63).

Future recharge (2080-2099) was estimated in the same way as the historic recharge (2000-2012). However, the values of rainfall and ET used to compute the estimate were based on future climate modeling of the RCP8.5 scenario using the following steps:

- Modeled top 5 GCM climate data were processed for historic (1990-2009) and future (2080-2099, RCP8.5) conditions.

- These processed future climate model data was used to compute projected mean monthly change factors for rainfall amount, number of rain days, and reference ET for Roi.
- Sets of daily rainfall fragments were created using the processed modeled climate data. The water-budget model for historic conditions was re-run and the processed modeled climate fragment sets were used to disaggregate observed monthly rainfall into daily rainfall.
- Future rainfall (2080-2099) was estimated using an altered time series of observed daily rainfall. The altered time series was created using the method outlined in Arnell and Reynard (1996) and accounted for changes in rainfall amounts and number of rain days per month.
- Future reference ET was estimated by multiplying the observed reference ET and the mean monthly change factor.
- A linear regression was used to estimate the amount of water for future conditions applied to the ground as artificial recharge near the freshwater lens.
- The SUTRA model and projected ET and rainfall datasets were used to compute recharge for future conditions.

Compared with recharge for historic conditions, recharge for future conditions was, on average, 2 percent less for the dry season, 12 percent less for the wet season, and 10 percent less annually.

Future sea levels and worst-case annual seawater flooding scenarios were estimated as described in the wave-driven flood modeling section. Scenarios of +0.4, +0.8, +1.2, and +1.6 meters of sea-level rise were simulated, corresponding to the IPCC-AR5 RCP8.5 estimates of sea-level rise at Roi-Namur in 2035, 2055, and 2075, respectively. The +1.6-meter sea-level rise scenario corresponds to the IPCC-AR5 RCP8.5+ice sheet collapse scenario estimates for 2075. For each scenario, the coastline of the island was reduced accordingly based on island topography and then the forecasted maximum seawater flooding distribution was applied to the model for a 2-day period each year. The response of the freshwater lens was evaluated by comparing the time-series plots of the salinity of water at the skimming well as the freshwater lens recovered. Some simulations were carried out for several years after a single overwash event so that the lens recovery during different scenarios and mitigation strategies could be evaluated. Finally, simulations of 3 consecutive years having annual overwash and flooding events during dry, average, and wet recharge conditions with representative withdrawal patterns for each year were completed.

Simulation analyses indicate that due to the berm on the north shoreline of Roi-Namur, even with increase in sea level of 1.6 meters, the salinity of pumped groundwater would be only mildly affected and would remain potable provided that annual seawater flooding did not occur (not shown). However, the island is expected to be subjected to annual overwash events in which seawater overtops the berm, and the extent of resultant inland flooding will increase with higher sea levels (FIGURE 45). Simulation analyses of overwash events for increased sea levels indicate that the freshwater supply will be more adversely impacted as sea level increases. The salinity of post-flood groundwater will become greater and the recovery time to potable water conditions at the well will increase at progressively higher sea-level stages. At the +1.6-meter sea-level rise stage, parts of the interior of Roi become saturated to the ground surface as the freshwater lens floats increasing higher relative to the ground surface. These areas were simulated as freshwater

bodies that lost water to evaporation, resulting in even higher salinities in the pumped water during the recovery period.

A simulation of a three-year period (dry, average, and wet years with representative pumping) at the +0.4-meter sea-level rise scenario (equal to 2035 for the RCP8.5 scenario) indicates that an annual cycle of seawater flooding will result in water at the skimming well that is continually above the 250-mg/L potability threshold, assuming artificial recharge is not applied at any time during the year (FIGURE 72). Therefore, the skimming well would not be able to provide any potable water even during wet years by 2035 due to the annual seawater flooding. Simulations with higher sea levels and larger volumes of annual seawater flooding, as expected, show even higher concentrations of water at the skimming well throughout the year.

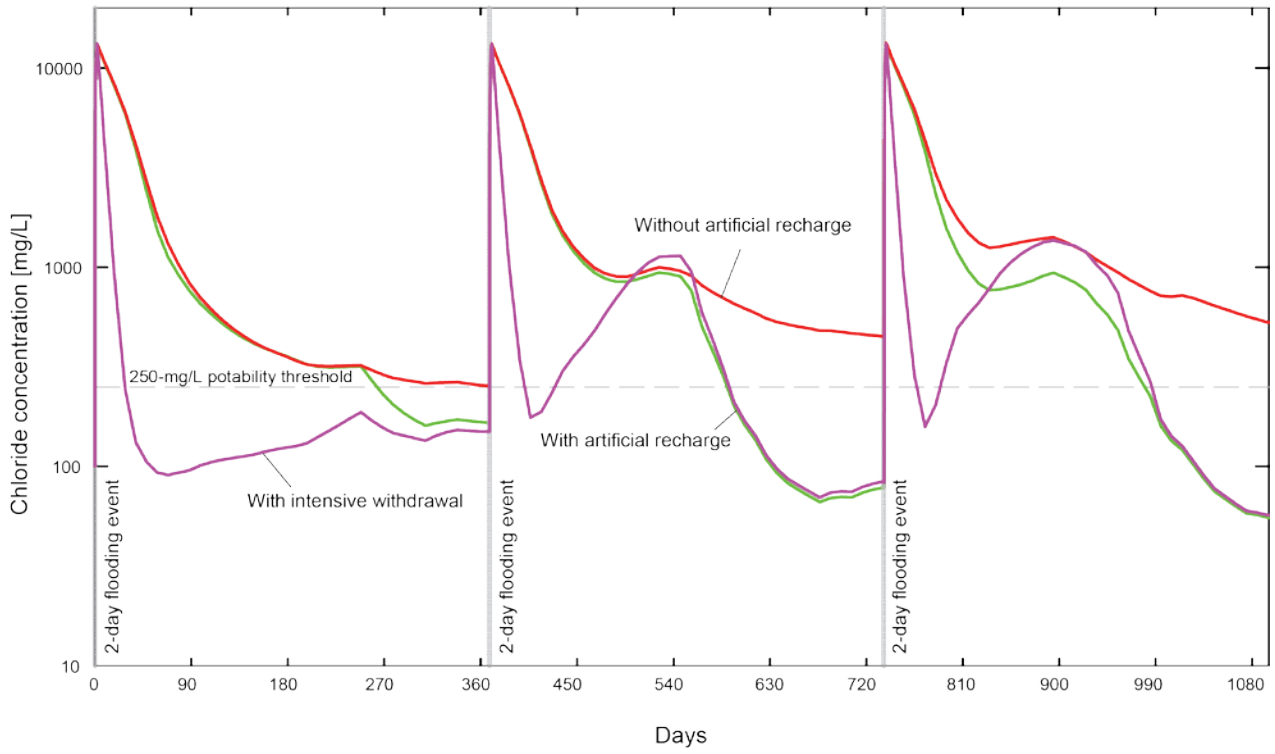

Figure 71. Time series showing the impact of annual wave-driven flooding events on groundwater potability over three years. Plot shows the evolution of chloride concentrations without artificial recharge (red), with artificial recharge (green), and with intensive withdrawal (purple) relative to the 250 milligrams/liter potability threshold.

3.10 Evaluation of Management Strategies

Based on understanding of the reasons for the measured response of the Roi groundwater potability to seawater flooding and of groundwater dynamics, several practical management/mitigation alternatives are evaluated. These SUTRA simulations provide insight into the effectiveness of the various simulated management and mitigation alternatives.

3.10.1 Artificial recharge

This is a mitigation intervention where excess catchment rainwater is used to recharge the aquifer and help to decrease the salinity in the freshwater lens (FIGURE 72). If the current practice of using excess catchment water to recharge the freshwater lens is continued, as has been done since 2009, simulations using future recharge estimates indicate that the freshwater lens will be able to supply water with Cl^- concentrations below the potability threshold, for at least part of each year, despite the expected annual seawater flooding (FIGURE 45). Typically, the months of highest rainfall would produce the most excess water available for artificial recharge and conversely these would be the months with the least groundwater withdrawal. The concentration of water in the skimming well decreases to below the potability limit during these months, whereas in the simulations without artificial recharge, the concentrations remain well above the potability limit.

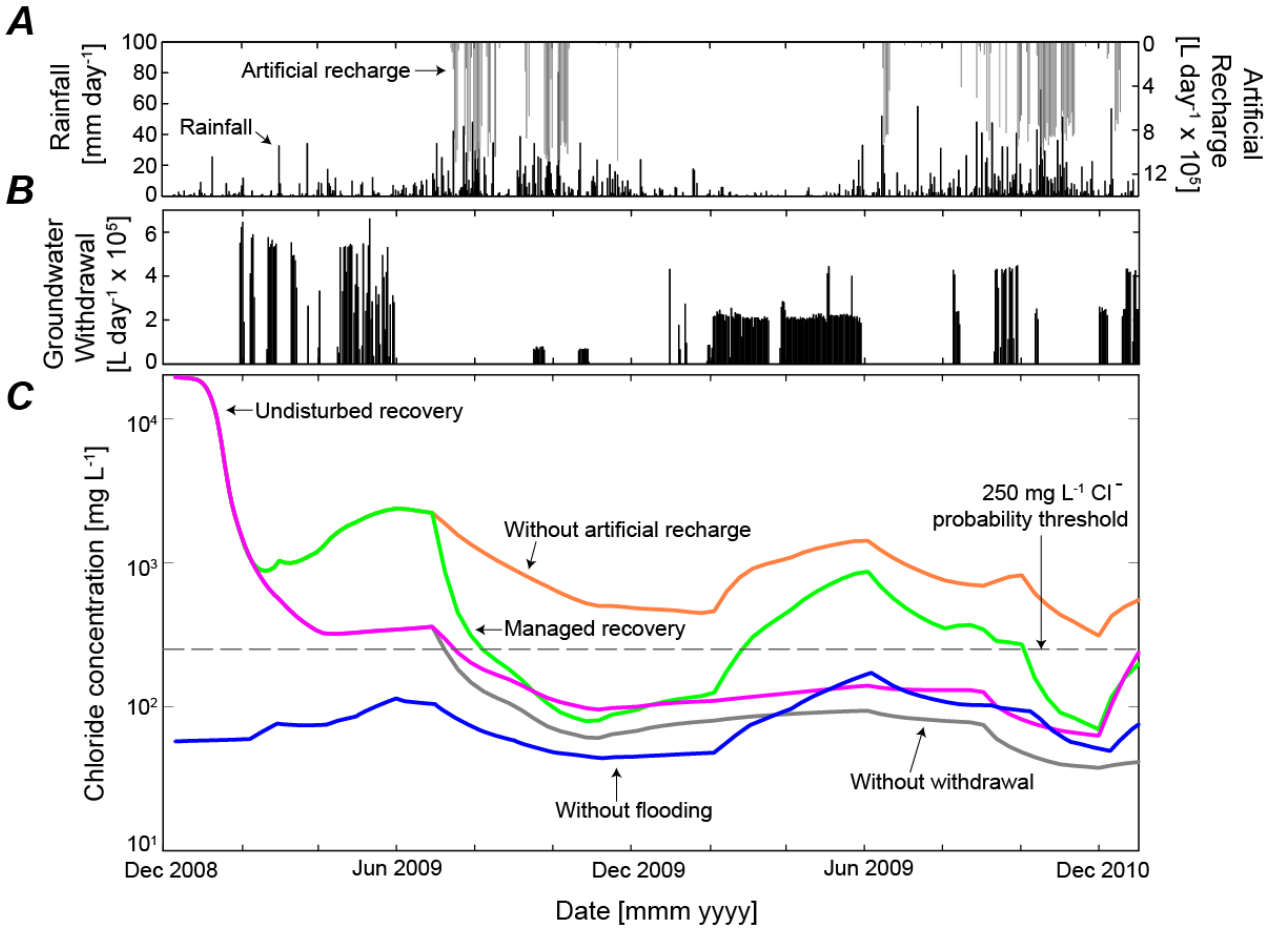

Figure 72. Time series showing impacts of the December 2008 seawater flooding event on groundwater and responses to various management options. A. Rainfall (black) and artificial recharge (gray). B. Groundwater withdrawals. C. Simulated chloride concentrations with undisturbed recovery (magenta line), with managed recovery (green line), without artificial recharge (orange line), without withdrawal (gray line), and without overwash and flooding (blue line). Managed recovery includes monthly recharge, monthly withdrawal, and artificial recharge relative to the 250 milligrams/liter potability threshold.

3.10.2 SUTRA Simulations of Intensive Post-overwash Pumping

This is a mitigation intervention involving intensive pumping of the water supply well immediately following the flooding event to remove some saltwater that has infiltrated the aquifer in the region of the well (FIGURE 72). It is found that this intervention is successful when pumping is done beginning immediately after cessation of the flooding event, with relatively intensive pumping (4.5-7.6 x 10^5 liters/day; 450-760 meters^3/day) for 5 to 20 days. Intensive pumping for longer than about 20 days to try to remove more infiltrated seawater causes upconing of the transition-zone seawater, an undesirable outcome even when no overwash has occurred. Thus the intensive pumping can only be done for a short period.

The pumping removes the infiltrated seawater adjacent to and just below the well and simultaneously impacts the variable-density flow field, causing some of the remaining nearby infiltrated seawater to move downward toward the transition zone at the bottom of the freshwater lens faster. This results in short-term and long-term improvements in pumped water quality at the skimming well with Cl^- concentrations within a month post-flood well below the potability limit of 250 milligrams/liter. Pumping 20-40 percent of the volume of seawater that would infiltrate the well capture-zone area, over 5 to 10 days works best for Roi. In the months following the overwash, pumped-water salinity increases depending on the amount of additional withdrawal for consumptive needs. This is due to seawater that infiltrates at a distance from the well (laterally and below the well), which was not removed by the intensive post-flood pumping, finally reaching the well in a diluted form. When the skimming well is not pumped heavily, the salinity at the well increases gradually, but when pumping rates increase, the salinity increases and sometimes surpasses the level expected without the intensive pumping mitigation (FIGURE 71).

3.10.3 SUTRA Simulations of a Levee with a Subsurface Wall

Building a levee or dike on the ocean side of the island (stretching from the north end of the runway to the northwestern-most point) to avoid overwash entirely for most overwash events is an obvious preventative measure that, whenever successful, totally avoids seawater flooding on the island surface. Adding a subsurface impermeable wall below the levee would block seawater from entering the aquifer in the subsurface and would ‘dam’ the inland freshwater where it would otherwise exit to the sea. Simulation analysis shows that, even without a flood, the subsurface barrier (extending 10 meters deep to the low-permeability geologic unit) increases the freshwater-lens thickness, with concomitant improvements in water quality at the supply well. Further, should the levee be breached during a storm event, with resultant inland seawater flooding, the thicker freshwater lens provides lower salinity at the water-supply well and shorter recovery times to potable well water.

3.10.4 SUTRA Simulations of an Infiltration Barrier within the Well Capture Zone

This preventive measure involves paving the ground surface (or laying an impermeable fabric or barrier) in the low-elevation region around the skimming well that corresponds approximately with the well’s capture zone. This would prevent seawater infiltration in the capture-zone area, which on Roi is typically flooded during an overwash event. The seawater that ponds on this barrier would be pumped out to sea once the overwash event ends. The paving requires vertical ports that allow natural and artificial recharge to pass through it during non-overwash periods. These ports must be closed prior to an expected overwash event.

Obviously, reducing seawater infiltration into the freshwater lens will have great benefits in reducing the impact of overwash on water-supply potability. This is borne out by simulation analysis of this management alternative, which demonstrates that the salinity of water pumped immediately after overwash is minimally impacted by the event, so that the well can continue to be used for water supply. In the weeks and months following an overwash, seawater that infiltrates in areas on Roi some distance from the paved well area (i.e., not within the well's capture zone) descends through the freshwater lens to the transition zone by density-driven flow, while mixing with freshwater-lens groundwater. Because this saline infiltration is not within the well's capture zone, it unobtrusively joins with the freshwater-saltwater transition zone and/or discharges to the coast within the freshwater lens, without impacting the potability of water pumped from the well.

3.10.5 Summary of Mitigation Alternative Analyses

Each of the considered management/mitigation alternatives can provide some improvement to well-water potability, either in terms of decreasing the recovery time to reach potability following a seawater flood, or improving potability during normal non-overwash periods on Roi. This has been demonstrated for simple implementations of each alternative; however, it might be expected that further improvements are possible when the engineering details of implementation are optimized.

For the post-flood pumping intervention, it is found that pumping heavily for a short period following the flood can significantly reduce the impact of flooding on potability for an extended post-overwash period. Building a levee obviously reduces the frequency of overwash events, but when levee breach occurs during potential overwash periods, the concomitant effect of a subsurface wall permanently increasing the thickness of the freshwater lens (providing better water quality during non-flood periods) also helps to reduce the post-overwash potability and recovery period. The management option of paving in the well area (with ports to allow artificial recharge that can be closed prior to overwash events) reduces overwash salinization of the aquifer nearest the well, providing a direct benefit to post-flood water quality.

4 Discussion

4.1 Implications of Climate Change Impacts to Roi-Namur and Kwajalein Atoll

The future climate simulation developed here (FIGURES 29-30 and TABLES 9-10) project that deep-water wave heights and wind speeds around Kwajalein Atoll will decrease slightly, resulting in a small decrease in the magnitude and frequency of the threat to marine operations. The decrease in the frequency of tropical storms and typhoons (FIGURES 48-51) will also reduce the frequency of weather-based disruptions to marine and terrestrial operations, although the slight increase in intensity of typhoons may result in greater impact of a given storm despite their much less frequent occurrence. The projected slight decrease in rainfall will cause a small reduction in freshwater availability. The projection of fewer but stronger TCs poses a number of policy implications for military planning, especially when considered together with other climate threats such as changing rainfall patterns and rising sea levels. On the one hand, less frequent typhoons are likely to be a positive consequence of greenhouse warming; however, the projection of stronger storms offsets any gains of fewer storms. Because TC damage potential increases logarithmically with wind speed, small increases in intensity of the strongest storms are likely to cause catastrophic consequences to affected islands (e.g., a 5-meters/second increase of a Category 4 storm results in nearly doubling the potential wind-related damage, thereby prolonging post-storm economic distress).

The potential effects of the meteorologic changes, however, will likely be insignificant in comparison to the impact of projected increases in sea level in the region (Hall et al., 2016). These increases in sea level will reduce deep-water wave breaking and energy dissipation at the reef crest, resulting in more IC- and IG-band wave energy propagating to the islands' shoreline and greater wave-driven runup and island flooding (FIGURE 39). Projected increases in coral bleaching events (Hoegh-Guldberg, 1999) and ocean acidification (Pandolfi et al., 2011) that reduce live coral coverage will result in reduced hydrodynamic roughness of the reefs. And this, in turn, will cause even greater wave-driven runup and island flooding.

While the island of Roi-Namur will not be significantly negatively impacted solely by sea-level rise inundation until sea level is 1.6 meters higher than at present (FIGURE 73), the impact of sea-level rise inundation combined with annual wave-driven flooding will begin to significantly negatively impact Roi-Namur when mean sea level (MSL) is 0.4 meters higher than at present. At this point, without active management measures, the annual amount of seawater flooded onto the island during storms will be of sufficient volume to make the groundwater non-potable year-round (FIGURE 72). At this level of sea-level rise, much of the isthmus that connects Roi and Namur will be flooded annually, negatively impacting the facilities in those locations (FIGURE 74). Thus the "tipping point" – the time at which potable groundwater on Roi-Namur will be unavailable – is projected to be reached before 2035 for the RCP8.5+icesheet collapse climate scenario, the 2030-2040 time frame for the RCP8.5 climate scenario, and 2055-2065 for the RCP4.5 scenario. The 10-year ranges in these time frames are because, in any given year, ENSO events can cause sea level at Kwajalein to go up or down 0.2 meters for a few months (Chowdhury et al., 2007).

Although active management practices such as post-flood short-term intensive withdrawal and artificial recharge will allow for 3-4 months of potable groundwater on Roi-Namur during the rainy season (FIGURE 72) at higher sea levels, it is not clear as to the sustainability of such operations over the long term with increasing frequency and intensity of wave-driven flooding and

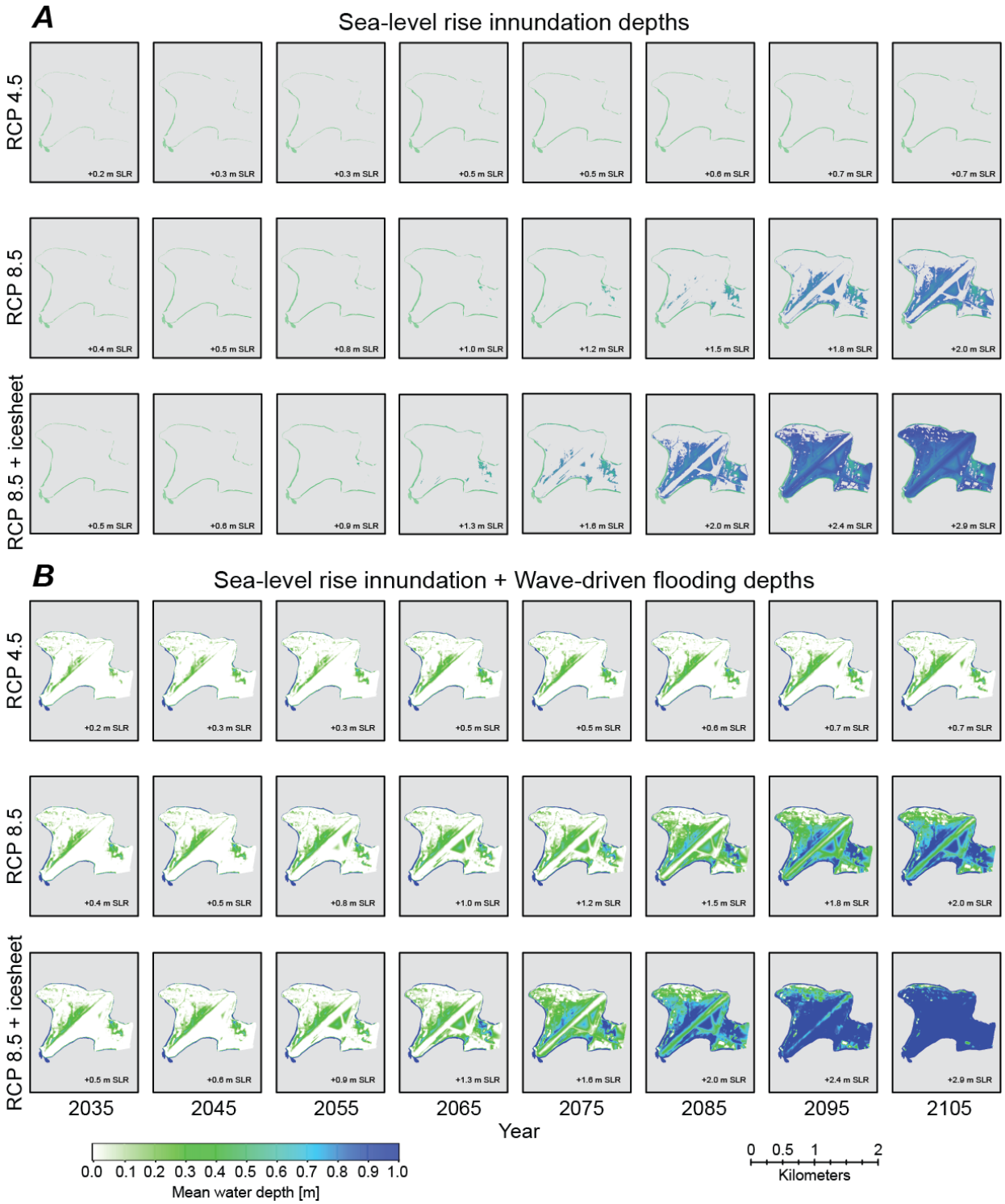

Figure 73. Maps showing the projected variation in seawater depth over the current island through time for different forcing conditions and climate scenarios. A. Water depths due to only sea-level rise inundation. B. Water depths due to sea-level rise inundation and annual wave-driven flooding. Columns denote years, whereas rows denote different climate scenarios. The years are approximate, and due to El Nino-induced annual sea-level variability, these should be considered ±5 years.

island overwash. Because many of the adjacent islands on Kwajalein Atoll that are inhabited and/or have DOD facilities (Ebeye, Ennylabegan, Ebadon, Ennubirr, Gagan, Gellinam, Gugeegue, Illeginni, Legan, Meck, Omelek) do not have pumping systems and large freshwater storage capacity, they, too, will reach their potable groundwater "tipping point", before 2035 for the RCP8.5+icesheet collapse climate scenario, the 2030-2040 time frame for the RCP8.5 climate scenario, and 2055-2065 for the RCP4.5 scenario.

Even if the groundwater supply was supplemented or replaced with another source (e.g., desalinization or delivery of freshwater from elsewhere), the annual wave-driven flooding will disrupt operations on Roi-Namur (FIGURE 74). When mean sea level is 1.0 m higher than at

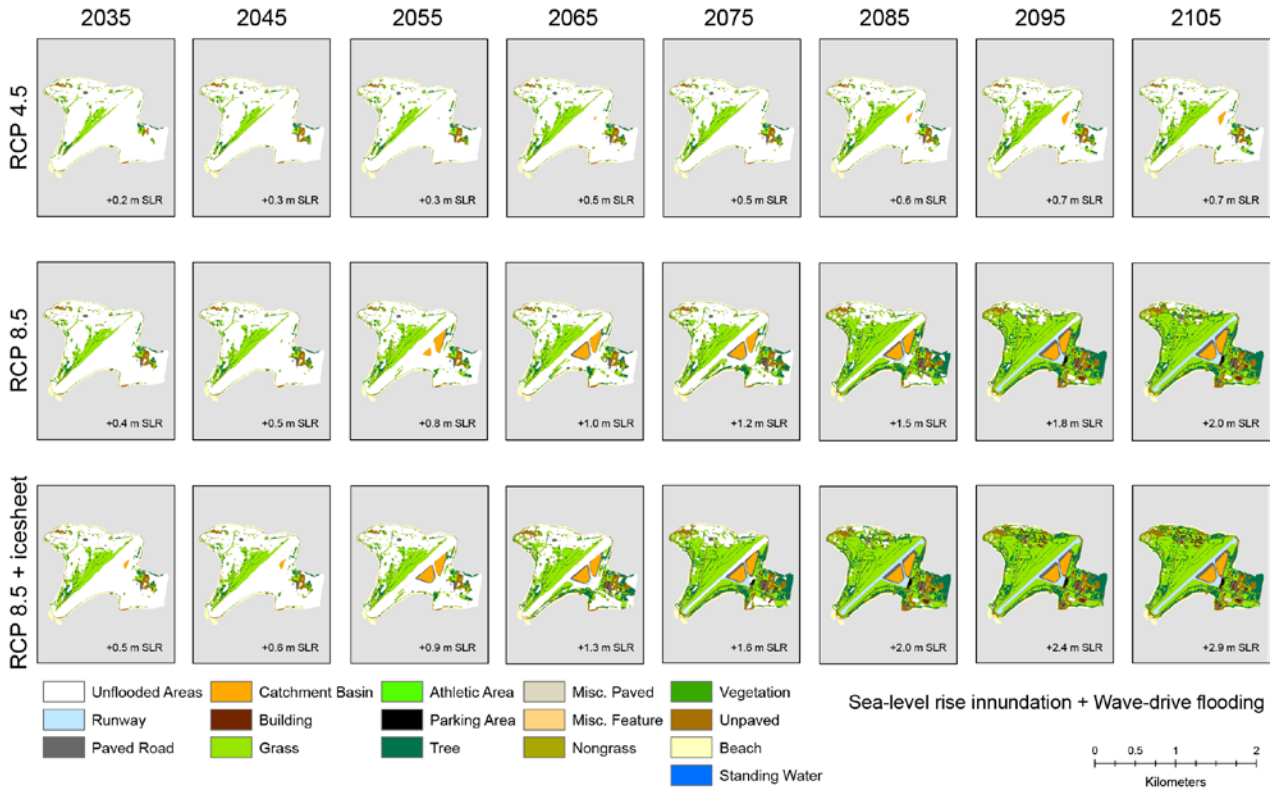

Figure 74. Maps showing the projected land cover classes on the current island annually impacted due to sea-level rise inundation and annual wave-driven flooding for different forcing conditions and climate scenarios. Columns denote years, whereas rows denote different climate scenarios. The years are approximate, and due to El Nino-induced annual sea-level variability, these should be considered ±5 years.

present due to sea-level rise, at least half of the island is projected to be flooded annually; the areas that will not experience annual flooding include just the runway, the southern portion of the isthmus and associated infrastructure, and the northern portion of Roi where the housing is located. This "tipping point" – at which the majority of Roi's land would be flooded annually – is projected to be reached in the 2055-2065 time frame for the RCP8.5+icesheet collapse climate scenario, the 2060-2070 time frame for the RCP8.5 climate scenario, and sometime after 2105 for the RCP4.5 scenario (FIGURE 75). More than 90 percent of the island's surface is projected to be

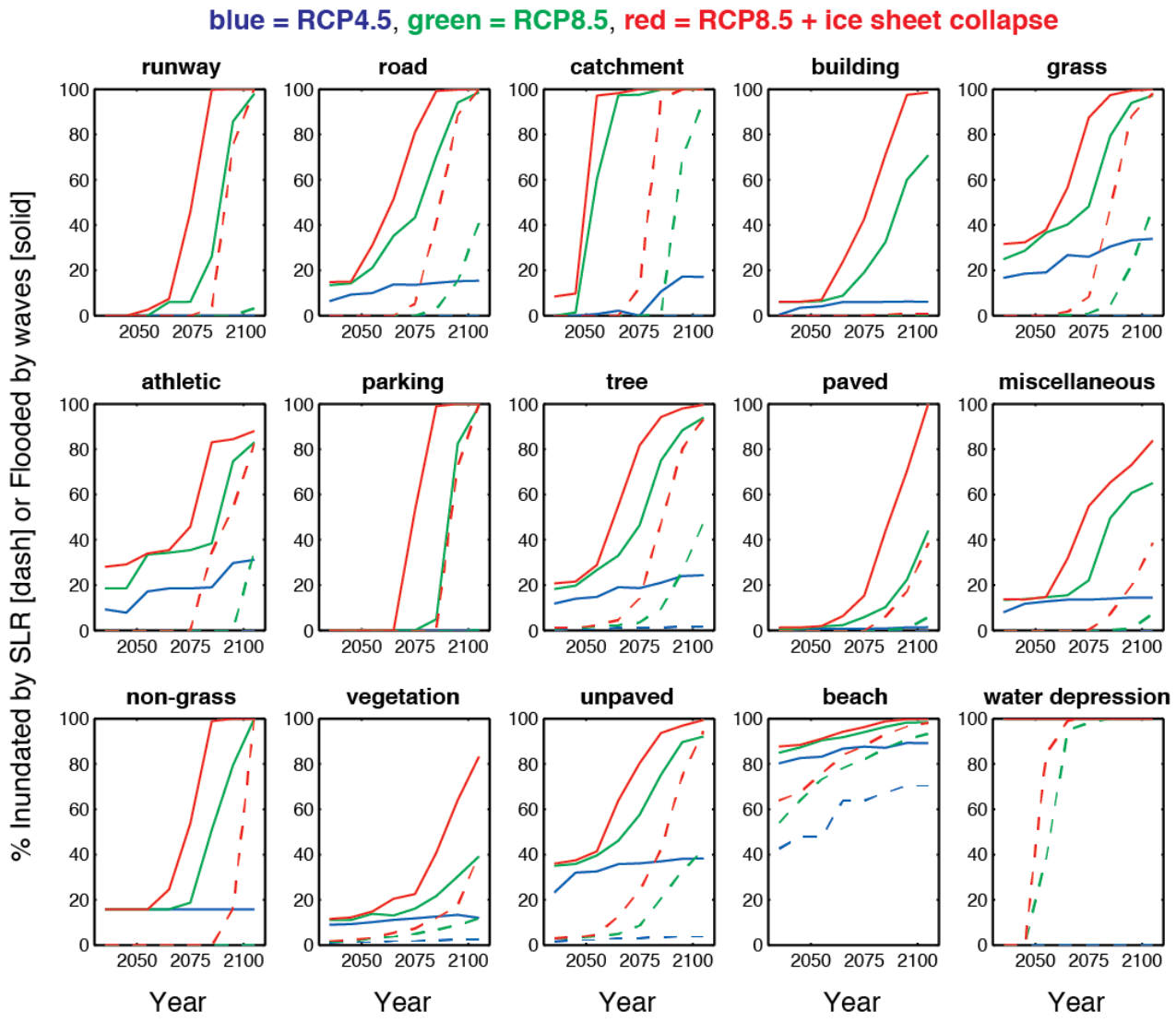

Figure 75. Time series plots showing the projected land cover classes on the current island impacted due to sea-level rise inundation and annual wave-driven flooding through time for different forcing conditions and climate scenarios. Percentage of areas solely inundated due to sea-level rise are denoted by dashed lines, whereas the areas impacted due to sea-level rise inundation and annual wave-driven flooding are denoted by solid lines. Climate scenarios RCP4.5, RCP8.5, and RCP8.5 plus ice sheet collapse are denoted by blue, green, and red lines, respectively. The years are approximate, and due to ENSO-induced annual sea-level variability, these should be considered ±5 years.

flooded annually when mean sea level is 1.8 m higher than present due to sea-level rise, which is projected to be reached in the 2075-2085 time frame for the RCP8.5+icesheet collapse climate scenario and the 2090-2100 time frame for the RCP8.5 climate scenario. Many of the adjacent islands on Kwajalein Atoll that are inhabited and/or have DOD facilities (Ebeye, Ennylabegan, Ebadon, Ennubirr, Gagan, Gellinam, Gugeegue, Illeginni, Legan, Meck, Omelek) will face a similar fate.

Considering the impacts of all the evaluated key hydrologic controls, it is clear that the key to rapid recovery of the freshwater lens as a potable water supply on low-elevation sandy islands of the Roi-Namur type (atoll and barrier islands) is the total post-flood recharge; more recharge, whether natural or artificial, decreases the duration of resource salinization. Furthermore, in situations where the rainfall recharge following seawater overwash events is limited (either occasionally or on a permanent basis), recharge enhancement by artificial recharge of freshwater is the most effective management/mitigation intervention possible for increasing freshwater supply and for shortening the post-flood length of time needed for pumped groundwater to become potable again.

4.2 Implications of Climate-change Impacts to Atolls Globally

Past efforts to predict how long before atolls become inhabitable have relied solely on passive inundation modeling, and have produced results suggesting that many atoll islands may remain suitable for human habitation for 100-150 years (Roy and Connell, 1991; Dickinson, 2009). The results presented here, however, predict greater impact, especially at higher sea-level rise scenarios, when wave-driven flooding is taken into account. These results indicate that low-lying atoll islands will be annually flooded by seawater sooner in the future than predicted by the previous efforts that only took sea-level rise inundation into account. Not only will such flooding impact terrestrial infrastructure and habitats, but more importantly, it will make the limited freshwater resources non-potable and thus may force inhabitants relying on groundwater to abandon their island-nations in decades, rather than centuries, as has been previously suggested. Based on the limited topographic (Roy and Connell, 1991; Dickinson, 2004; Woodroffe, 2008; Dickinson, 2009; Fletcher and Richmond, 2010; Hoeke et al., 2013; Storlazzi et al., 2015b) and hydrogeologic (Underwood et al., 1992; Falkland, 1994; Hunt, 1996; Anthony, 2007; Hunt, 2007; Peterson, 2007; Bailey et al., 2010; Terry and Falkland, 2010) data available for the region, the size and elevation of Roi-Namur is characteristic of many, if not most, of the rest of the atolls in the world's oceans. Assuming this is the case, then the "tipping point", at which point potable groundwater on the majority of atoll islands will be unavailable, is projected to be reached by the 2030s for the RCP8.5+icesheet collapse climate scenario, by the 2040s for the RCP8.5 climate scenario, and 2060s for the RCP4.5 scenario. For those islands where groundwater is not a limiting resource (due to rainfall capture, desalinization facilities, transport from elsewhere, etc.), the "tipping point" at which the majority of the atoll islands would be flooded annually is projected to be reached in the 2060s for the RCP8.5+icesheet collapse climate scenario, the 2070s time frame for the RCP8.5 climate scenario, and sometime after the 2110s for the RCP4.5 scenario. These findings have relevance not only to current or decommissioned DOD facilities on Pacific atolls (Kwajalein, Wake, Johnston, Bikini, and Enewetak Atolls), but those utilized by DOD (Diego Garcia in the British Indian Ocean Territory), US Minor Outlying Islands (Baker, Howland, and Jarvis Islands) and those under the US defense umbrella (Republic of the Marshall Islands and the Federated States of Micronesia). Together, these results provide an improved understanding of the planning and management strategies necessary to protect infrastructure and natural resources on low-lying atoll islands globally in the face of future climate change.

4.3 Implications of Climate-change Impacts to Coral Reef-lined Shorelines Globally

The results presented herein indicate that coasts fronted by relatively narrow reefs with steep fore reef slopes and deeper, smoother reef flats are expected to experience the greatest coastal flooding. Coastal flooding will increase with sea-level rise, higher waves, and coral degradation, all of which are expected to occur in parts of the world's tropical oceans due to climate change. Rising sea levels and climate change will therefore have a significant negative impact on the ability of coral reefs to mitigate the effects of coastal hazards in the future. Although the focus of the effort presented here was on low-lying atoll islands, there is high relevance of the findings presented here to other tropical, reef-lined islands. Because most high-elevation tropical islands, such as those found in the Hawaiian, Mariana, American Samoa, and US Virgin Island chains, receive sufficient rainfall on their mountains, wave-driven flooding will not threaten their freshwater resources; however, the majority of these islands' housing and critical infrastructure (ports, roads, airports, hospitals, power plants, water treatment plants, etc.) are located within a few meters of current sea level and thus confront threats similar to those faced by atolls resulting from increased wave-driven flooding due to sea-level rise. The results presented here, therefore, provide coastal managers an estimate of the effect of different oceanographic, geomorphic, geologic, and hydrologic characteristics on potential coastal hazards caused by wave-driven flooding of coral reef-lined coasts globally and how these may change in the future.

4.4 Potential Next Steps

Most future climate projections (e.g., IPCC-AR5 report) forecast increased rates of sea-level rise and decreased precipitation in most of the Tropics. As atoll islands are quite porous, a higher sea level implies a shallower aquifer and facilitates an increased frequency of wave overwash relative to present. Combined with less rainfall, freshwater aquifers will take longer to recover. Because of this and the findings of RC-2334 listed above, it appears that the focus for additional follow-on studies could be constrained to primarily focus on storm wave-induced flooding, which is the primary driver of impacts to coastal infrastructure, freshwater resources, agriculture, and habitats for threatened and endangered species. Here we detail three proposed avenues of future research to build on the results of RC-2334, along with approximate durations and costs.

4.4.1 Sea-level Rise Inundation and Wave-driven Flood Modeling of all Active DOD Coastal Assets on Pacific Islands: Future Projections and Development of a Real-time Warning System for Current Conditions

DOD has $10s of billions of coastal infrastructure and oversees coastal habitats for numerous threatened and endangered species on islands extending across 1000s of kilometers of the tropical Pacific Ocean that is becoming increasingly threatened due to climate change and sea-level rise. These coastal facilities on both low-lying (maximum elevations <4 meters) atolls and along the low-lying coastal fringes of high-elevation, volcanic islands are fronted by coral reefs ranging from coral habitat on insular slopes to fringing and barrier reefs to atolls. Such reef environments, with high bathymetric complexity and hydrodynamic roughness due to the presence of corals, result in complex wave and flow patterns that are not captured by most coastal

models developed for simple, relatively linear, low-slope sandy shorelines that typify the US Gulf and East Coasts. In RC-2334, we adapted one of the industry-standard coastal storm-driven flooding models, XBeach, for use in a coral reef environment at Kwajalein Atoll using field data on waves and water levels to calibrate and validate the model.

The next logical step would be to use the modified XBeach model developed for atoll reefs in RC-2334, and extend it to model the rest of the active DOD coastal sites in the tropical Pacific: western Guam, Mariana Islands (Naval Base Guam); Tinian Island, Commonwealth of the Northern Mariana Islands (CNMI, proposed site to move III Marine Expeditionary Force from Okinawa); Wake Island (Ronald Reagan Ballistic Missile Test Site); western Kauai, Hawaii (Pacific Missile Range Facility Barking Sands); southern Oahu, Hawaii (Naval Station Pearl Harbor), and eastern Oahu, Hawaii (Marine Corps Air Station Kaneohe); all sites currently have seamless topobathy digital elevation models (DEMs) upon which the models would be run. The new extreme water levels and meteorological forcing produced by recently-funded RC-2644 and DOD's Coastal Assessment Regional Scenario Working Group (Hall et al., 2016) sea-level rise scenarios could be used as boundary conditions. Six-month field deployments of wave/tide gauges, along the lines of those conducted in support of RC-2334, would be used to calibrate the XBeach model for new reef/coastal configurations: a barrier reef at Barking Sands, Kauai; a reef slope without a reef flat at Kaneohe, Oahu; and a harbor fronted by fringing reefs at Pearl Harbor, Oahu. These calibration and validation data would make it possible to more accurately model these and the other sites (Tinian Island, Naval Base Guam, etc.).

The goal would be to compute spatially- and temporally-explicit projections of annual wave-driven flooding of each of the sites for different climate-change scenarios, similar to what was developed here for Roi-Namur Island on Kwajalein Atoll for RC-2334. Such projections would be the basis for better ex-ante (before the event) planning of new investments in base infrastructure and developing coastal resiliency and/or adaptation actions. Furthermore, the feasibility of a real-time warning system that predicts the impact (extent of coastal flooding) as a function of offshore conditions (waves and water levels, which are already available from NOAA wave and tidal models provided by NWS marine forecasts) could be demonstrated for one site. This system will be achieved by storing the pre-computed projections of computed flooding in a Bayesian Network database and coupling this database to real-time predictions of offshore wave and water-level conditions. Such techniques have been developed previously for the U.S. East Coast and sites in Europe.

4.4.2 Sea-level Rise Inundation and Wave-driven Flood Modeling of Runit Island, Enewetak Atoll

Runit Island is part of Enewetak Atoll, which along with Bikini Atoll composed the former US Pacific Proving Grounds. As part of the clean-up of the atoll following the cessation of US nuclear weapons testing in the Pacific Proving Grounds, radioactive soil and debris were deposited by the US Defense Nuclear Agency in a 150-meter 'Cactus' crater on Runit Island and capped it with concrete; this containment cap is generally referred to as the "Runit Dome". Although recent surveys have shown the concrete Runit Dome is stable, island overwash events have been noted. Findings developed by RC-2334 project that such storm wave-driven overwash events will occur with increasing frequency in the coming decades, negatively impacting the concrete cap and its ability to contain long-lasting radionuclides from being released into the environment. Projections of when this might occur under different climate-change scenarios are necessary for planning mitigation and/or restoration efforts.

Because Enewetak Atoll has similar coral ecosystems as Kwajalein Atoll, there is no need to collect field data to calibrate and validate the hydrodynamic roughness needed to employ the modified XBeach numerical model, as developed here for Kwajalein, reducing potential costs. There is no existing topography and bathymetry of the island, however, and these data are critical for assessments and predictions using a physics-based numerical model. Thus the proposed effort would require a short field campaign to collect topographic and bathymetric field data to develop a seamless topographic and bathymetric digital elevation model of the island and adjacent reefs, along the lines of what was developed here for Roi-Namur Island on Kwajalein Atoll for RC-2334. This digital elevation model would be the foundational dataset for the proposed two-dimensional XBeach model for Runit Island. This model would, in turn, be used to project annual wave-driven flooding of the island and the Runit Dome along the lines of what was developed here in RC-2334. The data and analyses from this effort would be critical for planning efforts aimed at increasing the resilience of the structure under the stressors of climate change and sea-level rise, and also make it possible to better project how sea-level rise and climate change will impact smaller atoll systems, which characterize the majority of US and US-Affiliated atolls.

4.4.3 Sea-level Rise Inundation and Wave-driven Flood Modeling of Wake Island

The current study of RC-2334 focuses on the largest atoll in the northern hemisphere with a lagoon with a diameter of 100 kilometers, where there is relatively little impact of wave-driven setup that could drive increased flooding of the island from the lagoon side (versus the general flooding from the ocean-side of the island). Conversely, studies by Aucan et al. (2012) show that this process of high setup in the lagoon is prevalent to many smaller atolls, such as Wake and Johnston Atolls. Wake Island is part of the Ronald Reagan Ballistic Missile Defense Test Site, and there is already existing topography and bathymetry of the island, critical data for assessments and predictions using a numerical model; similarly, NOAA has already developed a spatially-varying habitat map for the island, further reducing potential costs. Because Wake Island is more than 1000 km north of Kwajalein, it has a different coral reef ecosystem, and although mapped, there are no field data to calibrate and validate the hydrodynamic roughness needed to employ the modified XBeach numerical model as was developed here for Roi-Namur Island on Kwajalein Atoll for RC-2334. The effort would need to include a field campaign to obtain wave and water level observations to calibrate a two-dimensional XBeach model for Wake Island. This calibrated and validated model would, in turn, be used to project annual wave-driven flooding of the island and its associated impacts on infrastructure and terrestrial habitats along the lines of what was developed here for Roi-Namur for RC-2334. The data and analyses from this effort would be crucial for future base and infrastructure planning, and also make it possible to better project how sea-level rise and climate change will impact smaller atoll systems, which characterize the majority of US and US-Affiliated atolls.

5 Acknowledgments

This project was funded by the US Department of Defense's (DOD) Strategic Environmental Research and Development Program (SERDP) under Project RC-2334, the USGS's Coastal and Marine Geology Program, and NOAA's National Centers for Coastal and Ocean Science. Andrea O'Neill (USGS), DOD, and SERDP contributed numerous excellent suggestions and a timely review of our work. Use of trademark names does not imply USGS endorsement of products.

6 Additional Digital Information

For more information on the United States Geological Survey's Pacific Coastal and Marine Science Center, please see:
http://walrus.wr.usgs.gov/

For more information on the National Oceanographic and Atmospheric Administration's National Centers for Coastal and Ocean Science, please see:
http://coastalscience.noaa.gov/

For more information on the Deltares' Coastal and Estuarine Systems Program, please see:
https://www.deltares.nl/en/issues/system-behaviour-coasts-estuaries-rivers/

For more information on the University of Hawaii's International Pacific Research Center, please see:
http://iprc.soest.hawaii.edu/

7 References Cited

Annamalai H, Okajima H, Watanabe M (2007) Possible impact of the Indian Ocean SST on the Northern Hemisphere circulation during El Niño, Journal of Climate, v. 20, p. 3164-3189.

Annamalai H, Sooraj, KP, Kumar A, Wang H (2011) Feasibility of dynamical seasonal precipitation prediction for the Pacific Islands. Science and Technology Infusion Climate Bulletin, NOAA.

Anthony SS (2007) Hydrogeology of selected islands of the Federated States of Micronesia. In Geology and Hydrogeology of Carbonate Islands. Developments in Sedimentology 54; Vacher HL, Quinn T, Eds.; Elsevier: Amsterdam, The Netherlands, p. 693-706.

Arnell NW, Reynard NS (1996) The effects of climate change due to global warming on river flows in Great Britain. Journal of Hydrology, v. 183(3–4), p. 397–424.

Aucan J, Hoeke RK, Merrifield MA (2012) Wave-driven sea level anomalies at the Midway tide gauge as an index of North Pacific storminess over the past 60 years. Geophysical Research Letters, v. 39, L17603

Bailey RT, Jenson JW, Olsen AE (2010) Estimating the ground water resources of atoll islands. Water, v. 2, p. 1-27.

Baird ME, Atkinson MJ (1997) Measurement and prediction of mass transfer to experimental coral reef communities. Limnology and Oceanography, v. 42, p. 1685–1693.

Battjes JA (1974) Surf similarity. Proceedings of the 14th Conference of Coastal Engineering, ASCE, p. 466–480.

Battjes JA (1975) Modeling of turbulence in the surf zone. Proceedings of Symposium on Modeling Technology, ASCE, p. 1050–1061.

Becker M, Meyssignac B, Letetrel C, Llovel W, Cazenave A, Delcroix T (2012) Sea level variations at tropical Pacific islands since 1950. Global and Planetary Change, v. 80–81, p. 85–98.

Buddemeier RW, Smith SV (1988) Coral reef growth in an era of rapidly rising sea levels: Predictions and suggestions for long-term research. Coral Reefs, v. 7, p. 51–56.

Burnett WC, Bokuniewicz H, Huettel M, Moore W, Taniguchi M (2003) Groundwater and pore water inpunts to the coastal zone. Biogeochemistry, v. 66, p. 3–33.

Burnett WC, Dulaiova H (2003) Estimating the dynamics of groundwater input into the coastal zone via continuous radon-222 measurements. Journal of Environmental Radioactivity, v. 69, p. 21–35.

Cheriton OM, Storlazzi CD, Rosenberger KJ (2016) Observations of wave transformation over a fringing coral reef and the importance of low-frequency waves and offshore water levels to runup, overwash, and coastal flooding. Journal of Geophysical Research Oceans, v. 121, p. 1–20.

Chowdhury MR, Chu P-S, Schroeder T (2007) ENSO and seasonal sea-level variability—A diagnostic discussion for the U.S.-Affiliated Pacific Islands. Theoretical and Applied Climatology, v. 88, p. 213–224.

Collins M, An S-I, Cai W, Ganachaud A, Guilyardi E, Jin F-F, Jochum M, Lengaigne M, Power S, Timmermann A, Vecchi G, Wittenberg A (2010) The impact of global warming on the tropical Pacific Ocean and El Nino. Nature Geoscience, v. 3, p. 391–397.

Coronado C, Candela J, Iglesias-Prieto R, Sheinbaum J, Lopez M, Oscampo-Torres FJ (2007) On the circulation in the Puerto Morales fringing reef lagoon. Coral Reefs, v. 26, p. 149–163.

Delcroix T, Cravatte S, McPhaden MJ (2007) Decadal variations and trends in tropical Pacific sea surface salinity since 1970. Journal of Geophysical Research, v. 112, C03012, doi:10.1029/2006JC003801.
Deser C, Philips AS, Alexander MA (2010) Twentieth century tropical sea surface temperature trends revisited. Geophysical Research Letters, v. 37, L107011.
Dickinson WR (2004) Impacts of eustasy and hydro-isostasy on the evolution and landforms of Pacific atolls. Palaeogeography, Palaeoclimatology, Palaeoecology, v. 213, p. 251–269.
Dickinson WR (2009) Pacific atoll living: How long already and until when? GSA Today, v. 19(3), p. 4–10.
Falter JL, Lowe RJ, Zhang Z, McCulloch M (2013) Physical and biological controls on the carbonate chemistry of coral reef waters: effects of metabolism, wave forcing, sea level, and geomorphology. PLoS ONE, v. 8(1), e53303.
Falkland AC (1994) Climate, hydrology and water resources of the Cocos (Keeling) Islands. Atoll Research Bulletin, v. 400, p. 1-23.
Federal Geographic Data Committee (FGDC) (1998) Geospatial Positioning Accuracy Standards Part 3: National Standard for Spatial Data Accuracy, FGDC-STD-007.3-1998, 28 pp.
Field DW (2007) Remote sensing of submerged habitats in the Dry Tortugas: a comparison of multiple sensors and classification techniques. Dissertation, University of South Carolina, Columbia, SC, 144 pp.
Fletcher CH, Richmond BM (2010) Climate change in the Federated States of Micronesia: Food and water security, climate risk management, and adaptive strategies. University of Hawaii Sea Grant Report TT-10-02, 32 pp.
Ford MR, Kench, PS (2015) Multi-decadal shoreline change in response to sea level rise in the Marshall Islands. Anthropocene, v. 11, p. 14-24.
Gawehn M, van Dongeren A, van Rooijen A, Storlazzi CD, Cheriton OM, Reniers A (2016) Identification and classification of very-low frequency waves on a coral reef flat. Journal of Geophysical Research–Oceans, v. 121, p. 1–20.
Gerritsen F (1980) Wave attenuation and wave set-up on a coastal reef. 17th International Conference on Coastal Engineering, Sydney, Australia, p. 444–461.
Gingerich SB (1996) Ground-water resources and contamination at Roi-Namur Island, Kwajalein Atoll, Republic of the Marshall Islands, 1990–91. U.S. Geological Survey Water-Resources Investigations Report 95-4275, 3 sheets.
Gingerich SB, Voss CI (2005) Three-dimensional variable density flow simulation of a coastal aquifer in southern Oahu, Hawaii, USA. Hydrogeology, v. 13, p. 436–450.
Gingerich SB, Voss CI, Johnson AG (2017) Seawater-flooding events and impact on freshwater lenses of low- lying islands: controlling factors, basic management and mitigation. Journal of Hydrology, in press.
Gourlay MR (1996) Wave set-up on coral reefs, 2: Set-up on reefs with various profiles. Coastal Engineering, v. 28, p. 17-55.
Green E, Mumby P, Edwards A, Clark C (2000) Remote sensing handbook for tropical coastal management, Coastal Management Sourcebooks 3, UNESCO, Paris, 316 pp.
Grinsted A, Moore JC, Jevrejeva S (2009) Reconstructing sea level from paleo and projected temperatures 200 to 2100 AD. Climate Dynamics, v. 34(4), p. 461–472
Hall JA, Gill S, Obeysekera J, Sweet W, Knuuti K, Marburger, J (2016) Regional Sea Level Scenarios for Coastal Risk Management: Managing the Uncertainty of Future Sea Level Change

and Extreme Water Levels for Department of Defense Coastal Sites Worldwide. U.S. Department of Defense, Strategic Environmental Research and Development Program, 224 pp.
Hearn C (1999) Wave-breaking hydrodynamics within coral reef systems and the effect of changing sea level. Journal of Geophysical Research, v. 104(C12), p. 30007–30019.
Hearn CJ, Atkinson MJ, Falter JL, (2001) A physical derivation of nutrient-uptake rates in coral reefs: effects of roughness and waves. Coral Reefs, v. 20, p. 347–356.
Hench JL, Rosman JH (2013) Observations of spatial flow patterns at the coral colony scale on a shallow reef flat. Journal of Geophysical Research, v. 118, p. 1142–1156.
Hodges K (1995) Feature tracking on the unit sphere. Monthly Weather Review, v. 123, p. 3458–3465.
Hodges K (1998) Feature-point detection using discrete transforms: application to tracking tropical convective complexes. Monthly Weather Review, v. 126, p. 785–795.
Hodges K (2008) Confidence intervals and significance tests for spherical data derived from feature tracking. Monthly Weather Review, v. 136, p. 1758–1777.
Hoegh-Guldberg O (1999) Climate change, coral bleaching and the future of the world's coral reefs. Marine and Freshwater Resources, v. 50, p. 839–866.
Hoeke RK, McInnes KL, Kruger JC, McNaught RJ, Hunter JR, Smithers SG (2013) Widespread inundation of Pacific islands triggered by distant-source wind-waves. Global and Planetary Change, v. 108, p. 128–138.
Hunt CD (1996) Ground-water resources and contamination at Kwajalein Island, Republic of the Marshall Islands, 1990–91. U.S. Geological Survey Water-Resources Investigations Report 94–4248, 3 sheets.
Hunt CD (2007) Hydrogeology of Diego Garcia. In Geology and Hydrogeology of Carbonate Islands. Developments in Sedimentology 54; Vacher HL, Quinn T, Eds.; Elsevier: Amsterdam, The Netherlands, p. 909-931.
Intergovernmental Panel on Climate Change (2007) Climate change 2007-The physical science basis, Contribution of Working Group I to the Fourth Assessment Report (AR4) of the Intergovernmental Panel on Climate Change, Eds. Solomon et al., Cambridge University Press, Cambridge, United Kingdom, 996 pp.
Jensen JR (2005) Introductory Digital Image Processing, A Remote Sensing Perspective, 3ed., Saddle River, NJ, Prentice-Hall Inc., 526 pp.
Johnson AG, Engott JA, Bassiouni, M (2014) Spatially distributed groundwater recharge estimated using a water-budget model for the Island of Maui, Hawai'i, 1978–2007. US Geological Survey, Scientific Investigations Report 2014–5168, 53 pp.
Jones NL, Lowe RJ, Pawlak G, Fong DA, Monismith SG (2008) Plume dispersion on a fringing coral reef system. Limnology and Oceanography, v. 53, p. 2273–2286.
Kanno A, Koibuchi Y, Isobe M (2011) Shallow water bathymetry from multispectral satellite images: extensions of Lyzenga's method for improving accuracy. Coastal Engineering Journal v. 53, p. 431–450.
Kanno A, Tanaka Y, Shinohara R, Kurosawa A, Sekine M (2014) Which spectral sands of WorldView-2 are useful in remote sensing of water depth? A case study in coral reefs. Marine Geodesy, v. 37 p. 283–292.
Kendall MS, Battista TA, Menza C (2012) Majuro Atoll, Republic of the Marshall Islands Coral Reef Ecosystems Mapping Report. NOAA National Centers for Coastal Ocean Science, Center for Coastal Monitoring, Biogeography Branch. Silver Spring, Maryland. NOAA Technical Memorandum, NOS NCCOS 144, 19 pp.

Knutson T, McBride JL, Chan J, Emanuel K, Holland G, Landsea C, Held I, Kossin JP, Srivastava, Sugi M (2010) Tropical cyclones and climate change. Nature Geoscience, v. 3, p. 157–163.

Kopp RE, Horton RM, Little CM, Mitrovica JX, Oppenheimer M, Rasmussen DJ, Strauss BH, and Tebaldi C (2014) Probabilistic 21st and 22nd century sea-level projections at a global network of tide-gauge sites. Earth's Future, v. 2, p.1–24.

Kraines SB, Yanagi T, Isobe M, Komiyama J (1998) Wind-wave driven circulation on the coral reef at Bora Bay, Miyako Island. Coral Reefs, v. 17, p. 133-143.

Lauer A, Wang Y, Phillips VTJ, McNaughton CS, Bennartz R, Clarke AD (2009) Simulating marine boundary layer clouds over the Eastern Pacific in a regional climate model with double-moment cloud microphysics. Journal of Geophysical Research-Atmospheres, v. 114, D21205.

Lauer A, Hamilton K, Wang Y, Phillips VTJ, Bennartz R (2010) The impact of global warming on marine boundary layer clouds over the Eastern Pacific – A regional model study. Journal of Climate, v. 23(21), p. 5844–5863.

Lee Z, Carder KL, Mobley CD, Steward RG, Patch JS (1999) Hyperspectral remote sensing for shallow waters: 2. Deriving bottom depths and water properties by optimization. Applied Optics, v. 38, p. 3831–3843.

Lee Z, Carder KL, Chen RF, Peacock TG (2001) Properties of the water column and bottom derived from Airborne Visible Imaging Spectrometer (AVIRIS) data. Journal of Geophysical Research, v.106, p. 11639–11651.

Lee Z, Carder KL (2002) Effect of spectral band numbers on the retrieval of water column and bottom properties from ocean color data. Applied Optics, v. 41, p. 2191–2201.

Lowe RJ, Falter JL, Bandet MD, Pawlak G, Atkinson MJ, Monismith SG, Koseff JR (2005) Spectral wave dissipation over a barrier reef. Journal of Geophysical Research, v. 110, C04001.

Lowe RJ, Falter JL, Monismith SG, Atkinson MJ (2009a) Wave-driven circulation of a coastal reef-lagoon system. Journal of Physical Oceanography, v. 39, p. 873–893.

Lowe RJ, Falter JL, Monismith SG, Atkinson MJ (2009b) A numerical study of circulation in a coastal reef-lagoon system. Journal of Geophysical Research, v. 114, C06022.

Lugo-Fernandez A, Roberts HH, Suhayda JN (1998) Wave transformations across a Caribbean fringing-barrier Coral Reef. Continental Shelf Research, v. 18, p. 1099–1124.

Lyzenga DR (1978) Passive remote sensing techniques for mapping water depth and bottom features. Applied Optics, v. 17, p. 379–383.

Lyzenga DR (1981) Remote sensing of bottom reflectance and water attenuation parameters in shallow water using aircraft and Landsat data. International Journal of Remote Sensing, v. 2, p. 71–82.

Lyzenga DR, Malinas NP, Tanis FJ (2006) Multispectral bathymetry using a simple physically based algorithm. IEEE Transactions on Geoscience and Remote Sensing, v. 44(8), p. 2251–2259

Manheim FT, Krantz DE, Bratton JF (2004) Studying ground water under Delmarva coastal bays using electrical resistivity. Ground Water, v. 42, p. 1052–1068.

Maritorena S, Morel A, Gentili, B (1994) Diffuse reflectance of oceanic shallow waters: Influence of water depth and bottom albedo. Limnology and Oceanography, v. 39, p. 1689–1703.

McDonald CB, Koseff JR, Monismith SG (2006) Effects of the depth to coral height ratio on drag coefficients for unidirectional flow over coral. Limnology and Oceanography, v. 51(3), p. 1294–1301.

Merrifield MA, Merrifield ST, Mitchum GT (2009) An anomalous recent acceleration of global sea-level rise. Journal of Climate, v. 22, p. 5772–5781.
Merrifield MA (2011) A shift in western tropical Pacific sea level trends during the 1990s. Journal of Climate, v. 24, p. 4126–4138.
Mishra D, Narumalani S, Lawson M, Rundquist D (2004a) Bathymetric mapping using IKONOS multispectral data. GIScience and Remote Sensing, v. 41, p. 301–321.
Mishra D, Narumalani S, Rundquist D, Lawson M (2004b) High-resolution ocean color remote sensing of benthic habitats: a case study at the Roatan Island, Honduras. Transactions on Geoscience and Remote Sensing, v. 43, p. 1592–1604.
Mishra D, Narumalani S, Rundquist D, Lawson M (2006) Benthic habitat mapping in tropical environments using QuickBird multispectral data. Photogrammetric Engineering & Remote Sensing, v. 72, p. 1037–1048.
Monismith SG, Herdman LMM, Ahmerkamp S, Hench JL (2013) Wave transformation and wave-driven flow across a steep coral reef. Journal of Physical Oceanography, v. 43, p. 1356–1379.
Monismith SG, Rogers JS, Koweek D, Dunbar RB (2015) Frictional wave dissipation on a remarkably rough reef. Geophysical Research Letters, v. 42, GL063804.
Montaggioni LF (2005) History of Indo-Pacific coral reef systems since the last glaciation: Development patterns and controlling factors. Earth Science Reviews, v. 71(1–2), p. 1–75.
National Oceanic and Atmospheric Administration, Center for Operational Oceanographic Products and Services (2003) Computational techniques for tidal datums handbook: NOAA Special Publication NOS CO-OPS 2, 98 pp.
National Oceanic and Atmospheric Administration, Center for Operational Oceanographic Products and Services (2013) Kwajalein, Marshall Islands, Station ID: 1820000, tide data. https://tidesandcurrents.noaa.gov/stationhome.html?id=1820000
Novatel, 2014, Base station coordinate determination using precise point positioning, 2 pp., http://www.novatel.com/assets/Documents/Papers/BaseStationCoordinateDeterminationUsingPPP.pdf
Nicholls RJ, Cazenave A (2010) Sea-level rise and its impact on coastal zones. Science, v. 328, p. 1517–1520.
Pandolfi JM, Connolly SR, Marshall DJ, Cohen AL (2011) Projecting coral reef futures under global warming and ocean acidification. Science, v. 333(6041), p. 418–422.
Péquignet AC, Becker JM, Merrifield MA, Aucan J (2009) Forcing of resonant modes on a fringing reef during tropical storm Man-Yi. Geophysical Research Letters, v. 36, L03607.
Péquignet AC, Becker JM, Merrifield MA, Boc SJ (2011) The dissipation of wind wave energy across a fringing reef at Ipam, Guam. Coral Reefs, v. 30, p. 71–82.
Peterson FL, Gingerich SB (1995) Modeling atoll groundwater systems, In: El-Kadi (ed) Groundwater models for resources analysis and management: CRC Press, Boca Raton, Florida, p. 275–292.
Peterson FL (2007) Hydrogeology of the Marshall Islands. In Geology and Hydrogeology of Carbonate Islands. Developments in Sedimentology 54; Vacher, H.L., Quinn, T., Eds.; Elsevier: Amsterdam, The Netherlands, p. 611-666.
Philpot RP (1989) Bathymetric mapping with passive multispectral imagery. Applied Optics, v. 28, p. 1569–1578.
Pomeroy A, Lowe RJ, Symonds G, van Dongeren AR, Moore C (2012) The dynamics of infragravity wave transformation over a fringing reef. Journal of Geophysical Research, v. 117, C11022.

Pomeroy AWM, Lowe RJ, Bowyer C, Zhang Z, Falter J, van Dongeren A, Roelvink D (2013) The influence of hydrodynamic forcing on sediment transport pathways and shoreline evolution in a coral reef environment. Coastal Dynamics 2013: 7th International Conference on Coastal Dynamics, Arcachon, France, p. 1265–1276.

Post VE, Simmons CT (2010) Free convective controls on sequestration of salts into low-permeability strata: insights from sand tank laboratory experiments and numerical modelling. Hydrogeology Journal, v. 18(1), p. 39–54.

Quataert E, Storlazzi CD, van Rooijen A, Cheriton OM, van Dongeren A (2015) The influence of coral reefs and climate change on wave-driven flooding of tropical coastlines. Geophysical Research Letters, v. 42, p. 6407–6415.

Reidenbach MA, Monismith SG, Koseff J, Yahel G, Genin A (2006) Boundary layer turbulence and flow structure over a fringing coral reef. Limnology and Oceanography, v. 51, p. 1956–1968.

Riahi K, Krey V, Rao S, Chirkov V, Fischer G, Kolp P, Kindermann G, Nakicenovic N, Rafai P (2010) RCP-8.5: Exploring the consequence of high emission trajectories. Climatic Change, v. 109(1-2), p. 33–57.

Roelvink D, Reniers A, van Dongeren A, de Vries JV, McCall R, Lescinski J (2009)

Modelling storm impacts on beaches, dunes and barrier islands, Coastal Engineering, v. 56(11-12), p. 1133–1152.

Rogers JS, Monismith SG, Dunbar RB, Koweek D (2015) Field observations of wave-driven circulation over spur and groove formations on a coral reef. Journal of Geophysical Research Oceans, v. 120, p. 145–160.

Rosman JH, Hench JL (2011) A framework for understanding drag parameterizations for coral reefs. Journal of Geophysical Research, v. 116, C08025.

Roy P, Connell J (1991) Climate change and the future of atoll states. Journal of Coastal Research, v. 7, p. 1057-1075.

Rydlund PH Jr, Densmore BK (2012) Methods of practice and guidelines for using survey-grade global navigation satellite systems (GNSS) to establish vertical datum in the United States Geological Survey: U.S. Geological Survey Techniques and Methods, Book 11, Chapter D1, 102 pp.

Shope JB, Storlazzi CD, Erikson LH, Hegermiller CA (2016) Changes to extreme wave climates of islands within the Western Tropical Pacific throughout the 21st century under RCP 4.5 and RCP 8.5, with implications for island vulnerability. Global and Planetary Change, v. 141, p. 25–38.

Sooraj KP, Annamalai H, Kumar A, Wang H (2012) A comprehensive assessment of CFS seasonal forecasts over the tropics. Weather and Forecasting, v. 27, p. 3–27.

Souza WR, Voss CI (1987) Analysis of an anisotropic coastal aquifer system using variable-density flow and solute transport simulation. Journal of Hydrology, v. 92, p. 17–41.

Storlazzi CD, Elias EPL, Berkowitz P (2015a) Many atolls may be uninhabitable within decades due to climate change. Nature-Scientific Reports, v. 5, 14546.

Storlazzi CD, Shope JB, Erikson LH, Hegermiller CA, Barnard PL (2015b) Future Wave and Wind Projections for U.S. and U.S.-Affiliated Pacific Islands. U.S. Geological Survey Open-File Report 2015–1001, 426 p.

Stowasser M., Wang Y, Hamilton K (2007) Tropical cyclone changes in the western North Pacific in a global warming scenario. Journal of Climate, v. 20, p. 2378–2396.

Stowasser M., Annamalai H, Hafner, J (2009) Response of the south Asian summer monsoon to global warming: Mean and synoptic systems. Journal of Climate, v. 22, p. 1014–1036.
Stumpf RP, Holderied K, Sinclair M (2003) Determination of water depth with high-resolution satellite imagery over variable bottom types. Limnology and Oceanography, v. 48(1/2), p. 547–556.
Svendsen IA (2003) Introduction to Nearshore Hydrodynamics. Advanced Series on Ocean Engineering, v 24, World Scientific, Singapore, 722 pp.
Swarzenski PW, Burnett WC, Greenwood WJ, Herut B, Peterson R, Dimova N, Shalem Y, Yechieli Y, Weinstein Y (2006) Combined time-series resistivity and geochemical tracer techniques to examine submarine groundwater discharge at Dor Beach, Israel. Geophysical Research Letters, v. 33, L24405.
Swarzenski PW, Kruse S, Reich C, Swarzenski WV (2007) Multi-channel resistivity investigations of the freshwater-saltwater interface: a new tool to study an old problem. In: A New Focus on Groundwater-Seawater Interactions, Proceedings of Symposium HS1001 at IUGG2007, Perugia, p. 1–7.
Swarzenski PW, Simonds FW, Paulson AJ, Kruse S, Reich C (2007) Geochemical and geophysical examination of submarine groundwater discharge and associated nutrient loading estimates into Lynch Cove, Hood Canal, WA. Environmental Science and Technology, v. 41, p. 7022–7029.
Swarzenski PW, Dailer ML, Glenn CR, Smith CG, Storlazzi CD (2013) A geochemical and geophysical assessment of coastal groundwater discharge at select sites in Maui and Oahu, Hawaii. Groundwater in the Coastal Zones of the Asia Pacific, p. 1–36.
Symonds G, Huntley DA, Bowen AJ (1982) Long wave generation by a time-varying breakpoint. Journal of Geophysical Research, v. 87(C1), p. 492–498.
Tamura H, Nadaoka K, Paringit EC (2007) Hydrodynamic characteristics of a fringing coral reef on the east coast of Ishigaki Island, southwest Japan. Coral Reefs, v. 26, p. 17–34.
Tarya A, Hoitink AJF, Van der Vegt M (2010) Tidal and subtidal flow patterns on a tropical continental shelf semi-insulated by coral reefs. Journal of Geophysical Research, v. 115, C09029.
Terry JP, Falkland AC (2010) Response of atoll freshwater lenses to storm-surge overwash in the Northern Cook Islands. Hydrogeology, v. 18, p. 749-759.
Thomas FIM, Atkinson MJ (1997) Ammonium uptake by coral reefs: Effects of water velocity and surface roughness on mass transfer. Limnology and Oceanography, v. 42, p. 81–88.
Thomson AM, Calvin KV, Smith SJ, Kyle GP, Volke A, Patel P, Delgado-Arias S, Bond Lamberty B, Wise MA, Clarke LE, Edmonds JA (2010) RCP4.5: A Pathway for Stabilization of Radiative Forcing by 2100. Climatic Change, v. 109(1-2), p. 77–94.
Tolman, HL (1997) User manual and system documentation of WAVEWATCH-III version 1.15. NOAA/NWS/NCEP/OMB Technical Note 151, 97 pp.
Tolman, HL (1999) User manual and system documentation of WAVEWATCH-III version 1.18. NOAA/NWS/NCEP/OMB Technical Note 166, 110 pp.
Tolman, HL (2009) User manual and system documentation of WAVEWATCH III version 3.14. NOAA/NWS/NCEP/MMAB Technical Note 276, 194 pp.
Underwood MR, Peterson FL, Voss CI (1992) Groundwater lens dynamics of Atoll Islands. Water Resources Research, v. 28, p. 2889–2902.

U.S. Geological Survey (1998) National field manual for the collection of water-quality data. U.S. Geological Survey Techniques of Water-Resources Investigations, Book 9, Chapters A1–A9. U.S. Geological Survey, Reston, VA.
Van der Westhuysen AJ (2010), Modeling of depth-induced wave breaking under finite depth wave growth conditions. Journal of Geophysical Research, v. 115(C1), C01008.
Van Dongeren AR, Reniers AJHM, Battjes JA (2003) Numerical modeling of infragravity wave response during DELILAH. Journal of Geophysical Research, v. 108(C9), 3288.
Van Dongeren A, Lowe R, Pomeroy A, Trang DM, Roelvink D, Symonds G, Ranasinghe R (2013) Numerical modeling of low-frequency wave dynamics over a fringing coral reef. Coastal Engineering, v. 73, p. 178–190.
Van Gent MRA (2001) Wave runup on dikes with shallow foreshores. Journal of Waterway, Port, Coastal and Ocean Engineering, v. 127, p. 254–262.
Vermeer M, Rahmstorf S (2009), Global sea level linked to global temperature. Proceedings of the National Academy of Sciences, v. 106, p. 21527–21532.
Vetter O, Becker JM, Merrifield MA, Pequignet A-C, Aucan J, Boc SJ, Pollock CE (2010) Wave setup over a Pacific Island fringing reef. Journal of Geophysical Research, v. 115, C12066.
Voss CI, Provost AM (2002) SUTRA: A model for saturated-unsaturated variable-density ground-water flow with solute or energy transport. U.S. Geological Survey Water-Resources Investigations Report 02-4231, 291 pp., Version of September 22, 2010.
Wang L, Wang Y, Lauer A, Xie S-P (2011) Simulation of seasonal variation of marine boundary layer clouds over the eastern Pacific with a regional climate model. Journal of Climate, v. 24, p. 3190–3210.
Webb AP, Kench PS (2010) The dynamic response of reef islands to sea-level rise: evidence from multi-decadal analysis of island change in the Central Pacific. Global and Planetary Change, v. 72, p. 234–246.
Wolanski E (1983) Tides on the northern Great Barrier Reef continental shelf. Journal of Geophysical Research, v. 88, p. 5953–5959.
Wolanski E, Bennett AF (1983) Continental shelf waves and their influence on the circulation around the Great Barrier Reef. Australian Journal of Marine and Freshwater Research, v. 34, p. 23–47.
Wolanski E, Pickard GL (1983) Currents and flushing of Britomart Reef, Great Barrier Reef. Coral Reefs, v. 2, p. 1–8.
Wolanski E, Thomson RE (1984) Wind-driven circulation on the northern Great Barrier Reef continental shelf in summer. Estuarine Coastal and Shelf Science, v. 18, p. 271–289.
Woodroffe CD (2008) Reef-island topography and the vulnerability of atolls to sea-level rise. Global and Planetary Change, v. 62, p. 77–96.
World Climate Research Programme (2011) CMIP5 - Coupled Model Intercomparison Project Phase 5 overview. http://cmip-pcmdi.llnl.gov/cmip5/
Wozencraft J, Lee M, Tuell G, Philpot, W (2003) Use of SHOALS data to produce spectrally-derived maps in Kaneohe Bay, Hawaii. U.S. Hydrographic Conference, Biloxi, MS, 24-27 March 2003.
Wright T (2006) Tropical storm Talas formation and impacts on Kwajalein atoll. Paper J16A.3 presented at the 27th American Meteorological Society Conference on Hurricanes and Tropical Meteorology.
Zektser IS, Dzyuba AV (2014) Submarine discharge into the Barents and White Seas. Environmental and Earth Sciences, v. 71, p. 723–729.

Zhang Z, Lowe R, Falter J, Ivey G (2011) A numerical model of wave- and current-driven nutrient uptake by coral reef communities. Ecological Modelling, v. 222, p. 1456–1470.

Appendix A1. List of Scientific and Technical Publications

PAPERS

Gingerich, SB, Voss, CI, Johnson AG (*in review*) Mitigation of impacts due to seawater-flooding events over lenses of low-lying islands in a future climate. Water Resources Management

Oberle, FKJ, Swarzenski PW, Storlazzi CD (*in review*). Atoll groundwater movement and its response to climatic and sea-level fluctuations. Water.

Pearson S, Storlazzi CD, van Dongeran A, Tissier M, Reniers A (*in review*) A Bayesian-based system to assess wave-driven flooding hazards on coral reef-lined coasts. Journal of Geophysical Research-Oceans.

Widlansky MJ, Annamalai H, Gingerich SB, Storlazzi, CD, Marra, JJ, Hodges KI (*in review*) Tropical cyclone projections: Changing climate threats for Pacific Island defense installations. Asia-Pacific Issues.

Gingerich, SB, Voss, CI, Johnson AG (2017) Seawater-flooding events and impact on freshwater lenses of low-lying islands: controlling factors, basic management and mitigation. Journal of Hydrology, v. 551, p. 676-688.

Vitousek SK, Barnard PL, Fletcher CH, Frazer N, Erikson LH, Storlazzi CD (*in press*) Exponential increase in coastal flooding frequency due to sea-level rise. Nature-Scientific Reports.

Hejazian M, Gurdak JJ, Swarzenski PW, Odigie KO, Storlazzi CD (2017) Land-use change and managed aquifer recharge effects on the hydrogeochemistry of two contrasting atoll island aquifers, Roi-Namur Island, Republic of the Marshall Islands. Applied Geochemistry, v. 80, p. 58-71.

Cheriton OM, Storlazzi CD, Rosenberger KJ (2016) Observations of wave transformation over a fringing coral reef and the importance of low-frequency waves and offshore water levels to runup, overwash, and coastal flooding." Journal of Geophysical Research-Oceans, v. 121, C011231.

Gawehn M, van Dongeren A, van Rooijen A, Storlazzi CD, Cheriton OM, Reniers A (2016) Identification and classification of very-low frequency waves on a coral reef flat. Journal of Geophysical Research-Oceans, v. 121, C011834.

Shope JB, Storlazzi CD, Erikson LH, Hegermiller CA (2016) Changes to extreme wave climates of islands within the Western Tropical Pacific throughout the 21st century under RCP 4.5 and RCP 8.5, with implications for island vulnerability. Global and Planetary Change, v. 141, p. 25-38.

Quataert E, Storlazzi CD, van Rooijen A, Cheriton OM, van Dongeren A (2015) The influence of coral reefs and climate change on wave-driven flooding of tropical coastlines. Geophysical Research Letters, v. 42, p. 6407-6415.

CONFERENCE PROCEEDINGS

Shope JB, Storlazzi CD, Erikson LH, Hegermiller CA (2015) Modeled changes in extreme wave climates of the tropical Pacific over the 21st century: Implications for U.S. and U.S.-Affiliated atoll islands. Proceedings of Coastal Sediments 2015, 0247, p. 1-13.

Gingerich SB, Voss CI (2014) Sea-level rise and seawater inundation of an atoll island, Roi-Namur, Kwajalein Atoll, Republic of the Marshall Islands. Wiederhold, H., Michaelsen, J.,

Hinsby, K., and Nommensen, B., eds.: Programme and Proceedings, SWIM 2014, 23rd Salt Water Intrusion Meeting, p. 129-131.
van Dongeren A, Storlazzi CD, Quataert E, Pearson S (2017) Wave dynamics and flooding on low-lying tropical reef-lined coasts. Proceedings of Coastal Dynamics 2017, p. 654-664.

THESES

James Shope, University of California at Santa Cruz, *Predicting Potential Impacts of Sea-Level Rise on Pacific Island Atolls*, Ph.D. 2016
Stuart Pearson, Delft University of Technology (The Netherlands), *Predicting Wave-induced Flooding on Low-lying Tropical Islands*, M.Sc., 2016
Matthijs Gawehn, Delft University of Technology (The Netherlands), *Processes Behind Wave Run-Up on an Atoll*, M.Sc., 2015
Ellen Quataert, Delft University of Technology (The Netherlands), *Wave Run-Up on Atoll* Reefs, M.Sc., 2015

CONFERENCE ABSTRACTS

Oberle FKJ, Swarzenski PW, Storlazzi CD (2017) Groundwater exchange on a low-lying carbonate atoll island: Roi Namur, Republic of the Marshall Islands. 2017 Goldschmidt Conference.
Hegermiller CA, Shope JB, Erikson LH, Storlazzi CD, Barnard PL, (2017) Projections of future wave conditions offshore of Pacific Islands. GSA 2017 Cordilleran Section Meeting.
Shope JB, Storlazzi CD (2017) Assessing morphologic controls on atoll island shoreline stability due to sea-level rise. GSA 2017 Cordilleran Section Meeting.
Storlazzi CD, Barnard PL (2017) Climate change, coral reefs, and atoll sustainability. GSA 2017 Cordilleran Section Meeting.
Oberle FKJ, Swarzenski PW, Storlazzi CD (2017) Coastal groundwater exchange on a small Pacific atoll island: Roi Namur, Republic of the Marshall Islands. European Geophysical Union 2017 General Assembly.
Cheriton OM, Storlazzi CD, Rosenberger KJ (2016) Wave transformation over a fringing coral reef and the importance of low-frequency waves and offshore water levels to runup and island overtopping. 2016 Ocean Sciences Meeting.
Storlazzi CD, Quataert, E., van Rooijen A., Cheriton O.M., and van Dongeren A., (2016) The influence of corals, coral reef morphology, and climate change on waves and wave-driven water levels along reef-lined coasts. 2016 Ocean Sciences Meeting.
Hejazian M, Swarzenski PW, Gurdak JJ, Odigie K, Storlazzi CD (2015) Effects of land-use change and managed aquifer recharge on geochemical reactions with implications for groundwater quantity and quality in atoll island aquifers, Roi-Namur, Republic of the Marshall Islands. American Geophysical Union 2015 Fall Meeting.
Swarzenski PW, Hejazian M, Gurdak JJ, Odigie K, Storlazzi CD (2015) Hydrogeology and geochemistry of the freshwater lens on Roi Namur atoll, the Republic of the Marshall Islands. American Geophysical Union 2015 Fall Meeting.
Hejazian M, Swarzenski PW, Gurdak JJ, Odigie K, Storlazzi CD (2015) A Tale of two islands: Influence of artificial recharge and carbon on the geochemistry of atoll island carbonate aquifers, Roi-Namur, Republic of the Marshall Islands. GSA 2015 Annual Meeting.

Storlazzi CD, Shope JB, Erikson LH, Hegermiller CA, Barnard PL (2015) Future Wave and Wind Projections for U.S. and U.S.-Affiliated Pacific Islands. Pacific Islands Climate Change Cooperative 2015 Meeting.

Cheriton OM, Storlazzi CD, Rosenberger KJ, Quataert E, van Dongeren A (2014) Swell-generated set-up and infragravity wave propagation over a fringing coral reef: Implications for wave-driven inundation of atoll islands. American Geophysical Union 2014 Fall Meeting